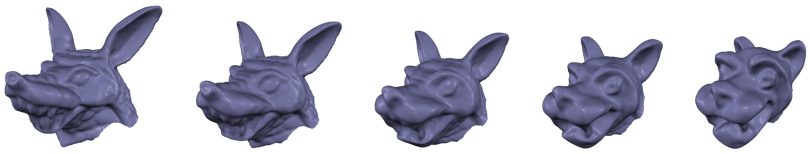

Processing Elastic Surfaces and Related Gradient Flows

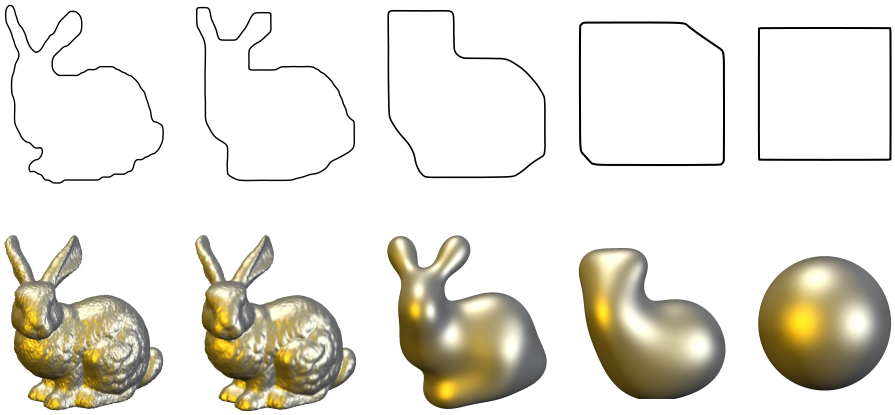

DISSERTATION

zur Erlangung des Doktorgrades (Dr. rer. nat.)
der Mathematisch–Naturwissenschaftlichen Fakultät
der Rheinischen Friedrich–Wilhelms–Universität Bonn

vorgelegt von Nadine Olischläger
aus Mönchengladbach

Bonn, April 2010

Angefertigt mit Genehmigung der Mathematisch–Naturwissenschaftlichen Fakultät
der Rheinischen Friedrich–Wilhelms–Universität Bonn
am Institut für Numerische Simulation

Diese Dissertation ist auf dem Hochschulschriftenserver der ULB Bonn
http://hss.ulb.uni-bonn.de/diss_online elektronisch publiziert.

Erscheinungsjahr 2010

1. Referent: Prof. Dr. Martin Rumpf
2. Referent: Prof. Dr. Holger Rauhut

Tag der Promotion: 21. Juli 2010

Preface

THIS thesis would not have been possible without the help, support and inspiration of many people. First of all I owe my deepest gratitude to my thesis advisor Prof. Dr. Martin Rumpf for all his help, support and guidance. Moreover, I would like to thank him for giving me the opportunity to widen my perspective through the active participation in workshops and conferences. I am grateful to Prof. Dr. Gerhard Dziuk for giving me the opportunity to learn about anisotropies when I enjoyed the hospitality of the Institute of Applied Mathematics at the University of Freiburg for several times. I would like to thank him for inspiring discussions on Willmore flow. I thank Prof. Dr. Holger Rauhut for being the co-referee.
During the work I always received help from my colleagues at the Institute for Numerical Simulation, University of Bonn. Especially, I would like to thank Benjamin Berkels, Martina Teusner and Orestis Vantzos who patiently answered all my questions on implementational topics as well as theoretical aspects. Furthermore, I am grateful to Orestis Vantzos for helping with the rendering in Figure 4.7. My roommates Stefan von Deylen and Benedict Geihe always endured my moods during the final phase of my thesis. Additionally, I thank my colleges Benjamin Berkels, Dr. Martin Lenz, Martina Teusner, Ole Schwen, Orestis Vantzos and Benedikt Wirth for proof reading selected chapters of my thesis and their valuable comments. I want to express my gratitude to my college Dr. Martin Lenz for his assistance, particularly in GRAPE related questions.
I had the opportunity to get a deep inside in the software package GRAPE that has been developed at the Collaborative Research Center 256 at the University of Bonn and at the Institute for Applied Mathematics at the University of Freiburg [162, 147, 98]. We developed i.a. visualization tools in cooperation with the Gesellschaft für Anlagen- und Reaktorsicherheit where I was part of the third project "Weiterentwicklung der Rechenprogramme d^3f und r^3t (E-DuR)" funded by the German Federal Ministry of Education and Research [90, 91, 95]. I would like to thank Prof. Dr. Dietmar Kröner and Mirko Kränkel from the Institute for Applied Mathematics, University of Freiburg, for their hospitality and literally fruitful teamwork on programming new visualization methods. Most of the visualization in my thesis was done in GRAPE. I am grateful to Nathan Litke, Ph.D., for providing me with the pictures in Chapter 7.
I especially thank the German Science foundation for their financial support, in particular via the DFG project "Anisotrope Krümmungsflüsse in der Flächenmodellierung", the Collaborative Research Center 611 and the Hausdorff Center for Mathematics in Bonn.
My deepest gratitude goes to my family for their unflagging love and support throughout my life. Especially, I am indebted to my mother, my father and my brother for their care and love. This dissertation is simply impossible without them. Last but not least I thank my companion in life as he is simply perfect. ∞^∞.

Bonn, April 2010 Nadine Olischläger

Abstract

SURFACE processing tools and techniques have a long history in the fields of computer graphics, computer aided geometric design and engineering. In this thesis we consider variational methods and geometric evolution problems for various surface processing applications including surface fairing, surface restoration and surface matching. Geometric evolution problems are often based on the gradient flow of geometric energies. The Willmore functional, defined as the integral of the squared mean curvature over the surface, is a geometric energy that measures the deviation of a surface from a sphere. Therefore, it is a suitable functional for surface restoration, where a destroyed surface patch is replaced by a smooth patch defined as the minimizer of the Willmore functional with boundary conditions for the position and the normal at the patch boundary.

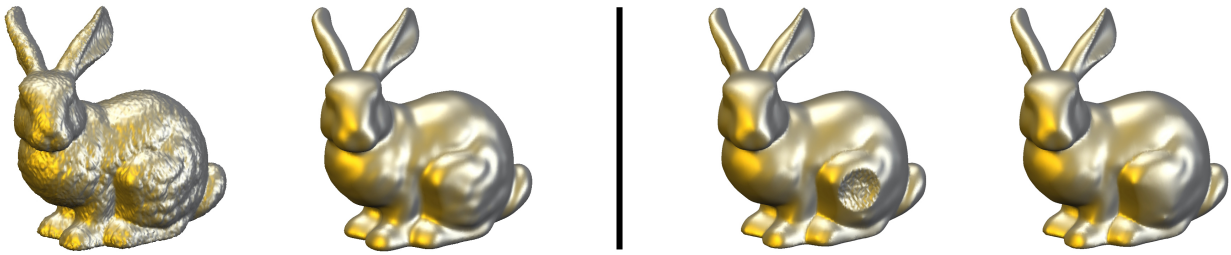

Surface denoising (left) and surface restoration (right) by the Willmore flow.

However, using the Willmore functional does not lead to satisfying results if an edge or a corner of the surface is destroyed. The anisotropic Willmore energy is a natural generalization of the Willmore energy which has crystal-shaped surfaces like cubes or octahedra as minimizers. The corresponding L^2-gradient flow, the anisotropic Willmore flow, leads to a fourth-order partial differential equation that can be written as a system of two coupled second second order equations. Using linear Finite Elements, we develop a semi-implicit scheme for the anisotropic Willmore flow with boundary conditions. This approach suffer from significant restrictions on the time step size. Effectively, one usually has to enforce time steps smaller than the squared spatial grid size. Based on a natural approach for the time discretization of gradient flows we present a new scheme for the time and space discretization of the isotropic and anisotropic Willmore flow. The approach is variational and takes into account an approximation of the L^2-distance between

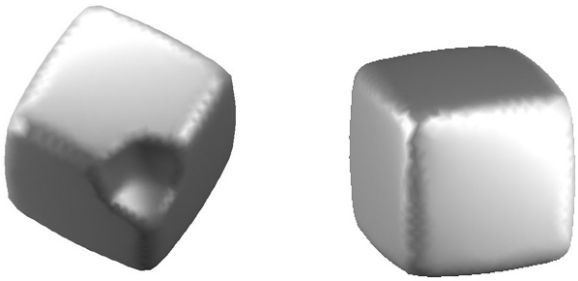

Surface restoration by the semi-implicit scheme of the anisotropic Willmore flow.

the surface at the current time step and the unknown surface at the new time step as well as a fully implicity approximation of the anisotropic Willmore functional at the new time step. To evaluate the anisotropic Willmore energy on the unknown surface of the next time step, we first ask for the solution of an inner, secondary variational problem describing a time step of anisotropic mean curvature motion. The time discrete velocity deduced from the solution of the latter problem is regarded as an approximation of the anisotropic mean curvature vector and enters the approximation of the actual anisotropic Willmore functional. The resulting two step time discretization of the Willmore flow is applied to polygonal curves and triangular surfaces and is independent of the co-dimension. Various numerical examples underline the stability of the new scheme, which enables time steps of the order of the spatial grid size.

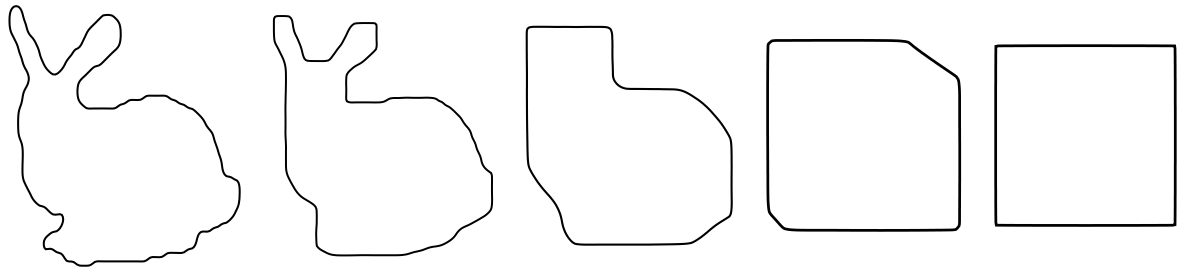

Different time steps of the two step time discretization for the anisotropic Willmore flow of an original bunny-shaped curve towards a square.

The Willmore functional of a surface is referred to as the elastic surface energy. Another interesting application of modeling elastic surfaces as minimizers of elastic energies is surface matching, where a correspondence between two surfaces is subject of investigation. There, we seek a mapping between two surfaces respecting certain properties of the surfaces. The approach is variational and based on well-established matching methods from image processing in the parameter domains of the surfaces instead of finding a correspondence between the two surfaces directly in 3D. Besides the appropriate modeling we analyze the derived model theoretically. The resulting deformations are globally smooth, one-to-one mappings. A physically proper morphing of characters in computergraphic is capable with the resulting computational approach.

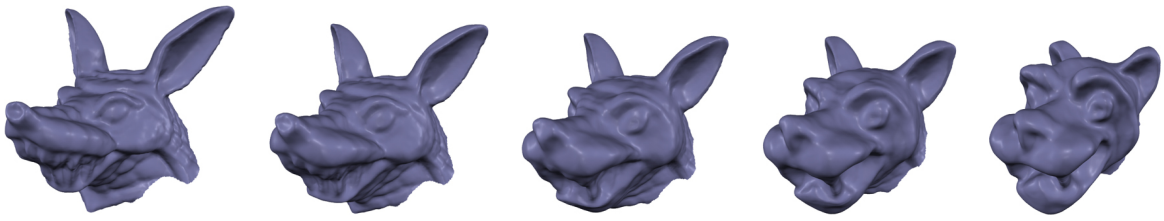

A 3D morph between two different faces is shown.

Contents

Notation

Geometric analysis

$\mathcal{M}$	d-dimensional surface embedded in $\mathbb{R}^m$ with $m \geq d+1$
$x : \mathcal{M} \to \mathbb{R}^m$	its parametrization (assumed to be the identity on the surface $\mathcal{M} = \mathcal{M}[x]$)
S^d	unit sphere in $\mathbb{R}^{d+1}$
$n : \mathcal{M} \to S^d$	Gauß map, normal mapping of $\mathcal{M}$, cf. Definition 2.1.1
$\mathcal{T}_p\mathcal{M}$	embedded tangent space, cf. Definition 2.1.2
$\partial\mathcal{M}$	boundary of $\mathcal{M}$
n^{co}	co-normal at the boundary of $\mathcal{M}$, perpendicular to n and $\partial\mathcal{M}$
$\partial_n\vartheta$	$= n \cdot \nabla_{\mathcal{M}}\vartheta$, derivative of ϑ in direction n
∇	usual gradient in $\mathbb{R}^{d+1}$
$\nabla_{\mathcal{M}}$	tangential gradient, orthogonal projection of ∇ onto $\mathcal{T}_p\mathcal{M}$, cf. Definition 2.1.3
$\mathbf{h}$	mean curvature, cf. Definition 2.1.7
$\mathrm{div}_{\mathcal{M}}$	tangential divergence, cf. Definition 2.1.4
$\Delta_{\mathcal{M}}$	$\mathrm{div}_{\mathcal{M}}\nabla_{\mathcal{M}}$ Laplace-Beltrami operator, cf. Definition 2.1.5
S	$= \nabla_{\mathcal{M}} n$ Weingarten map or Shape operator, cf. Definition 2.1.6

Concept of Anisotropy

γ	elliptical integrand $\gamma : \mathbb{R}^{d+1} \to \mathbb{R}_0^+ \in \mathcal{C}^3(\mathbb{R}^{d+1} \setminus 0) \cap \mathcal{C}^0(\mathbb{R}^{d+1})$, positive, positively homogeneous of degree one, convex, cf. Definition 2.2.1
γ_z	first derivative of γ
γ_{zz}	second derivaive of γ
$\mathcal{F}_\gamma$	Frank diagram of γ, cf. Definition 2.2.2
$\mathcal{W}_\gamma$	Wulff shape of γ, cf. Definition 2.2.2
n_γ	$= \gamma_z \circ n : \mathcal{M} \to \mathcal{W}_\gamma$ Cahn–Hoffmann vector, cf. Definition 2.2.3
$\mathbf{h}_\gamma$	anisotropic mean curvature, cf. Definition 2.2.3
S_γ	$= \nabla_{\mathcal{M}} n_\gamma = \gamma_{zz}\nabla_{\mathcal{M}} n$ generalized Weingarten map, cf. Definition 2.2.4
Δ_γ	$= \mathrm{div}_{\mathcal{M}}(\gamma_{zz}\ \nabla_{\mathcal{M}})$ generalized Laplace-Beltrami operator, cf. Definition 2.2.5

Generalized gradient flows

$e[x]$	general energy functional
$a[x]$	$= \int_{\mathcal{M}} \mathrm{d}a$ area functional
$a_\gamma[x]$	$= \int_{\mathcal{M}} \gamma(n)\,\mathrm{d}a$ anisotropic area functional
$w[x]$	$= \frac{1}{2}\int_{\mathcal{M}} \mathbf{h}^2\,\mathrm{d}a$ Willmore functional
$w_\gamma[x]$	$= \frac{1}{2}\int_{\mathcal{M}} \mathbf{h}_\gamma^2\,\mathrm{d}a$ anisotropic Willmore functional
$\langle e'[x], \vartheta\rangle$	$= \partial_\epsilon\big\vert_{\epsilon=0} e[x+\epsilon\vartheta]$ first variation of e at x in direction ϑ
ϑ	test function $\vartheta \in \mathcal{C}^1(\mathcal{M}, \mathbb{R}^m)$, cf. Equation (3.1)

Discretization

$\mathcal{M}[X]$	simplicial mesh, approximation of the surface $\mathcal{M}[x]$
$\mathcal{M}^{int}[X]$	$\subset \mathcal{M}[X]$ surface with inner nodes of $\mathcal{M}[X]$, cf. Equation (2.45)
$\mathcal{V}(\mathcal{M}[X])$	Finite Element space corresponding to $\mathcal{M}[X]$, cf. Equation (2.34)
$\mathcal{V}^{int}(\mathcal{M}[X])$	Finite Element space of $\mathcal{M}[X]$ with vanishing boundary values, cf. Equation (2.34)
X	$\in \mathcal{V}(\mathcal{M}[X])^m$, identity on the simplicial mesh $\mathcal{M}[X]$
$\bar{X}$	vector of vertex positions of the mesh
$M[X]$	mass matrix, cf. Equation (2.36)
$L[X]$	stiffness matrix, cf. Equation (2.37)
$L^\gamma[X]$	weighted stiffness matrix, $\gamma : \mathcal{M}[X] \to \mathbb{R}$ scalar weight, cf. Equation (2.38)
$L^\mu[X]$	weighted stiffness matrix, $\mu : \mathcal{M}[X] \to \mathbb{R}^{m,m}$ matrix-valued weight, cf. Equation (2.39)
$L^\mu_{\gamma_{zz}}[X]$	weighted anisotropic stiffness matrix, $\mu : \mathcal{M}[X] \to \mathbb{R}^{m,m}$ matrix-valued weight, cf. Equation (2.42)
E	extension operator, cf. Equation (2.47)
R	restriction operator, cf. Equation (2.48)

Miscellaneous

$\mathbb{I}$	identity mapping
$\mathcal{I}$	Lagrange interpolation on the linear Finite Element space
$\cdot$	Euclidean scalar product
δ_{ij}	Kronecker symbol
$a \otimes b$	$\in \mathbb{R}^{d+1,d+1}$, $a \otimes b := (a_i\, b_j)_{1\le i,j\le d+1}$ tensor product matrix
$a_i b_i$	$= \sum_i a_i b_i$, Einstein summation convention
$a \wedge b$	cross product of $a, b \in \mathbb{R}^3$
e_s	sth coordinate direction in $\mathbb{R}^m$
P_s	projection onto the plane spanned by the vectors e_{s-1} and e_{s+1}
D_s^α	counter-clockwise rotation by α degrees in the above plane
D^α	counter-clockwise rotation by α degrees in $\mathbb{R}^2$
$V^\perp$	$= D^{\frac{\pi}{2}} V$ for $V \in \mathbb{R}^2$

Chapter 1

Introduction

In this thesis a new approach for the time discretization of the discrete isotropic and anisotropic Willmore flow of polygonal curves and triangulated surfaces is presented. The Willmore flow is the L^2-gradient flow of surfaces for the Willmore energy, which measures the squared mean curvature on the surface. Let $\mathcal{M}$ be a two-dimensional surface embedded in $\mathbb{R}^3$. Then, the Willmore energy is given by

$$w(\mathcal{M}) = \frac{1}{2}\int_{\mathcal{M}} \mathbf{h}^2 \,\mathrm{d}a,$$

where $\mathbf{h}$ denotes the mean curvature, i.e. $\mathbf{h}$ is the sum of the principle curvatures on $\mathcal{M}$ and $\mathrm{d}a$ is the area element of the induced metric of $\mathcal{M}$. It is named after the English geometer Tom Willmore [170] and referred to as the elastic surface energy. Modeling elastic surfaces as minimizers of elastic energies appears in many research areas including biology, physics, solid mechanics and computer graphics. In *biology, biophysics* and *bioengineering* bending energies arise to model cell membranes, vesicles and liquid bilayers [154, 79]. The lipid bilayer of a biological membrane forms the boundary of a cell and consists of many different lipids and proteins that are embedded in the lipid bilayer to ensure the essential functional properties of the biomembrane like cell adhesion, ion channel conductance and cell signaling. The intracellular cytoskeleton is anchored to the membrane endowing it with further structural stability and elasticity, which is particularly observed in red blood cells. They can squeeze through tiny capillaries and still recover their shape. Mathematically, the cell membrane can be modeled as an embedded two-dimensional surface $\mathcal{M}$, because the thickness of a lipid bilayer is significantly smaller then the other dimensions of the whole layer. The shape of such elastic surfaces is determined by minimizing a general bending energy that was introduced by Canham [35], Helfrich [109] and Evans [89]. Provided that the constants $\alpha, \beta, h_0, \gamma$ fulfill certain structural inequalities, this energy reads

$$w_H(\mathcal{M}) = \int_{\mathcal{M}} \alpha + \beta(\mathbf{h} - h_0)^2 - \gamma\,\mathbf{k}\,\mathrm{d}a\,. \tag{1.1}$$

Here, $\mathbf{k}$ is the Gauß curvature, i.e. $\mathbf{k}$ is the product of the principle curvatures on $\mathcal{M}$. For $\alpha = \gamma = h_0 = 0$ and $\beta = \frac{1}{2}$ this model reduces to the Willmore energy. In *solid mechanics* it arises as the limit energy for thin plate theory, cf. [45, 46, 106, 105, 94, 93].

Figure 1.1: Surface fairing of the Stanford armadillo [2].

In *computer aided geometric design* and *computer graphics* the Willmore energy appears in the context of surface fairing and restoration of smooth surfaces [70, 176, 51, 25]. The advent of laser range scan technology in the last decade enables high-resolution models of real world surfaces and sculptures. The triangulated surfaces generated from this data are typically disturbed by noise, which is often due to local measurement errors. Therefore, these models have to be denoised in a post-processing step for further use. Often, parts of these surfaces are destroyed and have to be restored in a suitable way. Since the mean curvature arises as the first variation of the area functional

$$a(\mathcal{M}) = \int_{\mathcal{M}} \mathrm{d}a,$$

one can define an anisotropic mean curvature $\mathbf{h}_\gamma$ as the minimizer of the anisotropic area functional

$$a_\gamma(\mathcal{M}) = \int_{\mathcal{M}} \gamma(n)\,\mathrm{d}a$$

depending on an anisotropy $\gamma : \mathbb{R}^3 \to \mathbb{R}$. Here, n denotes the normal field on the surface $\mathcal{M}$. The anisotropic mean curvature plays an important role in *crystallography*. In 1901 Wulff [174] found a method to determine the equilibrium shape of a crystal of fixed volume inside a separate phase. The shape of this perfect crystal is referred to as Wulff shape and appears as the minimizer of the anisotropic area functional with prescribed volume. In the context of restoration of surfaces with edges and corners one is interested in a fourth-order energy having Wulff shapes as minimizers. The generalization of the classical Willmore functional, the anisotropic Willmore energy, is given by

$$w_\gamma(\mathcal{M}) = \frac{1}{2}\int_{\mathcal{M}} \mathbf{h}_\gamma^2\,\mathrm{d}a.$$

Clarenz [50] proved that Wulff shapes are its only minimizers. Another interesting application of bending energies appears in the context of surface matching, where a correspondence between two surfaces is the subject of investigation. Comparing a scan of a physical object with a CAD description or fitting a canonical surface model to triangular mesh data from a 3D scanning system is an important application of surface matching. There, we seek a mapping $\phi_{\mathcal{M}}$ between two surfaces $\mathcal{M}_A$ and $\mathcal{M}_B$ respecting certain properties of the surfaces.

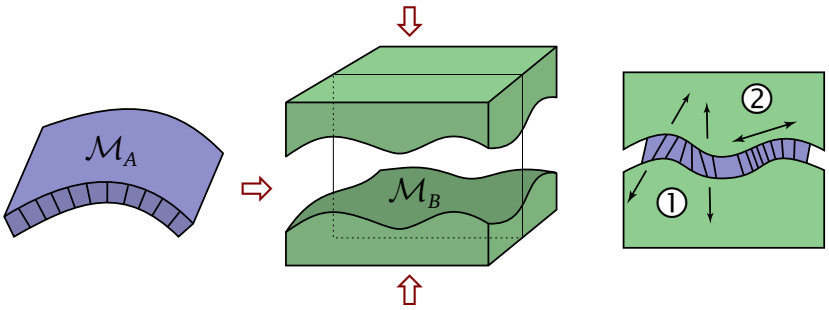

Figure 1.2: A physical interpretation of $\phi_{\mathcal{M}}$ is the pressing of a thin shell $\mathcal{M}_A$ into a mould of the surface $\mathcal{M}_B$ to be matched. The bending of normals (1) and stretching (2) of the thin shell is measured by the proposed matching energy. Image courtesy of LITKE ET AL. [126].

We consider the first surface $\mathcal{M}_A$ as a thin elastic shell which is pressed into a mould representing the second surface $\mathcal{M}_B$. One can distinguish between stresses induced by stretching and compression, and stresses induced by bending that occur in the surface if the shell is pressed into the mould, cf. Figure 1.2. Thus, $\phi_{\mathcal{M}}$ can be regarded as the deformation of such a thin elastic shell. Since we are aiming for a proper correspondence of shape, we incorporate the bending of normals. The bending energy is then given by

$$w_{bend}(\phi_{\mathcal{M}}) = \int_{\mathcal{M}_A} \left(\mathbf{h}_B \circ \phi_{\mathcal{M}} - \mathbf{h}_A\right)^2 \, \mathrm{d}a,$$

where $\mathbf{h}_A$ and $\mathbf{h}_B$ denote the mean curvature on the surface $\mathcal{M}_A$ and $\mathcal{M}_B$, respectively.

The thesis is organized as follows. In the following section we give a short overview of the Willmore functional and its L^2-gradient flow. In Section 1.2 we show how to incorporate boundary conditions to blend and restore surfaces. The extension to the anisotropic version is described in Section 1.3. Finally, in Section 1.4 the surface matching method is illustrated. In Chapter 2 we recapitulate some useful definitions and results from differential geometry and Finsler geometry. To calculate the continuous flow for the anisotropic Willmore functional we need the conceptual framework for general gradient flows. To discretize continuous gradient flows we introduce a suitable space discretization based on piecewise affine Finite Elements. We calculate the first variation of the anisotropic Willmore functional and its corresponding L^2-gradient flow following DIEWALD [71] and provide a semi-implicit Finite Element scheme for the anisotropic Willmore flow with boundary conditions in Chapter 3. The resulting scheme is used to restore surface patches with corner and edge type singularities. In Chapter 4 we develop a completely new scheme for Willmore flow based on the two step time discretization scheme for general gradient flows. We apply the developed numerical algorithm to the evolution of curves in $\mathbb{R}^2$ and $\mathbb{R}^3$ and of two-dimensional surfaces in $\mathbb{R}^3$ and compare the new approach to the semi-implicit scheme. The main advantage of this new method is that it is robust and allows time steps of the order of the spatial grid size. To restore surfaces we extend the two step time discretization of Willmore flow to surfaces with boundaries in Chapter 5. The anisotropic version is developed in Chapter 6. A variational method with corresponding existence results for surface matching is given in Chapter 7.

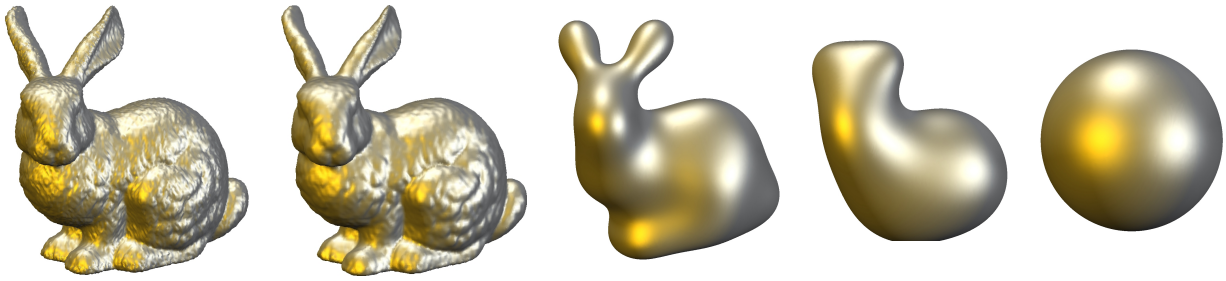

Figure 1.3: Different time steps of the two step time discretization for the isotropic Willmore flow of the Stanford bunny [2] towards a sphere.

1.1 The Willmore flow

The formulation of the Willmore flow problem depends on the mathematical model, which is chosen, to represent the surface or interface. We consider parametric surfaces, i.e. the surface is prescribed by a parametrization, instead of an implicit (level set) representation as in DROSKE & RUMPF [77], where the surface is prescribed as the zero level set of a real valued function. The Willmore flow for graphs was intensively investigated by DECKELNICK & DZIUK [65]. Let $\mathcal{M}$ be a closed d-dimensional surface embedded in $\mathbb{R}^m$ with $m \geq d+1$ and denote by x the identity map on $\mathcal{M} = \mathcal{M}[x]$. Then the Willmore energy is defined as

$$w[x] := \frac{1}{2}\int_{\mathcal{M}} \mathbf{h}^2 \, \mathrm{d}a$$

with mean curvature $\mathbf{h}$ and surface area element $\mathrm{d}a$. The Willmore flow in the hypersurface case ($m = d+1$) can be described by the following highly nonlinear fourth order parabolic evolution problem

$$\partial_t x(t) = \left(\Delta_{\mathcal{M}(t)}\mathbf{h}(t) + \mathbf{h}(t) \left(|S(t)|_2^2 - \frac{1}{2}\mathbf{h}(t)^2 \right) \right) n(t), \tag{1.2}$$

which defines for a given initial surface $\mathcal{M}_0$ a family of surfaces $\mathcal{M}(t)$ for $t \geq 0$ with $\mathcal{M}(0) = \mathcal{M}_0$. Here, $\Delta_{\mathcal{M}(t)}$ is the Laplace Beltrami operator on $\mathcal{M}(t)$, $S(t)$ denotes the shape operator on $\mathcal{M}(t)$, $n(t)$ the normal field on $\mathcal{M}(t)$, and $|\cdot|_2$ the Frobenius norm on the space of endomorphisms on the tangent bundle $\mathcal{T}\mathcal{M}(t)$. Critical points of the Willmore functional are referred to as Willmore surfaces and play an important role in many areas. Since the Willmore functional is invariant under conformal transformations of the metric of the ambient space [169, 41], the property of being Willmore surface is preserved under conformal transformations. This property makes the Willmore functional also an important functional in the *theory of surfaces* and study of *conformal geometry* [170, 173]. A geometric analysis concerning the structure of integrands such as (1.1) is due to NITSCHE [132]. Any minimal surface, i.e. any surface with $\mathbf{h} = 0$, is an absolute minimum of w, since the Euler–Lagrange equation of the Willmore functional can be written as

$$\Delta_{\mathcal{M}}\mathbf{h} + \frac{1}{2}\mathbf{h}(\mathbf{h}^2 - \mathbf{k}) = 0.$$

Figure 1.4: Solutions of the Willmore flow for an initial coarse polygonal approximation of a sphere and a torus towards a sphere and the Clifford torus.

In the literature many Willmore surfaces are known [139, 170]. Since the Möbius group is non-compact, minimizers of the Willmore energy can not be found via a direct method. Nevertheless, if S^2 denotes the two-dimensional sphere in $\mathbb{R}^3$ ($m = d + 1 = 3$), it holds for all surfaces $\mathcal{M}$ that

$$w(\mathcal{M}) \geq 4\pi = w(S^2), \tag{1.3}$$

and spheres are absolute minimizers of the Willmore functional. A proof for embedded surfaces in co-dimension one can be found in Willmore [172, Theorem 7.2.2]. There are no closed minimal surfaces in $\mathbb{R}^3$ due to the maximum principle. Instead, the Clifford torus

$$\mathcal{T}_{Cliff} := \frac{1}{\sqrt{2}}(S^1 \times S^1) \subset \mathbb{R}^3$$

is a minimal surface in S^3. Stereographic projections of compact minimal surfaces in S^3 produce Willmore surfaces in $\mathbb{R}^3$ by a result of Weiner [167]. The stereographic projection of the Clifford torus

$$\mathcal{M}_{Cliff} = \left\{ x \in \mathbb{R}^3 \middle| (1 - \sqrt{x_1^2 + x_2^2})^2 + x_3^2 = \frac{1}{2} \right\}$$

is a Willmore torus in $\mathbb{R}^3$ with $w(\mathcal{M}_{Cliff}) = 2\pi^2$. In 1965, Willmore conjectured that the Willmore energy of a torus $\mathcal{T}^2$ immersed in $\mathbb{R}^3$ is at least $2\pi^2$:

$$w(\mathcal{T}^2) \geq w(\mathcal{T}_{Cliff}) = a(\mathcal{T}_{Cliff}) = 2\pi^2$$

with $a(\cdot)$ being the area of the surface, cf. Figure 1.4. Simon proved in [156] that there exists a torus which minimizes the Willmore energy under all tori in $\mathbb{R}^m$. For further existence and regularity results for closed Willmore surfaces of prescribed genus we refer to [156, 164, 16, 125, 121]. Recently, Rivière [144] extended results of Kuwert & Schätzle [120] for co-dimension 3 to arbitrary co-dimension. Via a point removability result established for Willmore surfaces he proved a weak compactness result for Willmore surfaces with energy less than 8π and a strong compactness of Willmore tori below the energy level 8π. He provided also a new formulation for the weak Euler–Lagrange equation of the Willmore functional for immersed surfaces in $\mathbb{R}^m$ as a nonlinear elliptic equation in divergence form.

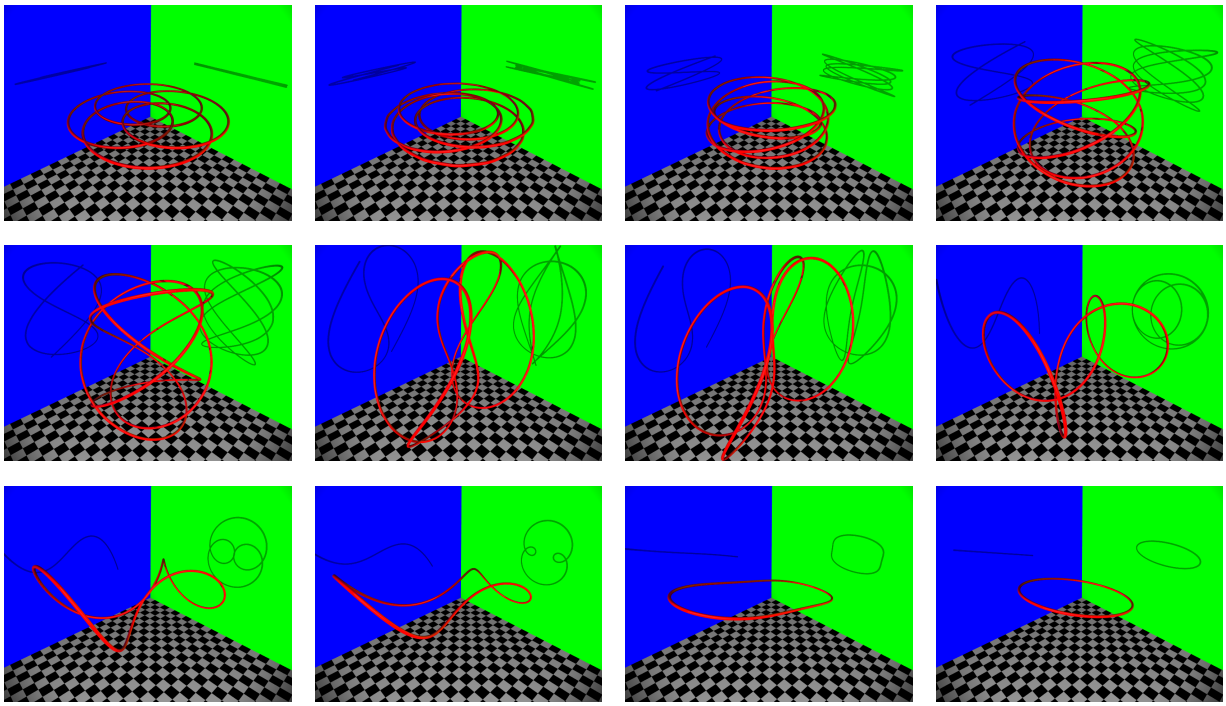

Figure 1.5: Elastic flow of a vertically perturbed hypocycloid towards a circle.

The analytic treatment of the Willmore flow has been considered for closed surfaces extensively. SIMONETT [157] was able to prove that a unique local solution of Equation (1.2) exists provided that $\mathcal{M}(0)$ is a compact closed immersed and orientable two-dimensional $\mathcal{C}^{2,\alpha}$-surface in $\mathbb{R}^3$. Existence results are obtained globally in time if $\mathcal{M}(0)$ is sufficiently close to a sphere in the $\mathcal{C}^{2,\alpha}$-topology. Using different methods KUWERT & SCHÄTZLE [117, 119, 118] obtained sharp results on long time existence and regularity. They proved that for two-dimensional surfaces of sphere type and initial energy less than or equal 8π, the Willmore flow converges to a round sphere. MAYER & SIMONETT [129] proved that the flow develops a singularity if the initial surface has energy greater than 16π. Willmore flow for curves is referred to as elastic flow of curves, cf. Figure 1.5, and has been considered by DZIUK, KUWERT & SCHÄTZLE in [85], where they generalize results of POLDEN [140, 141] for planar curves.

Numerical methods for Willmore flow on triangulated surfaces were developed by RUSU [148], BARRETT, GARCKE & NÜRNBERG [14], BOBENKO & SCHRÖDER [25], and DZIUK [84]. For numerous results concerning the numerical treatment of the elastic flow of curves we refer to DZIUK [82], DZIUK, KUWERT & SCHÄTZLE [85], DECKELNICK & DZIUK [66], BARRETT, GARCKE & NÜRNBERG [14]. On the numerical treatment of the Willmore flow problem using level set methods we refer to DROSKE & RUMPF [77]. The evolution of two-dimensional graphs under Willmore flow was investigated by DECKELNICK & DZIUK [65]. Introducing a weighted mean curvature as new variable, the fourth order problem can be split into two coupled second order problems with height and the new variable as unkowns. Numerical approaches are often characterized by an explicit or semi-implicit time discretization, which requires the solution of a linear system of equations in each time step. One observes significant restrictions on the time step size. Effectively, one usually has to enforce time steps $\tau = O(h^2)$, where h is the

spatial grid size. This shortcoming motivates the development of a new concept for the time discretization of Willmore flow in picking up the variational time discretization of general gradient flows. Given an energy $e[\cdot]$ on a manifold the gradient flow $\dot{x} = -\mathrm{grad}_g e[x]$ with initial data x^0 defines a sequence of time discrete solutions $(x^k)_{k=0,1,\dots}$, where $x_k \approx x(k\tau)$ for the time step size τ via a variational problem, to be solved in each time step, i.e.

$$x^{k+1} = \arg\min_x \left(\mathrm{dist}(x, x^k)^2 + 2\tau\, e[x] \right),$$

where

$$\mathrm{dist}(x, x^k) = \inf_{\gamma \in \Gamma} \int_0^1 \sqrt{g_{\gamma(s)}(\dot{\gamma}(s), \dot{\gamma}(s))}\, \mathrm{d}\sigma$$

is the shortest path length on the manifold, given the metric $g(\cdot,\cdot)$. Here Γ denotes the set of smooth curves γ with $\gamma(0) = x^k$ and $\gamma(1) = x$. As an immediate consequence, one obtains the energy estimate

$$e[x^{k+1}] + \frac{1}{2\tau}\mathrm{dist}(x^{k+1}, x^k)^2 \leq e[x^k] + 0\,.$$

We refer to OTTO [136] for the conceptual framework for general gradient flows. For geometric problems, this approach has already been considered by LUCKHAUS & STURZENHECKER [127] in the case of mean curvature motion, which is the L^2-gradient flow of the surface area. They proposed a corresponding fully implicit time discretization based on a variational problem in BV to be solved in each time step. In fact, in each time step the symmetric distance between two consecutive shapes corresponding to the current and the next time step is balanced by the time step τ multiplied by the perimeter of the shape at the next time step. CHAMBOLLE [36] investigated a reformulation of this approach in terms of a level set method. A related method for anisotropic mean curvature motion is discussed in [18, 37].

In the case of Willmore flow, we proceed as follows. We aim at balancing the squared distance of the unknown surface at time $t_{k+1} = t_k + \tau$ from the current surface at time t_k and a suitable approximation of the Willmore energy at time t_{k+1} scaled by twice the time step size. Solving a fully implicit time discrete problem for the mean curvature motion of the unknown surface at time t_{k+1}, we are able to regard the corresponding difference quotient in time as a time discrete, fully implicit approximation of the mean curvature vector. Based on this mean curvature vector, the Willmore functional can be approximated. Thus, we are led to a nested minimization problem in each time step. In the inner problem on the new time step, an implicit mean curvature vector is identified. Then, the outer problem is the actual implicit variational formulation of Willmore flow. Indeed, the resulting two step time discretization experimentally turns out to be unconditionally stable and effectively allows for time steps of the order of the spatial grid size. To solve the resulting nested variational problem in each time step, a sequential quadratic programming approach and numerical relaxation theory from PDE constraint optimization is used. The approach is applied to polygonal curves and triangular surfaces and is independent of the co-dimension, cf. Figures 1.5 and 1.3. Part of this work has already been published in OLISCHLÄGER & RUMPF [135].

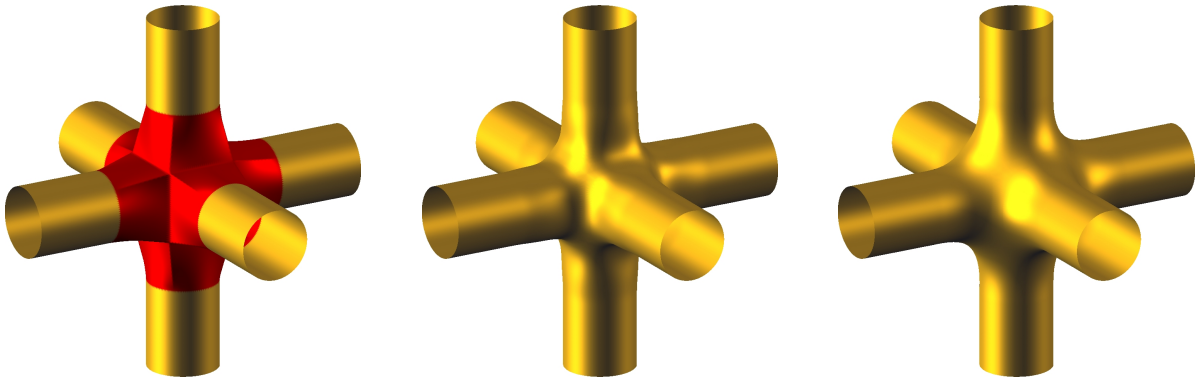

Figure 1.6: Evolution of the blending problem of a higher genus topology by the isotropic Willmore flow with boundary condition determined by six cylinders is depicted. The surface patch to be replaced is shown in red. We show the surface at time step $k = 0$, 2 and 4.

1.2 Surface blending and surface restoration

To restore surfaces we have to incorporate boundary conditions into the Willmore flow. Since the corresponding flow leads to a system of fourth order partial differential equations, we can prescribe Dirichlet and Neumann boundary conditions to achieve $\mathcal{C}^1$-continuity at the patch boundary. Suppose $\mathcal{M}[x(t)] \subset \mathbb{R}^m$, $m \leq d+1$, is a bounded d-dimensional surface with parametrization $x(t)$ over itself and $n(t)$ its Gauß map. $\mathcal{M}[x^0]$ is the initial surface with parametrization x^0 and Gauß map n^0. We assume a surface $\widetilde{\mathcal{M}}[x^0]$ to be given such that

$$\mathcal{M}[x^0] \subset \widetilde{\mathcal{M}}^0$$

is a subset visually not fitting with the surrounding surface. Either $\mathcal{M}[x^0]$ is a destroyed region on the surface $\widetilde{\mathcal{M}}[x^0]$, where the remaining surface

$$\mathcal{M}^{ext}[x^0] := \widetilde{\mathcal{M}}[x^0] \setminus \mathcal{M}[x^0]$$

is in good condition, or $\mathcal{M}[x^0]$ is an initial blending surface closing a given surface $\mathcal{M}^{ext}[x^0]$. In both cases we ask for a $\mathcal{C}^1$-surface restoration or blending. We are searching for a surface patch $\mathcal{M}[x]$ that minimizes the Willmore energy

$$w[x] = \int_{\mathcal{M}[x]} \mathbf{h}^2 \, \mathrm{d}a$$

over all C^1-surfaces with fixed exterior surface $\mathcal{M}^{ext}[x] = \widetilde{\mathcal{M}}[x] \setminus \mathcal{M}[x]$. Considering the L^2-gradient flow

$$\partial_t x(t) = -\mathrm{grad}_{L^2} w[x(t)]$$

with boundary conditions

$$x(t) = x^0 \qquad \text{and} \qquad n(t) = n^0$$

on $\partial\mathcal{M}[x(t)]$ we expect that $\mathcal{M}[x(t)]$ converges to a critical point of the Willmore problem.

Figure 1.7: Initial (left) and restored surface (right) of a Egea head dataset.

The classical form of the above initial boundary value problem for the Willmore energy is then given by

$$\partial_t x(t) = \Delta_{\mathcal{M}[x(t)]}\, \mathbf{h}(t)\, n(t) + \mathbf{h}(t) \left(\left| \nabla_{\mathcal{M}} n \right|_2^2 - \frac{1}{2} \mathbf{h}(t)^2 \right) n(t) .$$

Instead of the normal n on the boundary we can also prescribe the outer co-normal field n^{co} on $\partial\mathcal{M}$. Existence of Willmore surfaces with boundaries has not been extensively studied yet. NITSCHE [131, 132] provides existence results for possible choices of boundary conditions. Recently, SCHÄTZLE [150] proved existence and regularity of branched Willmore immersions in S^m satisfying prescribed boundary conditions. For existence and classical regularity of axially symmetric Willmore surfaces with arbitrary symmetric Dirichlet boundary conditions we refer to [60, 21, 61].

Numerically, fourth order problems with boundary conditions are very popular in the context of image inpainting and surface restoration [23, 22, 51, 143, 175]. For the restoration of surfaces, second order approaches do not lead to satisfying results, since one can prescribe boundary conditions for the position vector only, but not for the surface normal. Hence, one cannot expect C^1-smooth surfaces. CLARENZ ET AL. [51] extended the approach of RUSU [148] to surfaces with boundaries and provided a proper weak formulation of the corresponding initial and boundary value Willmore flow problem, to discretize this in space consistently using a Finite Element scheme on triangular grids, and in time applying a semi-implicit backward Euler discretization. For several methods based on the same or similar ideas we refer to [151, 152, 176]. An early variational approach for surface modeling is described in WELCH & WITKIN [168]. A surface blending method was presented by GREINER [103, 104], where in a fix point iteration parameterized patches are constructed which minimize a linearized total curvature. Using a fourth order method and constructing a surface of prescribed mean curvature, where the mean curvature is obtained by elliptic interpolation of the mean curvature at the boundary, KOBBELT & SCHNEIDER [152] obtained smoothness of the surface at the boundary. A gradient descent method for a discrete version of the

Willmore energy has been presented by YOSHIZAWA & BELYAEV [176] for the restoration of surfaces. Starting with the Euler–Lagrange equation $\Delta_{\mathcal{M}}\mathbf{h} + \frac{1}{2}\mathbf{h}(\mathbf{h}^2 - \mathbf{k}) = 0$ they defined a discrete Willmore flow by assembling the components from individual, well-known discrete operators. In particular the mean curvature is evaluated applying the umbrella operator [114]. Since the time discretization is explicit they need a large number of time steps even for moderately fine discretized surfaces. Due to the Gauß–Bonnett theorem [170, pp. 146] the integral of the Gauß curvature is a topological invariant. Therefore, it is equivalent to minimizing the integral of $\frac{1}{2}\mathbf{h}^2 - \mathbf{k}$ instead of the Willmore energy. BOBENKO & SCHRÖDER [25] prefer this integrand since it is invariant under Möbius transformations [24]. Obviously, it is invariant under translations and rotations. The invariance under uniform scale and inversion follow from the change of variable formula [40]. Their derivation of the discrete Willmore energy is based on this observation. Let us denote that the integrand of the Willmore energy is not Möbius invariant, only the energy itself is conformal invariant.
We incorporate boundary conditions in our nested variational minimization in each time step as follows. In the inner problem, on the new time step we solve a fully implicit time discrete problem for the mean curvature motion of the unknown surface at time t^{k+1} with prescribed Neumann boundary condition. Then, in the outer problem, the actual implicit variational formulation of Willmore flow, we prescribe Dirichlet boundary conditions for the new time step. If the inner time step size converges to zero, the co-normal for the new time step converges to the prescribed co-normal of the inner problem. For the discretization of the Neumann boundary condition, we introduce two different numerical methods. The first one considers the boundary conditions to be explicitly calculated whereas in the second one the co-normal is implicitly incorporated to avoid its calculation. The integration domain for the inner mean curvature functional is changed to $\widetilde{\mathcal{M}}[x]$ and the integral over the boundary is omitted. We apply the developed numerical algorithm with boundary conditions to the evolution of curves in $\mathbb{R}^2$ and two dimensional surfaces in $\mathbb{R}^3$. Various numerical examples underline the stability of the new scheme, cf. Figure 1.1 and Figure 1.6, which enables time steps of the order of the spatial grid size.

1.3 The anisotropic Willmore flow

Real world restoration problems often have an anisotropic character. Using the isotropic Willmore functional does not lead to results respecting the edges and corners of a surface, cf. Figure 1.8. Therefore, one is interested in a fourth order anisotropic flow where surfaces evolve to crystal-shaped surfaces like cubes or octahedra, for examples Wulff shapes, which appear as minimizers of anisotropic surface energies of the form

$$a_\gamma[x] = \int_{\mathcal{M}} \gamma(n)\,\mathrm{d}a$$

where $\gamma : \mathbb{R}^{d+1} \to \mathbb{R}_0^+ \in C^3(\mathbb{R}^{d+1} \setminus 0) \cap C^0(\mathbb{R}^{d+1})$ is a given anisotropy function. γ is assumed to be elliptic, i.e. positive, positively homogeneous of degree one and convex. The unique isoperimetric property of the Wulff shape was first proved by TAYLOR [159, 160, 161] in a geometric measure theory setting. For a proof with analytic methods we refer to FONSECA &

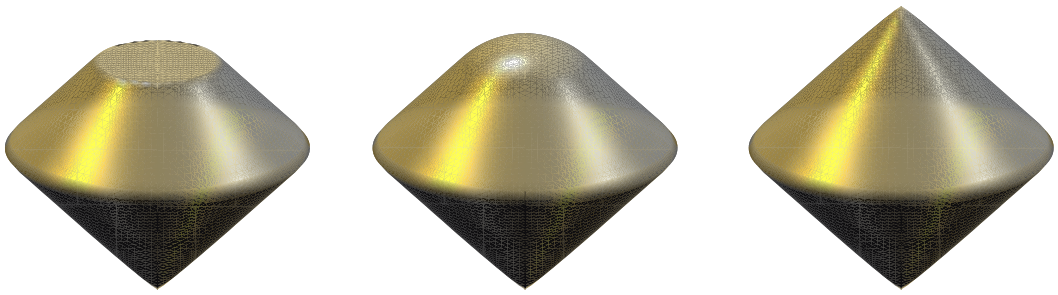

Figure 1.8: The destroyed surface on the left hand side is restored by the isotropic Willmore flow (middle) and in comparison by the anisotropic Willmore flow (right).

MÜLLER [92]. If $\gamma(z) = |z|$ this energy reduces to the area functional $a[\cdot]$. The first variation of $a[\cdot]$ with respect to a test function $\vartheta \in \mathcal{C}^1(\mathcal{M}, \mathbb{R}^m)$ is given by

$$\langle a'[x], \vartheta \rangle := \partial_\epsilon \big|_{\epsilon=0} a[x + \epsilon\,\vartheta] = \int_{\mathcal{M}} \mathbf{h}\, n \cdot \vartheta \,\mathrm{d}a.$$

For the first variation of the anisotropic version of the area functional we get

$$\left\langle (a_\gamma)'[x], \vartheta \right\rangle = \int_{\mathcal{M}} \operatorname{div}_{\mathcal{M}} \left(\gamma_z(n)\right) \cdot \vartheta \,\mathrm{d}a,$$

where $\gamma_z := D\gamma$ denotes the gradient of γ. For a proof we refer to CLARENZ [48, 49] for surfaces without boundaries and to DIEWALD [71] for surfaces with boundaries. The corresponding anisotropic curvature flow has been studied for instance by BELLETTINI & PAOLINI [20]. For an application to surface fairing we refer to CLARENZ, DZIUK & RUMPF [55]. It is quite natural to define the *anisotropic mean curvature* as the L^2-gradient of the anisotropic area functional

$$\mathbf{h}_\gamma := \operatorname{div}_{\mathcal{M}} \left(\gamma_z(n)\right) .$$

The corresponding *anisotropic Willmore functional* is then given by

$$w_\gamma[x] = \frac{1}{2} \int_{\mathcal{M}} \mathbf{h}_\gamma^2 \,\mathrm{d}a\,.$$

CLARENZ [50] has shown that Wulff shapes are the only minimizers of this highly nonlinear fourth order functional which makes it well suited for anisotropic restoration problems. In the literature, one can find only a few existence results for the anisotropic Willmore functional. Recently, BELLETTINI & MUGNAI [19] discussed the anisotropic Willmore functional and computed its first variation in the smooth case. CLARENZ [49] and PALMER [137, 138] studied variational problems involving anisotropic bending energies for surfaces with and without boundaries. Numerically, DIEWALD [71] extended the approach of RUSU [148] to the parametric anisotropic Willmore flow. NEMITZ [130] used the anisotropic Willmore functional to restore and engrave surfaces in the level-set context. The Euler–Lagrange equation for the anisotropic Willmore functional is given by

$$-\Delta_\gamma \mathbf{h}_\gamma - \mathbf{h}_\gamma \left|\nabla_{\mathcal{M}} n\right|_\gamma^2 + \frac{1}{2}\,\mathbf{h}\,\mathbf{h}_\gamma^2 = 0,$$

where $\Delta_\gamma := \operatorname{div}_{\mathcal{M}}(\gamma_{zz}(n)\,\nabla_{\mathcal{M}})$ is the generalized Laplace–Beltrami operator and $\gamma_{zz} = D^2\gamma$ the second derivatives of the anisotropy function γ. We review the calculation in Chapter 3,cf. Proposition (3.1.1). Considering the corresponding L^2-gradient flow for the anisotropic Willmore energy with initial and Dirichlet boundary conditions we are interested in solutions of the evolution problem

$$\begin{aligned}
\partial_t x &= \left(\Delta_\gamma \mathbf{h}_\gamma + \mathbf{h}_\gamma \left|\nabla_{\mathcal{M}} n\right|_\gamma^2 - \frac{1}{2}\mathbf{h}\,\mathbf{h}_\gamma^2\right) n \qquad && \text{on } (0,T]\times\mathcal{M},\\
x &= x^0 && \text{on } (0,T]\times\partial\mathcal{M},\\
n &= n^0 && \text{on } (0,T]\times\partial\mathcal{M},\\
x(0) &= x^0\,.
\end{aligned}$$

One can derive a variational form for the parametric Willmore flow which uses a mixed method with position and mean curvature vector as independent variables and allows using piecewise linear Finite Elements for the spatial discretization. This method is founded upon the corresponding approach of Rusu [148] for the isotropic Willmore flow of surfaces without boundary. We are searching for a family of bounded surfaces $\{\mathcal{M}(t)\}$ with coordinate vector $x(t)$ and an accompanying vector field $y(t)$ on $\mathcal{M}(t)$, such that

$$\begin{aligned}
\int_{\mathcal{M}} \partial_t x\cdot\vartheta\,\mathrm{d}a &= 2\int_{\mathcal{M}} n_i n_l\;\nabla_{\mathcal{M}} y_i\cdot\left(\gamma_{zz}(n)\,\nabla_{\mathcal{M}}\vartheta_l\right)\,\mathrm{d}a - \int_{\mathcal{M}} \nabla_{\mathcal{M}} y : \gamma_{zz}(n)\,\nabla_{\mathcal{M}}\vartheta\,\mathrm{d}a\\
&\quad - \frac{1}{2}\int_{\mathcal{M}} |y|^2\;\nabla_{\mathcal{M}} x : \nabla_{\mathcal{M}}\vartheta\,\mathrm{d}a\,,\\
\int_{\mathcal{M}} y\cdot\psi\,\mathrm{d}a &= \int_{\mathcal{M}} \left(\nabla_{\mathcal{M}} x\,\gamma_z(n)\right)\cdot\left(\nabla_{\mathcal{M}}\psi\,n\right)\,\mathrm{d}a - \int_{\mathcal{M}} \gamma(n)\;\nabla_{\mathcal{M}} x : \nabla_{\mathcal{M}}\psi\,\mathrm{d}a\\
&\quad + \int_{\partial\mathcal{M}} \gamma(n)\,\psi\cdot n^{co}\,dH^1 - \int_{\partial\mathcal{M}} \gamma_z(n)\cdot n^{co}\,n\cdot\psi\,dH^1\,,
\end{aligned}$$

for all $\vartheta\in H_0^1(\mathcal{M},\mathbb{R}^3)$, $\psi\in H^1(\mathcal{M},\mathbb{R}^3)$, and for almost every $t\in(0,T]$. Furthermore, we assume $x = x^0$ on $(0,T]\times\partial\mathcal{M}$ and $x(0) = x^0$. For the case without boundary conditions we refer to Diewald [71]. We review the calculation in Chapter 3, cf. Proposition 3.2.3. Using a Finite Element scheme on triangular grids in space and applying a semi-implicit backward Euler discretization in time, the resulting scheme is used to restore surface patches with corner and edge type singularities. It turns out that severe tangential distortions have to be compensated, if we choose time step sizes of the order of the square of the spatial grid size. This compensation is realized via mesh adaptation. Indeed, the use of edge swapping and edge collapsing turned out to be beneficial to compensate these artifacts for surfaces with boundaries. For compact closed surfaces the Willmore energy is conformally invariant [24, 169, 173] which can lead to grid degeneration caused by Möbius transformations. For closed surfaces one can optimize the grid via conformal parametrization as described in Clarenz & Dziuk [54] and Olischläger [134, Chapter 5], where a good parametrization of

a sphere is mapped onto the surface to reparametrize the mesh via a conformal mapping. To overcome this difficulty we extend the two step time discretization for discrete isotropic Willmore flow to the anisotropic case. To evaluate the anisotropic Willmore energy on the unknown surface of the next time step, we first solve an inner, secondary variational problem describing a time step of anisotropic mean curvature motion, which only involves the anisotropy but not its derivatives. In the anisotropic case we end up with a scheme for a single fully implicit time step of anisotropic mean curvature motion to be solved with a Newton approach, instead solving a linear system of equations in the isotropic model. The difference quotient in time between the given surface and the next time step surface of the anisotropic mean curvature motion can again be regarded as a time discrete, fully implicit approximation of the anisotropic mean curvature vector. Based on this anisotropic mean curvature vector, the generalized Willmore functional can be approximated. The approach is applied to polygonal curves, where the anisotropy could be chosen almost crystalline. Various numerical examples underline again the stability of the new scheme, which enables time steps of the order of the spatial grid size.

1.4 Surface matching

Finding a correspondence between two surfaces is a fundamental step in many geometry processing operations. For example one can use the matching function to map displacements or textures between surfaces, cf. Figure 1.9, or to blend the surfaces to generate a 3D animation between two different shapes. Given two surface patches, $\mathcal{M}_A$ and $\mathcal{M}_B$, we would like to find a non-rigid spatial deformation,

$$\phi_{\mathcal{M}} : \mathcal{M}_A \to \mathbb{R}^3,$$

such that corresponding regions of $\mathcal{M}_A$ are mapped onto regions of $\mathcal{M}_B$. Instead of matching the surfaces directly in 3D, we apply well-established matching methods from image processing in the parameter domains of the surfaces. If ω_A and ω_B, respectively, denote the parameter domains of the surfaces, we are searching for an elastic deformation $\phi : \omega_A \to \omega_B$. Variations of normals are represented in the metric by the shape operator which is the surface gradient of the normal mapping. If S_A and S_B are the corresponding shape operators of the surface patches $\mathcal{M}_A$ and $\mathcal{M}_B$, respectively,

$$\operatorname{tr}(S_B \circ \phi) - \operatorname{tr}(S_A)$$

is a local measure for the bending of normals. Since the trace of the shape operator is the mean curvature, we can instead aim to compare the mean curvature $\mathbf{h}_B = \operatorname{tr}(S_B)$ of the surface $\mathcal{M}_B$ at the deformed position $\phi_{\mathcal{M}}(x)$ and the mean curvature $\mathbf{h}_A = \operatorname{tr}(S_A)$ of the surface $\mathcal{M}_A$. A similar observation was used by GRINSPUN ET AL. [105] to define a bending energy for discrete thin shells. Finally, we define the following bending energy

$$\mathcal{E}_{bend}[\phi] = \int_{\omega_A} (\mathbf{h}_B \circ \phi - \mathbf{h}_A)^2 \sqrt{\det g_A}\, d\xi\,,$$

where g_A denote the induced metric on the surface patches. By minimizing this energy, we ensure that the deformation properly matches mean curvature on the surfaces. The corresponding minimization problem is ill-posed if one considers the full space of deformations

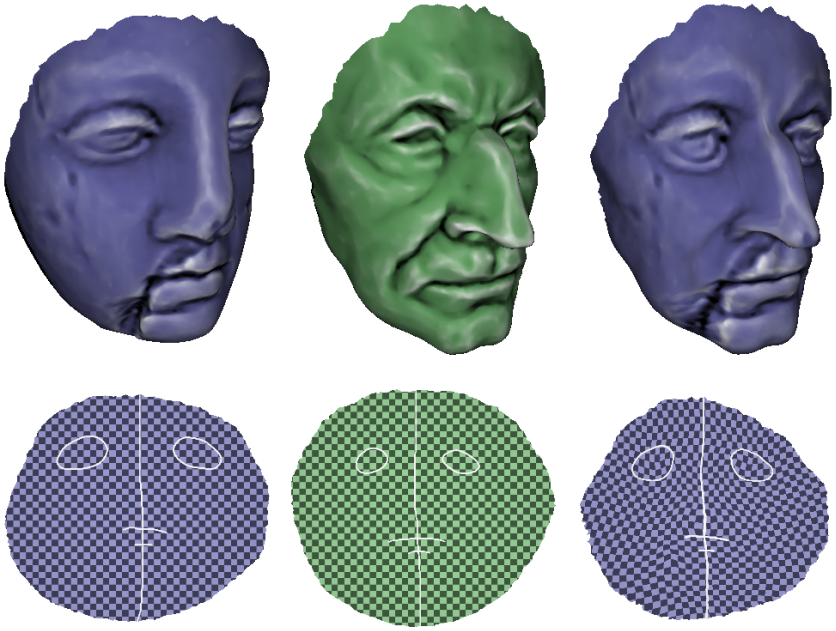

Figure 1.9: Instead of finding a correspondence between the two surfaces directly in 3D we apply well-established matching methods from image processing in the parameter domains of the surfaces (first and second figure, bottom). The optimal matching deformation between the first and second surface is shown in the parameter domain on the right (bottom). Quantities such as texture maps can be mapped between the surfaces (third surface, top).

[101, 165]. Therefore, one asks for a suitable regularization energy which in particular also allows the control of area shrinkage and simultaneously ensures continuity and injectivity for the minimizing deformation. We confine to hyperelastic energy functionals on deformations ϕ based on classical concepts from continuum mechanics and in particular from the theory of elasticity [44, 128] and incorporate a regularization energy $\mathcal{E}_{reg}$ to control length and area changes in the induced non-rigid deformation between the two surfaces. Another difficulty is the proper alignment of selected features during the parametrization process. Early work used parametrizations of the meshes over a common parameter domain to establish a direct correspondence between the two surfaces [122]. Typically these methods are driven by user-supplied feature correspondences which are then used to drive a mutual parametrization. GU & VEMURI [107] considered one-to-one correspondence of topological spheres through conformal maps with applications to brain matching. Therefore they do not have to address the difficult problem of partial correspondences between surfaces with boundaries. In our approach we cover the two parameter domains of the surfaces to be matched with user-defined feature characteristics. A feature energy $\mathcal{E}_{\mathcal{F}}$ then measures the mismatch of features and we avoid theoretical problems introduced by point-wise constraints [44]. Numerically, we mark the desired feature sets in the image domains which are discretized by regular grids. Therefore, the actual feature lines are pixel lines or regions drawn by the user on the texture image with a pen of at least one pixel width. Thus the feature lines are now two-dimensional sets and we avoid the theoretical treatment of the Hausdorff measure.

The variational method for matching two-dimensional surfaces in $\mathbb{R}^3$ based on finding a minimizing deformation between their two-dimensional parameter domains was developed by LITKE ET AL. [126]. In this thesis we provide a proof for the existence of minimizers of the matching energy, which are the optimal matching deformations, by applying the direct methods from the Calculus of Variations. We analyze under which assumptions the optimal matching deformations are global injective, so that we can expect to obtain smooth deformations that are free of folds and singularity. The matching energy does not lend itself to a robust numerical minimization, thus we establish a suitable approximation and prove the existence of minimizing deformations for the approximation. We show by Γ-convergence that the sequence of minimizers of the approximating energy converges to the solution of the limit problem.

Chapter 2

Foundations

THE aim of this chapter is to recapitulate some useful definitions and results from differential geometry and Finsler geometry that we need in the following chapters. We refer to [100, 99, 73, 111, 113, 38] for a more detailed exposition of this material. To calculate the continuous flow for the anisotropic Willmore functional in Chapter 3 we need the conceptual framework for general gradient flows from Section 2.3. We refer to [136, 75] for an overview on general gradient flows. For generalized surface flows for mesh processing we refer to [87, 86]. To discretize continuous gradient flows we introduce a suitable space discretization based on piecewise affine Finite Elements in Section 2.4.

2.1 Some geometric analysis

Let $\mathcal{M}$ be a d-dimensional surface embedded in $\mathbb{R}^{d+1}$. Its parameterization $x : \mathcal{M} \to \mathbb{R}^{d+1}$ is assumed to be the identity on the surface $\mathcal{M} = \mathcal{M}[x]$,

$$\begin{aligned} x : \mathcal{M} &\to \mathbb{R}^{d+1} \\ p &\mapsto x(p) = p\,. \end{aligned}$$

The metric on $\mathcal{M}$ is induced by the ambient space. The corresponding area element will be denoted by $\mathrm{d}a$.

Definition 2.1.1. (Gauß map)
Let S^d be the unit sphere in $\mathbb{R}^{d+1}$. The *Gauß map* is defined as the normal mapping

$$\begin{aligned} n : \mathcal{M} &\to S^d \\ p &\mapsto n(p)\,, \end{aligned}$$

where $n(p)$ is the outer normal on the surface $\mathcal{M}$ at point $p \in \mathcal{M}$.

Definition 2.1.2. (Tangent space)
The *tangent space* $\mathcal{T}_p\mathcal{M}$ is the d-dimensional linear subspace of $\mathbb{R}^{d+1}$ that is orthogonal to the normal $n(p)$ at a point $p \in \mathcal{M}$,

$$\mathcal{T}_p\mathcal{M} = \{v \in \mathbb{R}^{d+1} \,|\, v \cdot n(p) = 0\}\,.$$

We will use the concept of the tangential or surface gradient of a function. See GILBARG & TRUDINGER [100, pp. 389] and DECKELNICK, DZIUK & ELLIOT [67, pp. 150] for a detailed exposition of this material.

Definition 2.1.3. (Tangential gradient)
The *tangential gradient* of a function $f : \mathcal{M} \to \mathbb{R}$ on the surface $\mathcal{M}$ with Gauß map n, which is differentiable in an open neighborhood of $\mathcal{M}$, is defined as

$$\nabla_{\mathcal{M}} f = \nabla_{\mathbb{R}^{d+1}} f - (n \cdot \nabla_{\mathbb{R}^{d+1}} f)\, n,$$

where $\cdot$ denotes the Euclidian scalar product and $\nabla_{\mathbb{R}^{d+1}}$ is the usual gradient in $\mathbb{R}^{d+1}$. For $f : \mathbb{R}^{d+1} \to \mathbb{R}$ the tangential gradient $\nabla_{\mathcal{M}} f$ is the orthogonal projection of $\nabla_{\mathbb{R}^{d+1}} f$ onto $\mathcal{T}_p\mathcal{M}$, $\nabla_{\mathcal{M}} f = P \nabla_{\mathbb{R}^{d+1}} f$, with

$$P_{ij} = \delta_{ij} - n_i n_j, \qquad i, j = 1, \cdots, d+1,$$

and δ_{ij} being the usual Kronecker symbol

$$\delta_{ij} := \begin{cases} 1 & i = j \\ 0 & \text{else.} \end{cases}$$

With $\mathbb{I}$ being the identity on the surface $\mathcal{M}$ we have $P = \mathbb{I} - n \otimes n$. $a \otimes b \in \mathbb{R}^{(d+1),(d+1)}$ is the tensor product matrix of two vectors $a, b \in \mathbb{R}^{d+1}$ and defined by $a \otimes b := a b^T = (a_i\, b_j)_{1 \le i,j \le d+1}$, where b^T is the transposed vector of b. We shall use the Einstein summation convention where it is convenient. Then, the tangential gradient of a function f is given by

$$\nabla_{\mathcal{M}} f = P \nabla_{\mathbb{R}^{d+1}} f = \left(\partial_i f - n_i n_j \partial_j f\right)_i =: \left(\nabla_{\mathcal{M},i} f\right)_i, \qquad 1 \le i \le d+1.$$

It is straightforward to show that $\nabla_{\mathcal{M}} f$ only depends on the values of f on $\mathcal{M}$. It holds that

$$\nabla_{\mathcal{M}} f \cdot n = \nabla_{\mathcal{M},i} f\; n_i = 0. \tag{2.1}$$

Let us denote that the tangential gradient is the unique Levi–Civita connection on $\mathcal{M}$. We refer to [158, 123, 39, 26] for a more detailed overview.

Lemma 2.1.1. (Sum and product rule for $\nabla_{\mathcal{M}}$)
If $f, g \in \mathcal{C}^1(\mathcal{M})$, then

$$\nabla_{\mathcal{M}}(f + g) = \nabla_{\mathcal{M}} f + \nabla_{\mathcal{M}} g, \tag{2.2}$$

$$\nabla_{\mathcal{M}}(f\, g) = \nabla_{\mathcal{M}} f\, g + f\, \nabla_{\mathcal{M}} g. \tag{2.3}$$

Proof. Direct consequence of the sum and product rule for the Euclidian gradient. □

Definition 2.1.4. (Tangential divergence)
Analogously the *tangential divergence* of a vector field $\vartheta \in \mathcal{C}^1(\mathcal{M}, \mathbb{R}^{d+1})$ is defined as the sum of the tangential partial derivatives of ϑ

$$\operatorname{div}_{\mathcal{M}} \vartheta = \nabla_{\mathcal{M},i} \vartheta_i = \operatorname{tr}\left(\nabla_{\mathcal{M}} \vartheta\right).$$

Lemma 2.1.2. (Sum and product rule for $\mathrm{div}_{\mathcal{M}}$)
Let $\vartheta_1, \vartheta_2 \in \mathcal{C}^1(\mathcal{M}, \mathbb{R}^{d+1})$ be two vector fields and $f \in \mathcal{C}^1(\mathcal{M})$. Then it holds that

$$\mathrm{div}_{\mathcal{M}}(\vartheta_1 + \vartheta_2) = \mathrm{div}_{\mathcal{M}}\vartheta_1 + \mathrm{div}_{\mathcal{M}}\vartheta_2,$$

$$\mathrm{div}_{\mathcal{M}}(f\vartheta_1) = f\,\mathrm{div}_{\mathcal{M}}\vartheta_1 + \nabla_{\mathcal{M}} f \cdot \vartheta_1.$$

Proof. Direct consequence of the product rule for the Euclidian divergence. □

Definition 2.1.5. (Laplace–Beltrami operator)
The *Laplace–Beltrami operator* of a function $f \in \mathcal{C}^1(\mathcal{M})$ is the tangential divergence of the tangential gradient

$$\Delta_{\mathcal{M}} f = \mathrm{div}_{\mathcal{M}}\left(\nabla_{\mathcal{M}} f\right) = \nabla_{\mathcal{M},i}\nabla_{\mathcal{M},i} f.$$

Let us next turn to the notion of mean curvature. The curvature of a plane curve parametrized by arc length is defined as the norm of the second derivative of its parameterization and measures the variation of the normal along the curve. On a surface the curvature measures the variation of the surface normal in tangential direction. An important concept is the Weingarten map S that measures the variation in direction of vectors of the tangent space $\mathcal{T}_p\mathcal{M}$. Since the variation of the normal in the direction of the surface normal n vanishes, S is an endomorphism on $\mathcal{T}_p\mathcal{M}$, $S : \mathcal{T}_p\mathcal{M} \to \mathcal{T}_p\mathcal{M}$.

Definition 2.1.6. (Weingarten map, Shape operator)
The extended Weingarten map or shape operator $S : \mathbb{R}^{d+1} \to \mathbb{R}^{d+1}$ is defined as the surface gradient of the Gauß map

$$S := \nabla_{\mathcal{M}} n,$$

with corresponding matrix entries

$$S_{ij} := \nabla_{\mathcal{M},i} n_j, \qquad 1 \le i, j \le d+1\,.$$

Since $|n| = 1$ on $\mathcal{M}$, it holds that

$$Sn = \nabla_{\mathcal{M},j} n_k\, n_k = \frac{1}{2}\nabla_{\mathcal{M},j}|n|^2 = 0\,. \tag{2.4}$$

Furthermore, S is symmetric. Let $v, w \in \mathcal{T}_p\mathcal{M}$ be tangent vectors, i.e. $n \cdot v = 0$, then it holds

$$\begin{aligned} & n_k v_k = 0 \\ \Rightarrow \quad & \nabla_{\mathcal{M},j} n_k\, v_k = -n_k\, \nabla_{\mathcal{M},j} v_k. \end{aligned}$$

Therefore, we obtain

$$\begin{aligned} Sv \cdot w &= w_j\, \nabla_{\mathcal{M},j} n_k\, v_k = -w_j\, n_k\, \nabla_{\mathcal{M},j} v_k = -n_k\, w_j \left(\partial_j v_k - n_j n_i \partial_i v_k\right) \\ &= -n_k\, w_j\, \partial_j v_k = -n_k\, \partial_w v_k = -n_k\, \partial_v w_k = -v_j\, n_k\, \nabla_{\mathcal{M},j} w_k = v_j\, \nabla_{\mathcal{M},j} n_k\, w_k \\ &= v \cdot Sw\,. \end{aligned}$$

Thus, S is symmetric on $\mathcal{T}_p\mathcal{M}$. Because of Equation (2.4), S is symmetric on $\mathbb{R}^{d+1}$, i.e.

$$S_{ij} = S_{ji}\,. \tag{2.5}$$

S has one eigenvalue which is equal to zero with corresponding eigenvector n. The remaining d eigenvalues $\kappa_1, \cdots, \kappa_d$ are referred to as the principal curvatures of $\mathcal{M}$. We now define the mean curvature of $\mathcal{M}$ as the trace of the matrix S.

Definition 2.1.7. (Mean curvature)
The *mean curvature* is defined as

$$\mathbf{h} = \sum_{i=1}^{d} \kappa_i = \operatorname{tr}\left(\nabla_{\mathcal{M}} n\right) = \operatorname{tr}(S)\,.$$

Note that this differs from the more common definition as the arithmetic average of the principal curvatures.

Lemma 2.1.3. *Let $f \in \mathcal{C}^1(\mathcal{M})$, n the surface normal of $\mathcal{M}$ and $\mathbf{h}$ its mean curvature. Then it holds*

$$\operatorname{div}_{\mathcal{M}}(f\, n) = f\, \mathbf{h}\,. \tag{2.6}$$

Proof. By definition of the tangential divergence, cf. Definition 2.1.4, we have

$$\operatorname{div}_{\mathcal{M}}(f\, n) = \nabla_{\mathcal{M},i}(f\, n_i)\nabla_{\mathcal{M},i} f\, n_i + f\, \nabla_{\mathcal{M},i} n_i$$

□

Choosing $f \equiv 1$ in Lemma 2.1.3 we derive the expression

$$\mathbf{h} = \operatorname{div}_{\mathcal{M}} n \tag{2.7}$$

for the mean curvature. Another useful formula can be obtained by choosing $f(x) = x_j$, $1 \le j \le d+1$, in Definition 2.1.5 and observing that $\nabla_{\mathcal{M},i} x_j = \delta_{ij} - n_j n_i$. We then deduce with Equation (2.7) that

$$\Delta_{\mathcal{M}} x_j = -\nabla_{\mathcal{M},i}(n_j n_i) = -\nabla_{\mathcal{M}} n_j \cdot n - n_j \operatorname{div}_{\mathcal{M}} n = -\mathbf{h}\, n_j$$

so that

$$\Delta_{\mathcal{M}} x = -\mathbf{h}\, n\,. \tag{2.8}$$

We also need the following lemmas for integration of vector fields on $\mathcal{M}$.

Lemma 2.1.4. (Integration by parts of tangential vector fields)
Let v be a tangential vector field and $f \in \mathcal{C}^1(\mathcal{M})$ be a continuously differentiable function on $\mathcal{M}$. Besides the normal mapping $n : \mathcal{M} \to S^d$ the immersion x induces a co-normal mapping $n^{co} : \partial\mathcal{M} \to S^d$ if $\partial\mathcal{M} \neq \emptyset$. n^{co} is perpendicular to n and perpendicular to the boundary $\partial\mathcal{M}$. The area element of $\mathcal{M}$ will be denoted by da. The induced area element on the boundary $\partial\mathcal{M}$ is denoted by $d\sigma$. Then it holds that

$$\int_{\mathcal{M}} \operatorname{div}_{\mathcal{M}} v f \; da = -\int_{\mathcal{M}} v \cdot \nabla_{\mathcal{M}} f \; da + \int_{\partial\mathcal{M}} v \cdot n^{co} f \, d\sigma\,. \tag{2.9}$$

Proof. A proof can be found in DO CARMO [74, p. 60]. □

Lemma 2.1.5. (Integration by parts of non-tangential vector fields)
Let w be a not necessarily tangential vector field and $f \in C^1(\mathcal{M})$ be a continuously differentiable function on $\mathcal{M}$. Then it holds that

$$\int_{\mathcal{M}} \operatorname{div}_{\mathcal{M}} w f \, da = -\int_{\mathcal{M}} w \cdot \nabla_{\mathcal{M}} f \, da + \int_{\mathcal{M}} \mathbf{h} w \cdot n f \, da + \int_{\partial\mathcal{M}} w \cdot n^{co} f \, d\sigma , \tag{2.10}$$

where n^{co} denotes the co-normal at the boundary of $\mathcal{M}$, n the surface normal and $\mathbf{h}$ the mean curvature.

Proof. A proof for $\partial\mathcal{M} = \emptyset$ can be found in CLARENZ [48, Lemma 1.2], for $\partial\mathcal{M} \neq \emptyset$ in DIEWALD [71, Korollar 53]. □

Lemma 2.1.6. (Green's formula on surfaces)
For functions $f \in H^2(\mathcal{M})$ and $\psi \in H^1(\mathcal{M})$ on a surface $\mathcal{M}$ with boundary the following integration by parts formula holds

$$\int_{\mathcal{M}} \nabla_{\mathcal{M}} f \cdot \nabla_{\mathcal{M}} \psi \, da = -\int_{\mathcal{M}} \Delta_{\mathcal{M}} f \, \psi \, da + \int_{\partial\mathcal{M}} \partial_{n^{co}} f \, \psi \, d\sigma . \tag{2.11}$$

Proof. A proof can be found in CLARENZ ET AL. [51, Lemma 3.1]. □

As matrix norm we choose the Frobenis norm:

Definition 2.1.8. (Frobenius norm)
The *Frobenius norm* on the space of matrices in $\mathbb{R}^{d,d}$ is denoted by $|A|_2 := \sqrt{\operatorname{tr}\left(A^T A\right)}$, with corresponding scalar product

$$A : B = \operatorname{tr}\left(A^T B\right) = a_{ij} b_{ij} .$$

Calculating in local coordinates

In Chapter 7 we need the above quantities in a more differential geometric setting. Suppose $\mathcal{M} \subset \mathbb{R}^{d+1}$ is a smooth immersed orientable d-dimensional surface, which is parametrized locally by a bijective mapping

$$\begin{aligned} x : \omega &\to \mathcal{M}, \\ \xi &\mapsto x(\xi) \end{aligned} \tag{2.12}$$

from the parameter domain $\omega \subset \mathbb{R}^d$ onto the surface $\mathcal{M}$. The vectors $\partial_{\xi_1} x, \cdots, \partial_{\xi_d} x$ form a basis of $\mathcal{T}_p\mathcal{M}$ at $p = x(\xi)$. The scalar product $\cdot$ of $\mathbb{R}^{d+1}$ induces the Riemannian metric on ω by

$$g_{ij}(\xi) := \partial_{\xi_i} x(\xi) \cdot \partial_{\xi_j} x(\xi), \qquad i, j = 1, \cdots, d,$$

with corresponding matrix

$$g := \nabla x^T \, \nabla x = (g_{ij})_{i,j=1,\cdots,d}.$$

Let g^{ij} be the components of the inverse matrix of g. We have the following formulae for the tangential gradient of a function f (defined in a neighborhood of $\mathcal{M}$) and the Laplace–Beltrami operator (cf. WILLMORE [171, pp. 231]):

$$\nabla_{\mathcal{M}} f = g^{ij} \partial_{\xi_j} (f \circ x) \partial_{\xi_i} x,$$
$$\Delta_{\mathcal{M}} f = \frac{1}{\sqrt{\det g}} \partial_{\xi_i} \left(\sqrt{\det g}\, g^{ij} \partial_{\xi_j} (f \circ x) \right).$$

The integral of a function $f : \mathcal{M} \to \mathbb{R}$ is then

$$\int_{\mathcal{M}} f \, \mathrm{d}a = \int_{\omega} f \circ x \sqrt{\det g}\, d\xi.$$

The metric g acts on tangent vectors v, w on the parameter domain ω with

$$(gv) \cdot w = \nabla x\, v \cdot \nabla x\, w\,,$$

which is simply the inner product of tangent vectors $\nabla x\, v, \nabla x\, w$ on the surface. Thus, it follows that the metric describes how length and area are distorted under the parameterization function:
Let $c : [0,1] \to \mathcal{M}$ be a differentiable curve on the surface $\mathcal{M}$. The length of the corresponding curve $x^{-1} \circ c$ in the parameter domain is given by

$$l[x^{-1} \circ c] = \int_0^1 \left| \partial_t \left(x^{-1} \circ c \right) \right| \mathrm{d}t = \int_0^1 \sqrt{g^{-1} \dot{c} \cdot \dot{c}}\, \mathrm{d}t. \tag{2.13}$$

Thus, $\sqrt{\mathrm{tr}\left(g^{-1}\right)}$ measures the average change of length of tangent vectors under the mapping from the surface onto the parameter plane. The corresponding change of area under the inverse parameterization x^{-1} is measured by $\sqrt{\det(g^{-1})}$:

$$\mathrm{area}(\Omega) = \int_{x^{-1}(\Omega)} \sqrt{\det(g^{-1})}\, d\xi \tag{2.14}$$

for a surface patch $\Omega \subset \mathcal{M}$.

2.2 The concept of anisotropy

In surface restoration problems it is often necessary to treat surfaces that evolve to anisotropic or even almost crystal-shaped surfaces like cubes or octahedra. Let $\gamma : S^d \to \mathbb{R}^+$ be a given smooth anisotropy function. To generalize the notion of mean curvature it will be necessary to restrict the admissible anisotropies to a certain class, cf. DZIUK [83, Definition 2.1].

Definition 2.2.1. (Elliptical integrand)
An *elliptical integrand* γ is a mapping $\gamma : \mathbb{R}^{d+1} \to \mathbb{R}_0^+$ with following properties:

1. Smoothness:
$$\gamma \in \mathcal{C}^3(\mathbb{R}^{d+1} \setminus 0) \cap \mathcal{C}^0(\mathbb{R}^{d+1}).$$
2. Positivity:
$$\gamma(z) > 0 \qquad \text{for } z \neq 0.$$
3. Positive homogeneity of degree one:
$$\gamma(\lambda z) = |\lambda|\gamma(z) \qquad \text{for all } \lambda \neq 0,\, z \neq 0. \tag{2.15}$$
4. Convexity:
   There exists $\gamma_0 > 0$ such that
$$\gamma_{zz}(z)\xi \cdot \xi \geq \gamma_0 |\xi|^2 \tag{2.16}$$
   holds for all $z, \xi \in \mathbb{R}^{d+1}$, $|z| = 1$ and $\xi \cdot z = 0$. $\gamma_z := \nabla\gamma$ denotes the first derivative and $\gamma_{zz} := \nabla^2\gamma$ the second derivative of γ.

An anisotropy function is referred to as admissible if it is an elliptical integrand. Any admissible anisotropy has the following properties, cf. DZIUK [83, Proposition 2.2]. For a detailed exposition of convex analysis, we refer to ROCKAFELLAR [145] and BONNESEN & FENCHEL [27].

Lemma 2.2.1. *The elliptical integrand γ is convex and fulfills*

$$\gamma_z(z) \cdot z = \gamma(z),\ \gamma_{zz}(z)z = 0, \tag{2.17}$$

$$\gamma_z(\lambda z) = \frac{|\lambda|}{\lambda}\gamma_z(z),\ \gamma_{zz}(\lambda z) = \frac{1}{|\lambda|}\gamma_{zz}(z) \tag{2.18}$$

for all $z \in \mathbb{R}^{d+1} \setminus \{0\}$ and $\lambda \neq 0$.

Proof. Partial differentiation of Equation (2.15) with respect to λ leads to

$$0 = \partial_\lambda \left(\gamma(\lambda z) - \lambda\gamma(z)\right) = \gamma_z(\lambda z) \cdot z - \gamma(z) \qquad \text{for all } \lambda > 0. \tag{2.19}$$

Differentiating Equation (2.19) with respect to λ yields

$$0 = \partial_\lambda \left(\gamma_z(\lambda z) \cdot z - \gamma(z)\right) = \gamma_{zz}(\lambda z)z \cdot z \qquad \text{for all } \xi \in \mathbb{R}^{d+1},\, \lambda > 0. \tag{2.20}$$

Choosing $\lambda = 1$ in Equations (2.19) and (2.20) proves Equation (2.17).

Differentiating Equation (2.15) twice with respect to z shows Equation (2.18):

$$0 = \partial_z \left(\gamma(\lambda z) - |\lambda|\gamma(z)\right) = \lambda\gamma_z(\lambda z) - |\lambda|\gamma_z(z),$$
$$0 = \partial_z \left(\lambda\gamma_z(\lambda z) - |\lambda|\gamma_z(z)\right) = \lambda^2\gamma_{zz}(\lambda z) - |\lambda|\gamma_{zz}(z).$$

Since γ is convex iff γ_{zz} is positive semi-definite, we have to show that

$$\gamma_{zz}(z)\xi \cdot \xi \geq 0 \qquad \forall \xi \in \mathbb{R}^{d+1}.$$

$\xi \in \mathbb{R}^{d+1}$ can be written as $\xi = \alpha z + \beta z^\perp$, where $z, z^\perp \in \mathbb{R}^{d+1} \setminus \{0\}$, $z \cdot z^\perp = 0$ and $\alpha, \beta \in \mathbb{R}$. Since γ_{zz} is symmetric, we get

$$\begin{aligned}
\gamma_{zz}(z)\xi \cdot \xi &= \gamma_{zz}(z)\left(\alpha z + \beta z^\perp\right) \cdot \left(\alpha z + \beta z^\perp\right) \\
&= \alpha^2 \underbrace{\gamma_{zz}(z)z \cdot z}_{\overset{(2.17)}{=}0} + 2\alpha\beta \underbrace{\gamma_{zz}(z)z \cdot z^\perp}_{\overset{(2.17)}{=}0} + \beta^2 \gamma_{zz}\left(\frac{z}{|z|}|z|\right) z^\perp \cdot z^\perp \\
&\overset{(2.18)}{=} \beta^2 \frac{1}{|z|}\gamma_{zz}\left(\frac{z}{|z|}\right) z^\perp \cdot z^\perp \\
&\overset{(2.16)}{\geq} \beta^2 \frac{1}{|z|}\gamma_0 \left|z^\perp\right|^2 \geq 0.
\end{aligned}$$

□

Lemma 2.2.2. *Let $p \in \mathcal{M}$ and let $n = n(p)$ denote the surface normal. An elliptical integrand γ induces a symmetric automorphism on the tangential space of the surface $\mathcal{M}$ as follows:*

$$\gamma_{zz}(n) : T_p\mathcal{M} \to T_p\mathcal{M}.$$

Proof. It holds for $v \in T_p\mathcal{M}$ that

$$\gamma_{zz}(n)v \cdot n \overset{(2.17)}{=} 0.$$

Therefore $\gamma_{zz}(n)v$ lies in $\{n\}^\perp = T_p\mathcal{M}$. □

In the context of the Frobenius norm we use the following abbreviation on the space of matrices in $\mathbb{R}^{d,d}$

$$|A|_\gamma := \sqrt{\operatorname{tr}\left(\gamma_{zz}A^TA\right)}. \tag{2.21}$$

Anisotropies are visualized using the Frank diagram and the Wulff shape:

Definition 2.2.2. (Wulff shape, Frank diagram)
Let γ be an elliptical integrand. The *Frank diagram* $\mathcal{F}_\gamma$ and the *Wulff shape* $\mathcal{W}_\gamma$ are given by

$$\mathcal{F}_\gamma = \left\{z \in \mathbb{R}^{d+1} | \gamma(z) \leq 1\right\},$$
$$\mathcal{W}_\gamma = \left\{z \in \mathbb{R}^{d+1} | \gamma^*(z) \leq 1\right\}.$$

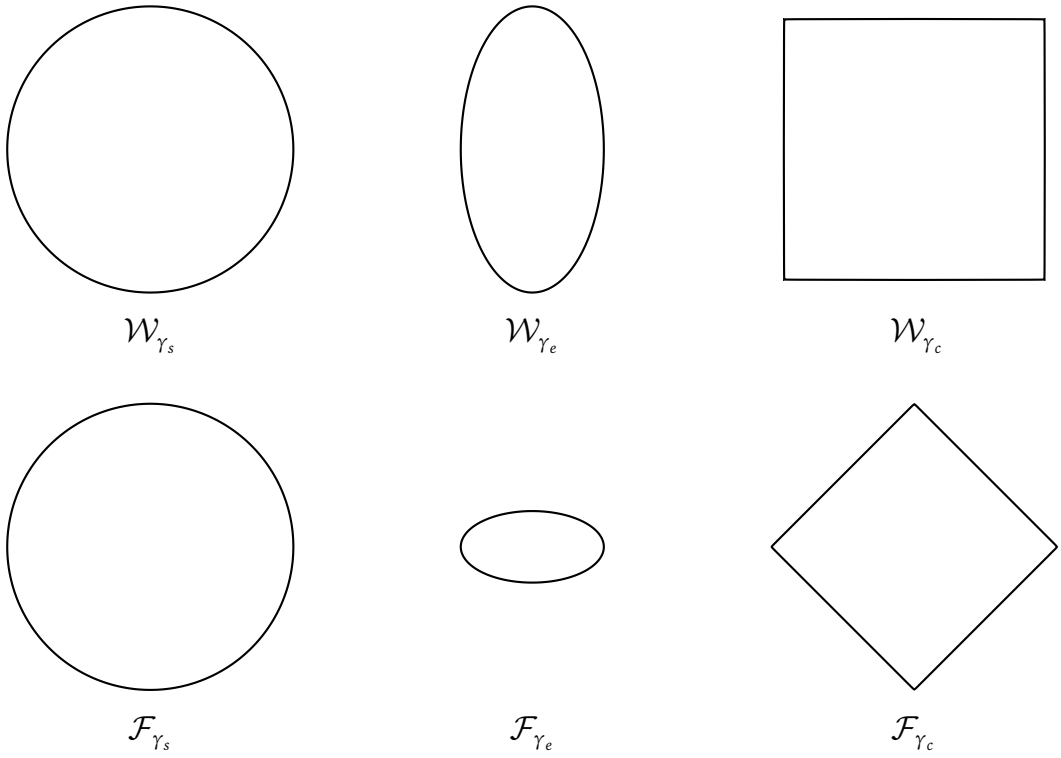

Figure 2.1: Two-dimensional visualization of the boundary of the Wulff shapes $\partial\mathcal{W}_\gamma$ (top) and corresponding Frank diagrams $\partial\mathcal{F}_\gamma$ (bottom) for different choices of the anisotropy γ. From left to right: sphere with anisotropy $\gamma_s(z) = |z|$ (cf. Example 2.2.6), ellipsoid with $\gamma_e(z) = \sqrt{z_1^2 + 2z_2^2}$ (cf. Example 2.2.7) and cube with $\gamma_c(z) = \sum_{l=1}^{2} \sqrt{0.00001\,|z|^2 + z_l^2}$ (cf. Example 2.2.9).

Here γ^* is the dual of γ, given by

$$\gamma^*(z) = \sup_{x \in \mathbb{R}^{d+1}\setminus\{0\}} \frac{z \cdot x}{\gamma(x)}.$$

The next proposition justifies the term „dual“:

Proposition 2.2.3. *Let $\gamma : \mathbb{R}^{d+1} \to \mathbb{R}_0^+$ be an elliptical integrand, then the duality relation $\gamma^{**} = \gamma$ holds.*

Proof. A proof can be found in LEICHTWEISS [124, page 127]. □

Lemma 2.2.4. *The Frank diagram $\mathcal{F}_\gamma$ and the Wulff shape $\mathcal{W}_\gamma$ is convex for an admissible anisotropy γ.*

Proof. Wulff shapes are convex due to Chapter 6.8 in VAN TIEL[166]. Frank diagrams for γ are always convex since γ is convex. □

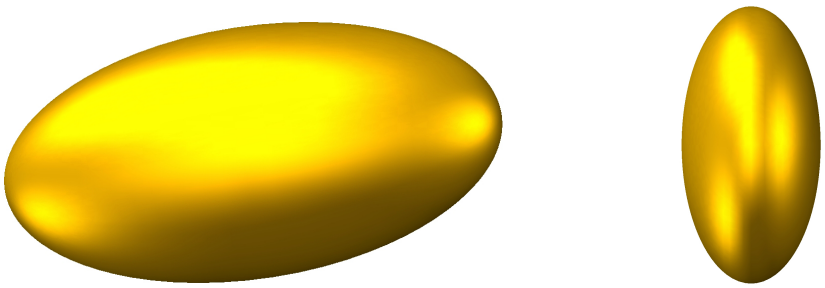

Figure 2.2: Wulff shape (left) and Frank diagram (right) for the anisotropy $\gamma(z) = \sqrt{z_1^2 + z_2^2 + 2z_3^2}$, cf. Example 2.2.7.

Lemma 2.2.5. *Let S^d be the unit sphere in $\mathbb{R}^{d+1}$. Then the boundaries of the Frank diagram $\partial\mathcal{F}_\gamma$ and the Wulff shape $\partial\mathcal{W}_\gamma$ are given as*

$$\partial\mathcal{F}_\gamma = \gamma\left(S^d\right)^{-1} S^d,$$
$$\partial\mathcal{W}_\gamma = \gamma_z\left(S^d\right).$$

Proof. A proof can be found in Clarenz [48, Lemma 5.3]. □

Let us consider some examples. Not all of them are admissible.

Example 2.2.6. (Isotropic case)
The choice

$$\gamma(z) = |z| \tag{2.22}$$

is referred to as the isotropic case. In particular, we have that

$$\mathcal{F}_\gamma = \mathcal{W}_\gamma = \{z \in \mathbb{R}^{d+1} \,|\, |z| \leq 1\} = B_1(0)$$

is the closed unit ball.

Example 2.2.7. (Ellipsoid)
Another example is the elliptical integrand $\gamma : \mathbb{R}^{d+1} \to \mathbb{R}_0^+$

$$\gamma(z) = \sqrt{\sum_{l=1,\cdots,d+1} a_l^2 z_l^2}, \tag{2.23}$$

where $a_i \in \mathbb{R}^+$. Although the formulation of the two step time discretization of the anisotropic Willmore flow incorporates only the anisotropy and not its derivatives, we need first and second derivatives of the anisotropy for a gradient decent method and also third derivatives for the SQP

approach. The derivatives of the anisotropy are

$$\gamma_{z_i}(z) = \frac{a_i^2 z_i}{\sqrt{\sum_{l=1,\cdots,d+1} a_l^2 z_l^2}},$$

$$\gamma_{z_i z_j}(z) = \frac{a_i^2\,\delta_{ij}}{\sqrt{\sum_{l=1,\cdots,d+1} a_l^2 z_l^2}} - \frac{a_i^2 a_j^2 z_i z_j}{\left(\sqrt{\sum_{l=1,\cdots,d+1} a_l^2 z_l^2}\right)^3},$$

$$\gamma_{z_i z_j z_k}(z) = -\frac{a_i^2 a_k^2\,\delta_{ij}\,z_k}{\left(\sqrt{\sum_{l=1,\cdots,d+1} a_l^2 z_l^2}\right)^3} - \frac{(a_i^2 a_j^2(\delta_{ik} z_j + \delta_{jk} z_k)}{\left(\sqrt{\sum_{l=1,\cdots,d+1} a_l^2 z_l^2}\right)^5} + \frac{3\,a_i^2 a_j^2 a_k^2 z_i z_j z_k}{\left(\sqrt{\sum_{l=1,\cdots,d+1} a_l^2 z_l^2}\right)^5},$$

with δ_{ij} being the Kronecker symbol. Since $\partial \mathcal{W}_\gamma = \gamma_z\left(S^{d-1}\right)$ the Wulff shape is an ellipsoid with semi-axes a_l, $l = 1,\cdots,d+1$. The Frank diagram $\mathcal{F}_\gamma = \left\{z \in \mathbb{R}^{d+1} | \gamma(z) \le 1\right\}$ is an ellipsoid with semi-axes $\frac{1}{a_l}$, $l = 1,\cdots,d+1$.

Example 2.2.8. (l^1-norm)
A typical choice for a positive, 1-homogeneous and convex function is the discrete l^1-norm,

$$\gamma(z) = \|z\|_1 = \sum_{l=1}^{d+1} |z_l|\,. \tag{2.24}$$

Its Wulff shape is the d-dimensional cube, whereas the Frank diagram is given by the d-dimensional octahedron.

Example 2.2.9. (Regularized l^1-norm)
Since the discrete l^1-norm is not differentiable we consider the regularized l^1-norm, cf. Figure 2.3,

$$\gamma(z) = \sum_{l=1}^{d+1} \sqrt{\epsilon |z|^2 + z_l^2}, \qquad \epsilon > 0\,.$$

Its derivatives are

$$\gamma_{z_i}(z) = \sum_{l=1}^{d+1} \frac{(\epsilon + \delta_{li}) z_i}{\sqrt{\epsilon |z|^2 + z_l^2}},$$

$$\gamma_{z_i z_j}(z) = \delta_{ij} \sum_{l=1}^{d+1} \frac{\epsilon + \delta_{li}}{\sqrt{\epsilon |z|^2 + z_l^2}} - \sum_{l=1}^{d+1} \frac{(\epsilon + \delta_{li})(\epsilon + \delta_{jl}) z_i z_j}{\left(\sqrt{\epsilon |z|^2 + z_l^2}\right)^3},$$

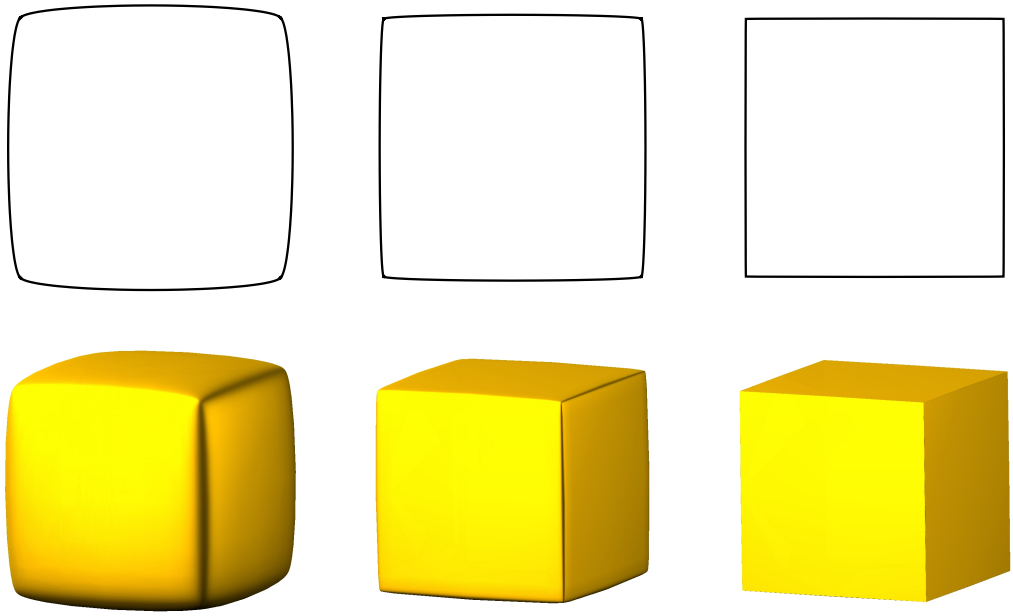

Figure 2.3: Boundaries of the Wulff shapes $\partial \mathcal{W}_\gamma$ for the regularized l^1-anisotropy $\gamma(z) = \sum_{l=1}^{d+1} \sqrt{\epsilon|z|^2 + z_l^2}$ with $\epsilon = 0.01, 0.001, 0.00001$ for curves ($d = 1$, top row) and surfaces ($d = 2$, bottom row), cf. Example 2.2.9.

$$\gamma_{z_i z_j z_k}(z) = -\delta_{ij} \sum_{l=1}^{d+1} \frac{(\epsilon + \delta_{li})(\epsilon + \delta_{kl}) z_k}{\left(\sqrt{\epsilon|z|^2 + z_l^2}\right)^3} - \sum_{l=1}^{d+1} \frac{(\epsilon + \delta_{li})(\epsilon + \delta_{jl})(\delta_{ki} z_j + \delta_{kj} z_i)}{\left(\sqrt{\epsilon|z|^2 + z_l^2}\right)^3}$$
$$+ \sum_{l=1}^{d+1} \frac{3\,(\epsilon + \delta_{li})(\epsilon + \delta_{jl})(\epsilon + \delta_{lk}) z_i z_j z_k}{\left(\sqrt{\epsilon|z|^2 + z_l^2}\right)^5}$$

For a more detailed exposition of the concept of anisotropies we refer to DIEWALD [71] and NEMITZ [130]. Here, we ask for a generalization of the mean curvature. Since $\mathbf{h} = \operatorname{div}_{\mathcal{M}} n$, cf. Equation (2.7), the next definition is justified.

Definition 2.2.3. (Cahn–Hoffmann vector and anisotropic mean curvature)
Suppose that γ is an admissible anisotropy function and that $\mathcal{M} \subset \mathbb{R}^{d+1}$ is an oriented d-dimensional surface with normal mapping $n : \mathcal{M} \to S^d$. We define the *Cahn–Hoffmann vector* $n_\gamma : \mathcal{M} \to \mathcal{W}_\gamma$ by

$$n_\gamma(p) := \gamma_z \circ n(p), \qquad p \in \mathcal{M},$$

and the *anisotropic mean curvature* $\mathbf{h}_\gamma$ by

$$\mathbf{h}_\gamma := \operatorname{div}_{\mathcal{M}}(n_\gamma(p)), \qquad p \in \mathcal{M}.$$

This generalization of the Gauß map n is named after and John W. Cahn and David W. Hoffmann [33, 34].

Note that $\mathbf{h}_\gamma = \mathbf{h}$ in the isotropic case. The Cahn–Hoffmann vector induces the definition of a generalized Weingarten map.

Definition 2.2.4. (Generalized Weingarten map)
Let γ be an admissible anisotropy function, $\mathcal{M} \subset \mathbb{R}^{d+1}$ an oriented d-dimensional surface with Cahn–Hoffmann vector n_γ. We define the generalized Weingarten map S_γ by

$$S_\gamma := \nabla_{\mathcal{M}} n_\gamma = \nabla_{\mathcal{M}} (\gamma_z \circ n) = \gamma_{zz}(n)\, \nabla_{\mathcal{M}} n\,.$$

The mean curvature was defined as $\mathbf{h} = \operatorname{tr}(S)$. The following lemma shows that $\mathbf{h}_\gamma$ is a natural generalization of mean curvature.

Lemma 2.2.10. *Let γ be an elliptical integrand as in Definition 2.2.1 and let n be the surface normal of surface $\mathcal{M}$. The anisotropic mean curvature can be written as*

$$\mathbf{h}_\gamma = \operatorname{tr}\left(S_\gamma\right). \tag{2.25}$$

Proof. Direct consequence of the definition of the tangential divergence, cf. Definition 2.1.4. □

Lemma 2.2.11. (Tangential gradient of the anisotropic mean curvature)
Let γ and n be given as in Lemma 2.2.10. The tangential gradient of the anisotropic mean curvature is given as

$$\nabla_{\mathcal{M}} \mathbf{h}_\gamma = \operatorname{div}_{\mathcal{M}} \left(\nabla_{\mathcal{M}} n\, \gamma_{zz}(n)\right).$$

Proof. This follows from Equation (12) in CLARENZ [50]. In CLARENZ & VON DER MOSEL [57, Corollary 4.2] a proof is given based on the calculation of a mixed second variation of a suitable functional. □

Definition 2.2.5. (Generalized Laplace–Beltrami operator)
Let γ be an elliptical integrand. The generalized Laplace–Beltrami operator applied to a smooth function $\varphi : \mathcal{M} \to \mathbb{R}$ is defined as

$$\Delta_\gamma \varphi := \operatorname{div}_{\mathcal{M}} \left(\gamma_{zz}(n)\, \nabla_{\mathcal{M}} \varphi\right)$$

Proposition 2.2.12. (Generalized Laplace–Beltrami operator of the Gauß map)

$$\Delta_\gamma n = \nabla_{\mathcal{M}} \mathbf{h}_\gamma - \left|\nabla_{\mathcal{M}} n\right|_\gamma^2 n \tag{2.26}$$

Proof. Due to Theorem 1.1 in CLARENZ & VON DER MOSEL[57] we get

$$\operatorname{div}_{\mathcal{M}} \left(\gamma_{zz}(n)\, \nabla_{\mathcal{M}} n\right) + \operatorname{tr}\left(\gamma_{zz}(n)\, \nabla_{\mathcal{M}}^T n\, \nabla_{\mathcal{M}} n\right) n = \operatorname{div}_{\mathcal{M}} \left(\nabla_{\mathcal{M}} n\, \gamma_{zz}(n)\right)$$

Together with Lemma 2.2.11 this proves Equation (2.26). □

2.3 General gradient flows

Let $\mathcal{M}$ be a closed d-dimensional surface embedded in $\mathbb{R}^m$, $m \geq d+1$, with parameterization $x : \mathcal{M} \to \mathbb{R}^m$ assumed to be the identity on $\mathcal{M}$. Our main goal in this thesis will be the minimization of the highly nonlinear anisotropic Willmore functional

$$w_\gamma[x] = \frac{1}{2} \int_{\mathcal{M}} \mathbf{h}_\gamma^2 \, \mathrm{d}a \,, \tag{2.27}$$

where $\mathbf{h}_\gamma$ is the generalized mean curvature. One method to find a solution of the minimization of an energy is to consider its gradient flow. Given an energy functional $e[\cdot]$, the corresponding gradient flow is the motion of the surface that follows the steepest descent of the energy functional given by its negative gradient. The derivative of e defined on an infinite-dimensional space is given by its first variation. Disturbing the parametrization x of a surface $\mathcal{M}[x]$ by a test function $\vartheta \in \mathcal{C}^1(\mathcal{M}, \mathbb{R}^m)$ we get

$$\left\langle e'[x], \vartheta \right\rangle := \partial_\epsilon e[x + \epsilon \vartheta]\Big|_{\epsilon=0} . \tag{2.28}$$

To measure the velocity of the evolution, we equip the space of deformations with a metric $g(\cdot,\cdot)$. Then, the gradient is defined by the representation of the first variation in the metric g, i.e.

$$g\left(\operatorname{grad}_g e[x], \vartheta\right) = \left\langle e'[x], \vartheta \right\rangle \qquad \forall \vartheta \in \mathcal{C}^1(\mathcal{M}, \mathbb{R}^m) . \tag{2.29}$$

Given energy and metric the corresponding gradient flow is the evolution of an initial parametrization x^0 of the surface $\mathcal{M}[x^0]$ in the direction of the negative gradient and defines a one parameter family of parametrizations $x(t)$ via

$$\begin{aligned} \partial_t x(t) &= -\operatorname{grad}_g e[x(t)] \,, \\ x(0) &= x^0 \,, \end{aligned} \tag{2.30}$$

which leads to finding a family of parametrizations $x(t)$, such that

$$\left(\partial_t x(t), \vartheta\right)_g = -\left\langle e'[x(t)], \vartheta \right\rangle \qquad \forall \vartheta \in \mathcal{C}^1(\mathcal{M}, \mathbb{R}^m) .$$

This evolution does preserve descent directions, i.e.

$$\left\langle e'[x(t)], -\operatorname{grad}_g e[x(t)] \right\rangle = g\left(\operatorname{grad}_g e[x(t)], -\operatorname{grad}_g e[x(t)]\right) \leq 0 .$$

One choice for the metric is the L^2-metric given by the intrinsic L^2-scalar product on $\mathcal{M}$, namely

$$g(\varphi, \vartheta) = (\varphi, \vartheta)_{L^2(\mathcal{M})} = \int_{\mathcal{M}} \varphi \, \vartheta \, \mathrm{d}a \,.$$

The gradient flow with respect to $(\cdot,\cdot)_{L^2(\mathcal{M})}$ is then given by

$$\partial_t x(t) = -\mathrm{grad}_{L^2(\mathcal{M})} e[x(t)]$$

or equivalently

$$\left(\partial_t x(t), \vartheta\right)_{L^2(\mathcal{M})} = -\left\langle e'[x(t)], \vartheta \right\rangle \qquad \forall \vartheta \in \mathcal{C}^1(\mathcal{M}, \mathbb{R}^m).$$

Let us first consider the steepest decent of the anisotropic area functional

$$a_\gamma[x] = \int_{\mathcal{M}} \gamma(n)\,\mathrm{d}a\,,$$

where n is the surface normal and γ is a given elliptical integrand as in Definition 2.2.1. To calculate the first variation of a_γ, we consider the disturbed surface $x_\epsilon = x + \epsilon\vartheta$ for test functions $\vartheta \in \mathcal{C}^1(\mathcal{M}, \mathbb{R}^m)$. The test function is decomposed into a normal and tangential part

$$\vartheta = \varphi\, n + v, \tag{2.31}$$

where $\varphi \in \mathcal{C}^1(\mathcal{M})$ is a smooth function and $v \in \mathcal{C}^1(\mathcal{M}, T_p\mathcal{M})$ is a smooth tangential vector field. We get the following proposition:

Proposition 2.3.1. *Let $x : \mathcal{M} \to \mathbb{R}^m$ be an immersion. For the derivative of the anisotropic area functional in direction ϑ given as in Equation* (2.31) *we have*

$$\left\langle a'_\gamma[x], \vartheta \right\rangle = \int_{\mathcal{M}} \mathbf{h}_\gamma\, n \cdot \vartheta\, da\,.$$

Proof. A proof can be found in Clarenz [49, p. 5]. □

It is well known that the steepest descent of the isotropic area functional corresponds to the evolution of the surface in normal direction weighted by the negative mean curvature. We refer to [64, 67, 13, 14] for a more detailed overview on the L^2-gradient flow of the area functional, the mean curvature motion for surfaces. The curve shortening flow was for example discussed in [97, 102]. Since $\mathbf{h}_\gamma$ appears as the first variation of the anisotropic area functional, $\mathbf{h}_\gamma$ is a natural generalization of the mean curvature. The gradient flow of the anisotropic area functional with respect to the L^2-metric is now given by

$$\partial_t x = -\mathbf{h}_\gamma\, n\,. \tag{2.32}$$

We refer to the works [20, 63, 83, 15] on the anisotropic mean curvature motion or anisotropic curve shortening flow. Let us remark that every inner product yields its own gradient and thus, a different gradient flow. Another example for the inner product is the H^{-1}-metric

$$g(\varphi,\vartheta) = (\varphi,\vartheta)_{H^{-1}(\mathcal{M})} = -\int_{\mathcal{M}} \Delta_{\mathcal{M}}^{-1}\varphi \cdot \vartheta\,\mathrm{d}a\,.$$

It is well known that surface diffusion

$$\partial_t x = (\Delta_{\mathcal{M}} \mathbf{h})\, n$$

is the gradient flow of the area functional with respect to the H^{-1}-metric [32, 12, 11]. One of its main applications is in the modeling of epitaxial growth of crystals [149, 10]. Anisotropic surface diffusion can be obtained similarly, see [31, 68, 69] for further details.

Let us remark that the first variation of a_γ is independent of tangential variations. Therefore, it is sufficient to consider only only variations w.r.t. normal direction, i.e. we only have to consider a family of surfaces with parametrizations $x_\epsilon = x + \epsilon\, \varphi\, n$. The same holds for the first variation of the anisotropic Willmore functional (2.27), where we have the following proposition for its gradient flow corresponding to the L^2-metric.

Proposition 2.3.2. *Let $x : \mathcal{M} \to \mathbb{R}^3$ be an immersion. For the derivative of the anisotropic Willmore functional in direction ϑ given as in Equation* (2.31) *we have*

$$\left\langle w_\gamma'[x], \vartheta \right\rangle = \int_{\mathcal{M}} \left(\Delta_\gamma \mathbf{h}_\gamma + \mathbf{h}_\gamma \left| \nabla_{\mathcal{M}}\, n \right|_\gamma^2 - \frac{1}{2}\, \mathbf{h}\, \mathbf{h}_\gamma^2 \right) n \cdot \vartheta \, da.$$

Proof. A proof can be found in Clarenz [50, (15)]. □

The L^2-gradient flow of the anisotropic Willmore functional for closed surfaces is then given by

$$\partial_t x = \left(\Delta_\gamma \mathbf{h}_\gamma + \mathbf{h}_\gamma \left| \nabla_{\mathcal{M}}\, n \right|_\gamma^2 - \frac{1}{2}\, \mathbf{h}\, \mathbf{h}_\gamma^2 \right) n. \tag{2.33}$$

We review the calculation for surfaces with boundaries in Section 3.2.

2.4 Finite Element space discretization

To discretize the semi-implicit scheme and the two step time discretization in space we use piecewise affine Finite Elements. The ingredients that will be needed in both algorithms are collected in this section. We follow the guideline for Finite Elements on surfaces introduced by Dziuk [80]. For further information we refer to Braess [28] and Brenner & Scott [30]. Thus, we consider simplicial meshes $\mathcal{M}[X]$ – polygonal curves for $d = 1$ and triangular surfaces for $d = 2$ – as approximations of the d-dimensional surfaces $\mathcal{M}[x]$. Here, X is the identity on the simplicial mesh $\mathcal{M}[X]$ embedded in $\mathbb{R}^m$, $m = 2, 3$ for curves and $m = 3$ for surfaces, which is described by a vector $\bar{X}$ of vertex positions of the mesh. To clarify the notation we will always denote discrete quantities with upper case letters to distinguish them from the corresponding continuous quantities in lower case letters. Furthermore, a bar on top of a discrete function indicates the corresponding nodal vector, i.e.

$$\bar{X} = (\bar{X}_i)_{i \in I},$$

where

$$\bar{X}_i = (X_i^1, \cdots, X_i^m)$$

is the coordinate vector of the ith vertex of the mesh and I denotes the index set of vertices. Using also local indices each element T of a polygonal curve is a line segment with nodes X_1 and X_2 and elements T of a triangulation are planar triangles with vertices X_0, X_1 and X_2 and face vectors $F_0 = X_2 - X_1$, $F_1 = X_0 - X_2$ and $F_2 = X_1 - X_0$. Given a simplicial surface $\mathcal{M}[X]$ we denote by

$$\mathcal{V}(\mathcal{M}[X]) := \left\{U \in C^0(\mathcal{M}[X]) \,|\, U|_T \in \mathcal{P}_1 \,\forall T \subset \mathcal{M}[X]\right\} \tag{2.34}$$

the corresponding piecewise affine Finite Element space consisting of those functions which are affine on each element T of $\mathcal{M}[X]$. $\mathcal{P}_1$ denotes the space of affine linear polynomials. With a slight misuse of notation the mapping X itself is considered as an element in $\mathcal{V}(\mathcal{M}[X])^m$. Let $\{\Phi_i\}_{i\in I}$ be the nodal basis of $\mathcal{V}(\mathcal{M}[X])$. Thus, for $U \in \mathcal{V}(\mathcal{M}[X])$ we obtain

$$U = \sum_{i\in I} U(X_i)\Phi_i, \qquad \bar{U} = (U(X_i))_{i\in I}, \tag{2.35}$$

in particular in accordance to our definition above we recover $\bar{X} = (X_i)_{i\in I}$.

Next, let us introduce the **mass matrix** $M[X]$ and the **stiffness matrix** $L[X]$ on the discrete surface $\mathcal{M}[X]$, whose entries are given by

$$M_{ij}[X] = \int_{\mathcal{M}[X]} \Phi_i \Phi_j \,\mathrm{d}a\,, \tag{2.36}$$

$$L_{ij}[X] = \int_{\mathcal{M}[X]} \nabla_{\mathcal{M}[X]}\Phi_i \cdot \nabla_{\mathcal{M}[X]}\Phi_j \,\mathrm{d}a\,, \tag{2.37}$$

$i, j \in I$. To apply mass and stiffness matrices to discrete maps from $\mathcal{M}[X]$ to $\mathbb{R}^m$, we need corresponding block matrices $\mathbf{M}[X]$ and $\mathbf{L}[X]$ in $\mathbb{R}^{m\sharp I, m\sharp I}$:

$$\mathbf{M}[X] = \begin{pmatrix} M[X] & & \\ & \ddots & \\ & & M[X] \end{pmatrix},$$

$$\mathbf{L}[X] = \begin{pmatrix} L[X] & & \\ & \ddots & \\ & & L[X] \end{pmatrix}.$$

Both, mass and stiffness matrix M and L can be assembled from corresponding local mass and stiffness matrices $m(T)$ and $l(T)$ for all simplices T on $\mathcal{M}[X]$. The global matrices are initialized with zero entries. Traversing over all simplices T we calculate local matrices with entries corresponding to all pairs of local nodal basis functions. Then the local matrix entries are added to the matching entries in the global matrix.

To discretize anisotropic energy functionals we also need two different kinds of anisotropic versions of the stiffness matrix, weighted stiffness matrices and weighted anisotropic stiffness matrices:

Weighted stiffness matrices. Let $\eta : \mathcal{M}[X] \to \mathbb{R}$ be a scalar weight and $\mu : \mathcal{M}[X] \to \mathbb{R}^{m,m}$ a matrix-valued weight, $\mu = (\mu_{kl})$, $k,l = 1,\cdots,m$. The entries of the weighted stiffness matrices $L^{\eta}[X]$ and $L^{\mu_{kl}}[X]$, $k,l = 1,\cdots,m$, on the discrete surface $\mathcal{M}[X]$ are given by

$$L^{\eta}_{ij}[X] = \int_{\mathcal{M}[X]} \eta \, \nabla_{\mathcal{M}[X]}\Phi_i \cdot \nabla_{\mathcal{M}[X]}\Phi_j \, \mathrm{d}a, \tag{2.38}$$

$$L^{\mu_{kl}}_{ij}[X] = \int_{\mathcal{M}[X]} \mu_{kl} \, \nabla_{\mathcal{M}[X]}\Phi_i \cdot \nabla_{\mathcal{M}[X]}\Phi_j \, \mathrm{d}a\,, \tag{2.39}$$

with corresponding block matrices $\mathbf{L}^{\eta}[X]$ and $\mathbf{L}^{\mu}[X]$ in $\mathbb{R}^{3\sharp I,3\sharp I}$

$$\mathbf{L}^{\eta}[X] = \begin{pmatrix} L^{\eta}[X] & & \\ & L^{\eta}[X] & \\ & & L^{\eta}[X] \end{pmatrix},$$

$$\mathbf{L}^{\mu}[X] = \begin{pmatrix} L^{\mu_{11}}[X] & L^{\mu_{12}}[X] & L^{\mu_{13}}[X] \\ L^{\mu_{21}}[X] & L^{\mu_{22}}[X] & L^{\mu_{23}}[X] \\ L^{\mu_{31}}[X] & L^{\mu_{32}}[X] & L^{\mu_{33}}[X] \end{pmatrix}.$$

for surfaces. Analogously, we get the corresponding block matrices $\mathbf{L}^{\eta}[X]$ and $\mathbf{L}^{\mu}[X]$ in $\mathbb{R}^{2\sharp I,2\sharp I}$ for polygonal curves. Both anisotropic stiffness matrices L^{η} and $L^{\mu_{kl}}$ can be assembled from corresponding local matrices $l^{\eta}(T)$ and $l^{\mu_{kl}}(T)$ for all simplices T on $\mathcal{M}[X]$. In the two step time discretization of the anisotropic Willmore flow we will need weighted mass and stiffness matrices with weights $\eta = \gamma$ or $\eta = N \otimes \gamma_z$, where γ is an elliptical integrand with derivative γ_z and N the surface normal. For the semi-implicit scheme we also need stiffness matrices weighted by $\eta = |Y|^2$. If the matrices are weighted by the anisotropy function γ depending on the normal mapping, we need the piecewise constant surface normal:

Surface normal. For simplicial meshes $\mathcal{M}[X]$ the normal N_T of an element T with segment F_0 for polygonal curves with $m = 2$ and sides F_0, F_1, F_2 for triangulated surfaces with $m = 3$, is given by

$$N_T = \frac{D^{90}F_0}{|F_0|} = \frac{D^{90}F_0}{|T|}, \quad N_T = \frac{F_2 \wedge F_1}{|F_2 \wedge F_1|} = \frac{1}{2}\frac{F_2 \wedge F_1}{|T|}, \tag{2.40}$$

respectively, where D^{90} denotes a counter-clockwise rotation by the angle of 90 degrees. The discrete surface normal N_i at node $i \in I$ is then given by

$$N_i = \frac{\sum_{\omega_i} |T| N_T}{\left|\sum_{\omega_i} |T| N_T\right|}, \tag{2.41}$$

where ω_i consists of all triangles that contain node $i \in I$.

Weighted anisotropic stiffness matrix. Besides weighted stiffness matrices L^{γ}, $L^{N\otimes\gamma_z}$, and $L^{|Y|^2}$ we need weighted anisotropic stiffness matrices in the semi-implicit discretization scheme in time for the anisotropic Willmore flow. Let γ be an elliptical integrand with second derivative γ_{zz} and $\mu : \mathcal{M}[X] \to \mathbb{R}^{m,m}$, $\mu = (\mu_{kl})$, $k,l = 1,\cdots,m$, a matrix-valued weight. The entries of the weighted anisotropic stiffness matrix $L^{\mu_{kl}}_{\gamma_{zz}}[X]$, $k,l = 1,\cdots,m$, on the discrete surface $\mathcal{M}[X]$ are given by

$$L^{\mu_{kl}}_{\gamma_{zz},ij}[X] = \int_{\mathcal{M}[X]} \mu_{kl}\, \gamma_{zz}(N)\, \nabla_{\mathcal{M}[X]}\Phi_i \cdot \nabla_{\mathcal{M}[X]}\Phi_j \,\mathrm{d}a \tag{2.42}$$

with corresponding block matrix $\mathbf{L}^{\mu}_{\gamma_{zz}}[X]$. Let

$$\mathbf{L}_{\gamma_{zz}}[X] = \mathbf{L}^{1}_{\gamma_{zz}}[X] \tag{2.43}$$

denote the non-weighted anisotropic stiffness matrix.

Let us give explicit formulae for the entries of the mass and all kinds of stiffness matrices. Later in Section 2.4.1 we will have to compute variations of these entries as well.

Polygonal curves. In the case of curves we consider a lumped mass matrix, cf. THOMÉE [163], with entries

$$M^{L}_{ij}[X] = M_{ij}[X] = \int_{\mathcal{M}[X]} \mathcal{I}(\Phi_i\Phi_j)\,\mathrm{d}a\,, \tag{2.44}$$

where $\mathcal{I}$ denotes the Lagrange interpolation on the linear Finite Element space. We obtain directly for the global matrices

$$M[X] = \operatorname{diag}\left(\frac{1}{2}(Q_i + Q_{i+1})\right),$$

$$L[X] = \operatorname{tridiag}\left(-\frac{1}{Q_i}, \frac{1}{Q_i} + \frac{1}{Q_{i+1}}, -\frac{1}{Q_{i+1}}\right),$$

where $Q_i = |X_i - X_{i-1}|$ is the length of the ith line segment and diag() and tridiag() denote diagonal or tridiagonal matrices with the corresponding entries in each row. Here, we assume a cyclic indexing, i.e. we identify the indices $i = 0$ and $i = \sharp I$ for closed curves with $X_0 = X_{\sharp I}$. Therefore, we get additional entries in the first and last bands of the matrices. We will consider piecewise constant weights η and μ and the corresponding anisotropic versions of the anisotropic matrices are given by

$$M^{\eta}[X] = \operatorname{diag}\left(\frac{1}{2}(\eta_i Q_i + \eta_{i+1} Q_{i+1})\right),$$

$$L^{\eta}[X] = \operatorname{tridiag}\left(-\frac{\eta_i}{Q_i}, \frac{\eta_i}{Q_i} + \frac{\eta_{i+1}}{Q_{i+1}}, -\frac{\eta_{i+1}}{Q_{i+1}}\right),$$

$$L^{\mu_{kl}}[X] = \operatorname{tridiag}\left(-\frac{\mu_{kl,i}}{Q_i}, \frac{\mu_{kl,i}}{Q_i} + \frac{\mu_{kl,(i+1)}}{Q_{i+1}}, -\frac{\mu_{kl,(i+1)}}{Q_{i+1}}\right),$$

where $\eta_i = \eta|_{T_i}$ and $\mu_{kl,i} = \mu_{kl}|_{T_i}$.

Triangular surfaces. Due to the greater variability of triangular surfaces compared to polygonal curves, let us consider the local matrices on triangles separately. Denoting the local basis function on a triangle T by Φ_0, Φ_1, Φ_2, where $\Phi_i(X_j) = \delta_{ij}$ with δ_{ij} being the Kronecker symbol we verify by a straightforward computation, cf. DIEWALD, MORIGI & RUMPF[72], that

$$m^\eta(T) = \left(\int_T \eta\, \Phi_i \Phi_j \,\mathrm{d}a \right)_{i,j=0,1,2} = \eta|_T \frac{|T|}{12} \begin{pmatrix} 2 & 1 & 1 \\ 1 & 2 & 1 \\ 1 & 1 & 2 \end{pmatrix},$$

with $|T| = \frac{1}{2}|F_2 \wedge F_1|$ being the area of the triangle T and the corresponding lumped version

$$m^\eta(T) = \left(\int_T \eta\, \mathcal{I}\left(\Phi_i \Phi_j\right) \,\mathrm{d}a \right)_{i,j=0,1,2} = \eta|_T \frac{|T|}{3} \begin{pmatrix} 1 & 0 & 0 \\ 0 & 1 & 0 \\ 0 & 0 & 1 \end{pmatrix}.$$

The local stiffness matrices are given by

$$l^\eta(T)_{ij} = \int_T \eta|_T \,\nabla_T \Phi_i \cdot \nabla_T \Phi_j \,\mathrm{d}a = \eta|_T \,\frac{F_i \cdot F_j}{4|T|},$$

where ∇_T is the gradient on the planar element T. There we have used that

$$\nabla_T \Phi_i = \frac{\nu_i}{h_i} = \frac{F_i}{h_i |F_i|} = \frac{F_i}{2|T|},$$

where ν_i is the outer normal to the edge F_i and h_i the height of the triangle over the edge F_i.

Dirichlet boundary condition. We will extend the anisotropic Willmore flow to surfaces with boundaries to solve surface restoration problems. Let $\mathcal{M}[X]$ be a surface with boundary $\partial\mathcal{M}[X]$. In Chapters 3 and 5 we study the discrete anisotropic Willmore flow of $\mathcal{M}[X]$ with fixed boundary $\partial\mathcal{M}[X]$, i.e. Dirichlet boundary conditions for the coordinate vector X. We define $\mathcal{M}^{int}[X] \subset \mathcal{M}[X]$ with

$$\mathcal{M}^{int}[X] = \{T \in \mathcal{M}[X] \;\big|\; T \cap \partial\mathcal{M}[X] = \emptyset\}. \tag{2.45}$$

Let I and I^{int} be the index sets of the vertices of $\mathcal{M}[X]$ and $\mathcal{M}^{int}[X]$. The set of nodes of $\mathcal{M}[X]$ is denoted by $\mathcal{N}$ and splits into interior nodes $\mathcal{N}^{int}$ and boundary nodes $\mathcal{N}^\partial$ with index set $I^\partial = I \setminus I^{int}$, i.e. $\mathcal{N} = \mathcal{N}^{int} \cup \mathcal{N}^\partial$. We denote by

$$\mathcal{V}^{int}(\mathcal{M}[X]) := \left\{ U \in C^0(\mathcal{M}[X]) \,|\, U|_T \in \mathcal{P}_1 \,\forall T \in \mathcal{M}[X], U|_{\partial\mathcal{M}[X]} = 0 \right\} \tag{2.46}$$

the piecewise affine Finite Element space of $\mathcal{M}[X]$ with vanishing boundary values and by $\mathcal{V}^{ext}(\mathcal{M}[X])$ with vanishing exterior values, i.e. we have

$$\mathcal{V}(\mathcal{M}[X]) = \mathcal{V}^{int}(\mathcal{M}[X]) \oplus \mathcal{V}^{ext}(\mathcal{M}[X]).$$

To map between the function spaces $\mathcal{V}(\mathcal{M}[X])$ and $\mathcal{V}^{int}(\mathcal{M}[X]])$ we define a restriction operator $R : \mathcal{V}(\mathcal{M}[X]) \to \mathcal{V}^{int}(\mathcal{M}[X])$ and an extension operator $E : \mathcal{V}^{int}(\mathcal{M}[X]) \to \mathcal{V}(\mathcal{M}[X])$ that extend a function on $\partial\mathcal{M}[X]$ by zero. With a slight misuse of notation

$$E : \mathbb{R}^{\sharp I^{int}} \to \mathbb{R}^{\sharp I} \tag{2.47}$$

and

$$R : \mathbb{R}^{\sharp I} \to \mathbb{R}^{\sharp I^{int}} \tag{2.48}$$

denote also the matrices corresponding to the operators. The corresponding block matrices are $\mathbf{R}$ in $\mathbb{R}^{m\sharp I^{int},m\sharp I}$and $\mathbf{E}$ in $\mathbb{R}^{m\sharp I,m\sharp I^{int}}$. Again, a bar on top of a discrete function indicates the corresponding nodal vector, i.e. $\bar{X}(t) = (\bar{X}_i(t))_{i\in I^{int}}$ is the coordinate vector of the interior vertices of the mesh. Let

$$E\bar{X} + \bar{X}^{ext} \tag{2.49}$$

be the corresponding nodal vector in $\mathbb{R}^{m\sharp I}$, where $\bar{X}^{ext}$ is the position vector for the boundary nodes with zero entries for all interior nodes.

2.4.1 Variations of the mass and stiffness matrix

Since the two step time dicretization of the Willmore flow is fully implicit, we have to compute variations of the mass and stiffness matrix with respect to test functions $\Theta \in \mathcal{V}(\mathcal{M}[X])^m$ of the simplicial grid,

$$\partial_X \mathbf{M}[X](\Theta) = \begin{pmatrix} \partial_X M[X](\Theta) & & \\ & \ddots & \\ & & \partial_X M[X](\Theta) \end{pmatrix},$$

$$\partial_X \mathbf{L}[X](\Theta) = \begin{pmatrix} \partial_X L[X](\Theta) & & \\ & \ddots & \\ & & \partial_X L[X](\Theta) \end{pmatrix},$$

where

$$\partial_X M[X](\Theta) = \frac{\partial}{\partial\epsilon} M[X + \epsilon\,\Theta]\Big|_{\epsilon=0} \quad \text{and} \quad \partial_X L[X](\Theta) = \frac{\partial}{\partial\epsilon} L[X + \epsilon\,\Theta]\Big|_{\epsilon=0}.$$

We will solve the minimization problem with a sequential quadratic programming (SQP) approach that is a Newton type method. Therefore we also need second derivatives of the mass and stiffness matrix with respect to test functions $\Theta, \Psi \in \mathcal{V}(\mathcal{M}[X])^m$,

$$\partial_X^2 \mathbf{M}[X](\Theta,\Psi) = \begin{pmatrix} \partial_X^2 M[X](\Theta,\Psi) & & \\ & \ddots & \\ & & \partial_X M[X](\Theta,\Psi) \end{pmatrix},$$

$$\partial_X^2 \mathbf{L}[X](\Theta,\Psi) = \begin{pmatrix} \partial_X^2 L[X](\Theta,\Psi) & & \\ & \ddots & \\ & & \partial_X^2 L[X](\Theta,\Psi) \end{pmatrix},$$

where

$$\partial_X^2 M[X](\Theta,\Psi) = \frac{\partial^2}{\partial\mu\,\partial\eta} M[X+\eta\,\Theta+\mu\,\Psi]\Big|_{\eta,\mu=0} \quad \text{and}$$

$$\partial_X^2 L[X](\Theta,\Psi) = \frac{\partial^2}{\partial\mu\,\partial\eta} L[X+\eta\,\Theta+\mu\,\Psi]\Big|_{\eta,\mu=0}.$$

Polygonal curves. We obtain for the derivatives of the mass matrix (using again the usual Kroneckersymbol δ_{ir}) with respect to a variation of node r in direction s

$$\partial_X M[X](\Phi_r e_s) = \operatorname{diag}\left(\frac{(X_{i-1}^s - X_i^s)(\delta_{(i-1)r}-\delta_{ir})}{2Q_i} + \frac{(X_i^s - X_{i+1}^s)(\delta_{ir}-\delta_{(i+1)r})}{2Q_{i+1}}\right),$$

where as above $Q_i = |X_i - X_{i-1}|$. Furthermore, we get for the derivatives for the stiffness matrix in the same direction

$$\partial_X L[X](\Phi_r e_s) = \operatorname{tridiag}(\partial_X L_{i-1}, \partial_X L_i, \partial_X L_{i+1}),$$

where

$$\begin{aligned}
\partial_X L_{i-1} &:= \frac{(X_{i-1}^s - X_i^s)(\delta_{(i-1)r} - \delta_{ir})}{Q_i^3},\\
\partial_X L_i &:= -\frac{(X_{i-1}^s - X_i^s)(\delta_{(i-1)r} - \delta_{ir})}{Q_i^3} - \frac{(X_i^s - X_{i+1}^s)(\delta_{ir} - \delta_{(i+1)r})}{Q_{i+1}^3},\\
\partial_X L_{i+1} &:= \frac{(X_i^s - X_{i+1}^s)(\delta_{ir} - \delta_{(i+1)r})}{Q_{i+1}^3}.
\end{aligned}$$

The second derivative of the mass matrix with respect to a first variation of node r in direction s and a second variation of node q in direction t is given by

$$\begin{aligned}
\partial_X^2 M[X](\Phi_r e_s, \Phi_q e_t) = \operatorname{diag}\Bigg(&\frac{\delta_{ts}(\delta_{(i-1)q} - \delta_{iq})}{2Q_i}\\
&- \frac{(X_{i-1}^s - X_i^s)(\delta_{(i-1)r} - \delta_{ir})(X_{i-1}^t - X_i^t)(\delta_{(i-1)q} - \delta_{iq})}{2Q_i^3}\\
&+ \frac{\delta_{ts}(\delta_{iq} - \delta_{(i+1)iq})}{2Q_i}\\
&- \frac{(X_i^s - X_{i+1}^s)(\delta_{ir} - \delta_{(i+1)r})(X_i^t - X_{i+1}^t)(\delta_{iq} - \delta_{(i+1)q})}{2Q_{i+1}^3}\Bigg).
\end{aligned}$$

We get for the second derivatives of the stiffness matrix in the same direction

$$\partial_X^2 L[X](\Phi_r e_s, \Phi_q e_t) = \operatorname{tridiag}(\partial_X^2 L_{i-1}, \partial_X^2 L_i, \partial_X^2 L_{i+1}),$$

where

$$\partial_X^2 L_{i-1} := \frac{\delta_{ts}(\delta_{(i-1)q} - \delta_{iq})(\delta_{(i-1)r} - \delta_{ir})}{Q_i^3} - 3 \cdot \frac{(X_{i-1}^s - X_i^s)(\delta_{(i-1)r} - \delta_{ir})(X_{i-1}^t - X_i^t)(\delta_{(i-1)q} - \delta_{iq})}{Q_i^5},$$

$$\partial_X^2 L_{i+1} := \frac{\delta_{ts}(\delta_{iq} - \delta_{(i+1)q})(\delta_{ir} - \delta_{(i+1)r})}{Q_{i+1}^3} - 3 \cdot \frac{(X_i^s - X_{i+1}^s)(\delta_{ir} - \delta_{(i+1)r})(X_i^t - X_{i+1}^t)(\delta_{iq} - \delta_{(i+1)q})}{Q_{i+1}^5},$$

$$\partial_X^2 L_i := -\partial_{XX}^2 L_{i-1} - \partial_{XX}^2 L_{i+1}.$$

Triangular surfaces. The first variation of $|T|$ with respect to a variation of node r in direction s is given by

$$\partial_X |T|(\Phi_r e_s) = \frac{1}{2} \frac{F_1 \wedge F_2}{|F_1 \wedge F_2|} \cdot D_s^{90} P_s F_r,$$

where $\wedge$ denotes the cross product. P_s is a projection onto the plane spanned by the vectors e_{s-1} and e_{s+1} and D_s^{90} a counter-clockwise rotation by 90 degree in this plane. Here, we assumed vertex indices to be in $\{0, 1, 2\}$ and take them modulo 2 if this is not the case. Now, we obtain for the derivative of the local mass matrix with respect to a variation of node r in direction s

$$\partial_X m(T)(\Phi_r e_s) = \frac{\partial_X |T|(\Phi_r e_s)}{12} \begin{pmatrix} 2 & 1 & 1 \\ 1 & 2 & 1 \\ 1 & 1 & 2 \end{pmatrix}.$$

The corresponding derivative of the local stiffness matrix is given by

$$\partial_X l(T)_{ij}(\Phi_r e_s) = \frac{1}{4|T|}((\delta_{r(i-1)} - \delta_{r(i+1)})F_j^s + (\delta_{r(j-1)} - \delta_{r(j+1)})F_i^s) - \frac{\partial_X |T|(\Phi_r e_s)}{4|T|^2} F_i \cdot F_j.$$

The second variation of $|T|$ with respect to a variation of node r in direction s and node q in direction t, respectively, is given by

$$\partial_X^2 |T|(\Phi_r e_s, \Phi_q e_t) = \frac{1}{2} \left(\frac{\partial_X (F_1 \wedge F_2)(\Phi_q e_t)}{|F_1 \wedge F_2|} - \frac{(F_1 \wedge F_2)((F_1 \wedge F_2) \cdot D_t^{90} P_t F_q)}{|F_1 \wedge F_2|^3} \right) \cdot D_s^{90} P_s F_r + \frac{1}{2} \frac{F_1 \wedge F_2}{|F_1 \wedge F_2|} \cdot \left((\delta_{q(r-1)} - \delta_{q(r+1)}) D_s^{90} P_s e_t \right)$$

with

$$\partial_X (F_1 \wedge F_2)(\Phi_q e_t) = (1 - \delta_{kt}) \left((\delta_{0q} - \delta_{2q}) F_2^{(5-t)} - (\delta_{1q} - \delta_{0q}) F_1^{(5-t)} \right) (1 - \delta_{(k+1)t}),$$

where we identify indices 4 and 1. For the second derivative of the local mass matrix with respect to a first variation of node r in direction s and a second variation of node q in direction t we have

$$\partial_X^2 m(T)(\Phi_r e_s, \Phi_q e_t) = \frac{\partial_X^2 |T|(\Phi_r e_s, \Phi_q e_t)}{12} \begin{pmatrix} 2 & 1 & 1 \\ 1 & 2 & 1 \\ 1 & 1 & 2 \end{pmatrix}.$$

The corresponding second derivative of the local stiffness matrix is given by

$$\begin{aligned} \partial_X^2 l(T)_{ij}(\Phi_r e_s, \Phi_q e_t) = \frac{\delta_{ts}}{4|T|}&((\delta_{r(i-1)} - \delta_{r(i+1)})(\delta_{q(j-1)} - \delta_{q(j+1)}) \\ &+ (\delta_{r(j-1)} - \delta_{r(j+1)})(\delta_{q(i-1)} - \delta_{q(i+1)})) \\ &- \frac{\partial_X |T|(\Phi_q e_t)}{16|T|^2}((\delta_{r(i-1)} - \delta_{r(i+1)})F_j^s + (\delta_{r(j-1)} - \delta_{r(j+1)})F_i^s) \\ &- \frac{\partial_X^2 |T|(\Phi_r e_s, \Phi_q e_t)|T| - 2\,\partial_X |T|(\Phi_r e_s)\partial_X |T|(\Phi_q e_t)}{4|T|^3} F_i \cdot F_j \\ &- \frac{\partial_X |T|(\Phi_r e_s)}{4|T|^2}((\delta_{q(i-1)} - \delta_{q(i+1)})F_j^t + (\delta_{r(j-1)} - \delta_{r(j+1)})F_i^t). \end{aligned}$$

Variations of the weighted mass and stiffness matrix. We have also implemented a SQP approach for the two step time discretization of the anisotropic Willmore flow for polygonal curves. Because of Equations (2.17) and (2.18) we can simplify the derivatives of the weighted mass and stiffness matrices with weight γ. The calculations are collected in Chapter 6. We also need the second variations of the mass and stiffness matrices to calculate the Hessian in the SQP approach. We refer to Chapter 6 for the derivatives for the anisotropic Willmore flow for polygonal curves.

Chapter 3

Review of the anisotropic Willmore flow for surfaces

IN this chapter we develop a semi-implicit time discretization of the anisotropic Willmore flow for parametric surfaces with boundaries. We compare the resulting scheme with the two step time discretization of the Willmore flow for closed surfaces in Section 4.5 of Chapter 4 and for surfaces with boundaries in Section 5.4 of Chapter 5. RUSU derived in [148] a variational form for the parametric Willmore flow which uses a mixed method with position and mean curvature vector as independent variables and allows the use of piecewise linear Finite Elements for the spatial discretization. This approach was extended by CLARENZ ET AL. [51] to surfaces with boundaries and applied to problems in surface restoration. There, a destroyed surface patch is restored by a smooth patch defined as the minimizer of the Willmore functional with boundary conditions for the position and the normal. Using the isotropic Willmore functional will not lead to results respecting the edges and corners of the surface, cf. Figure 3.1. DIEWALD [71] extended the approach of RUSU [148] to the anisotropic Willmore flow for surfaces without boundaries. In this chapter we discuss surface restoration based on Willmore flow with boundary conditions. In Section 3.1 we calculate the first variation of the anisotropic Willmore functional following DIEWALD [71]. Then we study the resulting boundary value problem in Section 3.2. In Section 3.3 we describe the Finite Element scheme on triangular grids in space and the semi-implicit backward Euler discretization in time. The resulting scheme is used to restore surface patches with corner and edge type singularities in Section 3.4. It turns out that severe tangential distortions have to be compensated for, if we choose time step sizes of the order of the square of the spatial grid size. This compensation is realized via mesh adaptation and is described in the last Section 3.4 of this chapter.

3.1 First variation of the anisotropic Willmore functional

We consider an oriented embedded surface $\mathcal{M} \subset \mathbb{R}^3$ with parameterization x being the identity on the surface $\mathcal{M}$ and boundary $\partial\mathcal{M}$. Let γ denote an elliptical integrand. In this section we collect the main results about the first variation of the anisotropic Willmore

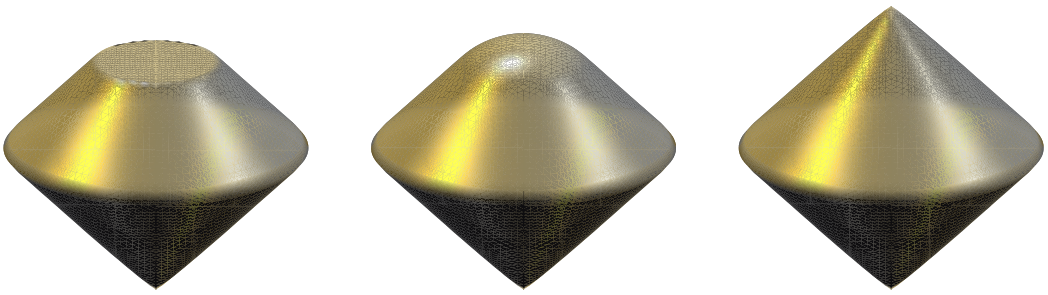

Figure 3.1: Using the isotropic Willmore functional will not lead to results respecting the edges and corners of the surface: The destroyed surface on the left is restored by the isotropic (center) and anisotropic Willmore flow with $\gamma(z) = \frac{1}{2}\left\{\left|\sqrt{z_1^2+z_2^2}+z_3\right|_\delta + \left|\sqrt{z_1^2+z_2^2}-z_3\right|_\delta\right\}$, where $|a| \approx |a|_\delta = \sqrt{a^2+\delta^2}$, $\delta = 0.00001$, cf. NEMITZ [130, Equation (79)] (right).

energy

$$w_\gamma[x] = \frac{1}{2}\int_{\mathcal{M}} \mathbf{h}_\gamma^2 \,\mathrm{d}a\,,$$

where $\mathbf{h}_\gamma = \dim_{\mathcal{M}}(\gamma_z \circ n)$ is the generalized mean curvature, cf. Definition 2.2.3. To calculate the first variation of w_γ, we consider the disturbed surface $x_\epsilon = x + \epsilon\,\vartheta$ for test functions $\vartheta \in \mathcal{C}^1(\mathcal{M}, \mathbb{R}^3)$. The test function is decomposed into a normal and tangential part

$$\vartheta = \varphi\, n + v, \tag{3.1}$$

where $\varphi \in \mathcal{C}^1(\mathcal{M})$ is a smooth function and $v \in \mathcal{C}^1(\mathcal{M}, T_p\mathcal{M})$ is a smooth tangential vector field. The classical version is not suited for a linear Finite Element approximation, because expressions containing the gradient of the Gauß map $\nabla_{\mathcal{M}} n$ appears:

Proposition 3.1.1. (First variation of w_γ, classical version)
Let $\mathcal{M} \subset \mathbb{R}^3$ be an oriented embedded surface with parameterization x being the identity on the surface $\mathcal{M}$ with boundary $\partial\mathcal{M}$. If γ is an elliptical integrand, the first variation of the anisotropic Willmore functional in direction of a test function ϑ given as in Equation (3.1) *is given by*

$$\begin{aligned}\left\langle w_\gamma'[x], \vartheta \right\rangle = &\int_{\mathcal{M}} \left(-\Delta_\gamma \mathbf{h}_\gamma - \mathbf{h}_\gamma \left|\nabla_{\mathcal{M}} n\right|_\gamma^2 + \frac{1}{2}\mathbf{h}\,\mathbf{h}_\gamma^2\right) n \cdot \vartheta \, da \\ &+ \int_{\partial\mathcal{M}} \left(\varphi\, \gamma_{zz}(n)\, \nabla_{\mathcal{M}} \mathbf{h}_\gamma - \mathbf{h}_\gamma\, \gamma_{zz}\, \nabla_{\mathcal{M}} \varphi + \frac{1}{2}\mathbf{h}_\gamma^2\, v\right) \cdot n^{co}\, d\sigma\end{aligned}$$

Proof. A proof can be found in CLARENZ [50, Equation (14)] for surfaces $\mathcal{M}$ with $\partial\mathcal{M} = \emptyset$ and in DIEWALD [71, Satz 68] for surfaces with $\partial\mathcal{M} \neq \emptyset$. □

The normal field of a triangulated surface is piecewise constant, so that its derivative vanishes. Therefore, we have to calculate the first variation of the anisotropic Willmore functional without incorporating $\nabla_{\mathcal{M}} n$. For simplicity we omit the argument for the second

derivatives of the anisotropy function γ and write γ_{zz} for $\gamma_{zz}(n)$. Let $\mathbf{h}_\gamma^\epsilon$ denote the generalized mean curvature and $\mathrm{d}a_\epsilon$ the area element of the disturbed surface x_ϵ. Then we get

$$\left\langle w_\gamma'[x], \vartheta \right\rangle = \partial_\epsilon \frac{1}{2} \int_{\mathcal{M}} \left(\mathbf{h}_\gamma^\epsilon\right)^2 \mathrm{d}a_\epsilon \Big|_{\epsilon=0} = \int_{\mathcal{M}} \mathbf{h}_\gamma \, \partial_\epsilon \mathbf{h}_\gamma^\epsilon \big|_{\epsilon=0} \, \mathrm{d}a + \frac{1}{2} \int_{\mathcal{M}} \mathbf{h}_\gamma^2 \, \partial_\epsilon \, \mathrm{d}a_\epsilon \big|_{\epsilon=0} .$$

The derivative of the area element was calculated by SIMON [155] and is given by

$$\partial_\epsilon \, \mathrm{d}a_\epsilon \big|_{\epsilon=0} = \mathrm{div}_{\mathcal{M}} \vartheta \, \mathrm{d}a .$$

Since we identify the surface $\mathcal{M}$ and its parametrization x, we get the following expression for the divergence of the test function

$$\mathrm{div}_{\mathcal{M}} \vartheta = \mathrm{tr}\left(\nabla_{\mathcal{M}} \vartheta\right) = \mathbb{I} : \nabla_{\mathcal{M}} \vartheta = \nabla_{\mathcal{M}} x : \nabla_{\mathcal{M}} \vartheta . \tag{3.2}$$

We reformulate the derivative of the area element and get

$$\partial_\epsilon \, \mathrm{d}a_\epsilon \big|_{\epsilon=0} = \nabla_{\mathcal{M}} x : \nabla_{\mathcal{M}} \vartheta . \tag{3.3}$$

Due to CLARENZ [50, Equation (13)], we get for the first variation of the generalized mean curvature $\mathbf{h}_\gamma$

$$\partial_\epsilon \mathbf{h}_\gamma^\epsilon \big|_{\epsilon=0} = -\Delta_\gamma \varphi - \left|\nabla_{\mathcal{M}} n\right|_\gamma \varphi + \nabla_{\mathcal{M}} \mathbf{h}_\gamma \cdot \nu , \tag{3.4}$$

where $\left|\nabla_{\mathcal{M}} n\right|_\gamma = \mathrm{tr}\left(\gamma_{zz} \, \nabla_{\mathcal{M}} n \, \nabla_{\mathcal{M}} n\right)$, cf. Equation (2.21). Using (3.4) and (3.3), we obtain

$$\left\langle w_\gamma'[x], \vartheta \right\rangle = \int_{\mathcal{M}} \mathbf{h}_\gamma \left(-\Delta_\gamma \varphi - \left|\nabla_{\mathcal{M}} n\right|_\gamma \varphi + \nabla_{\mathcal{M}} \mathbf{h}_\gamma \cdot \nu\right) \mathrm{d}a + \frac{1}{2} \int_{\mathcal{M}} \mathbf{h}_\gamma^2 \, \nabla_{\mathcal{M}} x : \nabla_{\mathcal{M}} \vartheta \, \mathrm{d}a$$

Following the calculation in the proof corresponding to Satz 71 in DIEWALD[71], we infer for the integrand of the first integral in the above formulation

$$\mathbf{h}_\gamma \left(-\Delta_\gamma \varphi - \left|\nabla_{\mathcal{M}} n\right|_\gamma \varphi + \nabla_{\mathcal{M}} \mathbf{h}_\gamma \cdot \nu\right) = -\mathbf{h}_\gamma n \cdot \left[\Delta_\gamma \vartheta + 2\, n \left(\gamma_{zz} \, \nabla_{\mathcal{M}} n : \nabla_{\mathcal{M}} \vartheta\right)\right]$$

and get a generalization of Lemma 2.1 in RUSU [148]:

Lemma 3.1.2. *Let the assumption of Proposition 3.1.1 be fulfilled. The first variation of the anisotropic Willmore functional in direction of the test function ϑ is given by*

$$\begin{aligned} \left\langle w_\gamma'[x], \vartheta \right\rangle = & -\int_{\mathcal{M}} \mathbf{h}_\gamma n \cdot \left[\Delta_\gamma \vartheta + 2n \left(\left(\gamma_{zz} \, \nabla_{\mathcal{M}} n\right) : \nabla_{\mathcal{M}} \vartheta\right)\right] da \\ & + \frac{1}{2} \int_{\mathcal{M}} \mathbf{h}_\gamma^2 \, \nabla_{\mathcal{M}} x : \nabla_{\mathcal{M}} \vartheta \, da . \end{aligned} \tag{3.5}$$

Let us remark that the calculation of the first variation of the anisotropic Willmore functional does not use integration by parts so that boundary integrals do not appear thus far. Lemma 3.1.2 is a generalization of Lemma 2.1 in RUSU [148]. Introducing an additional variable y, we are able to remove the gradient from the Gauß map. Therefore, we define the generalized mean curvature vector

$$y := -\mathbf{h}_\gamma\, n.$$

Now, following RUSU [148], we can rewrite the first summand of Equation (3.5) using the next lemma.

Lemma 3.1.3. *Let x and γ be as in Proposition 3.1.1. If $y = -\mathbf{h}_\gamma\, n$ denotes the generalized mean curvature vector, we get*

$$\int_{\mathcal{M}} y \cdot n \left(\left(\gamma_{zz}\, \nabla_{\mathcal{M}}\, n \right) : \nabla_{\mathcal{M}}\, \vartheta \right) da = \int_{\mathcal{M}} \nabla_{\mathcal{M}}\, y : \left(\gamma_{zz}\, \nabla_{\mathcal{M}}\, \vartheta \right) - n_i n_l\, \nabla_{\mathcal{M}}\, y_i \cdot \left(\gamma_{zz}\, \nabla_{\mathcal{M}}\, \vartheta_l \right) da\,.$$

Proof. Rewriting the integrand on the left with summation convention and applying the product rule gives

$$\begin{aligned}
y \cdot n \left(\left(\gamma_{zz}\, \nabla_{\mathcal{M}}\, n \right) : \nabla_{\mathcal{M}}\, \vartheta \right) &= y \cdot n\, \nabla_{\mathcal{M}}\, n : \left(\gamma_{zz}\, \nabla_{\mathcal{M}}\, \vartheta \right) \\
&= y_i n_i\, \nabla_{\mathcal{M}}\, n_l \cdot \left(\gamma_{zz}\, \nabla_{\mathcal{M}}\, \vartheta_l \right) \\
&= \left(\nabla_{\mathcal{M}} \left(y_i n_i n_l \right) - \nabla_{\mathcal{M}} \left(y_i n_i \right) n_l \right) \cdot \left(\gamma_{zz}\, \nabla_{\mathcal{M}}\, \vartheta_l \right) \\
&= \nabla_{\mathcal{M}}\, y_l \cdot \left(\gamma_{zz}\, \nabla_{\mathcal{M}}\, \vartheta_l \right) - \left(\nabla_{\mathcal{M}}\, y_i\, n_i n_l \right) \cdot \left(\gamma_{zz}\, \nabla_{\mathcal{M}}\, \vartheta_l \right) \\
&\quad - y_i n_l\, \nabla_{\mathcal{M}}\, n_i \cdot \left(\gamma_{zz}\, \nabla_{\mathcal{M}}\, \vartheta_l \right).
\end{aligned}$$

Since the shape operator $\nabla_{\mathcal{M}}\, n$ is symmetric, cf. Equation (2.5), and $y_i = -\mathbf{h}_\gamma n_i$ the last term vanishes. □

The next proposition is a generalization of Proposition 3.2 in CLARENZ ET AL. [51] to the anisotropic functional for surfaces with boundaries.

Proposition 3.1.4. (First variation of w_γ in weak form)
Let x and γ be as in Proposition 3.1.1. Using the definition $y = -\mathbf{h}_\gamma\, n$, the derivative of the anisotropic Willmore functional in direction ϑ is given by

$$\begin{aligned}
\left\langle w_\gamma'[x], \vartheta \right\rangle = &\int_{\mathcal{M}} \nabla_{\mathcal{M}}\, y : \left(\gamma_{zz}\, \nabla_{\mathcal{M}}\, \vartheta \right) da - 2 \int_{\mathcal{M}} n_i n_l\, \nabla_{\mathcal{M}}\, y_i \cdot \left(\gamma_{zz}\, \nabla_{\mathcal{M}}\, \vartheta_l \right) da \\
&+ \frac{1}{2} \int_{\mathcal{M}} |y|^2\, \nabla_{\mathcal{M}}\, x : \nabla_{\mathcal{M}}\, \vartheta\, da + \int_{\partial \mathcal{M}} \gamma_{zz}\, \nabla_{\mathcal{M}}\, \vartheta \cdot n^{co}\, d\sigma\,,
\end{aligned}$$

where n^{co} denotes the co-normal at the boundary of $\mathcal{M}$.

Proof. The first summand in Equation (3.5) can be written as

$$\begin{aligned}\int_{\mathcal{M}} y \cdot \Delta_\gamma \vartheta \,\mathrm{d}a &= \int_{\mathcal{M}} y \cdot \operatorname{div}_{\mathcal{M}} \left(\gamma_{zz} \nabla_{\mathcal{M}} \vartheta\right) \mathrm{d}a \\ &\overset{(2.9)}{=} -\int_{\mathcal{M}} \nabla_{\mathcal{M}} y : \left(\gamma_{zz} \nabla_{\mathcal{M}} \vartheta\right) \mathrm{d}a + \int_{\partial\mathcal{M}} \gamma_{zz} \nabla_{\mathcal{M}} \vartheta \cdot n^{co} \,\mathrm{d}\sigma\,.\end{aligned}$$

Using Lemma 3.1.3 we get for the second summand in Equation (3.5)

$$\begin{aligned}\int_{\mathcal{M}} y \cdot 2n \left(\gamma_{zz} \nabla_{\mathcal{M}} n : \nabla_{\mathcal{M}} \vartheta\right) \mathrm{d}a &= 2\int_{\mathcal{M}} \nabla_{\mathcal{M}} y : \left(\gamma_{zz} \nabla_{\mathcal{M}} \vartheta\right) \mathrm{d}a \\ &\quad - 2\int_{\mathcal{M}} n_i n_l \, \nabla_{\mathcal{M}} y_i \cdot \left(\gamma_{zz} \nabla_{\mathcal{M}} \vartheta_l\right) \mathrm{d}a\,.\end{aligned}$$

Now, we can rewrite the first variation of the anisotropic Willmore functional given as in (3.5) and verify the assertion. □

3.2 Boundary value problem for the anisotropic Willmore flow

In this section we calculate the anisotropic Willmore flow with boundary conditions. Since we are interested in smooth boundary condition at the boundary $\partial\mathcal{M}$ of the surface $\mathcal{M}$, we prescribe Dirichlet boundary conditions for the coordinate vector $x \in \partial\mathcal{M}$ and Neumann boundary conditions. The L^2-gradient flow of the anisotropic Willmore functional w_γ is defined as

$$\left(\partial_t x, \vartheta\right)_{L^2} = -\left\langle w_\gamma'[x], \vartheta \right\rangle\,,$$

where $(\,,\,)_{L^2}$ denotes the L^2-scalar product (cf. Section 2.3). We have to choose the set of admissible test function carefully to ensure proper $\mathcal{C}^1$-type boundary conditions. Let $\partial_{n^{co}}$ denote the directional derivative in direction of the co-normal n^{co}, i.e. $\partial_{n^{co}}\vartheta = \nabla_{\mathcal{M}}\vartheta \cdot n^{co}$ for a test function ϑ. The set of admissible test functions is given by

$$\mathcal{A} := \left\{\vartheta \in \mathcal{C}^1(\mathcal{M}, \mathbb{R}^3) \,\middle|\, \vartheta|_{\partial\mathcal{M}} = 0 \text{ and } \partial_{n^{co}}\vartheta\big|_{\partial\mathcal{M}}\right\}.$$

Splitting an admissible test function ϑ into a normal and tangential part as in Equation (3.1), we get the following lemma

Lemma 3.2.1. *If the test function $\vartheta \in \mathcal{A}$ is decomposed into a normal and tangential part $\vartheta = \varphi\, n + v$, where $\varphi \in \mathcal{C}^1(\mathcal{M})$ is a smooth function and $v \in \mathcal{C}^1(\mathcal{M}, T_p\mathcal{M})$ is a smooth tangential vector field, the following boundary conditions hold*

$$\varphi\big|_{\partial\mathcal{M}} = v|_{\partial\mathcal{M}} = \partial_{n^{co}}\varphi\big|_{\partial\mathcal{M}} = 0\,.$$

Proof. Multiplying equation $0 = \vartheta|_{\partial\mathcal{M}} = \varphi n\big|_{\partial\mathcal{M}} + \nu|_{\partial\mathcal{M}}$ by n and using $n \cdot \nu = 0$ gives the first two conditions. Analogously, multiplying equation

$$0 = \partial_{n^{co}}\vartheta\big|_{\partial\mathcal{M}} = \partial_{n^{co}}\varphi\, n\big|_{\partial\mathcal{M}} + \varphi\, \partial_{n^{co}} n\big|_{\partial\mathcal{M}} + \partial_{n^{co}}\nu\big|_{\partial\mathcal{M}}$$

by n and using $n \cdot n = 1$, $\partial_{n^{co}} n \cdot n = 0$ and the product rule we get

$$0 = \partial_{n^{co}}\varphi\big|_{\partial\mathcal{M}} + \partial_{n^{co}}(\nu \cdot n)\big|_{\partial\mathcal{M}} + \nu \cdot \partial_{n^{co}} n\big|_{\partial\mathcal{M}}\,.$$

Since $\nu \cdot n = 0$ and $\nu|_{\partial\mathcal{M}} = 0$, the proof of the lemma is finished. □

Because of Lemma 3.2.1 and Proposition 3.1.1 the classical version of the initial boundary value problem for the anisotropic Willmore flow is given as follows:

$$\begin{aligned}
\partial_t x &= \left(\Delta_\gamma \mathbf{h}_\gamma + \mathbf{h}_\gamma \left|\nabla_{\mathcal{M}} n\right|_\gamma^2 - \frac{1}{2}\mathbf{h}\,\mathbf{h}_\gamma^2\right) n && \text{on } (0,T]\times\mathcal{M}, \\
x &= x^0 && \text{on } (0,T]\times\partial\mathcal{M}, \\
n &= n^0 && \text{on } (0,T]\times\partial\mathcal{M}, \\
x(0) &= x^0
\end{aligned} \tag{3.6}$$

for some $T > 0$. Here, $\{\mathcal{M}(t)\}$ is a family of bounded surfaces and $x(t)$ indicates the parameterization of $\mathcal{M}(t)$ over itself and $n(t)$ its Gauß map. $\mathcal{M}^0$ is the initial surface with parameterization x^0 and Gauß map n^0. Now, we derive the corresponding weak formulation. Using Proposition 3.1.4 the L^2-gradient flow of the anisotropic Willmore flow for test functions $\vartheta \in \mathcal{A}$ is given by

$$\begin{aligned}
\int_{\mathcal{M}} \partial_t x \cdot \vartheta \,\mathrm{d}a = &-\int_{\mathcal{M}} \nabla_{\mathcal{M}} y : \left(\gamma_{zz}\,\nabla_{\mathcal{M}}\vartheta\right)\,\mathrm{d}a + 2\int_{\mathcal{M}} n_i n_l\,\nabla_{\mathcal{M}} y_i \cdot \left(\gamma_{zz}\,\nabla_{\mathcal{M}}\vartheta_l\right)\,\mathrm{d}a \\
&-\frac{1}{2}\int_{\mathcal{M}} |y|^2\,\nabla_{\mathcal{M}} x : \nabla_{\mathcal{M}}\vartheta\,\mathrm{d}a.
\end{aligned} \tag{3.7}$$

Next, we have to calculate the weak form of the generalized mean curvature vector:

Lemma 3.2.2. (Weak definition of the generalized mean curvature vector)
Let $\psi \in \mathcal{C}^1(\mathcal{M},\mathbb{R}^3)$ be a test function. We get

$$\begin{aligned}
-\int_{\mathcal{M}} \mathbf{h}_\gamma\, n\cdot\psi\, da = &\int_{\mathcal{M}} \left(\nabla_{\mathcal{M}} x\,\gamma_z(n)\right)\cdot\left(\nabla_{\mathcal{M}}\psi\, n\right)\, da - \int_{\mathcal{M}} \gamma(n)\,\nabla_{\mathcal{M}} x : \nabla_{\mathcal{M}}\psi\, da \\
&+\int_{\partial\mathcal{M}} \gamma(n)\,\psi\cdot n^{co}\, d\sigma - \int_{\partial\mathcal{M}} \gamma_z(n)\cdot n^{co}\, n\cdot\psi\, d\sigma
\end{aligned}$$

Proof. We decompose the test function ψ into a normal and tangential part $\psi = \zeta\, n + w$, where ζ is a smooth function and $w \in T_p\mathcal{M}$ is a smooth tangential vector field, cf. Equation (3.1). Using integration by parts, cf. Lemma 2.1.5 and Lemma 2.1.4, we infer

$$
\begin{aligned}
-\int_{\mathcal{M}} \mathbf{h}_\gamma\, n\cdot\psi \,\mathrm{d}a &= -\int_{\mathcal{M}} \mathbf{h}_\gamma\, n\cdot(\zeta\, n + w)\,\mathrm{d}a = -\int_{\mathcal{M}} \mathbf{h}_\gamma\,\zeta\,\mathrm{d}a = -\int_{\mathcal{M}} \operatorname{div}_{\mathcal{M}}\gamma_z(n)\,\zeta\,\mathrm{d}a \\
&= \int_{\mathcal{M}} \gamma_z(n)\cdot\nabla_{\mathcal{M}}\zeta\,\mathrm{d}a - \int_{\mathcal{M}} \underbrace{h\,\zeta}_{\substack{(2.10)\\=\\ \operatorname{div}_{\mathcal{M}}(\zeta\, n)\\ =\psi - w}} \underbrace{\gamma_z(n)\cdot n}_{\substack{(2.17)\\=\gamma(n)}}\,\mathrm{d}a - \int_{\partial\mathcal{M}} \gamma_z(n)\cdot n^{co}\,\zeta\,\mathrm{d}\sigma \\
&= \int_{\mathcal{M}} \gamma_z(n)\cdot\nabla_{\mathcal{M}}\zeta\,\mathrm{d}a - \int_{\mathcal{M}} \gamma(n)\operatorname{div}_{\mathcal{M}}\psi\,\mathrm{d}a + \int_{\mathcal{M}} \gamma(n)\operatorname{div}_{\mathcal{M}} w\,\mathrm{d}a \\
&\quad - \int_{\partial\mathcal{M}} (\gamma_z(n)\cdot n^{co})\,(n\cdot\psi)\,\mathrm{d}\sigma \\
&= \int_{\mathcal{M}} \gamma_z(n)\cdot\nabla_{\mathcal{M}}\zeta\,\mathrm{d}a - \int_{\mathcal{M}} \gamma(n)\operatorname{div}_{\mathcal{M}}\psi\,\mathrm{d}a - \int_{\mathcal{M}} \nabla_{\mathcal{M}}\gamma(n)\cdot w\,\mathrm{d}a \\
&\quad + \int_{\partial\mathcal{M}} \gamma(n)\, w\cdot n^{co}\,\mathrm{d}\sigma - \int_{\partial\mathcal{M}} (\gamma_z(n)\cdot n^{co})\,(n\cdot\psi)\,\mathrm{d}\sigma
\end{aligned}
$$

Using $\nabla_{\mathcal{M}}\gamma(n) = \gamma_z(n)\,\nabla_{\mathcal{M}} n$, Equation (3.2) and the symmetry of $\nabla_{\mathcal{M}} n$, cf. Equation (2.5), we get

$$
\begin{aligned}
-\int_{\mathcal{M}} \mathbf{h}_\gamma\, n\cdot\psi\,\mathrm{d}a &= \int_{\mathcal{M}} \gamma_z(n)\cdot\left(\nabla_{\mathcal{M}}\zeta - \nabla_{\mathcal{M}} n\, w\right)\mathrm{d}a - \int_{\mathcal{M}} \gamma(n)\,\nabla_{\mathcal{M}} x : \nabla_{\mathcal{M}}\psi\,\mathrm{d}a \\
&\quad + \int_{\partial\mathcal{M}} \gamma(n)\,\psi\cdot n^{co}\,\mathrm{d}\sigma - \int_{\partial\mathcal{M}} (\gamma_z(n)\cdot n^{co})\,(n\cdot\psi)\,\mathrm{d}\sigma
\end{aligned}
$$

Writing the integrand of the first term on the right hand side with summation convention and applying the product rule, cf. Equation (2.3), gives

$$
\begin{aligned}
\nabla_{\mathcal{M}}\zeta - \nabla_{\mathcal{M}} n\, w &= \nabla_{\mathcal{M},i}\zeta - \nabla_{\mathcal{M},i} n_j\, w_j = \nabla_{\mathcal{M},i}\zeta - \nabla_{\mathcal{M},i}\big(\underbrace{n_j\, w_j}_{=0}\big) + n_j\,\nabla_{\mathcal{M},i} v_j \\
&= \nabla_{\mathcal{M},i}\zeta\,\underbrace{n_j\, n_j}_{=1} + \zeta\,\underbrace{\nabla_{\mathcal{M},j} n_i\, n_j}_{\substack{(2.1)\\=0}} + \nabla_{\mathcal{M},i} v_j\, n_j \\
&= \left(\nabla_{\mathcal{M},i}\zeta\, n_j + \zeta\nabla_{\mathcal{M},i} n_j + \nabla_{\mathcal{M},i} v_j\right) n_j = \nabla_{\mathcal{M},i}\left(\zeta\, n_j + v_j\right) n_j \\
&= \nabla_{\mathcal{M}}\psi\, n\,.
\end{aligned}
$$

Since we identify $\mathcal{M}$ and $x(\mathcal{M})$ we verify the assertion. □

Applying Proposition 3.1.4 and Lemma 3.2.2 we get a weak formulation for the anisotropic Willmore flow. For numerical stability, RUSU [148] suggests to subtract the first summand of the right hand side of Equation (3.7) from both sides of the equation for the isotropic Willmore flow. In the anisotropic case this leads to

Problem 3.2.3. (Weak formulation of anisotropic Willmore flow)
Find a family of bounded surfaces $\{\mathcal{M}(t)\}$ *with coordinate vector* $x(t)$ *and an accompanying vector field* $y(t)$ *on* $\mathcal{M}(t)$*, such that*

$$\begin{aligned}\int_{\mathcal{M}} \partial_t x \cdot \vartheta \, da - \int_{\mathcal{M}} \nabla_{\mathcal{M}} y : \left(\gamma_{zz} \nabla_{\mathcal{M}} \vartheta\right) da = &-2 \int_{\mathcal{M}} \nabla_{\mathcal{M}} y : \left(\gamma_{zz} \nabla_{\mathcal{M}} \vartheta\right) da \\ &+ 2 \int_{\mathcal{M}} n_i n_l \, \nabla_{\mathcal{M}} y_i \cdot \left(\gamma_{zz} \nabla_{\mathcal{M}} \vartheta_l\right) da \\ &- \frac{1}{2} \int_{\mathcal{M}} |y|^2 \, \nabla_{\mathcal{M}} x : \nabla_{\mathcal{M}} \vartheta \, da \,,\end{aligned} \tag{3.8}$$

$$\begin{aligned}\int_{\mathcal{M}} y \cdot \psi \, da = &\int_{\mathcal{M}} \left(\nabla_{\mathcal{M}} x \, \gamma_z(n)\right) \cdot \left(\nabla_{\mathcal{M}} \psi \, n\right) da - \int_{\mathcal{M}} \gamma(n) \, \nabla_{\mathcal{M}} x : \nabla_{\mathcal{M}} \psi \, da \\ &+ \int_{\partial \mathcal{M}} \gamma(n) \, \psi \cdot n^{co} \, d\sigma - \int_{\partial \mathcal{M}} (\gamma_z(n) \cdot n^{co}) (n \cdot \psi) \, d\sigma \,,\end{aligned} \tag{3.9}$$

for all $\vartheta \in H_0^1(\mathcal{M}, \mathbb{R}^3)$*,* $\psi \in H^1(\mathcal{M}, \mathbb{R}^3)$ *and for almost every* $t \in (0, T]$*. Furthermore we assume* $x = x^0$ *on* $(0, T] \times \partial \mathcal{M}$ *and* $x(0) = x^0$*.*

3.3 Semi-implicit space discretization scheme

Let us now consider a Finite Element discretization for Problem 3.2.3, the weak formulation of the anisotropic Willmore flow. To apply the resulting semi-implicit space discretization scheme to surface restoration or bending problems, we have to carefully construct discrete ansatz spaces for x and y to ensure proper $\mathcal{C}^1$-type boundary conditions. We will use the notation of CLARENZ ET AL. [51], where a Finite Element discretization for a suitable boundary value problem for the isotropic Willmore flow is presented. As in CLARENZ ET AL. [51] we will discuss two different numerical schemes for anisotropic Willmore flow with boundary conditions that differ with respect to the actual handling of the boundary condition for the surface normals. Suppose a triangulated surface $\widetilde{\mathcal{M}}[X^0]$ is given and a subset $\mathcal{M}[X^0] \subset \widetilde{\mathcal{M}}[X^0]$ is either a destroyed region on the surface $\widetilde{\mathcal{M}}[X^0]$, where the remaining surface

$$\mathcal{M}^{ext}[X^0] := \widetilde{\mathcal{M}}[X^0] \setminus \mathcal{M}[X^0]$$

is in good shape, or $\mathcal{M}[X^0]$ is an initial blending surface closing a given surface $\mathcal{M}^{ext}[X^0]$. We seek a family of discrete surfaces $(\mathcal{M}[X(t)])_{0<t}$ which obey a discrete anisotropic Willmore flow under prescribed discrete boundary conditions. $\mathcal{M}^{ext}[X(t)]$ is supposed to be

fixed in time, i.e. $\mathcal{M}^{ext}[X^0] = \mathcal{M}^{ext}[X(t)]$. For the actual handling of the boundary condition for the surface normals we present two methods. In the first variant (Variant I below) we prescribe the co-normal on the boundary whereas in (Variant II) we consider a whole boundary layer consisting of all triangles T in $\mathcal{M}^{ext}[X^0]$ with $T \cap \partial\mathcal{M}[X^0] \neq \emptyset$, where we assume triangles to be closed sets. In this sense, we take into account an inner boundary $\mathcal{M}[X^0]$ and an outer boundary defined by the layer. Fixing inner and outer boundary for the position vector means obviously fixing the normal on triangles of the boundary layer. We use the notation of Section 2.4 and define $\mathcal{M}^{int}[X(t)] \subset \mathcal{M}[X(t)] \subset \widetilde{\mathcal{M}}[X(t)]$ with

$$\mathcal{M}[X(t)] = \{T \in \widetilde{\mathcal{M}}[X(t)] \,\big|\, T \cap \partial\widetilde{\mathcal{M}}[X(t)] = \emptyset\}$$

and

$$\mathcal{M}^{int}[X(t)] = \{T \in \mathcal{M}[X(t)] \,\big|\, T \cap \partial\mathcal{M}[X(t)] = \emptyset\}.$$

Let I^{int}, I and $\tilde{I}$ be the index sets of the vertices of $\mathcal{M}^{int}[X(t)]$, $\mathcal{M}[X(t)]$ and $\widetilde{\mathcal{M}}[X(t)]$, cf. Equation (2.45). The set of nodes of $\mathcal{M}[X(t)]$ is denoted by $\mathcal{N}(t)$ and splits into interior nodes $\mathcal{N}^{int}(t)$ and boundary nodes $\mathcal{N}^{\partial}(t)$, i.e. $\mathcal{N}(t) = \mathcal{N}^{int}(t) \cup \mathcal{N}^{\partial}(t)$ with index set $I^{\partial} = I \setminus I^{int}$.

Let $X(t)|_{\mathcal{M}^{int}[X(t)]}$, $X(t)|_{\mathcal{M}[X(t)]}$ and $X(t)|_{\widetilde{\mathcal{M}}[X(t)]}$ be the identities on the simplicial meshes $\mathcal{M}^{int}[X(t)]$, $\mathcal{M}[X(t)]$ and $\widetilde{\mathcal{M}}[X(t)]$, respectively. With a slight misuse of notation the mapping $X(t)|_{\mathcal{M}[X(t)]}$ itself is considered as an element in the corresponding piecewise affine Finite Element space $\mathcal{V}(\mathcal{M}[X(t)])^3$ on the time-dependent surfaces: $X(t) \in \mathcal{V}(\mathcal{M}[X(t)])^3$, cf. Equation (2.34).

We consider the discrete anisotropic Willmore flow of $\widetilde{\mathcal{M}}[X(t)]$ with fixed boundary and fixed triangles in $\mathcal{M}^{ext}[X(t)] = \widetilde{\mathcal{M}}[X(t)] \setminus \mathcal{M}[X(t)]$, i.e. we consider the evolution of $\mathcal{M}[X(t)]$ with fixed boundary $\partial\mathcal{M}[X(t)]$, but in addition taking into account also information about the surface normal on $\mathcal{M}^{ext}[X^0] = \mathcal{M}^{ext}[X(t)]$ during the discrete evolution process. Hence, in the discrete case, we consider the above weak formulation (3.8) not for all test functions $\vartheta \in H_0^1(\mathcal{M}[X(t)], \mathbb{R}^3)$, but now for test functions $\Theta(t) \in (\mathcal{V}^{int}(\mathcal{M}[X(t)]))^3$, where $\mathcal{V}^{int}(\mathcal{M}[X(t)])$ are the linear Finite Element functions of $\mathcal{M}[X(t)]$ with vanishing boundary values, cf. Equation (2.46).

To map between the function spaces $\mathcal{V}(\mathcal{M}[X(t)])$ and $\mathcal{V}^{int}(\mathcal{M}[X(t)]])$ we define a restriction operator

$$R : \mathcal{V}(\mathcal{M}[X(t)]) \to \mathcal{V}^{int}(\mathcal{M}[X(t)])$$

and an extension operator

$$E : \mathcal{V}^{int}(\mathcal{M}[X(t)]) \to \mathcal{V}(\mathcal{M}[X(t)])$$

that extend a function on $\partial\mathcal{M}[X(t)]$ by zero. The corresponding block operators are denoted by $\mathbf{R} : \mathcal{V}(\mathcal{M}[X(t)])^3 \to \mathcal{V}^{int}(\mathcal{M}[X(t)])^3$ and $\mathbf{E} : \mathcal{V}^{int}(\mathcal{M}[X(t)])^3 \to \mathcal{V}(\mathcal{M}[X])^3$.

Again, a bar on top of a discrete function indicates the corresponding nodal vector, i.e. $\bar{X}(t) = (\bar{X}_i(t))_{i \in I^{int}}$, where $\bar{X}_i(t) = (X_i^1(t), X_i^2(t), X_i^3(t))$ is the coordinate vector of the ith inner vertex of the mesh. As in Section 2.4, a nodal vector in $\mathbb{R}^{3\#I}$ is then $E\bar{X}(t) + \bar{X}^{ext}(t)$, cf. Equation (2.49), where $\bar{X}^{ext}(t)$ is the position vector for the boundary nodes with zero entries for all interior nodes. Now, we are able to formulate the two variants of the discrete anisotropic Willmore flow for the case with boundary.

Variant I: Explicitly encoding the co-normal N^{co}

At first we explicitly encode the discrete co-normal N^{co}. If T is a triangle with at least one edge on $\partial\mathcal{M}[X(t)]$ than N^{co} lies in the plane of T pointing outwards. N^{co} is a fixed function on $\partial\mathcal{M}[X(t)]$ being piecewise constant on the edges. The piecewise constant normal on each edge is denoted by $N(t)$ in the following, cf. Equations (2.40) and (2.41).

Problem 3.3.1. (Variant I of the semi-discrete anisotropic Willmore flow)
Find a family of triangulated surfaces $\mathcal{M}[X(t)]$ with parametrization

$$X(t) = (X^1(t), X^2(t), X^3(t)) \in \mathcal{V}(\mathcal{M}[X(t)])^3$$

with fixed boundary $\mathcal{M}^{ext}[X(t)]$ and a family of accompanying vector-valued functions

$$Y(t) = (Y^1(t), Y^2(t), Y^3(t)) \in \mathcal{V}(\mathcal{M}[X(t)])^3$$

such that

$$\begin{aligned}
&\int_{\mathcal{M}[X(t)]} \partial_t \mathbf{R}X(t)\cdot\Theta(t)\,da - \int_{\mathcal{M}[X(t)]} \nabla_{\mathcal{M}[\mathrm{X(t)}]}\, Y(t) : \gamma_{zz}(N(t))\,\nabla_{\mathcal{M}[\mathrm{X(t)}]}\,\Theta(t)\,da \\
&\qquad = -2\int_{\mathcal{M}[X(t)]} \nabla_{\mathcal{M}[\mathrm{X(t)}]}\, Y(t) : \gamma_{zz}(N(t))\,\nabla_{\mathcal{M}[\mathrm{X(t)}]}\,\Theta(t)\,da \\
&\qquad\quad + 2\int_{\mathcal{M}[X(t)]} N^i(t)N^l(t)\,\nabla_{\mathcal{M}[\mathrm{X(t)}]}\, Y^i(t)\cdot\left(\gamma_{zz}(N(t))\,\nabla_{\mathcal{M}[\mathrm{X(t)}]}\,\Theta(t)^l\right)\,da \\
&\qquad\quad - \frac{1}{2}\int_{\mathcal{M}[X(t)]} |Y(t)|^2\,\nabla_{\mathcal{M}[\mathrm{X(t)}]} X(t) : \nabla_{\mathcal{M}[\mathrm{X(t)}]}\,\Theta(t)\,da\,,
\end{aligned} \tag{3.10}$$

holds for all test functions $\Theta(t) \in \mathcal{V}^{int}(\mathcal{M}[X(t)])^3$, $t > 0$ and

$$\begin{aligned}
\int_{\mathcal{M}[X(t)]} Y(t)\cdot\Psi(t)\,da = &\int_{\mathcal{M}[X(t)]} \left(\nabla_{\mathcal{M}[\mathrm{X(t)}]} X(t)\,\gamma_z(N(t))\right)\cdot\left(\nabla_{\mathcal{M}[\mathrm{X(t)}]}\,\Psi(t)N\right)\,da \\
&- \int_{\mathcal{M}[X(t)]} \gamma(N(t))\,\nabla_{\mathcal{M}[\mathrm{X(t)}]} X(t) : \nabla_{\mathcal{M}[\mathrm{X(t)}]}\,\Psi(t)\,da \\
&+ \int_{\partial\mathcal{M}[X(t)]} \gamma(N(t))N^{co}\cdot\Psi(t)\,d\sigma \\
&- \int_{\partial\mathcal{M}[X(t)]} \gamma_z(N(t))\cdot N^{co}N(t)\cdot\Psi(t)\,d\sigma\,,
\end{aligned} \tag{3.11}$$

holds for all test functions $\Psi(t) \in \mathcal{V}(\mathcal{M}[X(t)])^3$ and $t > 0$.

We can rewrite this problem in matrix formulation as follows. Let $\{\Phi_i(t)\}_{i\in I}$ be the nodal basis of $\mathcal{V}(\mathcal{M}[X(t)])$. Then $\{\Phi_i(t)\}_{i\in I^{int}}$ is a basis of $\mathcal{V}^{int}(\mathcal{M}[X(t)])$. The representation of $\mathbf{R}X(t)$ and $X(t)$ in the basis is then given by

$$\mathbf{R}X(t) = \sum_{j\in I^{int}} \bar{X}_j(t)\Phi_j(t),$$

$$X(t) = \sum_{j\in I^{int}} \bar{X}_j(t)\Phi_j(t) + \sum_{j\in I\setminus I^{int}} \bar{X}_j\Phi_j(t).$$

For the representation of $Y(t)$ we have

$$Y(t) = \sum_{j\in I} \bar{Y}_j(t)\Phi_j(t).$$

The degrees of freedom are the position vectors $\bar{X}_i(t) \in \mathbb{R}^3$ for all nodes in $\mathcal{N}^{int}(t)$ and coupled with the vector $\bar{Y}(t) \in \mathbb{R}^{3\sharp I}$ for all nodes in $\mathcal{N}(t)$. Using the notation for the mass and stiffness matrix we are able to rewrite this problem in matrix formulation:

Let $M[X(t)]$ denote the lumped mass matrix on the discrete surface $\mathcal{M}[X(t)]$, cf. Equations (2.36) and (2.44),

$$M_{ij}[X(t)] = \int_{\mathcal{M}[X(t)]} \mathcal{I}(\Phi_i(t)\Phi_j(t))\,\mathrm{d}a\,. \tag{3.12}$$

Via restriction and extension, the mass matrix $M^{int}[X(t)] \in \mathbb{R}^{\#I^{int},\#I^{int}}$ corresponds only to the inner nodes $\mathcal{N}^{int}(t)$ is defined as $M^{int}[X(t)] = RM[X(t)]E$. $\mathbf{M}^{int}[X(t)]$ is the corresponding block matrix. The stiffness matrices are $L^{\gamma(N(t))}[X(t)]$, $L^{|Y(t)|^2}[X(t)]$ (cf. Equation (2.38)), $L^{N(t)\otimes\gamma_z(N(t))}[X(t)]$ (cf. Equation (2.39)), $L^{N(t)\otimes N(t)}_{\gamma_{zz}(N(t))}[X(t)]$ (cf. Equation (2.42)) and $L_{\gamma_{zz}(N(t))}[X(t)]$ (cf. Equation (2.43)). Furthermore, we define the following vectors

$$\bar{N}^{co,\gamma}[X(t)] := \bar{N}^{co}_{\gamma}[X(t)] - \bar{N}^{co}_{\gamma_z}[X(t)] \in \mathbb{R}^{3\sharp I}, \qquad \text{with}$$

$$\bar{N}^{co}_{\gamma}[X(t)] := \left(\int_{\partial\mathcal{M}[X](t)} \gamma(N(t))N^{co}\,\Phi_i(t)\,\mathrm{d}\sigma\right)_{i\in I} \in \mathbb{R}^{3\sharp I},$$

$$\bar{N}^{co}_{\gamma_z}[X(t)] := \left(\int_{\partial\mathcal{M}[X](t)} \gamma_z(N(t))\cdot N^{co}N(t)\,\Phi_i(t)\,\mathrm{d}\sigma\right)_{i\in I} \in \mathbb{R}^{3\sharp I},\,.$$

The corresponding matrix formulation is then given by

$$\mathbf{M}^{int}[X(t)]\partial_t\bar{X}(t) - \mathbf{R}\mathbf{L}_{\gamma_{zz}(N(t))}[X(t)]\bar{Y}(t) =$$

$$-2\mathbf{R}\left(\mathbf{L}_{\gamma_{zz}(N(t))}[X(t)] - \mathbf{L}^{N(t)\otimes N(t)}_{\gamma zz}[X(t)]\right)\bar{Y}(t) - \frac{1}{2}\mathbf{R}\mathbf{L}^{|Y(t)|^2}[X(t)](\mathbf{E}\bar{X}(t) + \bar{X}^{ext}(t))$$

with

$$\bar{Y}(t) = \\ -(\mathbf{M}[X(t)])^{-1}\left(\left(\mathbf{L}^{\gamma(N(t))}[X(t)] - \mathbf{L}^{\gamma_z(N(t))\otimes N(t)}[X(t)]\right)(\mathbf{E}\bar{X}(t) + \bar{X}^{ext}(t)) - \bar{N}^{co,\gamma}[X(t)]\right).$$

Finally, we use a usual Euler time stepping for $\partial_t X$ and approximate

$$\partial_t \bar{X}((k+1)\tau) \approx \frac{\bar{X}^{k+1} - \bar{X}^k}{\tau},$$

where $\tau > 0$ is the time step size and $(\bar{X}^k)_{k=0,1,\dots} \subset \mathbf{R}^{3\sharp I^{int}}$ the sequence of nodal vectors for each time step. Considering the matrices for the old surface we introduce a sequence of fully discrete anisotropic mean curvature vectors $\left(\bar{Y}^k\right)_{k=0,1,\dots} \subset \mathbb{R}^{3\sharp I}$, with

$$\bar{Y}^{k+1} = \\ -(\mathbf{M}[X^k])^{-1}\left(\mathbf{L}^{\gamma(N^k)}[X^k] - \mathbf{L}^{\gamma_z(N^k)\otimes N^k}[X^k]\right)(\mathbf{E}\bar{X}^{k+1} + \bar{X}^{ext}) + (\mathbf{M}[X^k])^{-1}\bar{N}^{co,\gamma(N^k)}[X^k].$$

The implicit time discretization and using matrices for the old surface result in the following fully discrete problem:

Problem 3.3.2. (Full discrete semi-implicit anisotropic Willmore flow, Variant I)
Given some initial surface $\mathcal{M}[X^0]$ we seek a sequence $(\mathcal{M}[X^k])_{k=1,\dots}$ of discrete surfaces such that

$$\left(\mathbf{M}^{int}[X^k] + \tau\mathbf{R}\mathbf{L}_{\gamma_{zz}}[X^k](\mathbf{M}[X^k])^{-1}\left(\mathbf{L}^{\gamma}[X^k] - \mathbf{L}^{\gamma_z\otimes N^k}[X^k]\right)\mathbf{E} + \tau\frac{1}{2}\mathbf{R}\mathbf{L}^{|Y|^2}[X^k]\mathbf{E}\right)\bar{X}^{k+1} \\ = \tau\bar{F}^k + \mathbf{M}^{int}[X^k]\bar{X}^k - \tau\mathbf{R}\mathbf{L}_{\gamma_{zz}}[X^k](\mathbf{M}[X^k])^{-1}\left(\left(\mathbf{L}^{\gamma}[X^k] - \mathbf{L}^{\gamma_z\otimes N^k}[X^k]\right)\bar{X}^{ext} - \bar{N}^{co,\gamma}[X^k]\right)$$

with

$$\bar{F}^k = 2\mathbf{R}\left(\mathbf{L}_{\gamma_{zz}}[X^k] - \mathbf{L}^{N^k\otimes N^k}_{\gamma zz}[X^k]\right)(\mathbf{M}[X^k])^{-1} \\ \left(\left(\mathbf{L}^{\gamma}[X^k] - \mathbf{L}^{\gamma_z\otimes N^k}[X^k]\right)(\mathbf{E}\bar{X}^k + \bar{X}^{ext}) - \bar{N}^{co,\gamma}[X^k]\right) \\ -\frac{1}{2}\mathbf{R}\mathbf{L}^{|Y^k|^2}[X^k]\bar{X}^{ext},$$

where $\gamma = (N^k)$, $\gamma_z = \gamma_z(N^k)$ and $\gamma_{zz} = \gamma_{zz}(N^k)$ are valuated at the surface normal N^k of the old surface X^k.

We end up with a linear system of equations to be solved in each time step.

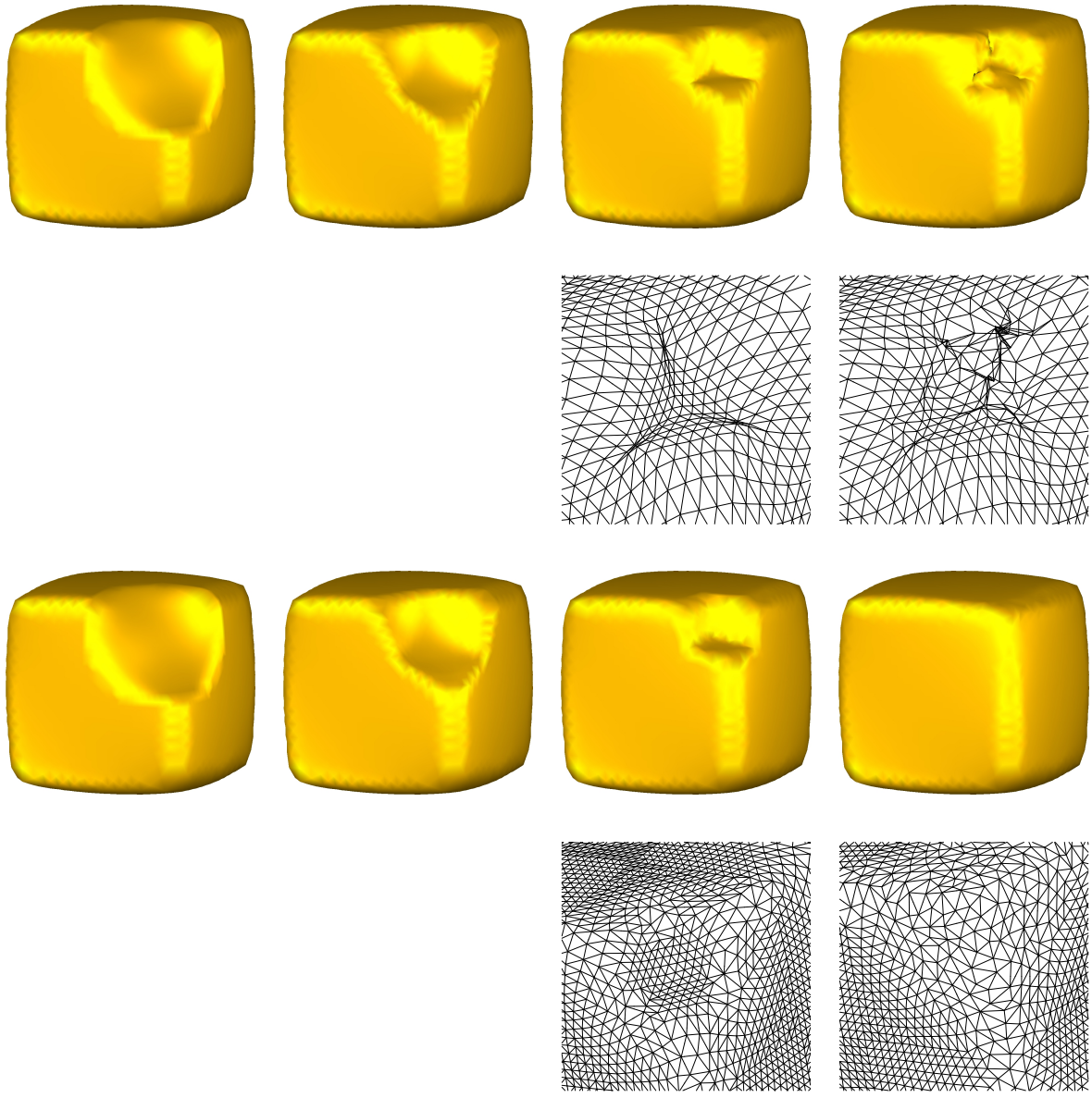

Figure 3.2: Restoration of a destroyed Wulff shape with anisotropy $\gamma(z) = \sum_{j=1}^{3} \sqrt{\delta^2 \|z\|^2 + z_j^2}$ ($\delta = 0.01$) without (first row) and with mesh modification (third row). The grid consists of 8192 triangles. The 5th, 25th and 85th iterations are shown above. Since the triangles degenerate without remeshing, the surface regularity deteriorates during the iterative scheme for Willmore flow (first row). Furthermore, a part of the destroyed area of the grid of the 25th and 85th iterations is shown (second and fourth row). In the fourth row the grids of the corresponding meshes involving edge swaps and edge collapses are shown.

Variant II: Implicitly encoding the co-normal N^{co}

As a variant of the above scheme we do not explicitly incorporate the co-normal but incorporate the discrete surface normals on $\mathcal{M}^{ext}[X(t)]$. Hence, we are not forced to compute $\bar{N}^{co,\gamma}[X(t)]$. We skip the integrals over the boundary $\partial\mathcal{M}[X(t)]$ in the Equation (3.11) and exchange the integration domain, replacing $\partial\mathcal{M}[X(t)]$ by $\partial\widetilde{\mathcal{M}}[X(t)]$. A motivation for this modification can be found in Nemitz [130, Section 5.7.3] and (5.8) in Chapter 5. We get

Problem 3.3.3. (Variant II of the semi-discrete anisotropic Willmore flow)
Find a family of triangulated surfaces $\mathcal{M}[X(t)]$ with parametrization $X(t) \in \mathcal{V}(\mathcal{M}[X(t)])^3$ with fixed boundary $\mathcal{M}^{ext}[X(t)]$ and a family of accompanying function $Y(t) \in \mathcal{V}(\mathcal{M}[X(t)])^3$ such that

$$\begin{aligned}
&\int_{\mathcal{M}[X(t)]} \partial_t \mathbf{R}X(t)\cdot\Theta(t)\,da - \int_{\mathcal{M}[X(t)]} \nabla_{\mathcal{M}[\mathrm{X(t)}]}\, Y(t) : \gamma_{zz}(N(t))\,\nabla_{\mathcal{M}[\mathrm{X(t)}]}\,\Theta(t)\,da \qquad (3.13)\\
&= -2\int_{\mathcal{M}[X(t)]} \nabla_{\mathcal{M}[\mathrm{X(t)}]}\, Y(t) : \gamma_{zz}(N(t))\,\nabla_{\mathcal{M}[\mathrm{X(t)}]}\,\Theta(t)\,da\\
&\quad -\frac{1}{2}\int_{\mathcal{M}[X(t)]} |Y(t)|^2\,\nabla_{\mathcal{M}[\mathrm{X(t)}]} X(t) : \nabla_{\mathcal{M}[\mathrm{X(t)}]}\,\Theta(t)\,da\\
&\quad +2\int_{\mathcal{M}[X(t)]} N^i(t)N^l(t)\,\nabla_{\mathcal{M}[\mathrm{X(t)}]}\, Y^i(t)\cdot\left(\gamma_{zz}(N(t))\,\nabla_{\mathcal{M}[\mathrm{X(t)}]}\,\Theta^l(t)\right)\,da,
\end{aligned}$$

for all test functions $\Theta(t) \in \mathcal{V}^{int}(\mathcal{M}[X(t)])^3$, $t > 0$ and

$$\begin{aligned}
\int_{\widetilde{\mathcal{M}}[X(t)]} Y(t)\cdot\Psi(t)\,da &= \int_{\widetilde{\mathcal{M}}[X(t)]} \left(\nabla_{\mathcal{M}[\mathrm{X(t)}]} X(t)\,\gamma_z(N(t))\right)\cdot\left(\nabla_{\mathcal{M}[\mathrm{X(t)}]}\,\Psi(t)N(t)\right)\,da\\
&\quad -\int_{\widetilde{\mathcal{M}}[X(t)]} \gamma(N(t))\,\nabla_{\mathcal{M}[\mathrm{X(t)}]} X(t) : \nabla_{\mathcal{M}[\mathrm{X(t)}]}\,\Psi(t)\,da
\end{aligned} \qquad (3.14)$$

holds for all test functions $\Psi(t) \in \mathcal{V}(\mathcal{M}[X(t)])^3$ and $t > 0$.

Let $\widetilde{\mathbf{M}}[X^k]$ and $\widetilde{\mathbf{L}}[X^k]$ denote the mass and stiffness matrices corresponding to the integration domain $\widetilde{\mathcal{M}}[X^k]$ instead of $\mathcal{M}[X^k]$, then we get

Problem 3.3.4. (Full discrete semi-implicit anisotropic Willmore flow (Variant II))
Given some initial surface $\mathcal{M}[X^0]$, find a sequence $(X^k)_{k=1,\dots}$ of parametrizations corresponding to a family of discrete surfaces such that

$$\begin{aligned}
&\left(\mathbf{M}^{int}[X^k] + \tau\mathbf{RL}_{\gamma_{zz}}[X^k](\widetilde{\mathbf{M}}[X^k])^{-1}\left(\widetilde{\mathbf{L}}^{\gamma}[X^k] - \widetilde{\mathbf{L}}^{\gamma_z\otimes N^k}[X^k]\right)\mathbf{E} + \tau\frac{1}{2}\mathbf{RL}^{|Y|^2}[X^k]\mathbf{E}\right)\bar{X}^{k+1}\\
&\qquad = \tau\bar{F}^k + \mathbf{M}^{int}[X^k] - \tau\mathbf{RL}_{\gamma_{zz}}[X^k](\widetilde{\mathbf{M}}[X^k])^{-1}\left(\widetilde{\mathbf{L}}^{\gamma}[X^k] - \widetilde{\mathbf{L}}^{\gamma_z\otimes N^k}[X^k]\right)\bar{X}^{ext}
\end{aligned}$$

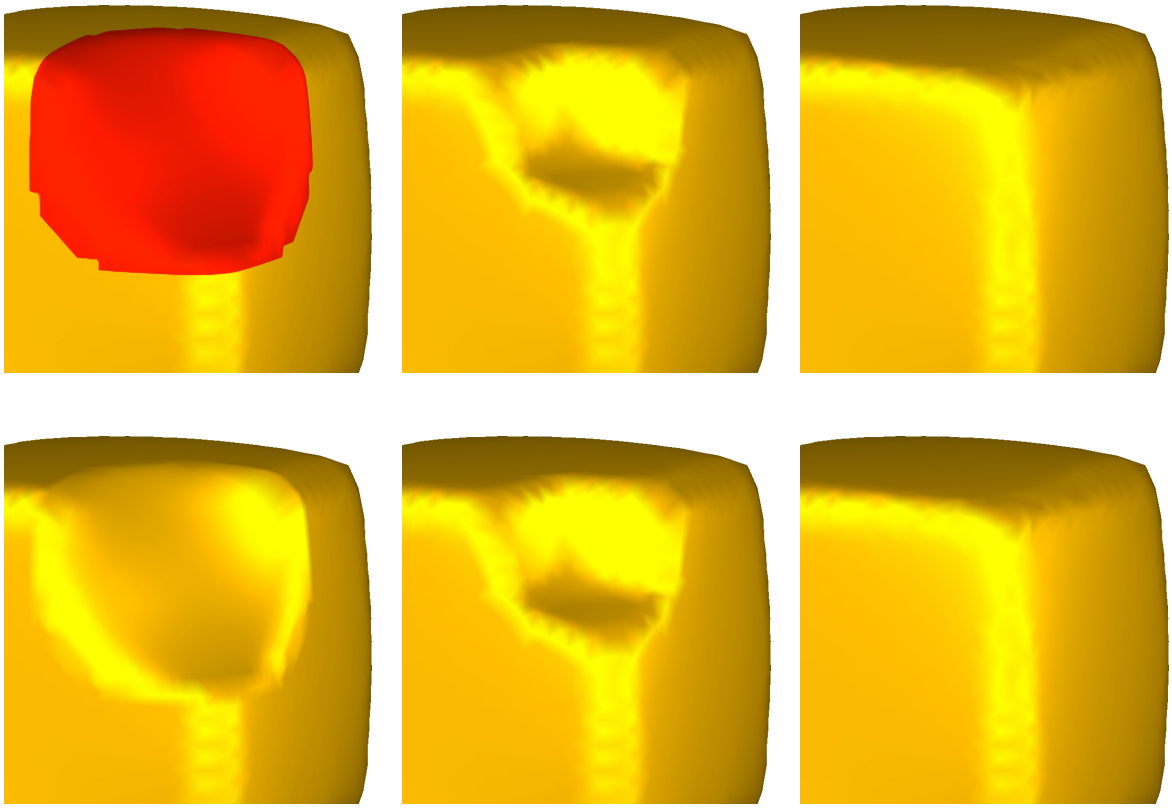

Figure 3.3: Restoration of a destroyed Wulff shape of Figure 3.2 with grid modifications. Comparison of variant I (bottom) and variant II (top) of the discretization. We show the initial surfaces on the left (above with a red surface patch $\mathcal{M}[X^0]$), intermediate time steps in the middle and the restored surfaces on the right. Both variants obviously lead to very similar results.

with

$$\bar{F}^k = 2\mathbf{R}\left(\mathbf{L}_{\gamma_{zz}}[X^k] - \mathbf{L}^{N\otimes N}_{\gamma zz}[X^k]\right)(\widetilde{\mathbf{M}}[X^k])^{-1}\left(\left(\widetilde{\mathbf{L}}^{\gamma}[X^k] - \widetilde{\mathbf{L}}^{\gamma_z\otimes N}[X^k]\right)(\mathbf{E}\bar{X} + \bar{X}^{ext})\right) - \frac{1}{2}\mathbf{R}\mathbf{L}^{|Y|^2}[X^k]\bar{X}^{ext},$$

where $\gamma = (N^k)$, $\gamma_z = \gamma_z(N^k)$ and $\gamma_{zz} = \gamma_{zz}(N^k)$ are valuated at the surface normal N^k of the old surface X^k.

The matrix corresponding to the system of equation is symmetric, but not necessarily positive definite. We use a biCG-method to solve the full discrete semi-implicit anisotropic Willmore flow, but our numerical experiments show that a simple CG-solver works well, too.

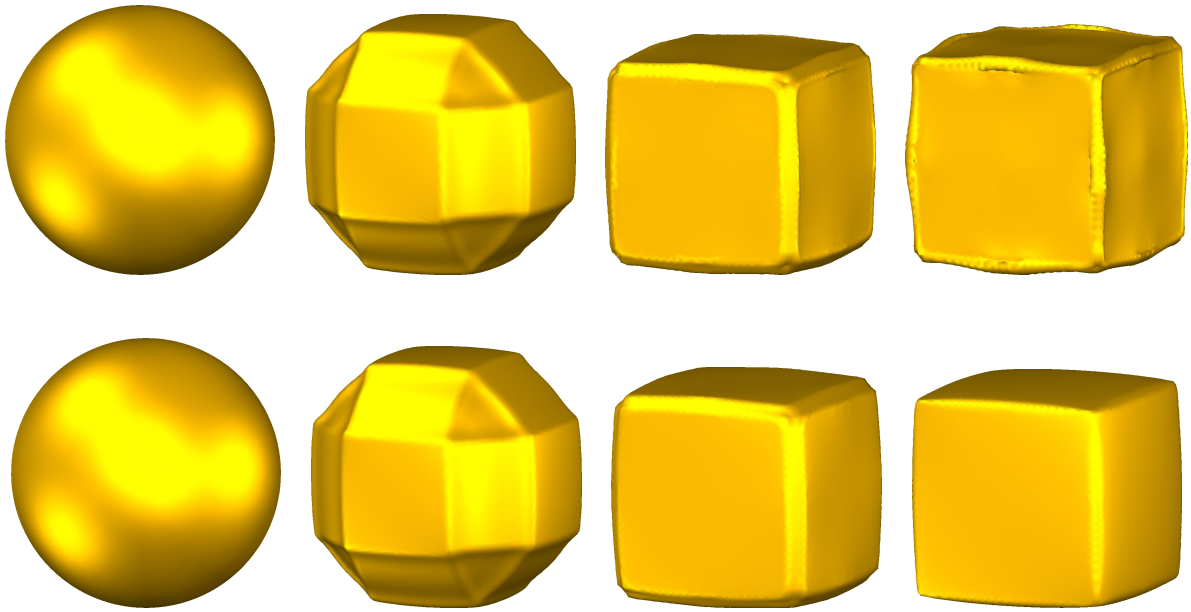

Figure 3.4: Anisotropic Willmore flow from an initial sphere with anisotropy $\gamma(z) = \sum_{j=1}^{3} \sqrt{\delta^2 \|z\|^2 + z_j^2}$ ($\delta = 0.001$) without (first row) and with mesh reparametrization (second row). The grid consists of 8192 triangles. Since the triangles degenerate without reparametrization, the surface regularity deteriorates during the iterative scheme for anisotropic Willmore flow (first row). $\partial \mathcal{M}[X] = \emptyset$. The grid size of the initial mesh varied between 0.038 and 0.025. The time step size was choosen $\tau = 10^{-6}$.

3.4 Numerical results

For smooth Wulff shapes the corresponding discrete evolutions turn out to be robust, at least in the experiments we ran. On the background of our surface restoration task, we are in particular interested in Wulff shapes with at least approximate edges which can be considered as templates for surfaces with destroyed edges. In case of these approximately singular Wulff shapes, even for the isotropic case, we observe a significant tangential shift of vertex positions on the discrete surface which deteriorates the mesh quality significantly, cf. Figure 3.2. Since spheres are stationary solutions of the isotropic Willmore flow, we expect that discrete spheres rearrange the nodes and then remain stationary in the discrete algorithm. But this is not the case for the full discrete semi-implicit Willmore flow corresponding to Problem 3.3.2 or Problem 3.3.4. For compact closed surfaces the Willmore energy is conformally invariant [24, 169, 173]. The only conformal automorphism of the sphere $S^2 \subset \mathbb{R}^3$ are the Möbius transformations [17, 134]. In Figure 4.8 of Section 4.5.2 we show the grid degeneration caused by this fact if we use no grid smoothing technique. For closed surfaces one can optimize the grid via conformal parametrization as described in Clarenz & Dziuk [54] and Olischläger [134, Chapter 5]. This, however, works only for closed surfaces. If the surface is not closed we have to use other topological mesh regularization during the discrete evolution. Indeed, the use of edge swapping and edge collapsing turned out to be beneficial

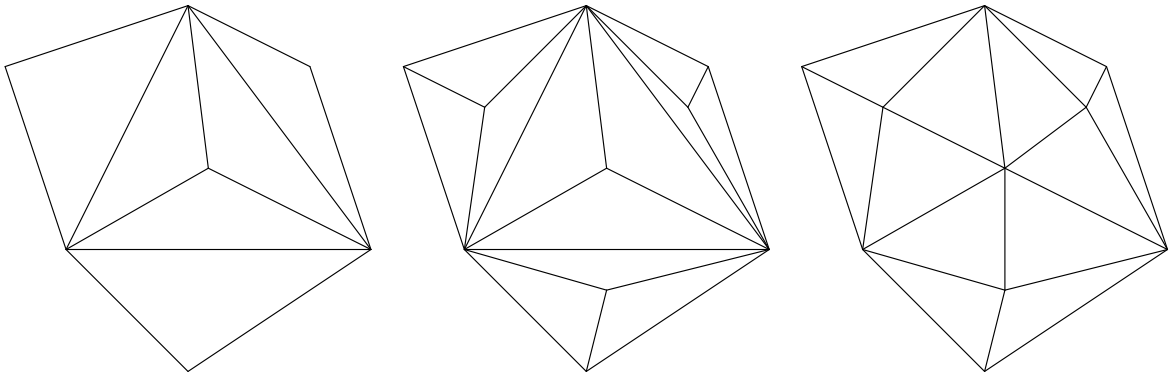

Figure 3.5: We perform node insertion (middle) of a given mesh (left). Then we traverse over all triangles and swap edges (right).

to compensate these artifacts for smooth Wulff shapes, cf. Figure 3.2. Node insertion or deletion improve the local length scale of the mesh. We perform edge swapping and edge collapsing, cf. Figure 3.5, to improve the mesh. Given two triangles $T_i = (X_i, X_2, X_3)$, $i = 0, 1$ incident to an edge $E = (X_2, X_3)$. Let Θ_i be the angle at the node X_i of the triangle T_i opposite the edge E. If $\Theta_i \leq \pi$, $i = 0, 1$ and $\Theta_0 + \Theta_1 > (\pi + \epsilon)$ we swap edge E to (X_0, X_1) and change the topology of the mesh. In our implementation we have chosen $\epsilon = 0.01$. An edge collapse takes an edge $E = (X_2, X_3)$ in the mesh and collapses it to a single vertex X_{new}, if the length of the edge E is smaller a small real value $\tilde{\epsilon}$. The edge is removed and the triangles containing this edge collapse to an edge. As mentioned above, the algorithm for surfaces with boundaries and mesh improvement via edge collapse works only for smooth Wulff shapes. Choosing $\delta < 0.01$ for the anisotropy in Figure 3.2 the resulting scheme is not stable any more. For surfaces without boundaries and reparametrization via the method by CLARENZ & DZIUK [54] we could choose $\delta = 0.001$, if the time step size is of the order of $(\Delta X)^2$, where ΔX is the spatial grid size, cf. Figure 3.4. To overcome this difficulties we have developed a completely new scheme for Willmore flow, which is present in the next chapter.

Chapter 4

Natural time discretization for the isotropic Willmore flow

THE developed Finite Element scheme for anisotropic Willmore flow in Chapter 3 has three disadvantages. At first, severe tangential distortions have to be compensated for. Secondly, the developed Finite Element scheme for anisotropic Willmore flow requires the evaluation of higher order derivatives of the anisotropy $\gamma(\cdot)$, even though in the relevant singular case the anisotropy is only Lipschitz continuous. Thirdly, one observes significant restrictions on the time step size in the above approach. Effectively, one usually has to enforce time steps $\tau << (\Delta X)^2$, where ΔX is the spatial grid size to ensure stability of the semi-implicit time discretization. To overcome this difficulties we develop a completely new scheme for Willmore flow that is based on the idea of natural time discretization schemes for gradient flows. In each time step a PDE constrained optimization problem has to be solved. This variational formulation is based on the splitting of dissipation and energy. The Willmore energy at the new time step is approximated based on an inner, secondary variational problem describing a time step of mean curvature motion. The latter approximation is given via the discrete velocity of an implicit Euler time step for mean curvature flow and regarded as an approximation of the mean curvature vector. It enters the approximation of the actual Willmore functional, so that the resulting new scheme can be interpreted as a variational two step scheme.

The starting point was the paper by LUCKHAUS & STURZENHECKER [127] on the natural discretization of mean curvature motion. They proposed a fully implicit time discretization based on a variational problem in BV to be solved in each time step. In fact, in each time step the symmetric distance between two consecutive shapes corresponding to the current and the next time step is balanced by the time step τ times the perimeter of the shape at the next time step. This implicit time discretization has already been proposed by ALMGREN ET AL. [4]. CHAMBOLLE [36] investigated a reformulation of this approach in terms of a level set method. A related method for anisotropic mean curvature motion is discussed in [18, 37].

We ask for a generalization of this type of approach to Willmore flow. Thus, we would like to balance the squared distance of the next time step geometry at time $t_{k+1} = t_k + \tau$ from the current time step geometry at time t_k and a suitable approximation of the Willmore energy at time t_{k+1} scaled by the time step size. Solving a fully implicit time discrete problem for mean curvature motion of the unknown surface at time t_{k+1}, we can regard the correspond-

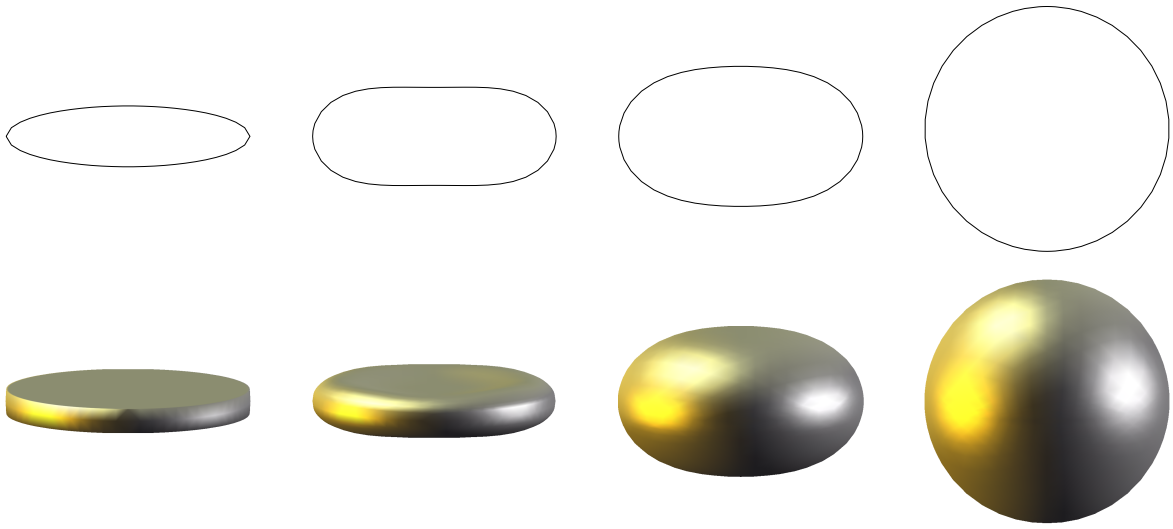

Figure 4.1: Different time steps of the Willmore flow of an original ellipsoid curve with 100 vertices is shown (top row). The time step size was chosen of the order of the spatial grid size $(\Delta X) = \tau = 0.0632847$. Willmore flow of a deformed sphere towards a round sphere is depicted in the bottom row. We show the surface at times $t = 0$, $t = \tau$, $t = 50\tau$ and $t = 150\tau$, where $\tau = \Delta X = 0.02325548045$.

ing difference quotient in time as a time discrete, fully implicit approximation of the mean curvature vector. Based on this mean curvature vector, we can define a Willmore functional. Thus, we are lead to a nested minimization problem in each time step. In the inner problem on the new time step an implicit mean curvature vector is identified. Then, the outer problem is the actual implicit, variational formulation of Willmore flow. Indeed, the resulting two step time discretization experimentally turns out to be unconditionally stable and effectively allows for time steps of the order of the spatial grid size. Furthermore, the anisotropic mean curvature vector can be approximated via a variational time step problem, which conceptually only involves the anisotropy γ but not its derivatives. Hence, the same will hold true for a corresponding two step discretization of anisotropic Willmore flow. This chapter has already been published in OLISCHLÄGER & RUMPF [135].

4.1 Natural time discretization for gradient flows

The new concept for the time discretization of the Willmore flow picks up the variational time discretization of general gradient flows. Suppose that we are given an energy functional $e[\cdot]$ on a d-dimensional Riemannian manifold $\mathcal{S}$ with metric g, $e : \mathcal{S} \to \mathbb{R}$. Functional minimization can be performed by the gradient flow with initial data $x^0 \in \mathcal{S}$ defining a curve $x(t)$ on the manifold $\mathcal{S}$, cf. Equation (2.30) in Section 2.3, via

$$\begin{aligned} \partial_t x &= -\operatorname{grad}_g e[x], \\ x(0) &= x^0. \end{aligned} \tag{4.1}$$

Let $p \in \mathcal{M}$, $v \in \mathcal{T}_p\mathcal{M}$ and $exp_p : \mathcal{T}_p\mathcal{M} \to \mathcal{S}$ be the exponential map defined to be $geo_v(0)$, where $geo_v : \mathbb{R} \to \mathcal{S}$, $t \mapsto geo(t)$, is the unique geodesic through p with velocity v at time 0, i.e. $geo_v(0) = p$ and $\partial_t geo_v(0) = v$. We refer to [158, 123, 39] for a more detailed overview. If g_p denotes the scalar product on the tangent space $\mathcal{T}_p\mathcal{M}$ induced by the Riemannian metric g of the manifold $\mathcal{S}$, then Equation (4.1) leads to finding a curve $x(t)$ with $x(0) = x^0$, such that

$$g_p(\dot{x}(t), v) = -\left\langle e'[x(t)], v\right\rangle = -\partial_\epsilon e\left[exp_p(\epsilon v)\right]\Big|_{\epsilon=0}, \qquad \forall v \in \mathcal{T}_p\mathcal{M}\,, \tag{4.2}$$

where $exp_p(\epsilon v) = geo_{\epsilon v}(1) = geo_v(\epsilon)$ for $0 \le \epsilon \le 1$, cf. Lee [123, Lemma 5.8]. Let

$$\xi(s) = (\xi_1(s), \cdots, \xi_d(s)) \in \mathbb{R}^d$$

be the local coordinates of x and $(g_{ij})_{i,j\in\{1,\cdots,d\}}$ the coefficent matrix corresponding to the Riemannian metric g, i.e. if $\{e_1, \cdots, e_d\}$ is a basis of $\mathcal{T}_p\mathcal{M}$, then we have $g_{ij} = g_p(e_i, e_j)$. Let g^{-1} denote its invers. Then, choosing $v = e_j$ in Equation (4.2) the gradient flow can be written in local coordinates:

$$\begin{aligned} & g_{ij}\dot{\xi}_j = -\partial_\xi e[x(\xi)], \qquad \forall j = 1, \cdots, d \\ \Leftrightarrow \qquad & \dot{\xi} = -g^{-1}\nabla_\xi e[x(\xi)]. \end{aligned}$$

Now, we construct time discrete solutions $(x^k)_{k=0,1,\cdots}$, where $x_k \approx x(k\tau)$ for the time step size τ iteratively by solving the following variational problem

$$x^{k+1} := \arg\min_x \operatorname{dist}(x, x^k)^2 + 2\tau\, e[x]\,, \tag{4.3}$$

where $\operatorname{dist}(\cdot,\cdot)$ is the shortest path length on the manifold, given the metric $g(\cdot,\cdot)$:

$$\operatorname{dist}(x, x^k) := \inf_{c\in\Gamma} \int_0^1 \sqrt{g(\dot{c}(s), \dot{c}(s))}\,\mathrm{d}s\,,$$

with

$$\Gamma := \left\{ c \in \mathcal{C}^1 \,\middle|\, c(0) = x^k \text{ and } c(1) = x \right\}.$$

As an immediate consequence, one obtains the energy estimate

$$e[x^{k+1}] + \frac{1}{2\tau}\operatorname{dist}(x^{k+1}, x^k)^2 \le e[x^k] + \frac{1}{2\tau}\operatorname{dist}(x^k, x^k)^2 = e[x^k]\,.$$

The new approach is motivated by the following considerations. Typically, in the context of geodesics in Riemannian geometry one introduces

$$\operatorname{sqrdist}(x, x^k) := \inf_{c\in\Gamma} \int_0^1 g(\dot{c}(s), \dot{c}(s))\,\mathrm{d}s\,.$$

It is then enough to minimize $\int_0^1 g(\dot{c}(s), \dot{c}(s))\,\mathrm{d}s$, owing to the Cauchy-Schwarz inequality for the L^2-scalar product

$$\left(\int_0^1 \sqrt{g(\dot{c}(s), \dot{c}(s))}\,\mathrm{d}s\right)^2 \le \int_0^1 g(\dot{c}(s), \dot{c}(s))\,\mathrm{d}s$$

with equality iff $|\dot{c}|$ is constant.

Furthermore, every $x \in \mathcal{M}$ can be written as

$$x = x^k + x - x^k = x^k + \int_0^1 \dot{c}(s)\,\mathrm{d}s\,, \qquad \forall c \in \Gamma\,. \tag{4.4}$$

To calculate the Euler–Lagrange equation for

$$\frac{1}{2\tau}\int_0^1 g\left(\dot{c},\dot{c}\right)\,\mathrm{d}s + e\left[x^k + \int_0^1 \dot{c}(s)\,\mathrm{d}s\right]$$

we consider for a test function $\vartheta \in \mathcal{C}^1$ the disturbed curve $c + \epsilon\,\vartheta$. We get

$$\partial_\epsilon\left(\frac{1}{2\tau}\int_0^1 g\left(\dot{c}+\epsilon\,\dot{\varphi},\dot{c}+\epsilon\,\dot{\varphi}\right)\,\mathrm{d}s + e\left[x^k + \int_0^1 (\dot{c}(s)+\epsilon\,\dot{\vartheta})\,\mathrm{d}s\right]\right)\Bigg|_{\epsilon=0} = 0 \tag{4.5}$$

One the other hand, we can rewrite the gradient flow $\partial_t x = -\operatorname{grad}_g e[x]$ by introducing the variable $s = \frac{1}{\tau}t$. Changing the time derivative ∂_t into $\frac{1}{\tau}\partial_s$ and using Equation (4.4) we can rewrite Equation (4.1) as

$$\frac{1}{\tau}\dot{c} + \operatorname{grad}_g e\left[x^k + \int_0^1 \dot{c}(s)\,\mathrm{d}s\right] = 0\,.$$

Multiplying this equation with $\dot{\vartheta}$ and integration over $\int_0^1$ we get

$$\int_0^1 g\left(\frac{1}{\tau}\dot{c} + \operatorname{grad}_g e\left[x^k + \int_0^1 \dot{c}(s)\,\mathrm{d}s\right], \dot{\vartheta}\right)\mathrm{d}\tilde{s} = 0$$

$$\Leftrightarrow \quad \tfrac{1}{\tau}\int_0^1 g\left(\dot{c},\dot{\vartheta}\right)\,\mathrm{d}s + \int_0^1 g\left(\operatorname{grad}_g e\left[x^k + \int_0^1 \dot{c}(s)\,\mathrm{d}s\right], \dot{\vartheta}\right)\mathrm{d}\tilde{s} = 0$$

For the second summand we have

$$\begin{aligned}
\int_0^1 g\left(\operatorname{grad}_g e\left[x^k + \int_0^1 \dot{c}(s)\,\mathrm{d}s\right], \dot{\vartheta}\right)\mathrm{d}\tilde{s} &\overset{(2.29)}{=} \int_0^1 \left\langle e'\left[x^k + \int_0^1 \dot{c}(s)\,\mathrm{d}s\right], \dot{\vartheta}\right\rangle \mathrm{d}\tilde{s} \\
&= \left\langle e'\left[x^k + \int_0^1 \dot{c}(s)\,\mathrm{d}s\right], \int_0^1 \dot{\vartheta}\,\mathrm{d}\tilde{s}\right\rangle \\
&\overset{(2.28)}{=} \partial_\epsilon e\left[x^k + \int_0^1 (\dot{c}(s)+\epsilon\,\dot{\vartheta})\,\mathrm{d}s\right]\Bigg|_{\epsilon=0}
\end{aligned}$$

Therefore, we get

$$\partial_\epsilon \left(\frac{1}{2\tau} \int_0^1 g\left(\dot{c} + \epsilon\,\dot{\vartheta}, \dot{c} + \epsilon\,\dot{\vartheta}\right) \mathrm{d}s + e\left[x^k + \int_0^1 (\dot{c}(s) + \epsilon\,\dot{\vartheta})\,\mathrm{d}s \right] \right) \Bigg|_{\epsilon=0} = 0\,,$$

which is the Euler–Lagrange equation (4.5). Finally, we end up with the following variational time discretization for a general gradient flow. In each time step the following problem has to be solved:

$$x^{k+1} = \arg\min_x \operatorname{sqrdist}(x, x^k) + 2\tau\, e[x].$$

Let us consider some examples for different gradient flows:

Euclidian case. Suppose $e[\cdot] : \mathbb{R}^d \to \mathbb{R}$ is a real valued function. Then we get for the natural time discretization

$$x^{k+1} = \arg\min_x \frac{1}{2\tau}|x - x^k|^2 + e[x]\,.$$

If x^{k+1} is a minimizer then it holds

$$0 = \frac{|x^{k+1} - x^k|}{\tau} \cdot v + e'[x^{k+1}](v) \qquad \forall v \in \mathbb{R}^d\,.$$

This results into an implicit Euler scheme as expected

$$\frac{|x^{k+1} - x^k|}{\tau} = -\nabla_x e[x^{k+1}]\,.$$

Generalization to the heat equation. For a function $u(x,t)$ with spatial variable $x \in \Omega \subset \mathbb{R}^d$ and time variable t, the heat equation is given by

$$\partial_t u - \Delta_x u = 0$$

with corresponding Euler–Lagrange equation

$$\int_\Omega \partial_t u\,\vartheta + \nabla_x u \cdot \nabla_x \vartheta\,\mathrm{d}x = 0\,, \tag{4.6}$$

for all test functions $\vartheta \in \mathcal{C}_0^1(\mathbb{R}^d, \mathbb{R})$. The heat equation describes the L^2-gradient flow of the Dirichlet integral

$$e(u) = \frac{1}{2}\int_\Omega |\nabla_x u|^2\,\mathrm{d}x\,.$$

The natural time discretization of the L^2-gradient flow corresponding to the Dirichlet integral is then

$$u^{k+1} = \arg\min_u \frac{1}{2\tau}\int_\Omega \left(u - u^k\right)^2 \mathrm{d}x + \frac{1}{2}\int_\Omega |\nabla_x u|^2\,\mathrm{d}x\,.$$

For a test functions $\vartheta \in \mathcal{C}^1$ we get the fully implicit Euler Scheme

$$0 = \int_\Omega \frac{u^{k+1} - u^k}{\tau} \vartheta + \nabla_x u^{k+1} \cdot \nabla_x \vartheta \, \mathrm{d}x \,. \tag{4.7}$$

4.2 Derivation of the two step time discretization

Before we consider the actual time discretization of Willmore flow, let us briefly review the time discretization of mean curvature motion.

4.2.1 Variational time discretization of mean curvature motion

Let $\mathcal{M}[y]$ be a d-dimensional surface embedded in $\mathbb{R}^m$ with $m \geq d+1$ and parameterized by a mapping y. Let $\mathbf{h}$ be the mean curvature. Following the above abstract approach the variational time discretization of mean curvature motion for a given surface $\mathcal{M} = \mathcal{M}[x]$ defines the mapping $y = y[x]$ surface $\mathcal{M}[y]$ of the next time step as

$$y[x] = \arg\min_y \operatorname{dist}(\mathcal{M}[y], \mathcal{M}[x])^2 + 2\tilde{\tau} \int_{\mathcal{M}[y]} \mathrm{d}a, \tag{4.8}$$

where $\tilde{\tau}$ is the considered time step, $\operatorname{dist}(\cdot,\cdot)$ is the L^2-distance between surfaces and the surface area of $\mathcal{M}[y]$ as the underlying energy. Then, the mean curvature motion is the L^2-gradient flow of the surface area

$$a[y] = \int_{\mathcal{M}[y]} \mathrm{d}a \,.$$

Since $-\mathbf{h}\, n = \Delta_{\mathcal{M}[y]} y$, cf. Equation (2.8), the flow is given by

$$\partial_t y = \Delta_{\mathcal{M}[y]} y \,.$$

The Euler–Lagrange equation for this problem is, cf. Equation (2.11),

$$0 = \int_{\mathcal{M}[y]} \partial_t y \cdot \vartheta \, \mathrm{d}a + \int_{\mathcal{M}[y]} \nabla_{\mathcal{M}[y]} y : \nabla_{\mathcal{M}[y]} \vartheta \, \mathrm{d}a$$

for all $\vartheta \in \mathcal{C}_0^1(\mathcal{M}[y], \mathbb{R}^m)$. $A : B = \operatorname{tr}(A^T B)$ denotes scalar product to the Frobenius norm, cf. Definition 2.1.8. Because the geometrical counterpart of the Euclidian Laplacian Δ on smooth surfaces is the Laplace–Beltrami operator $\Delta_{\mathcal{M}[y]}$ the Euler–Lagrange equation can be considered as a generalization for the variational formulation of the heat equation, cf. Equation (4.6).

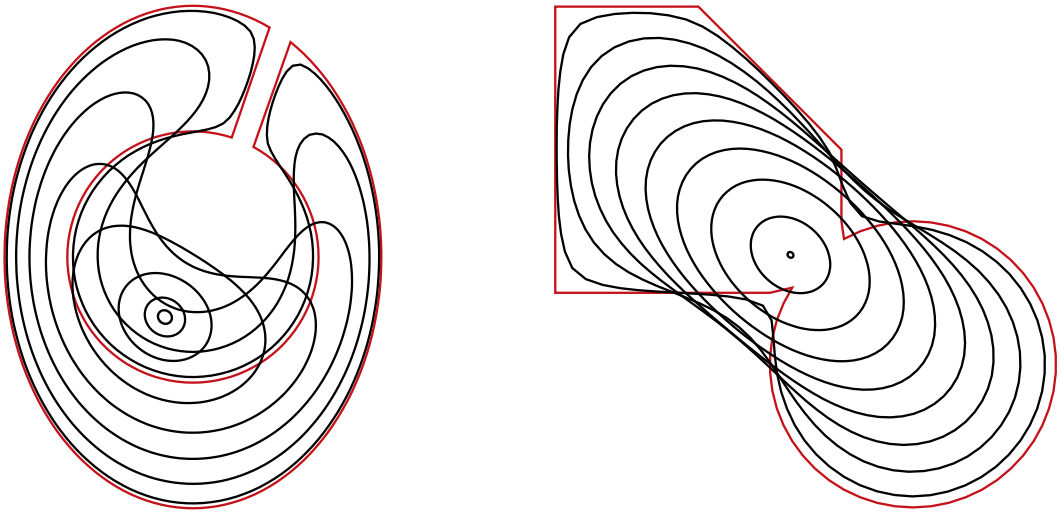

Figure 4.2: We pick up two examples of CHAMBOLLE [36] for the evolution under the curve shortening flow with the variational time discretization of mean curvature motion. The time step τ is chosen of the order of the spatial grid size. The red curve is the initial curve that converges to a round point. We show the evolution of the left examples for iterations 1, 3, 5, 7, 9, 11, 13, 15, 17 and for the second examples for iterations 1, 5, 10, 15, 20, 25, 27, 28.

Applying a classical scheme for a single semi-implicit time step of mean curvature motion already proposed by DZIUK [81] the resulting weak form of the Euler–Lagrange equations is

$$0 = \int_{\mathcal{M}[x]} (y - x) \cdot \vartheta + \tilde{\tau} \nabla_{\mathcal{M}[x]} y : \nabla_{\mathcal{M}[x]} \vartheta \, \mathrm{d}a$$

for test functions ϑ, cf. Equation (4.7). Considering the corresponding strong form the corresponding Euler–Lagrange equations we obtain the following variational problem:

Given a surface $\mathcal{M}[x]$ parameterized by a mapping x we ask for a mapping $y = y[x]$ which solves the minimization problem

$$\begin{aligned} y[x] &= \arg\min_y e[x, y], \quad \text{with} \\ e[x, y] &= \int_{\mathcal{M}[x]} (y - x)^2 + \tilde{\tau} |\nabla_{\mathcal{M}[x]} y|^2 \, \mathrm{d}a \end{aligned} \tag{4.9}$$

for given x. In what follows the time step size $\tilde{\tau}$ is chosen independent of the time step size for the actual time discrete Willmore flow. In our later spatially discrete model we consider a $\tilde{\tau}$ equal to the square of the spatial grid size. In Figure 4.2 we show two examples for the evolution under the curve shortening flow with the variational time discretization of mean curvature motion.

4.2.2 Two step time discretization for the isotropic Willmore flow

In this section we derive the two step time discretization for the isotropic Willmore flow. The idea is to solve the fully implicit time discrete problem (4.9) for mean curvature motion for the unknown surface. We can then regard the corresponding difference quotient in time as a time discrete, fully implicit approximation of the mean curvature vector. Based on this mean curvature vector, we can define a Willmore functional and the corresponding natural time discretization:
We deduce from the time continuous evolution equation $\partial_t x = \mathbf{h}\, n$ that the difference quotient $\frac{y[x]-x}{\tilde{\tau}}$, where $y[x]$ is a solution for the fully implicit time discrete problem (4.9) for mean curvature motion, can be considered as a regularized approximation of the mean curvature vector $\mathbf{h}\, n$ on $\mathcal{M}[x]$. Thus, the functional

$$\frac{1}{2}\int_{\mathcal{M}[x]} \frac{(y[x]-x)^2}{\tilde{\tau}^2}\,\mathrm{d}a$$

approximates the Willmore functional on $\mathcal{M}[x]$. This enables us to define a time discretization of Willmore flow which does no require the explicit evaluation of the mean curvature on the unknown surface of the next time step. Indeed, in the abstract variational problem

$$\operatorname{dist}(\mathcal{M}[x], \mathcal{M}[x^k])^2 + \tau \int_{\mathcal{M}[x]} \mathbf{h}^2\,\mathrm{d}a \to \min$$

we consider the same linearization of the L^2-distance as for mean curvature motion and use the above approximation of the Willmore energy. Finally, we obtain the following scheme:

Given an initial surface $\mathcal{M}[x^0]$ we define a sequence of surfaces $\mathcal{M}[x^k]$ with $k = 1, 2, \cdots$, where x^{k+1} minimizes the functional

$$w[x^k, x, y[x]] = \int_{\mathcal{M}[x^k]} (x - x^k)^2\,\mathrm{d}a + \frac{\tau}{\tilde{\tau}^2}\int_{\mathcal{M}[x]} (y[x]-x)^2\,\mathrm{d}a$$

for given x_k. Hence, x^k is assumed to approximate $x(t_k)$ with $t_k = k\tau$ for the given time step τ. Thus, in each time step we have to solve the nested variational problem

$$x^{k+1} = \arg\min_x w[x^k, x, y[x]] \quad \text{with} \tag{4.10}$$

$$y[x] = \arg\min_y e[x, y]\,. \tag{4.11}$$

The inner problem is quadratic, hence the Euler–Lagrange equation is a linear elliptic PDE and we end up with a PDE constrained optimization problem for each time step.

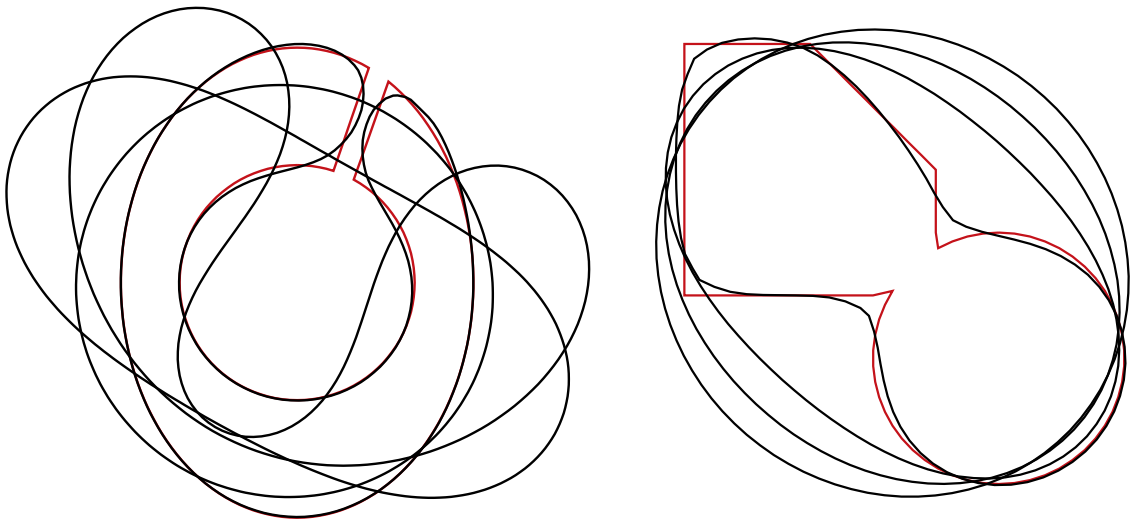

Figure 4.3: Evolution of the two examples from Figure 4.2 under the two step time discretization of the Willmore flow. The computational data are $\tau = \Delta X$ and $\tilde{\tau} = (\Delta X)^2$, where $\Delta X = 0.19$ in the left example and $\Delta X = 0.34$ in the right example of the initial red curve. λ was chosen 0.03. We show the evolution of the left examples for iterations 1, 5, 10, 20 and for the second examples for iterations 1, 10, 20, 40.

To be more explicit, let us examine circles in the plane. Under Willmore flow circles expand according the ODE

$$\dot{R}(t) = \frac{1}{2} R(t)^{-3}$$

for the radius. In comparison to this the radius R^{k+1} in the above time discrete scheme turns out to be a solution of the nonlinear equation

$$\frac{R - R_k}{\tau} = \frac{1}{2} \frac{R^4 - 3R^2\tau}{(R^2 + \tau)^3 R_k},$$

which is an implicit first order scheme for the above ODE. For a more detailed exposition we refer to Section 4.5.1.

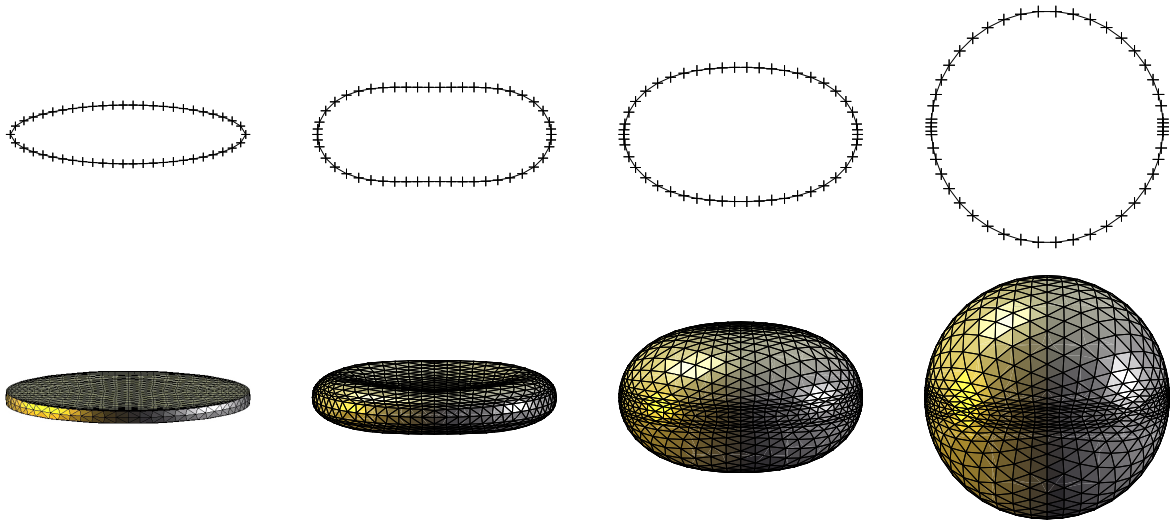

Figure 4.4: The grids of the evolution under Willmore flow of the initial ellipsoid curve and deformed sphere of Figure 4.1 are shown at the same times. We did not reparametrize the curve since our scheme does not suffer from significant tangential motions.

4.3 Finite Element space discretization

In this section we discretize Equations (4.10) and 4.11 in space with piecewise affine Finite Elements as already introduced in Section 2.4. Again, we consider simplicial meshes $\mathcal{M}[X]$ - polygonal curves for $d = 1$ and triangular surfaces for $d = 2$ - as approximations of the d-dimensional surfaces $\mathcal{M}[x]$. As above, X is the identity on the simplicial mesh $\mathcal{M}[X]$ which is described by a vector $\bar{X}$ of vertex positions of the mesh. As in Section 2.4 we use upper case letter for discrete quantities and lower case letter for the corresponding continuous quantities. Furthermore, a bar on top of a discrete function indicates the corresponding nodal vector, i.e. $\bar{X} = (\bar{X}_i)_{i\in I}$, where $\bar{X}_i = (X_i^1, \cdots, X_i^m)$ is the coordinate vector of the ith vertex of the mesh and I denotes the index set of vertices. With a slight misuse of notation the mapping X itself is considered as an element in the corresponding piecewise affine Finite Element space $\mathcal{V}(\mathcal{M}[X])^m$. In particular in accordance to Definition 2.35 in Section 2.4 we recover $\bar{X} = (X_i)_{i\in I}$. Hence, given some initial parametrization X^0 of the surface $\mathcal{M}[X^0]$ we seek a sequence $(X^k)_{k=1,2,\dots}$ of parametrizations corresponding to discrete surfaces $(\mathcal{M}[X^k])_{k=1,2,\dots}$.

Now, we have all the ingredients at hand to derive the fully discrete two step time discretization of Willmore flow, cf. Figure 4.4, which can be regarded as a discrete counterpart of (4.10). Given a discrete surface $\mathcal{M}[X^k]$ in time step k we define $X^{k+1} \in \mathcal{V}(\mathcal{M}[X^k])^m$ as the minimizer of the following spatially discrete, nested variational problem

$$\begin{aligned} X^{k+1} &= \operatorname*{arg\,min}_{X\in\mathcal{V}(\mathcal{M}[X^k])^m} W[X^k, X, Y[X]] \quad \text{with} \\ Y[X] &= \operatorname*{arg\,min}_{Y\in\mathcal{V}(\mathcal{M}[X])^m} E[X, Y], \end{aligned} \tag{4.12}$$

where

$$\begin{aligned} E[X,Y] &:= \int_{\mathcal{M}[X]} (Y-X)^2 + \tilde{\tau}|\nabla_{\mathcal{M}[X]} Y|^2 \,\mathrm{d}a \\ &= \mathbf{M}[X](\bar{Y}-\bar{X})\cdot(\bar{Y}-\bar{X}) + \tilde{\tau}\mathbf{L}[X]\bar{Y}\cdot\bar{Y}\,, \\ W[X^k,X,Y] &:= \int_{\mathcal{M}[X^k]} (X-X^k)^2 \,\mathrm{d}a + \frac{\tau}{\tilde{\tau}^2}\int_{\mathcal{M}[X]} (Y-X)^2 \,\mathrm{d}a \\ &= \mathbf{M}[X^k](\bar{X}-\bar{X}^k)\cdot(\bar{X}-\bar{X}^k) + \frac{\tau}{\tilde{\tau}^2}\mathbf{M}[X](\bar{Y}-\bar{X})\cdot(\bar{Y}-\bar{X}) \end{aligned}$$

are the straightforward spatially discrete counterpart of the functionals $e[x,y]$ and $w[x^k,x,y]$, respectively. Here, $M[X]$ denote the mass matrix and $L[X]$ the stiffness matrix, i.e.

$$\begin{aligned} M_{ij}[X] &= \int_{\mathcal{M}[X]} \Phi_i \Phi_j \,\mathrm{d}a\,, \\ L_{ij}[X] &= \int_{\mathcal{M}[X]} \nabla_{\mathcal{M}[X]}\Phi_i \cdot \nabla_{\mathcal{M}[X]}\Phi_j \,\mathrm{d}a\,, \end{aligned}$$

$i,j \in I$, with corresponding block matrices $\mathbf{M}[X]$ and $\mathbf{L}[X]$ in $\mathbb{R}^{m\sharp I, m\sharp I}$

$$\begin{aligned} \mathbf{M}[X] &= \begin{pmatrix} M[X] & & \\ & \ddots & \\ & & M[X] \end{pmatrix}, \\ \mathbf{L}[X] &= \begin{pmatrix} L[X] & & \\ & \ddots & \\ & & L[X] \end{pmatrix}, \end{aligned}$$

cf. Equations (2.36), (2.44) and (2.37) in Section 2.4. In analogy to the continuous case for given X $Y[X]$ requires to solve

$$\begin{aligned} 0 = \partial_Y E[X,Y](\Theta) &= \partial_\epsilon E[X, Y+\epsilon\,\Theta]\big|_{\epsilon=0} \\ &= \int_{\mathcal{M}[X]} (Y-X)\cdot\Theta + \tilde{\tau}\nabla_{\mathcal{M}[X]}Y : \nabla_{\mathcal{M}[X]}\Theta \,\mathrm{d}a \end{aligned}$$

for all test functions $\Theta \in \mathcal{V}(\mathcal{M}[X])^m$. Therefore the nodal vector $\bar{Y}[X]$ solves the linear system of equations

$$(\mathbf{M}[X] + \tilde{\tau}\mathbf{L}[X])\,\bar{Y}[X] = \mathbf{M}[X]\,\bar{X}\,. \tag{4.13}$$

4.4 Numerical solution of the optimization problem

In this section, we discuss how to numerically solve in each time step the nonlinear optimization problem (4.12). Here, we will confine to a gradient descent approach or a sequential quadratic programming (SQP) approach that is a Newton like method and take into account a suitable duality technique to effectively compute the gradient and the Hessian of the energy functional

$$\widehat{W}[X] := W[X^k, X, Y[X]]$$

given the fact that the argument $Y[X]$ is a solution of the inner minimization problem and as such solves the linear system of equations (4.13). Indeed, we obtain for the variation of $\widehat{W}$ in a direction $\Theta \in \mathcal{V}(\mathcal{M}[X^k])^m$

$$\partial_X \widehat{W}[X](\Theta) = \partial_X W[X^k, X, Y[X]](\Theta) + \partial_Y W[X^k, X, Y[X]] \left(\partial_X Y[X](\Theta)\right).$$

A direct computation of $\partial_X Y[X](\Theta)$ would require the solution of the inner minimization problem and thus specifically a linear system, cf. (4.13), would have to be solved for every test function Θ. This can be avoided applying the following duality argument, cf. Haslinger & Mäkinen [108, Chapter 3] and Hinze et al. [110, Chapter 1.6]:

From the optimality of $Y[X]$ in the inner problem, we deduce the equation

$$0 = \partial_Y E[X, Y[X]](\Psi)$$

for any test function $\Psi \in \mathcal{V}(\mathcal{M}[X])^m$. Now, differentiating with respect to X we obtain

$$\begin{aligned} 0 &= \partial_X \left(\partial_Y E[X, Y[X]](\Psi)\right)(\Theta) \\ &= \partial_X \partial_Y E[X, Y](\Psi, \Theta) + \partial_Y^2 E[X, Y[X]](\Psi, \partial_X Y[X](\Theta)) \end{aligned}$$

for any test function Ψ. Let us now define $P \in \mathcal{V}(\mathcal{M}[X^k])^m$ as the solution of the dual problem

$$\partial_Y^2 E[X, Y[X]](P, \Upsilon) = \partial_Y W[X^k, X, Y[X]](\Upsilon). \tag{4.14}$$

for all test functions $\Upsilon \in \mathcal{V}(\mathcal{M}[X^k])^m$. Now, choosing $\Upsilon = \partial_X Y[X](\Theta)$ and $\Psi = P$ one obtains

$$\left(\partial_Y W\right)[X^k, X, Y[X]] \left(\partial_X Y[X](\Theta)\right) = -\partial_X \partial_Y E[X, Y](P, \Theta).$$

Thus, we can finally rewrite the variation of $\widehat{W}$ with respect to X in a direction Θ as

$$\partial_X \widehat{W}[X](\Theta) = \partial_X W[X^k, X, Y[X]](\Theta) - \partial_X \partial_Y E[X, Y](P, \Theta). \tag{4.15}$$

The solution P of the dual problem (4.14) requires to solve

$$\int_{\mathcal{M}[X]} P \cdot \Psi + \tilde{\tau} \nabla_{\mathcal{M}[X]} P : \nabla_{\mathcal{M}[X]} \Psi \, \mathrm{d}a = \int_{\mathcal{M}[X]} \frac{\tau}{\tilde{\tau}^2} (Y - X) \cdot \Psi \, \mathrm{d}a$$

for all test functions Ψ. In matrix vector notation, this can be written as the linear system of equations

$$(\mathbf{M}[X] + \tilde{\tau} \mathbf{L}[X]) \bar{P} = \frac{\tau}{\tilde{\tau}^2} \mathbf{M}[X](\bar{Y} - \bar{X}).$$

The terms on the right hand side of (4.15) are evaluated as follows

$$\begin{aligned}\left(\partial_X W\right)[X^k,X,Y](\Theta) &= 2\,\mathbf{M}[X^k](\bar{X}-\bar{X}^k)\cdot\bar{\Theta}+2\frac{\tau}{\tilde{\tau}^2}\mathbf{M}[X](\bar{X}-\bar{Y})\cdot\bar{\Theta}\\ &\quad+\frac{\tau}{\tilde{\tau}^2}(\partial_X\mathbf{M}[X](\Theta))(\bar{Y}-\bar{X})\cdot(\bar{Y}-\bar{X}),\end{aligned}$$

$$\begin{aligned}\partial_X\partial_Y E[X,Y](P,\Theta) &= \partial_X\left(2\mathbf{M}[X](\bar{Y}-\bar{X})\cdot\bar{P}+2\tilde{\tau}\mathbf{L}[X]\bar{Y}\cdot\bar{P}\right)(\Theta)\\ &= 2(\partial_X\mathbf{M}[X](\Theta))(\bar{Y}-\bar{X})\cdot\bar{P}-2\mathbf{M}[X]\bar{\Theta}\cdot\bar{P}\\ &\quad+2\tilde{\tau}(\partial_X\mathbf{L}[X](\Theta))\bar{Y}\cdot\bar{P}\,.\end{aligned}$$

The variations of the mass and stiffness matrix with respect to a variation Θ of the simplicial grid,

$$\partial_X\mathbf{M}[X](\Theta)=\begin{pmatrix}\partial_X M[X](\Theta) & & \\ & \partial_X M[X](\Theta) & \\ & & \partial_X M[X](\Theta)\end{pmatrix},$$

$$\partial_X\mathbf{L}[X](\Theta)=\begin{pmatrix}\partial_X L[X](\Theta) & & \\ & \partial_X L[X](\Theta) & \\ & & \partial_X L[X](\Theta)\end{pmatrix},$$

where

$$\partial_X M[X](\Theta)=\partial_\epsilon M[X+\epsilon\,\Theta]\Big|_{\epsilon=0}\quad\text{and}\quad\partial_X L[X](\Theta)=\partial_\epsilon L[X+\epsilon\,\Theta]\Big|_{\epsilon=0},$$

are calculated in Section 2.4.1. Finally, we can compute the descent direction in $\mathbb{R}^{m\sharp I}$ of the energy $\widehat{W}$ at a given simplicial mesh $\mathcal{M}[X]$ described by the nodal vector $\bar{X}$ and obtain

$$\overline{\operatorname{grad}_X\widehat{W}[X]}=\left(\partial_X\widehat{W}[X](\Phi_r e_s)\right)_{r\in I,s=1,\cdots,m},$$

where e_s denotes the sth coordinate direction in $\mathbb{R}^m$.

In the concrete numerical Algorithm 4.1 we now perform a **gradient descent method with the Amijo step size control** [7, 134] starting from the initial position given by the previous time step. The Armijo's line search strategy consists of finding

$$\begin{aligned}&\text{ArmijoStepSize}\left[\widehat{W},X,D\right]\\ &\qquad:=\max\left\{\beta^n:\ n\in\mathbb{Z}\text{ and }\widehat{W}[X+\beta^n D]\le\widehat{W}[X]+\alpha\,\beta^n\,\overline{\operatorname{grad}_X\widehat{W}[X]}\cdot D\right\},\end{aligned}$$

with $\alpha,\beta\in(0,1)$ be fixed and D be a given decent direction, such that $\overline{\operatorname{grad}_X\widehat{W}[X]}\cdot D<0$. We choose the parameters as $\alpha=0.25$ and $\beta=0.5$ in the alogorithm. This strategy ensures that the energy decreases in every step.

Algorithm 4.1: Gradient decent method for two step time discrete Willmore flow

input data: surface $\mathcal{M}[X^0]$;
calculate spatial grid size ΔX^0;
set time step sizes $\tau = \Delta X^0$ and $\tilde{\tau} = \tau^2$;
set $\bar{X}^k = \bar{X}^0$;
set counter for the two step time discretization $k = 0$;
repeat
  set counter of the gradient decent method $l = 0$;
  set $\bar{X}^{k,l} = \bar{X}^k$;
  repeat
    solve $\left(\mathbf{M}[X^{k,l}] + \tilde{\tau}\mathbf{L}[X^{k,l}]\right)\bar{Y} = \mathbf{M}[X^{k,l}]\bar{X}$;
    solve $\left(\mathbf{M}[X^{k,l}] + \tilde{\tau}\mathbf{L}[X^{k,l}]\right)\bar{P} = \frac{\tau}{\tilde{\tau}^2}\mathbf{M}[X^{k,l}](\bar{Y} - \bar{X}^{k,l+1})$;
    $D = \left(\partial_X W[X^k, X^{k,l}, Y](\Phi_r e_s) - \partial_X \partial_Y E[X^{k,l}](P, \Phi_r e_s)\right)_{r\in I, s=1,\cdots,m}$;
    $\bar{X}^{k,l+1} = \bar{X}^{k,l} -$ ArmijoStepSize$\left[\widehat{W}, X^{k,l}, D\right]$ D;
    $l \leftarrow l + 1$;
  until $|\bar{X}^{k,l+1} - \bar{X}^{k,l}| < \epsilon$;
  $\bar{X}^{k+1} = \bar{X}^k$;
  $k \leftarrow k + 1$;
until $|\bar{X}^{k+1} - \bar{X}^k| < \epsilon$;

One of the most effective methods for nonlinear constrained optimization generates steps by solving quadratic subproblems. We refer to NOCEDAL & WRIGHT [133] for an overview on numerical optimization. This **sequential quadratic programming (SQP) approach** can be used to solve problems with significant nonlinearities in the contraints. The simplest derivation of SQP methods views them as an application of Newton's methods to the Karush–Kuhn–Tucker (also known as KKT) optimality conditions, cf. KARUSH [112] and KUHN & TUCKER [116]. The KKT conditions are the necessary condition for a solution in nonlinear programming to be optimal. We consider the following Lagrangian function for problem (4.12)

$$L[X, Y, P] = W[X^k, X, Y] - \partial_Y E[X, Y](P)$$

for the now independent unknowns $X, Y \in \mathbb{R}^{m\sharp I}$ and Lagrange parameter $P \in \mathbb{R}^{m\sharp I}$. The first-order KKT conditions are

$$\begin{pmatrix} \partial_X L[X,Y,P](\Theta) \\ \partial_Y L[X,Y,P](\Theta) \\ \partial_P L[X,Y,P](\Theta) \end{pmatrix} = \begin{pmatrix} \partial_X W[X^k,X,Y](\Theta) - \partial_X\partial_Y E[X,Y](P,\Theta) \\ \partial_Y W[X^k,X,Y](\Theta) - \partial_Y\partial_Y E[X,Y](P,\Theta) \\ -\partial_Y E[X,Y](\Theta) \end{pmatrix} = 0,$$

for any test functions $\Theta \in \mathcal{V}(\mathcal{M}[X^k])^m$. The first equation corresponds to equation (4.15), the second to equation (4.14) and the third to equation (4.13). Together with the above

calculations the gradient of L is given by

$$\overline{\mathrm{grad}_{[X,Y,P]}L[X,Y,P]} = \begin{pmatrix} \partial_X L[X,Y,P](\Phi_r e_s) \\ \partial_Y L[X,Y,P](\Phi_r e_s) \\ \partial_P L[X,Y,P](\Phi_r e_s) \end{pmatrix}_{r\in I, s=1,\cdots,m}.$$

For a test functions $\Theta \in \mathcal{V}(\mathcal{M}[X^k])^m$ the components of the gradient of L are

$$\begin{aligned}\partial_X L[X,Y,P](\Theta) =& 2\,\mathbf{M}[X^k](\bar{X}-\bar{X}^k)\cdot\bar{\Theta} + 2\frac{\tau}{\tilde{\tau}^2}\mathbf{M}[X](\bar{X}-\bar{Y})\cdot\bar{\Theta} \\ &+ (\partial_X\mathbf{M}[X](\Theta))(\bar{Y}-\bar{X})\cdot\left(\frac{\tau}{\tilde{\tau}^2}(\bar{Y}-\bar{X}) - 2\,\bar{P}\right) \\ &+ 2\mathbf{M}[X]\bar{\Theta}\cdot\bar{P} - 2\tilde{\tau}(\partial_X\mathbf{L}[X](\Theta))\bar{Y}\cdot\bar{P}\,,\end{aligned}$$

$$\partial_Y L[X,Y,P](\Theta) = 2\,\frac{\tau}{\tilde{\tau}^2}\mathbf{M}[X](\bar{Y}-\bar{X})\cdot\bar{\Theta} - 2\,(\mathbf{M}[X] + \tilde{\tau}\mathbf{L}[X])\,\bar{P}\cdot\bar{\Theta},$$

$$\partial_P L[X,Y,P](\Theta) = 2\,\mathbf{M}[X]\bar{X}\cdot\bar{\Theta} - 2\,(\mathbf{M}[X] + \tilde{\tau}\mathbf{L}[X])\,\bar{Y}\cdot\bar{\Theta}.$$

Now, to set up Newton's method, we also need the Hessian of L,

$$\overline{\mathrm{Hess}_{[X,Y,P]}L[X,Y,P]} = \begin{pmatrix} \partial_X\partial_X L(\Phi_r e_s, \Phi_{\tilde{r}} e_{\tilde{s}}) & \partial_Y\partial_X L(\Phi_r e_s, \Phi_{\tilde{r}} e_{\tilde{s}}) & \partial_P\partial_X L(\Phi_r e_s, \Phi_{\tilde{r}} e_{\tilde{s}}) \\ \partial_X\partial_Y L(\Phi_r e_s, \Phi_{\tilde{r}} e_{\tilde{s}}) & \partial_Y\partial_Y L(\Phi_r e_s, \Phi_{\tilde{r}} e_{\tilde{s}}) & \partial_P\partial_Y L(\Phi_r e_s, \Phi_{\tilde{r}} e_{\tilde{s}}) \\ \partial_X\partial_P L(\Phi_r e_s, \Phi_{\tilde{r}} e_{\tilde{s}}) & \partial_Y\partial_P L(\Phi_r e_s, \Phi_{\tilde{r}} e_{\tilde{s}}) & \partial_P\partial_P L(\Phi_r e_s, \Phi_{\tilde{r}} e_{\tilde{s}}) \end{pmatrix}$$

with $r,\tilde{r} \in I$ and $s,\tilde{s} = 1,\cdots,m$. For test functions $\Theta,\Psi \in \mathcal{V}(\mathcal{M}[X^k])^m$ the components of the first row of the Hessian of L are given by

$$\begin{aligned}\partial_X\partial_X L(\Theta,\Psi) =& 2\mathbf{M}[X^k]\bar{\Psi}\cdot\bar{\Theta} + 2\frac{\tau}{\tilde{\tau}^2}\mathbf{M}[X]\bar{\Psi}\cdot\bar{\Theta} - 2\tilde{\tau}(\partial_X^2\mathbf{L}[X](\Theta,\Psi))\bar{Y}\cdot\bar{P} \\ &+ (\partial_X^2\mathbf{M}[X](\Theta,\Psi))(\bar{Y}-\bar{X})\cdot\left(\frac{\tau}{\tilde{\tau}^2}(\bar{Y}-\bar{X}) - 2\,\bar{P}\right) \\ &+ 2(\partial_X\mathbf{M}[X](\Theta))\left(\frac{\tau}{\tilde{\tau}^2}(\bar{X}-\bar{Y}) + \bar{P}\right)\cdot\bar{\Psi} \\ &+ 2(\partial_X\mathbf{M}[X](\Psi))\left(\frac{\tau}{\tilde{\tau}^2}(\bar{X}-\bar{Y}) + \bar{P}\right)\cdot\bar{\Theta},\end{aligned}$$

$$\begin{aligned}\partial_Y\partial_X L(\Theta,\Psi) =& -2\,\frac{\tau}{\tilde{\tau}^2}\mathbf{M}[X]\bar{\Psi}\cdot\bar{\Theta} - 2\tilde{\tau}(\partial_X\mathbf{L}[X](\Theta))\bar{\Psi}\cdot\bar{P} \\ &- 2(\partial_X\mathbf{M}[X](\Theta))\left(\frac{\tau}{\tilde{\tau}^2}(\bar{X}-\bar{Y}) + \bar{P}\right)\cdot\bar{\Psi},\end{aligned}$$

$$\begin{aligned}\partial_P\partial_X L(\Theta,\Psi) =& -2\,(\partial_X\mathbf{M}[X](\Theta))(\bar{Y}-\bar{X})\cdot\bar{\Psi} \\ &+ 2\mathbf{M}[X]\bar{\Theta}\cdot\bar{\Psi} - 2\tilde{\tau}(\partial_X\mathbf{L}[X](\Theta))\bar{Y}\cdot\bar{\Psi}\,,\end{aligned}$$

whereas for the components of the second row of the Hessian of L we have

$$\begin{aligned}
\partial_X \partial_Y L(\Theta, \Psi) =& \partial_Y \partial_X L(\Psi, \Theta),\\
\partial_Y \partial_Y L(\Theta, \Psi) =& 2\,\frac{\tau}{\tilde{\tau}^2}\mathbf{M}[X]\bar{\Psi}\cdot\bar{\Theta},\\
\partial_P \partial_Y L(\Theta, \Psi) =& -2\,(\mathbf{M}[X] + \tilde{\tau}\mathbf{L}[X])\,\bar{\Psi}\cdot\bar{\Theta}\,.
\end{aligned}$$

The third row of the Hessian of L consists of the entries $\partial_X \partial_P L(\Theta, \Psi) = \partial_P \partial_X L(\Psi, \Theta)$, $\partial_Y \partial_P L(\Theta, \Psi) = \partial_P \partial_Y L(\Psi, \Theta)$ and $\partial_P \partial_P L(\Theta, \Psi) = 0$. Thus, the Newton step from the iterate $(X^{k,l}, Y^l, P^l)$ is given by

$$\begin{pmatrix} \bar{X}^{k,l+1} \\ \bar{Y}^{l+1} \\ \bar{P}^{l+1} \end{pmatrix} = \begin{pmatrix} \bar{X}^{k,l} \\ \bar{Y}^{l} \\ \bar{P}^{l} \end{pmatrix} + \begin{pmatrix} \Delta\bar{X}^{l} \\ \Delta\bar{Y}^{l} \\ \Delta\bar{P}^{l} \end{pmatrix}, \tag{4.16}$$

where we have to solve in each iteration of the Newton Algorithm 4.2

$$\overline{\mathrm{Hess}_{[X,Y,P]} L[X^{k,l}, Y^l, P^l]}\left(\Delta\bar{X}^l, \Delta\bar{Y}^l, \Delta\bar{P}^l\right)^T = -\overline{\mathrm{grad}_{[X,Y,P]} L[X^{k,l}, Y^l, P^l]}\,. \tag{4.17}$$

There is an alternative way to view iteration (4.16) and (4.17) namely as the solution of a quadratic program. At first we introduce some notation. We identify the variations of the mass and stiffness matrix with third order tensors $\partial_X \mathbf{M}$ and $\partial_X \mathbf{L}$ that map a vector $\bar{V} = (V_j^k)_{j\in I, k=1,\cdots,m} \in \mathbb{R}^{m\sharp I}$ to a matrix via

$$(\partial_X \mathbf{M})\bar{V} = \left(\partial_X M_{(\tilde{r},\tilde{s})(j,k)}[X](\Phi_r e_s)V_j^k\right)_{r,\tilde{r}\in I, s,\tilde{s}=1,\cdots,m} \in \mathbb{R}^{m\sharp I, m\sharp I} \tag{4.18}$$

and

$$(\partial_X \mathbf{L})\bar{V} = \left(\partial_X L_{(\tilde{r},\tilde{s})(j,k)}[X](\Phi_r e_s)V_j^k\right)_{r,\tilde{r}\in I, s,\tilde{s}=1,\cdots,m} \in \mathbb{R}^{m\sharp I, m\sharp I}\,. \tag{4.19}$$

Then we are able to define a matrix

$$\begin{aligned}
A[X, Y] :=& \,\mathrm{grad}_{[X,Y]}(\partial_P L[X, Y, P])\\
=& -\mathrm{grad}_{[X,Y]}(\partial_Y E[X, Y])\\
=& -2\begin{pmatrix} (\partial_X \mathbf{M})(\bar{Y} - \bar{X}) - \mathbf{M}[X] + \tilde{\tau}(\partial_X \mathbf{L}[X])\bar{Y} \\ \mathbf{M}[X] + \tilde{\tau}\mathbf{L}[X] \end{pmatrix}.
\end{aligned}$$

Let us remark that A is independent of P and that we identify

$$A[X, Y](P) = -\mathrm{grad}_{[X,Y]}(\partial_Y E[X, Y](P))\,.$$

Algorithm 4.2: Newton method for two step time discrete isotropic Willmore flow

input data: surface $\mathcal{M}[X^0]$;
calculate spatial grid size ΔX^0;
set time step sizes $\tau = \Delta X^0$ and $\tilde{\tau} = \tau^2$;
set $\bar{X}^k = \bar{X}^0$;
set counter for the two step time discretization $k = 0$;
repeat
  set counter of the Newton method $l = 0$;
  set $\bar{X}^{k,l} = \bar{X}^k$;
  set $\bar{Y}^l = \bar{X}^k$;
  set $\bar{P}^l = 0$;
  repeat
    calculate $H := \overline{\mathrm{Hess}_{[X,Y,P]} L[X^{k,l}, Y^l, P^l]}$;
    calculate $G := \overline{\mathrm{grad}_{[X,Y,P]} L[X^{k,l}, Y^l, P^l]}$;
    solve $H \left(\Delta\bar{X}, \Delta\bar{Y}, \Delta\bar{P}\right)^T = -G$;
    $D := \left(\Delta\bar{X}, \Delta\bar{Y}, \Delta\bar{P}\right)^T$;
    $\sigma :=$ArmijoStepSize$\left[g, \left(\bar{X}^{k,l}, \bar{Y}^l, \bar{P}^l\right)^T, D\right]$;
    $\left(\bar{X}^{k,l+1}, \bar{Y}^{l+1}, \bar{P}^{l+1}\right)^T = \left(\bar{X}^{k,l}, \bar{Y}^l, \bar{P}^l\right)^T + \sigma D$;
    $l \leftarrow l + 1$;
  until $D < \epsilon$;
  $\bar{X}^{k+1} = \bar{X}^k$;
  $k \leftarrow k + 1$;
until $|\bar{X}^{k+1} - \bar{X}^k| < \epsilon$;

Together with $\bar{P}^{l+1} = \bar{P}^l + \Delta\bar{P}^l$ we can write iteration (4.17) as

$$\begin{pmatrix} \mathrm{Hess}_{[X,Y]} L[X^{k,l}, Y^l, P^l] & A[X^{k,l}, Y^l] \\ A^T[X^{k,l}, Y^l] & 0 \end{pmatrix} \begin{pmatrix} (\Delta\bar{X}^l, \Delta\bar{Y}^l) \\ \Delta\bar{P}^l \end{pmatrix}$$
$$= \begin{pmatrix} -\mathrm{grad}_{[X,Y]} W[X^k, X^{k,l}, Y^l] + \mathrm{grad}_{[X,Y]}(\partial_Y E[X^{k,l}, X^l](P^l)) \\ \partial_Y E[X^{k,l}, Y^l] \end{pmatrix}. \quad (4.20)$$

If we subtract $\mathrm{grad}_{[X,Y]}(\partial_Y E[X^{k,l}, X^l](P^l))$ from both sides of the first equation of (4.20) we obtain

$$\begin{pmatrix} \mathrm{Hess}_{[X,Y]} L[X^{k,l}, Y^l, P^l] & A[X^{k,l}, Y^l] \\ A^T[X^{k,l}, Y^l] & 0 \end{pmatrix} \begin{pmatrix} (\Delta\bar{X}^l, \Delta\bar{Y}^l) \\ \bar{P}^{l+1} \end{pmatrix} = \begin{pmatrix} -\mathrm{grad}_{[X,Y]} W[X^k, X^{k,l}, Y^l] \\ \partial_Y E[X^{k,l}, Y^l] \end{pmatrix}.$$

Suppose that at the iterate $(X^{k,l}, Y^l, P^l)$ we model problem (4.12) using the **quadratic program**

$$\min_{(\Delta\bar{X},\Delta\bar{Y})} \quad W[X^k, X^{k,l}, Y^l] + \operatorname{grad}_{[X,Y]} W[X^k, X^{k,l}, Y^l] \cdot (\Delta\bar{X}, \Delta\bar{Y}) \tag{4.21}$$
$$+ \frac{1}{2}(\Delta\bar{X}, \Delta\bar{Y})^T \operatorname{Hess}_{[X,Y]} L[X^{k,l}, Y^l, P^l](\Delta\bar{X}, \Delta\bar{Y})$$

$$\text{subject to} \quad A^T[X^{k,l}, Y^l](\Delta\bar{X}, \Delta\bar{Y}) - \partial_Y E[X^{k,l}, Y^l] = 0. \tag{4.22}$$

If $\operatorname{Hess}_{[X,Y]} L[X, Y, P]$ is positive definite on the tangent space of the optimality condition of Y, that is, $\bar{Z}^T \operatorname{Hess}_{[X,Y]} L[X, Y, P]\bar{Z} > 0$ for all $\bar{Z} \neq 0$ such that $A[X, Y]\bar{Z} = 0$, this problem has a unique solution $(\Delta\bar{X}^l, \Delta\bar{Y}^l, \bar{Z}^l)$ that satisfies

$$0 = \operatorname{Hess}_{[X,Y]} L[X^{k,l}, Y^l, P^l](\Delta\bar{X}^l, \Delta\bar{Y}^l) + \operatorname{grad}_{[X,Y]} W[X^k, X^{k,l}, Y^l] \tag{4.23}$$
$$+ A[X^{k,l}, Y^l]\bar{Z}^l$$

$$0 = A^T[X^{k,l}, Y^l](\Delta\bar{X}^l, \Delta\bar{Y}^l) - \partial_Y E[X^{k,l}, Y^l]. \tag{4.24}$$

The vectors $(\Delta\bar{X}^l, \Delta\bar{Y}^l)$ and $\bar{Z}^l$ can be identified with the solution of the Newton equation (4.20). We have that $\bar{P}^{l+1} = \bar{Z}^l$ and that $(\Delta\bar{X}^l, \Delta\bar{Y}^l)$ solves (4.21), (4.22) and (4.17).

The new iterate $(X^{k,l+1}, Y^{l+1}, P^{l+1})$ can therefore be defined either as the solution of the quadratic programm (4.21), (4.22) or as the iterate generated by the Newton method (4.16), (4.17). For the analysis the Newton point of view is useful, whereas the SQP framework enables us to derive practical algorithms, cf. Algorithm 4.3.

We solve the quadratic programm by solving the linear system of equations (4.23) and (4.24) that are the KKT-conditions for the quadratic programm. If we replace the linear term $\operatorname{grad}_{[X,Y]} W[X^k, X^{k,l}, Y^l] \cdot (\Delta\bar{X}, \Delta\bar{Y})$ by $\operatorname{grad}_{[X,Y]} L[X^{k,l}, Y^l, P^l] \cdot (\Delta\bar{X}, \Delta\bar{Y})$ in the objected (4.21) of the quadratic program, (4.21) is a quadratic approximation of the Lagrangian function. This motivates our choice of the quadratic model. We first replace the nonlinear program (4.12) by the problem of solving the KKT optimality conditions for the corresponding Lagrangian, then we make a quadratic approximation to the Lagrangian and a linear approximation to the constrains to obtain (4.21) and (4.22). Replacing $\operatorname{Hess}_{[X,Y]} L[X^{k,l}, Y^l, P^l]$ in (4.21) by the identity matrix leads to the gradient decent method, whereas an update matrix to a Quasi–Newton method. The SQP approach with $\operatorname{Hess}_{[X,Y]} L[X^{k,l}, Y^l, P^l]$ can be shown to be quadratically convergent, cf. NOCEDAL & WRIGHT[133, Theorem 18.4].

In our case, the Hessian of L, $\operatorname{Hess}_{[X,Y,P]} L[X, Y, P]$, is symmetric, but in general not positive definite. Nevertheless, we can use a CG-solver in the Newton and SQP method. We observed that in some cases, i.e. if the grid consists of triangles, where the ration between longest edge and radius of the inscribed circle is greater or equal of the order of 10^{-6}, cf. e.g. Figure 4.16, the matrix is symmetric but not positive definite. Then, we apply a Cholesky solver after multiplying the linear system of equations with the transpose of the system matrix, i.e. instead of solving $A\bar{X} = \bar{B}$, $A \in \mathbb{R}^{r,r}$, $\bar{X}, \bar{B} \in \mathbb{R}^r$ with $r = \{2, 3\}m\sharp d$, we solve $A^T A\bar{X} = A^T\bar{B}$. Let $Z = (Z_X, Z_Y) \neq 0$, $Z_X, Z_Y \in \mathcal{V}(\mathcal{M}[X])^m$, then, the tangent space of the optimality conditions

Algorithm 4.3: SQP method for two step time discrete isotropic Willmore flow

input data: surface $\mathcal{M}[X^0]$;
calculate spatial grid size ΔX^0;
set time step sizes $\tau = \Delta X^0$ and $\tilde{\tau} = \tau^2$;
set $\bar{X}^k = \bar{X}^0$;
set counter for the two step time discretization $k = 0$;
repeat
  set counter of the SQP method $l = 0$;
  set $\bar{X}^{k,l} = \bar{X}^k$;
  set $\bar{Y}^l = \bar{X}^k$;
  set $\bar{P}^l = 0$;
  repeat
    calculate $W[X^k, X^{k,l}, Y^l]$ and $\mathrm{grad}_{[X,Y]} W[X^k, X^{k,l}, Y^l]$;
    calculate $\mathrm{Hess}_{[X,Y]} L[X^{k,l}, Y^l, P^l]$;
    calculate $A^T[X^{k,l}, Y^l]$ and $-\partial_Y E[X^{k,l}, Y^l]$;
    solve (4.21), (4.22) to obtain $(\Delta\bar{X}^l, \Delta\bar{Y}^l)$ and $\bar{Z}^l$;
    set $\bar{X}^{k,l+1} = \bar{X}^{k,l} + \Delta\bar{X}^l$;
    set $\bar{Y}^{l+1} = \bar{Y}^l + \Delta\bar{Y}^l$;
    set $\bar{P}^{l+1} = \bar{Z}^l$;
    $l \leftarrow l + 1$;
  until $|(X^{k,l+1}, Y^{l+1}, P^{l+1}) - (X^{k,l}, Y^l, P^l)| < \epsilon$;
  $\bar{X}^{k+1} = \bar{X}^k$;
  $k \leftarrow k + 1$;
until $|\bar{X}^{k+1} - \bar{X}^k| < \epsilon$;

of Y, i.e. $A[X,Y]\bar{Z} = 0$, is $0 = -\mathrm{grad}_{[X,Y]}(\partial_Y E[X,Y](Z))$ or equivalently

$$0 = \begin{pmatrix} 2(\partial_X \mathbf{M})(\bar{X} - \bar{Y})\bar{Z}_X + 2\mathbf{M}[X]\bar{Z}_X - 2\tilde{\tau}(\partial_X \mathbf{L}[X])\bar{Y}\bar{Z}_X \\ \mathbf{M}[X]\bar{Z}_Y + \tilde{\tau}\mathbf{L}[X]\bar{Z}_Y \end{pmatrix}. \tag{4.25}$$

Differenziation of the two Equations in (4.25) w.r.t. X in direction P and multiplication with $\bar{Z}_X^T$ and $\bar{Z}_Y^T$, respectively, reduces inequality $\bar{Z}^T \mathrm{Hess}_{[X,Y]} L[X,Y,P]\bar{Z} > 0$ to

$$2\bar{Z}_X^T \mathbf{M}[X^k]\bar{Z}_X + 2\frac{\tau}{\tilde{\tau}^2}\bar{Z}_X^T \mathbf{M}[X]\bar{Z}_X + 2\frac{\tau}{\tilde{\tau}^2}\bar{Z}_X^T \mathbf{M}[X]\bar{Z}_X > 0.$$

Using mass lumping, cf. Equation (2.44) and THOMÉE [163]), the mass matrices are diagonal with positive diagonal entries and therefore positive definite. Since additionally

$$\bar{Z}^T L[X] Z = \int_{\mathcal{M}[X]} \nabla_{\mathcal{M}[X]} Z_k \cdot \nabla_{\mathcal{M}[X]} Z_k > 0$$

for $Z \in \mathcal{V}(\mathcal{M}[X])$ with non-vanishing support, the matrix $\mathbf{M}[X] + \tau\mathbf{L}[X]$ is positive definite and we use a CG-solver in the gradient decent method.

Following the same arguments in the anisotropic case we also end up with a gradient descent or SQP method, where the inner problem, i.e. a single fully implicit time step of anisotropic mean curvature motion, is solved with a Newton method, too. There, we also use a Cholesky solver.

4.5 Numerical results

We have applied the developed numerical algorithm to the evolution of curves in $\mathbb{R}^2$ and $\mathbb{R}^3$ and of two-dimensional surfaces in $\mathbb{R}^3$. Here, the presented results in particular demonstrate the robustness of the proposed method. In fact, the applications underline that time steps up to the order the spatial grid size ΔX are feasible.

4.5.1 Elastic flow for curves

Since circles expand under the Willmore flow, we consider a slight generalization of the above Willmore flow model. In fact, we add $\lambda a[x]$ to the Willmore energy, where λ is a fixed constant and $a[x]$ denotes the length of the curve. Here, λ can be regarded as a Lagrangian multiplier with respect to a length constraint. Hence, for proper choices of λ the generalized model avoids expansion.
Let $\mathcal{M}[X]$ represents a discrete closed curve as in Section 2.4, i.e. each element T_i, $i \in I$, of a polygonal curve is a line segment with nodes X_{i-1} and X_i. Here, we assume a cyclic indexing, i.e. we identify the indices $i = 0$ and $i = \sharp I$ for closed curves with $X_0 = X_{\sharp I}$. Then, we obtain for the discrete length functional

$$A[X] = \sum_{i \in I} Q_i,$$

where $Q_i = |X_i - X_{i-1}|$ is the length of the ith line segment. Furthermore, its gradient vector in $\mathbb{R}^{m\sharp I}$ is given by

$$\overline{\operatorname{grad}_X A[X]} = L[X]\bar{X}.$$

At first we have studied the evolution of circles in $\mathbb{R}^2$:

Comparison to exact solutions for radially symmetric evolution

The mean curvature for a circle $\mathcal{M}[x]$ in the plane with radius r is given by $\mathbf{h} = r^{-1}$. If n is the normal to the curve we get $|\nabla_{\mathcal{M}[X]} n|^2 = \|n'(t,s)\|^2 = r(t)^{-2}$. Then, for radially symmetric evolution of curves under the Willmore flow we see by Equation (2.33) that the solution can be described by an ordinary differential equation of the radius

$$\dot{r}(t) = \frac{1}{2} r(t)^{-3}.$$

Therefore, for a positiv initial radius $r(0) = r_0$ the evolution in time of the Willmore flow for the radius r is given by

$$r(t) = \left(r_0^4 + 2t\right)^{\frac{1}{4}}.$$

Step (k)	**Exact solution** $(r_0(t))$	**Numerical solution** (R^{k+1})	L^∞**-Error**
0	1.0019	1.0019	$6.5337*10^{-6}$
1	1.0039	1.0039	$1.2959*10^{-5}$
2	1.0058	1.0058	$1.9278*10^{-5}$
3	1.0078	1.0077	$2.5493*10^{-5}$
4	1.0097	1.0096	$3.1607*10^{-5}$
5	1.0116	1.0115	$3.7623*10^{-5}$
10	1.0210	1.0209	$6.6291*10^{-5}$
10^2	1.1578	1.1574	$3.5201*10^{-4}$
10^3	1.7272	1.7267	$5.6002*10^{-4}$
10^4	2.9901	2.9897	$3.9209*10^{-3}$

Table 4.1: A circle of radius $r_0 = 1$ expands in two dimension due to its propagation via Willmore flow. The exact solution $(r_0(t) = (r_0^4 + 2t)^{\frac{1}{4}})$ and the corresponding discrete solution computed by the SQP approach of the two step time discretization for 2000 polygon vertices and a time step size which equals the grid size are calculated for different time steps. The L^∞-Error is the maximum of the absolut value of the difference between $r_0((k+1)\tau)$ and $\|\bar{X}^{k+1}\|$.

To calculate the in space continuous and time discrete radially symmetric solutions for (4.11) we have to solve the mean curvature flow for y, that is

$$\dot{r}(t) = -r(t)^{-1}.$$

The evolution in time of the radius must hence be given by

$$r(t) = \left(r_0^2 - 2t\right)^{\frac{1}{2}}.$$

Let $\tilde{r}$ be the radius of the curve y that solves the time discrete, but spatially continuous mean curvature flow

$$\frac{y - x}{\tilde{\tau}} = \Delta_{\mathcal{M}[x]} y\,. \tag{4.26}$$

Then, by simple calculations, it holds that

$$\frac{\tilde{r} - r}{\tilde{\tau}} = -\frac{\tilde{r}}{r^2} \quad \Leftrightarrow \quad \tilde{r} = \frac{r^3}{r^2 + \tilde{\tau}}\,. \tag{4.27}$$

Let $\tau, \tilde{\tau}$ be fixed and $x^k = \partial B_{r_k}$ be the circle with radius r_k, $x = \partial B_{r(\tau)}$ be the circle with radius $r := r(\tau)$ and $y = \partial B_{\frac{r^3}{r^2+\tilde{\tau}}}$ the time discrete solution of the evolution of the mean curvature flow.

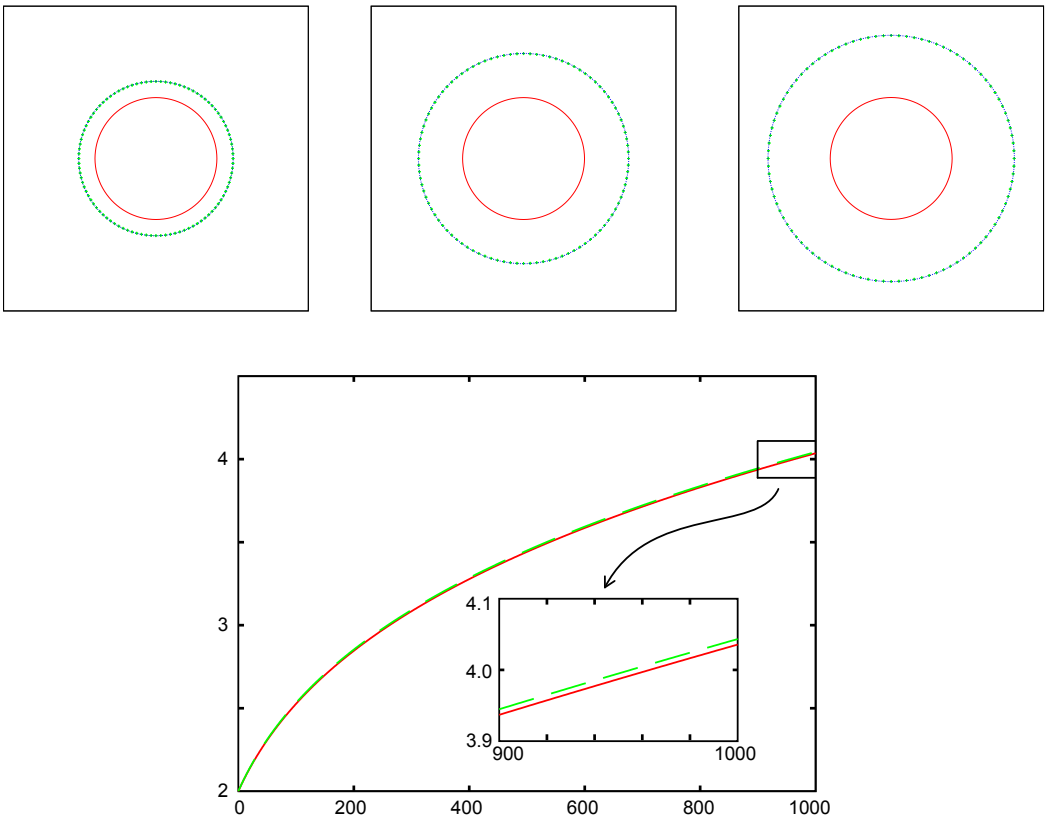

Figure 4.5: A circle of radius $r_0 = 2$ expands in two dimension under Willmore flow (top row)). The exact solution (blue dashed line) and the corresponding discrete solution computed by the two step time discretization for 200 polygon vertices and a time step size which equals the grid size (green crosses) are plotted for different times $t = 100(\Delta X)^2$, $500(\Delta X)^2$, $1000(\Delta X)^2$. The radius of growing circles under Willmore flow is plotted for the known continuous solution (green) and the discrete solution (red). (bottom row)

We consider the Willmore energy for radial symmetric solutions without length term:

$$\begin{aligned} w[r] = &\int_{\partial B_{r_k}} (x - x^k)^2 d\sigma + \frac{\tau}{\tilde{\tau}^2} \int_{\partial B_r} (y - x)^2 d\sigma \\ =&2\pi r_k \left(r - r_k\right)^2 + \frac{\tau}{\tilde{\tau}^2} 2\pi r \left(\frac{r^3}{r^2 + \tilde{\tau}} - r\right)^2, \end{aligned}$$

where $d\sigma$ is the arc length element. Therefore we get

$$\begin{aligned} 0 = \partial_r w[r] = &4\pi r_k (r - r_k) + 4\pi r \frac{\tau}{\tilde{\tau}^2} \left(\frac{r^3}{r^2 + \tilde{\tau}} - r\right) \left(\frac{3r^2(r^2 + \tilde{\tau}) - r^3\, 2r}{\left(r^2 + \tilde{\tau}\right)^2} - 1\right) \\ &+ 2\pi \frac{\tau}{\tilde{\tau}^2} \left(\frac{r^3}{r^2 + \tilde{\tau}} - r\right)^2. \end{aligned}$$

That is equivalent to

$$\begin{aligned}
0 =& r_k(r-r_k) + r\frac{\tau}{\tilde{\tau}^2}\left(\frac{r^3 - r(r^2+\tilde{\tau})}{r^2+\tilde{\tau}}\right)\left(\frac{3r^4+3r^2\tilde{\tau}-2\,r^4-(r^2+\tilde{\tau})^2}{(r^2+\tilde{\tau})^2}\right) \\
&+ \frac{\tau}{\tilde{\tau}^2}\frac{\left(r^3 - r(r^2+\tilde{\tau})\right)^2}{2(r^2+\tilde{\tau})^2} \\
=& r_k(r-r_k) + r\frac{\tau}{\tilde{\tau}^2}\left(\frac{-r\tilde{\tau}}{r^2+\tilde{\tau}}\right)\left(\frac{r^2\tilde{\tau}-\tilde{\tau}^2}{(r^2+\tilde{\tau})^2}\right) + \frac{\tau}{\tilde{\tau}^2}\frac{r^2\tilde{\tau}^2}{2(r^2+\tilde{\tau})^2} \\
=& r_k(r-r_k) + \tau\frac{1}{2}\frac{-r^4+3r^2\tilde{\tau}}{(r^2+\tilde{\tau})^3}
\end{aligned}$$

And finally the radius r^{k+1} in the time discrete scheme turns out to be a solution of the nonlinear equation

$$\frac{r-r_k}{\tau} = \frac{1}{2}\frac{r^4-3r^2\tilde{\tau}}{(r^2+\tilde{\tau})^3\, r_k},$$

which is an implicit first order scheme for the above ODE. Let us remark that it is very important to integrate the approximation of the mean curvature over the new curve. E.g. one can easily show that if one integrate over the old surface x_k we get

$$\frac{r-r_k}{\tau} = \frac{r^3 - r\tilde{\tau}}{(r^2+\tilde{\tau})^3}. \tag{4.28}$$

We observe that the radius of the discrete evolution would grow twice as fast.

Evolution of an ellipse towards a circle

As a first example for the resulting flow we consider the evolution of an ellipse towards a circle under the elastic flow, cf. the first rows in Figure 4.1 and 4.4. The initial parametrization is given as

$$x_0(t) = (\sin(t), 4\ \cos(t), 0) \text{ for } t \in [0, 2\pi].$$

The computational parameters are $h = 0.0632847$, $\tau = h$ and $\lambda = 0.025$. One observes that the ellipse evolves to a circle and the polygonal vertices stay well-distributed on the evolving curve.

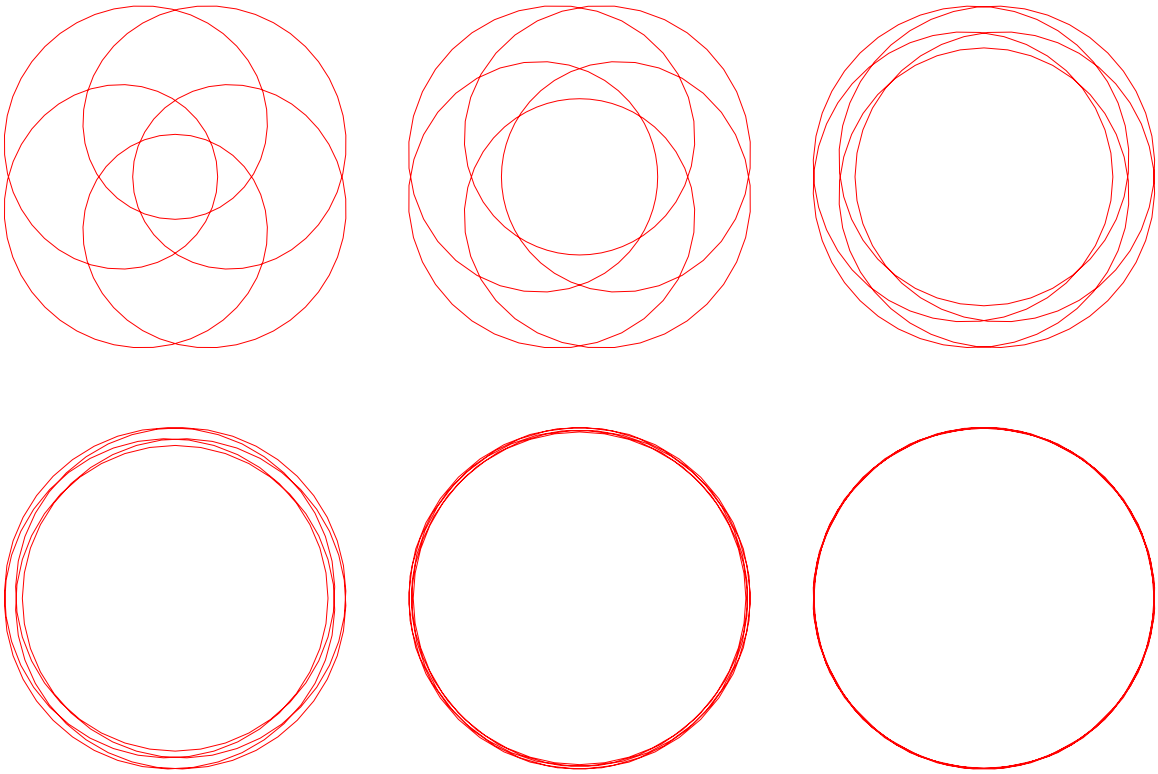

Figure 4.6: Different time steps of the evolution of a planar hypocycloid towards a fivefold covering of a circle with $\delta = 0$ under the two step time discretization of Willmore flow. The curves are scaled to diameter one. The computational parameters are $N = 200$, $\lambda = 0.025$, $\tau = \Delta X = 0.5$ and $\tilde{\tau} = (\Delta X)^2$. We show the curve at times $t = 0$, $t = 560$, $t = 2940$, $t = 4690$, $t = 7070$ and $t = 9870$.

Hypocycloid

In the next application we pick up an example already discussed by DZIUK & DECKELNICK [66], where a hypocycloid is considered as initial data. The parametrization of the initial curve is given by

$$X_0(t) = \left(-\frac{5}{2}\cos(t) + 4\ \cos(5t), -\frac{5}{2}\sin(t) + 4\ \sin(5t), \delta\ \sin(3t) \right).$$

It is well known, cf. POLDEN [141], that multiple coverings of a circle are stable stationary solutions for codimension one, i.e. for $d = 2$. This is not true for higher codimension ($d \geq 3$). Obviously, for $d = 2$, the initial curve evolves to a fivefold covering of a circle, cf. Figure 4.6. Here, the computational parameters were $\lambda = 0.025$, $N = 200$ and $\tau = (\Delta X_0) = 0.5$. The evolution is almost the same as in the example in DZIUK & DECKELNICK [66, Figure 3], also the time scale is similar. If we start with an initial curve which is slightly perturbed in vertical direction, i.e. δ was chosen 0.1, the curve begins to unfold and evolves to a single circle. This is shown in Figure 4.7. We observe similar phenomena as in DZIUK & DECKELNICK [66, Figure 6], i.e. for small time steps the evolution is almost identical to the case in two-dimension. Then, the curve starts to unfold in a sightly different way, compared to DZIUK & DECKELNICK [66, Figure 6] and converges to single circle.

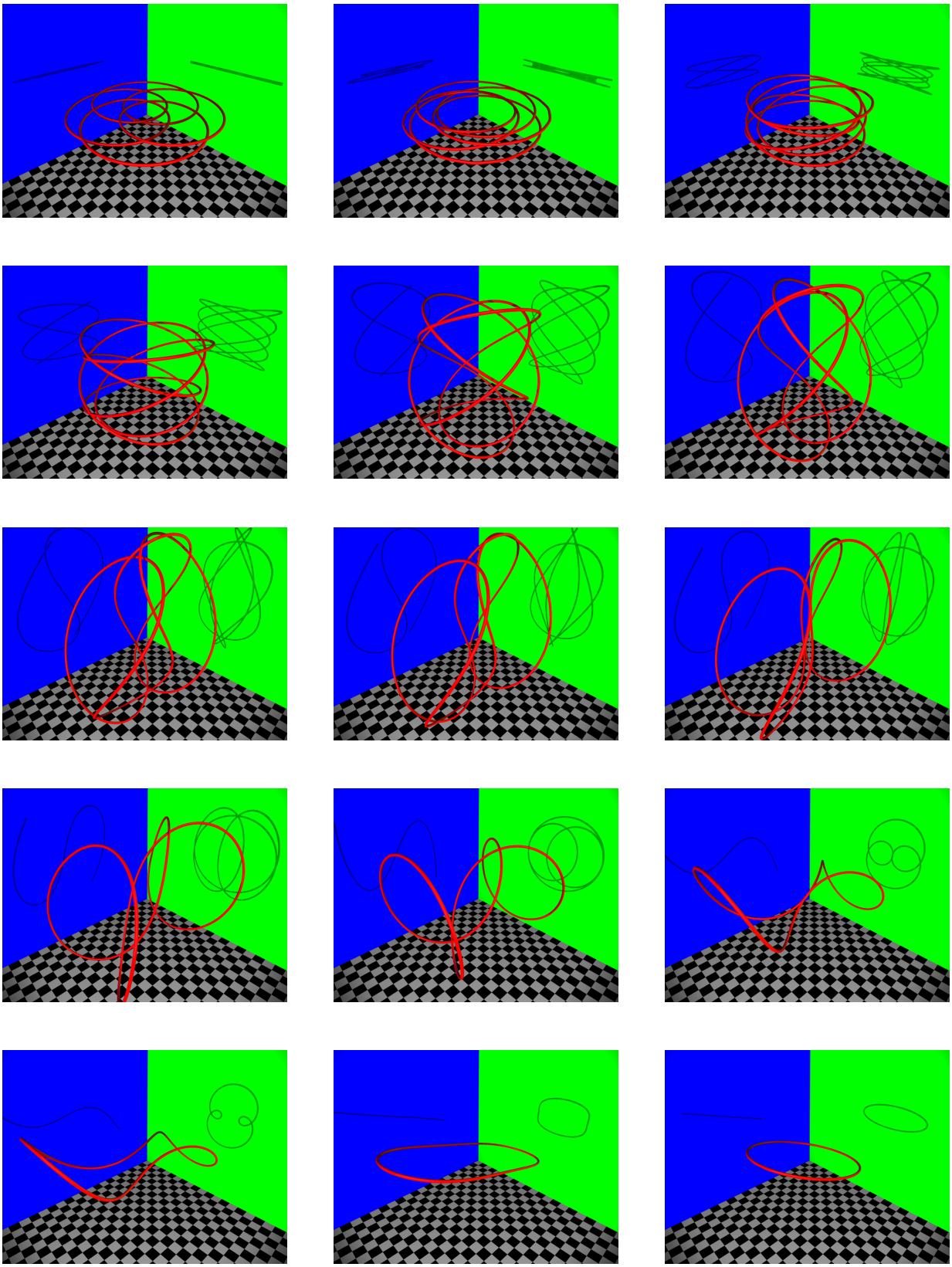

Figure 4.7: Different time steps of the evolution of a vertically perturbed hypocycloid towards a circle with $\delta = 0.1$, $\lambda = 0.025$, $N = 200$, $\tau = \Delta X = 0.5$ and $\tilde{\tau} = (\Delta X)^2 = 0.25$. We show the curve at times $t = 0.0$, $t = 1348.9$, $t = 4467.1$, $t = 5511.4$, $t = 6555.7$, $t = 6839.3$, 7123.0, $t = 7406.6$, $t = 8257.2$, $t = 8682.8$, $t = 9108.4$, $t = 9297.0$, $t = 9361.3$, $t = 9426.8$, $t = 9489.1$.

EOC-analysis for radially symmetric evolution

We study the experimental order of convergence (EOC) for successively refined curves. The number of nodes N is doubled so that the discretization parameter ΔX, the spacial grid size, is halved in every refinement step. If $\bar{X}_N^{k+1}$ is the nodal vector of the discrete solution computed by the SQP approach of the two step time discretization for a time step size which equals the grid size and the L^∞-Error $\|\bar{X}_N^{k+1} - r_0((k+1)\tau)\|_{L^\infty}$ is the maximum of the absolut value of the difference between $r_0((k+1)\tau)$ and $\|\bar{X}_N^{k+1}\|$ then the EOC is given by:

$$\mathrm{EOC}_N := \log_2 \left(\frac{\|\bar{X}_N^{k+1} - r_0((k+1)\tau)\|_{L^\infty}}{\|\bar{X}_{2N}^{k+1} - r_0((k+1)\tau)\|_{L^\infty}} \right)$$

with $k = 500$, $r_0 = 2$, $\tau = \Delta X_{1600} = 7.9 * 10^{-3}$ and $\tilde{\tau} = (\Delta X_{1600})^2 = 6.2 * 10^{-5}$. As expected we verify that $\|\bar{X}_{2N}^{k+1} - r_0((k+1)\tau)\|_{L^\infty} \leq C(\Delta X_{2N})^2$, hence the numerical error of the converged solution is in the order of the interpolation error (see Table 4.2).

N	50	100	200	400	800	1600
EOC_N		2.03	1.98	1.78	1.99	1.78

Table 4.2: EOC-analysis for radially symmetric evolution.

4.5.2 Willmore flow for surfaces

Spheres are minima of the Willmore functional with energy 8π. In our first example for two dimensional surfaces in $\mathbb{R}^3$ we show the evolution of a cubical surface into a round sphere, cf. Figures 4.10 and 4.11. In Figure 4.12 we depict the evolution of a coarse polygonal approximation of a torus towards the Clifford torus

$$\mathcal{M}_{Cliff} = \left\{ x \in \mathbb{R}^3 \middle| (1 - \sqrt{x_1^2 + x_2^2})^2 + x_3^2 = \frac{1}{2} \right\}.$$

Finally, in Figure 4.13 we compare the discrete evolution at a fixed time for different choices of the time step τ used in the computation.

Comparison of algorithms

Since spheres are stationary solutions of Willmore flow. We expect that discrete spheres rearrange the nodes and then remain stationary in the discrete algorithm. This is not the case for the full discrete semi-implicit anisotropic Willmore flow presented in Chapter 3 with isotropic elliptical integrand $\gamma(z) = |z|$. For compact closed surfaces the Willmore energy is conformally invariant [24, 169, 173]. The only conformal automorphism of the sphere $S^2 \subset \mathbb{R}^3$ are the Möbius transformations [17, 134]. In Figure 4.8 we show the grid degeneration caused by this fact if we use no grid smoothing technique. If we choose the time step of the semi-implicit algorithm of the order of the spacial grid size, the grid degenerates, too, cf. Figure 4.9.

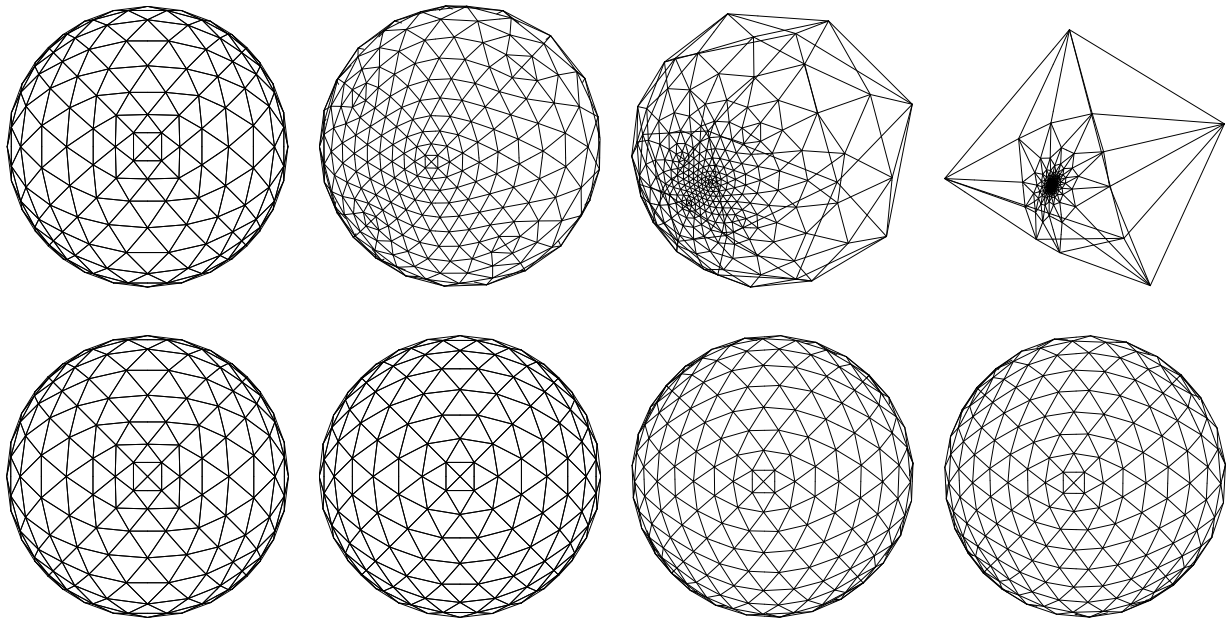

Figure 4.8: Spheres are stationary solutions of Willmore flow. We expect that discrete spheres rearrange the nodes and then remain stationary in the discrete algorithm (bottom tow for the two step time discretization). This is not the case for the semi-implicit algorithm of Chapter 3 , where a Möbius transformation leads to a grid degeneration if we use no grid smoothing technique (top row). The initial discrete sphere is shown for times $t = 0.0$, $t = 2381.9$, $t = 2442.2$, $t = 2472.4$. The sphere has 258 nodes and 512 traingles. The computational data are $\Delta X = 0.301512$, $\tau = (\Delta X)^4$ in both methods and $\tau \tilde{=} (\Delta X)^4$ for the two step time discretization of Willmore flow.

Surface denoising

One application for Willmore flow is surface denoising. For example 3d scans are often corrupted by noise. In Figure 4.15 we show the denoising of the Stanford bunny and in Figure 4.16 of the Stanford armadillo [2]. Because of the non-shrinking nature of the Willmore flow mesh smoothing via Willmore flow is favored over standard approaches based on mean curvature flow. Figure 4.14 shows the evolution of the Stanford bunny towards the sphere.

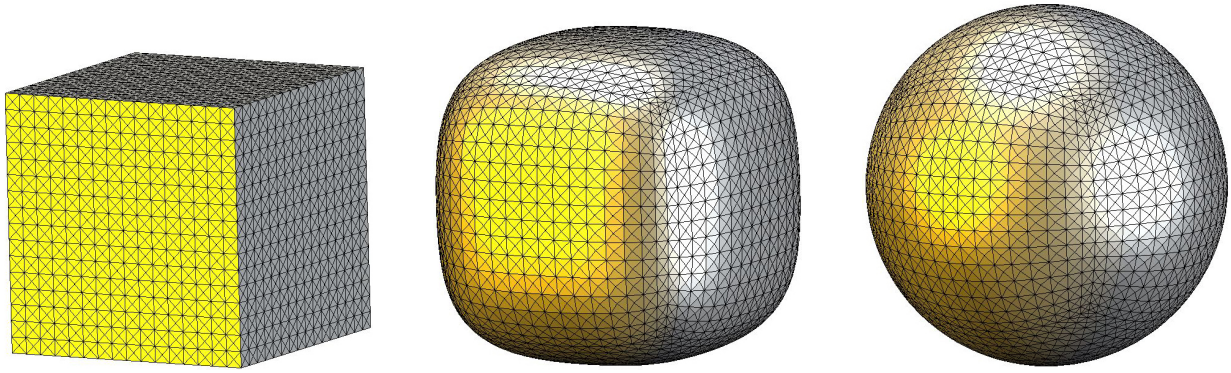

$\tau = \tilde{\tau} = 0.1 * (\Delta X)$

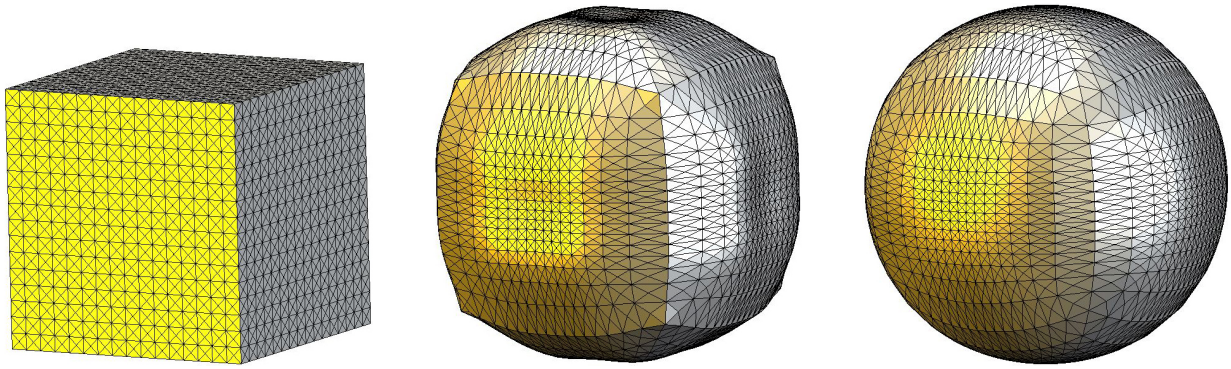

$\tau = 0.1 * (\Delta X)$

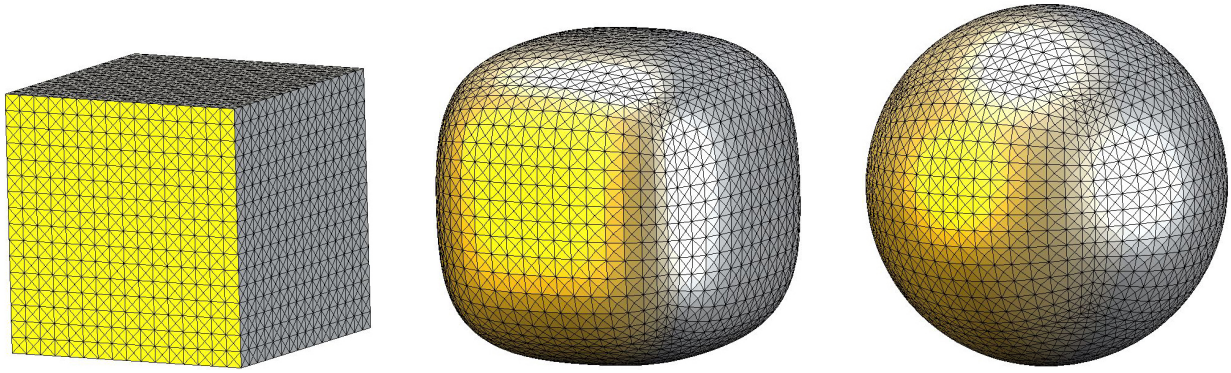

$\tau = (\Delta X)^4$

Figure 4.9: Comparison of the Willmore flow for an initial cubical surface with 6144 elements at times $t = 0.0$, $t = 0.1464$ and $t = 0.366$, where $\Delta X = 0.02589$ between the semi-implicit algorithm of Chapter 3 (second row) and the two step time discretization (first row) for $\tau = 0.1(\Delta X)$. $\tilde{t}au = \tau = 0.1(\Delta X)$ in the first row. In the third row the Willmore flow of the semi-implicit algorithm is shown for $\tau = (\Delta X)^4$.

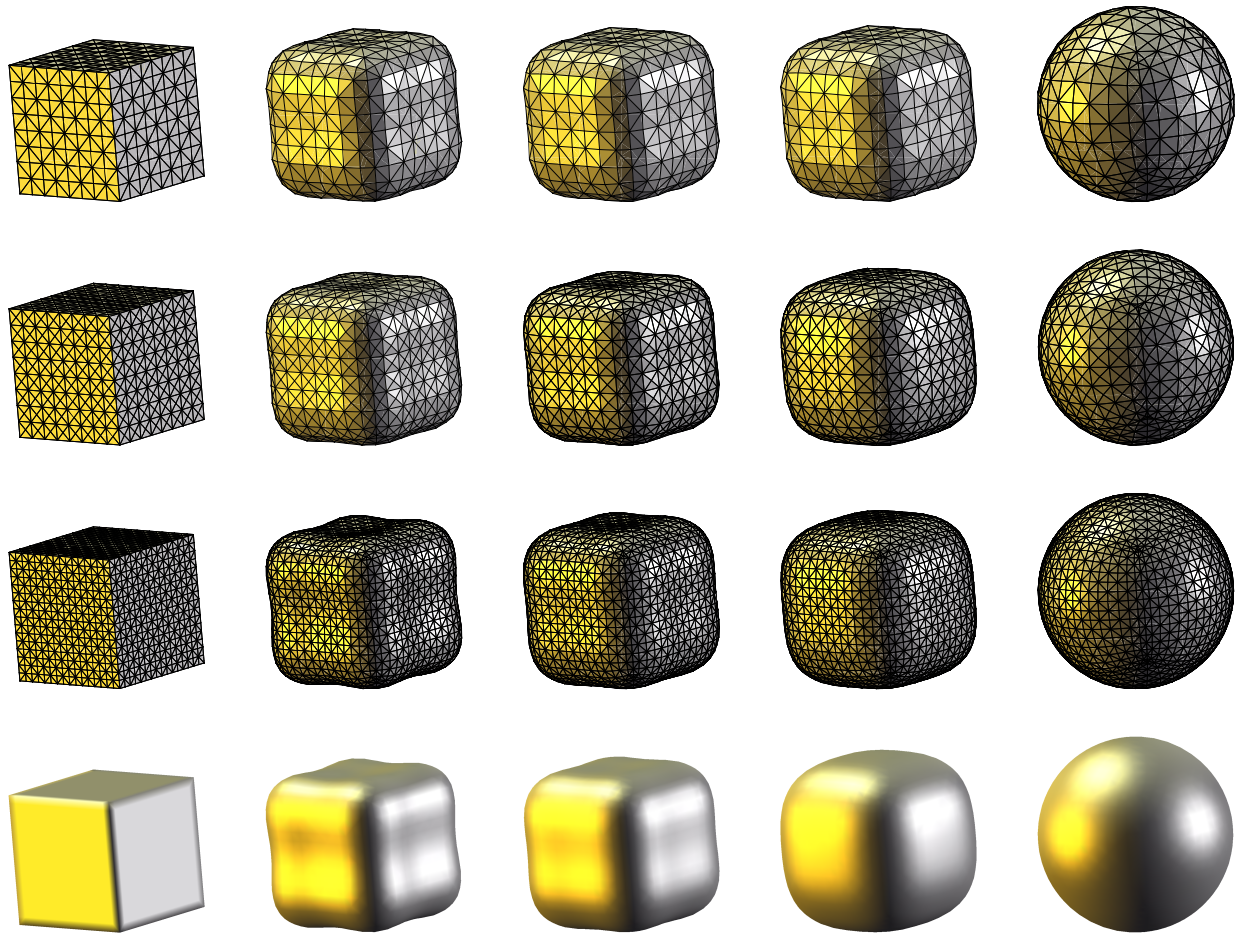

Figure 4.10: Willmore flow for an initial cubical surface with 768 (1st row), 1536 elements (2nd row) and 3072 elements (3rd, 4th rows) are shown at times $t = 0.0$, $t = 0.0366$, $t = 0.0732$, $t = 0.1464$ and $t = 0.366$. The computational data were $\Delta X = 0.07322$ and $\tau = 0.5\,(\Delta X) = 0.0366$ in the first row, $\Delta X = 0.05178$ and $\tau = 0.707\,(\Delta X) = 0.0366$ in the second row, $\Delta X = 0.0366$ and $\tau = (\Delta X) = 0.0366$ in the third row. $\tilde{\tau} = 1.34 * 10^{-3}$ for all calculations.

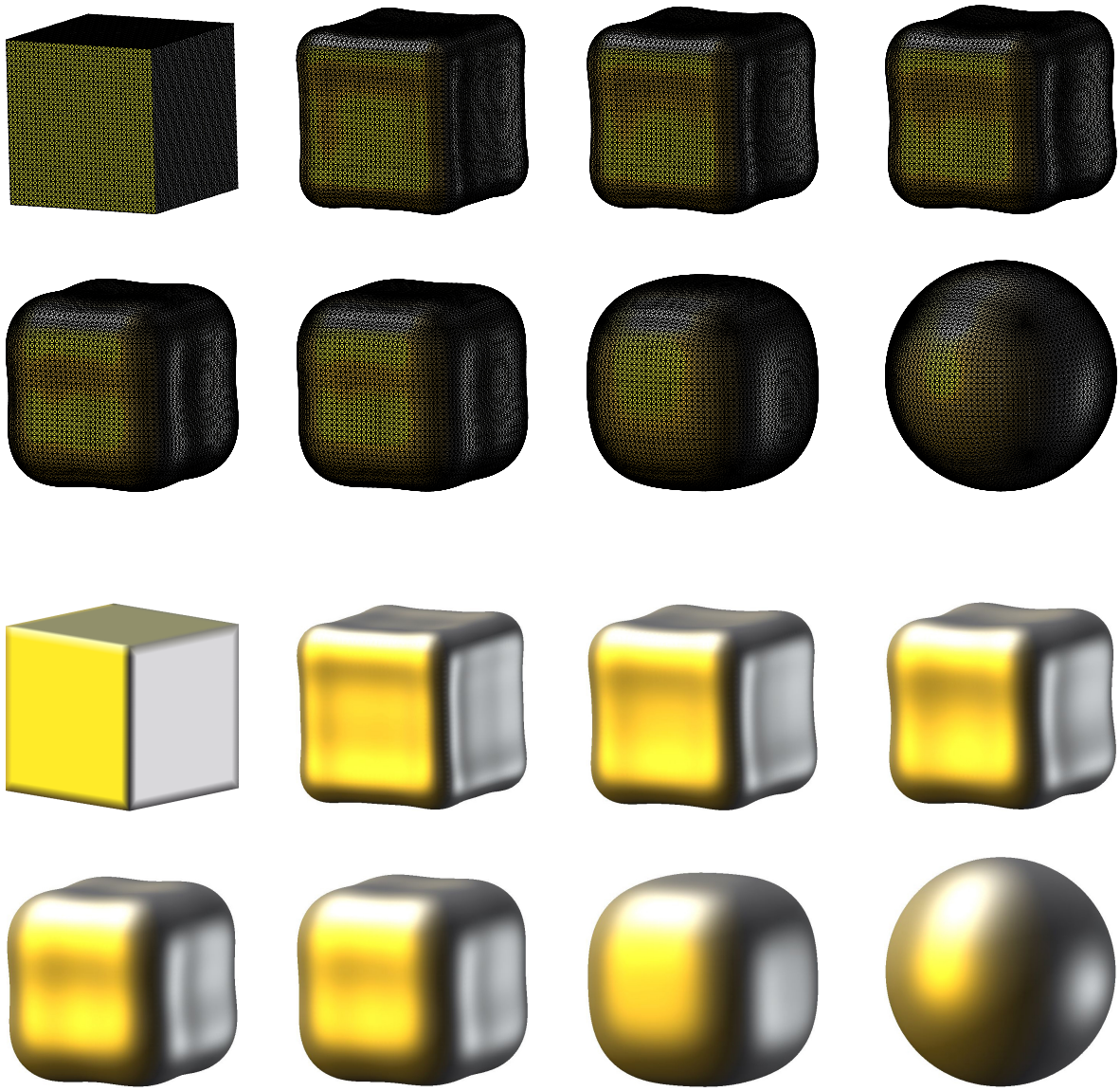

Figure 4.11: Willmore flow for an initial cubical surface with 24576 elements is shown at times $t = 0.0$, $t = 0.0046$, $t = 0.0092$, $t = 0.0137$, $t = 0.0366$, $t = 0.0732$, $t = 0.1464$ and $t = 0.366$, where $(\Delta X) = 0.01294$, $\tau = 0.36(\Delta X) = 0.0046$ and $\tilde{\tau} = 1.34 * 10^{-3}$.

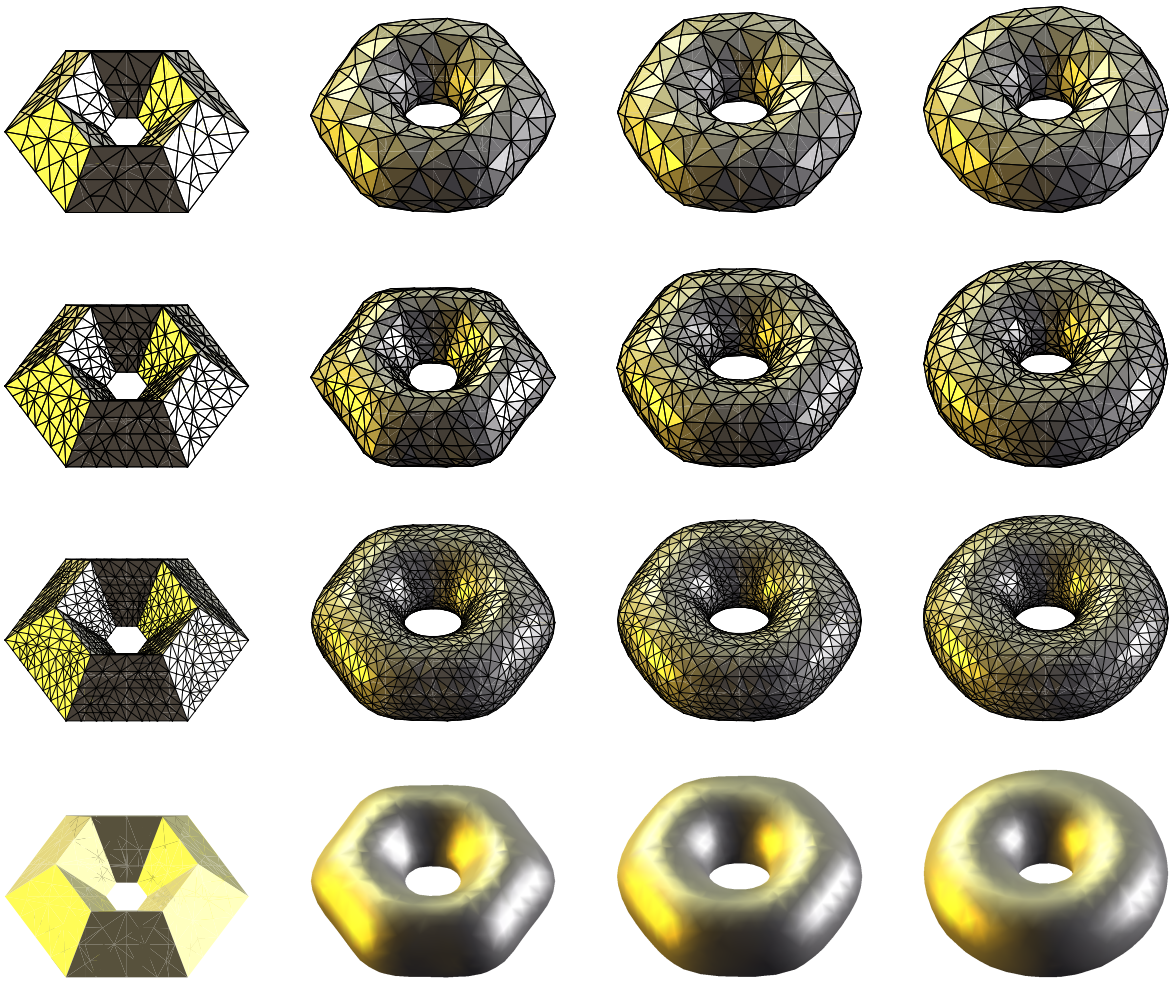

Figure 4.12: Different time steps of Willmore flow towards the Clifford torus $\mathcal{M}_{Cliff}$ for an initial macro torus with 522 (1st row), 1224 (2nd row) and 2736 elements (3rd and 4th row). We render the surfaces at times $t = 0.0$, $t = 0.09$, $t = 0.15$ and $t = 0.97$, where $\Delta X = 0.0977$, $\Delta X = 0.0745$ and $\Delta X = 0.0089$, respectively. The computational data were $\tau = 0.09 * (\Delta X)$, $\tau = 0.12 * (\Delta X)$ and $\tau = (\Delta X)$. $\tilde{\tau} = (\Delta X)^2$ for all calculations.

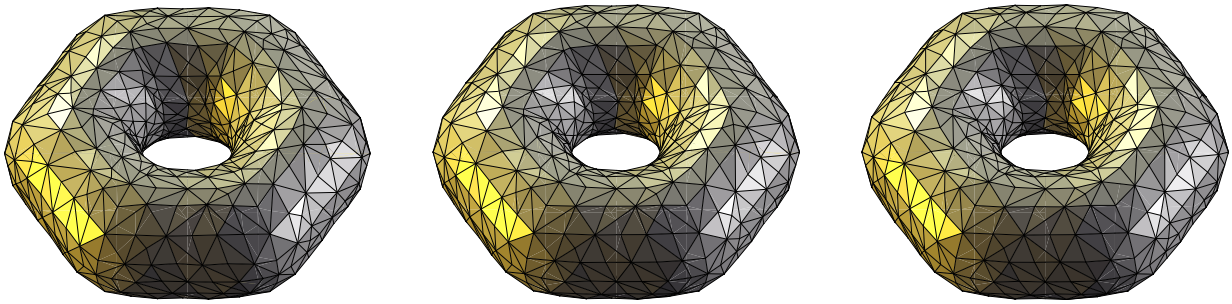

Figure 4.13: From the evolution towards the Clifford torus $\mathcal{M}_{Cliff}$, cf. Figure 4.12, discrete surfaces at time $t = 0.3735$ are shown based on a computation with time step sizes towards a sphere for an initial macro torus with 1224 elements for different time steps sizes (from left to right) $\tau = (\Delta X)^4$, $\tau = (\Delta X)^2$ and $\tau = \Delta X$, where $\Delta X = 0.0745$. $\tilde{\tau} = (\Delta X)^2$ for all calculations.

Figure 4.14: Evolution of the Stanford bunny [2] towards the sphere. The grid consists of 40648 nodes and 81292 triangles. The time step size equals the spacial grid size. $\tilde{\tau} = \tau^2$.

Figure 4.15: Denoising of the Stanford bunny [2]. The noisy initial surface and the first time step under the Willmore flow for different time steps sizes $\tau = (\Delta X)^4$, $\tau = (\Delta X)^2$ and $\tau = \Delta X$ are shown. $\tilde{\tau} = \tau^2$.

Figure 4.16: Denoising of the Stanford armadillo [2]. The grid consists of 172974 nodes and 345944 triangles. The grid size of the initial mesh varies between 10^{-7} and $\Delta X = 0.01226$. The initial object is scaled to diameter 1. The noisy initial surface is shown in the left picture of the first row. The first time step under the Willmore flow for different time steps sizes $\tau = \tilde{\tau} = 0.1 * (\Delta X)^4 = 2.26 * 10^{-9}$, $\tau = \tilde{\tau} = (\Delta X)^3 = 1.84 * 10^{-6}$ and $\tau = \tilde{\tau} = (\Delta X)^2 = 1.5 * 10^{-4}$ are shown.

Chapter 5

Surface restoration based on the two step time discrete isotropic Willmore flow

IN Chapter 3 we developed the semi-implicit scheme for the anisotropic Willmore flow with boundary condition to restore crystal-like surfaces, i.e. Wulff shapes. Extending the two step time discretization of the isotropic Willmore flow to boundary conditions, we present isotropic surface restoration in this chapter. E.g. we apply the new scheme to a real world restoration problem, where we reconstruct damaged regions of an Egea sculpture. Suppose $\mathcal{M}[x(t)] \subset \mathbb{R}^m$, $m \leq d+1$, is a bounded d-dimensional surface with parametrization $x(t)$ over itself and $n(t)$ its Gauß map. $\mathcal{M}[x^0] \subset \widetilde{\mathcal{M}}[x^0]$ is the initial surface with parameterization x^0 and Gauß map n^0. We use the notation of Chapter 3 and denote by

$$\mathcal{M}^{ext}[x^0] = \widetilde{\mathcal{M}}[x^0] \setminus \mathcal{M}[x^0]$$

the fixed surrounding surface. Since we are interest in smooth boundary condition, we have to carefully choose boundary conditions in the nested variational problem for the two step time discretization for the unknown y and the next time step surface x. To achieve C^0-continuity condition at the patch boundary, we prescribe Dirichlet boundary condition for x. It turned out that we can only predict the co-normal field of the surface x, denoted by $n^{co}[x]$, if we prescribe Neumann boundary conditions for y. Let us review the boundary value problem for the isotropic Willmore flow. In the hypersurface case ($m = d+1 = 3$) we are searching for a family $\{\mathcal{M}[x(t)]\}$, $\mathcal{M}[x(t)] = \mathcal{M}[x]$ of bounded two-dimensional surfaces that solve the classical form of the initial boundary value problem for the Willmore energy, i.e.

$$\partial_t x = \Delta_{\mathcal{M}[x]} \mathbf{h}\, n + \mathbf{h}\left(|S|_2^2 - \frac{1}{2}\mathbf{h}^2\right) n \quad \text{on } (0,T] \times \mathcal{M}[x], \tag{5.1}$$

$$x = x^0 \quad \text{on } (0,T] \times \partial\mathcal{M}[x], \tag{5.2}$$

$$n = n^0 \quad \text{on } (0,T] \times \partial\mathcal{M}[x], \tag{5.3}$$

$$\mathcal{M}(0) = \mathcal{M}^0 \tag{5.4}$$

for some $T > 0$, where $S = \nabla_{\mathcal{M}} n$ is the shape operator defined as the surface gradient of the Gauß map, cf. Definition 2.1.6. As seen in Chapter 3 we can also prescribe the outer

co-normal field n^{co} on $\partial\mathcal{M}$ instead of the normal n on the boundary. To understand that prescribing Dirichlet boundary condition for y does not lead to the desired boundary condition on the normal mapping at the patch boundary, we recall the coupled variational problem to the isotropic Willmore flow and show that its weak solutions solve the classical problem (5.1) with the above boundary conditions (5.2), (5.3) and (5.4) following the arguments of CLARENZ ET. AL [51]. Therefore, let us recall the coupled weak formulation for the isotropic Willmore flow. Introducing a second variable y, one can rewrite the Willmore flow as a system of equations for the parametrization x and the mean curvature vector y, cf. Equations (3.8), (3.9) and CLARENZ ET. AL [51, Equations (10) and (11)]. Then, we are searching for a family of bounded surfaces $\{\mathcal{M}[x(t)]\}$ with coordinate vector $x = x(t)$ and an accompanying vector field $y = y(t)$ on $\mathcal{M}[x(t)]$, such that

$$\begin{aligned}\int_{\mathcal{M}[x]} \partial_t x \cdot \vartheta \,\mathrm{d}a = &- \int_{\mathcal{M}[x]} \nabla_{\mathcal{M}[x]}\, y : \nabla_{\mathcal{M}[x]}\, \vartheta \,\mathrm{d}a + 2 \int_{\mathcal{M}[x]} n_i n_l \,\nabla_{\mathcal{M}[x]}\, y_i \cdot \nabla_{\mathcal{M}[x]}\, \vartheta_l \,\mathrm{d}a \\ &- \frac{1}{2} \int_{\mathcal{M}[x]} |y|^2 \,\nabla_{\mathcal{M}[x]}\, x : \nabla_{\mathcal{M}[x]}\, \vartheta \,\mathrm{d}a\,,\end{aligned} \tag{5.5}$$

$$\int_{\mathcal{M}[x]} y \cdot \psi \,\mathrm{d}a = - \int_{\mathcal{M}[x]} \nabla_{\mathcal{M}[x]}\, x : \nabla_{\mathcal{M}[x]}\, \psi \,\mathrm{d}a + \int_{\partial\mathcal{M}[x]} \psi \cdot n^{co} \,\mathrm{d}\sigma\,, \tag{5.6}$$

for all $\vartheta \in H^1_0(\mathcal{M}, \mathbb{R}^3)$, $\psi \in H^1(\mathcal{M}, \mathbb{R}^3)$ and for almost every $t \in (0, T]$. Furthermore, we assume $x = x^0$ on $(0, T] \times \partial\mathcal{M}$ and $x(0) = x^0$. n^{co} is an a priori given and prescribed vector field on the boundary $\partial\mathcal{M}$.

If $\mathcal{M} = \mathcal{M}[x(t)]$ is a $\mathcal{C}^2$-surface for almost every $t \in (0, T]$, then a solution of the above variational problem is a solution of the classical problem with the above boundary conditions (5.2), (5.3) and (5.4), cf. CLARENZ ET AL. [51, Lemma 3.3]. The boundary condition (5.3) is coded solely in the second Equation (5.6) of the variational problem. Applying Green's formula on surfaces (2.1.6) we get

$$\int_{\partial\mathcal{M}} \left(\partial_{n^{co}[x]} x - n^{co}\right) \psi \,\mathrm{d}\sigma = \int_{\mathcal{M}} \left(y - \Delta_{\mathcal{M}} x\right) \psi \,\mathrm{d}a$$

for all $\psi \in H^1(\mathcal{M})$. Choosing $\psi \in H^1_0(\mathcal{M})$ we obtain that $y = \Delta_{\mathcal{M}} x$ almost everywhere in $\mathcal{M}$ by the Fundamental lemma in the Calculus of Variations, cf. ALT[5, 2.21]. Hence, the right hand side vanishes and again by the Fundamental lemma with respect to $\partial\mathcal{M}$ we get

$$\partial_{n^{co}[x]} x = n^{co}.$$

Since x is the identity map on $\mathcal{M}$, it holds that

$$\partial_{n^{co}[x]} x = \nabla_{\mathcal{M}} x \, n^{co}[x] = \mathbb{I}\, n^{co}[x] = n^{co}[x]$$

for the co-normal $n^{co}[x]$ of the surface x and we get the desired boundary condition (5.3).

The boundary condition can also be achieved by changing the integration domain of the boundary integral in Equation (5.6) to the external surface $\widetilde{\mathcal{M}}[x] = \widetilde{\mathcal{M}}$ instead of $\mathcal{M}$:

$$\int_{\widetilde{\mathcal{M}}} y \cdot \psi \, \mathrm{d}a = -\int_{\widetilde{\mathcal{M}}} \nabla_{\mathcal{M}} x : \nabla_{\mathcal{M}} \psi \, \mathrm{d}a \,. \tag{5.7}$$

Applying again Green's formula on surfaces (2.1.6) we get

$$\begin{aligned}
\int_{\widetilde{\mathcal{M}}} y \cdot \psi \, \mathrm{d}a &= -\int_{\widetilde{\mathcal{M}}} \nabla_{\mathcal{M}} x : \nabla_{\mathcal{M}} \psi \, \mathrm{d}a = -\int_{\mathcal{M}} \nabla_{\mathcal{M}} x : \nabla_{\mathcal{M}} \psi \, \mathrm{d}a - \int_{\widetilde{\mathcal{M}} \setminus \mathcal{M}} \nabla_{\mathcal{M}} x : \nabla_{\mathcal{M}} \psi \, \mathrm{d}a \\
&= \int_{\mathcal{M}} \Delta_{\mathcal{M}} x \; \psi \, \mathrm{d}a - \int_{\partial \mathcal{M}} n^{co}[x] \psi \, \mathrm{d}\sigma \\
&\quad + \int_{\widetilde{\mathcal{M}} \setminus \mathcal{M}} \Delta_{\mathcal{M}} x \, \psi \, \mathrm{d}a + \int_{\partial \mathcal{M}} n^{co} \, \psi \, \mathrm{d}\sigma - \int_{\partial \widetilde{\mathcal{M}}} n^{co}[x] \, \psi \, \mathrm{d}\sigma \\
&= \int_{\widetilde{\mathcal{M}}} \Delta_{\mathcal{M}} x \; \psi \, \mathrm{d}a + \int_{\partial \mathcal{M}} (n^{co} - n^{co}[x]) \, \psi \, \mathrm{d}\sigma
\end{aligned}$$

for all $\psi \in H_0^1(\widetilde{\mathcal{M}})$. Choosing $\psi \in H_0^1(\mathcal{M})$ we obtain by the Fundamental lemma that $y = \Delta_{\mathcal{M}} x$ almost everywhere in $\mathcal{M}$. Restricting to test functions $\psi \in H_0^1(\widetilde{\mathcal{M}} \setminus \mathcal{M})$ we get again by the Fundamental lemma that $y = \Delta_{\mathcal{M}} x$ almost everywhere in $\widetilde{\mathcal{M}}$. Hence the integrals over $\widetilde{\mathcal{M}}$ vanishes and again by the Fundamental lemma with respect to $\partial \mathcal{M}$ we get the boundary condition

$$\partial_{n^{co}[x]} x = n^{co}. \tag{5.8}$$

We would like to extend the two step time discretization of the isotropic Willmore flow to boundary conditions using the same ideas as above.

5.1 Boundary value problem for the isotropic Willmore flow

Let us review the two step time discretization for the isotropic Willmore flow. If x^k is assumed to approximate $x(t_k)$ with $t_k = k\tau$ for the given time step τ, in each time step we have to solve the nested variational problem

$$\begin{aligned}
x^{k+1} &= \arg\min_x w[x^k, x, y[x]] \quad \text{with} \\
y[x] &= \arg\min_y e[x, y] \,,
\end{aligned}$$

Recall that

$$w[x^k, x, y[x]] = \int_{\mathcal{M}[x^k]} (x - x^k)^2 \, \mathrm{d}a + \frac{\tau}{\tilde{\tau}^2} \int_{\mathcal{M}[x]} (y[x] - x)^2 \, \mathrm{d}a \,,$$

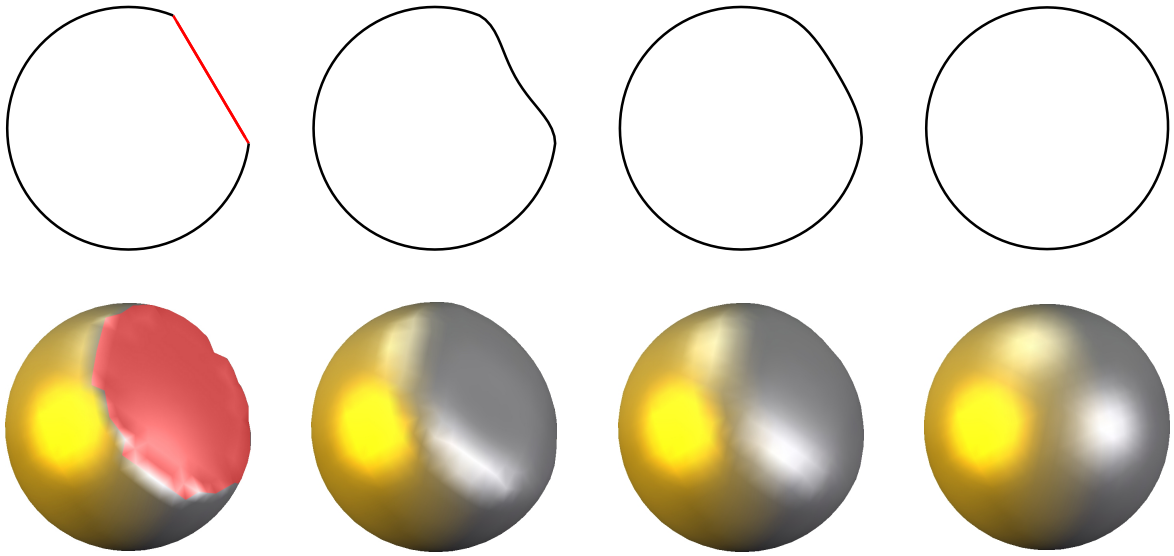

Figure 5.1: Different time steps of the Willmore flow with Dirichlet boundary conditions for X and Neumann boundary conditions for Y of an original destroyed circle with 100 vertices is shown (top row). The red line denotes inner line segments, whereas the black line corresponds to Dirichlet nodes for the curve X. The time step size was chosen of the order of the spatial grid size $\tau = \Delta X = 0.0632847$. We show the curve at times $t = 0$, $t = \tau$, $t = 2\tau$, and $t = 3\tau$. Different time steps of Willmore flow with Dirichlet boundary conditions for X and Neumann boundary conditions for Y towards a sphere for an initial spherical surface with flattened part is depicted in the bottom row. The surface $\mathcal{M}[X^0]$ is marked in red on the left. We show the surface at times $t = 0$, $t = 0.0224245$, $t = 0.44849$ and $t = 1.121225$, where $\tau = \Delta X = 0.0224245$ and $\tilde{\tau} = (\Delta X)^2$.

and

$$e[x, y] = \int_{\mathcal{M}[x]} (y - x)^2 + \tilde{\tau} |\nabla_{\mathcal{M}[x]} y|^2 \, \mathrm{d}a \,.$$

We aim for $\mathcal{C}^1$-continuity at the patch boundary, in particular

$$x^{k+1} = x^0 \qquad \text{on } \partial\mathcal{M}[x^0], \tag{5.9}$$

$$n^{k+1} = n^0 \qquad \text{on } \partial\mathcal{M}[x^0]. \tag{5.10}$$

Since no derivatives of x appear in w, we can only prescribe Dirichlet boundary conditions (5.9) for x. We have to incorporate Dirichlet or Neumann boundary conditions for y into our scheme to achieve smooth boundary conditions for x. If we choose Dirichlet boundary conditions for y on $\partial\mathcal{M}[x]$. i.e.

$$y[x] = x^0 \qquad \text{on } \partial\mathcal{M}[x^0],$$

the resulting surface for a spherical surface with a flattened part is a flattened sphere, cf. Figure 5.2:

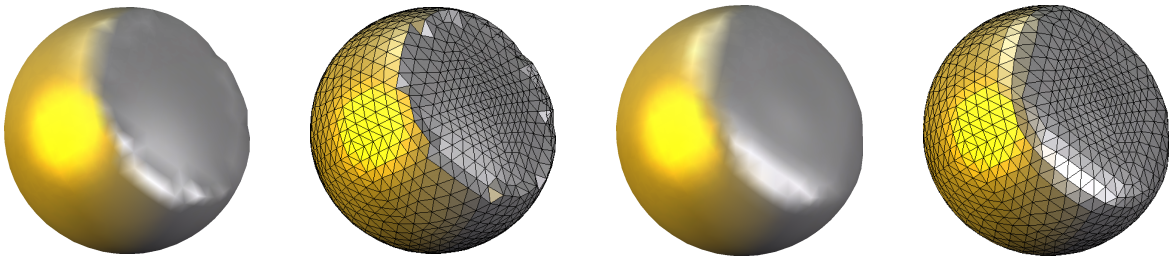

Figure 5.2: We have to carefully choose boundary conditions in the nested variational problem for the two step time discretization for the unknown y and the next timestep surface x. Choosing Dirichlet boundary condition for x and y does not lead to the desired result. The solution (third and forth picture) of an initial spherical surface with a flattened part (first and second picture) is not a sphere, but a flatted sphere.

If y is a minimizer of e, we get for test functions $\psi \in H^1(\mathcal{M}[x])$

$$\begin{aligned} 0 = \frac{1}{2\tilde{\tau}} \langle e'[x], \psi \rangle &= \int_{\mathcal{M}[x]} \frac{y-x}{\tilde{\tau}} \cdot \psi + \nabla_{\mathcal{M}[x]} y \, \nabla_{\mathcal{M}[x]} \psi \, \mathrm{d}a \\ &= \int_{\mathcal{M}[x]} \left(\frac{y-x}{\tilde{\tau}} - \Delta_{\mathcal{M}[x]} y \right) \cdot \psi \, \mathrm{d}a + \int_{\partial \mathcal{M}[x]} \partial_{n^{co}[x]} y \cdot \psi \, \mathrm{d}\sigma \,. \end{aligned}$$

Choosing $\psi \in H_0^1(\mathcal{M})$ we obtain by the Fundamental lemma that

$$\frac{y-x}{\tilde{\tau}} = \Delta_{\mathcal{M}[x]} y$$

almost everywhere in $\mathcal{M}$. Again by the Fundamental lemma with respect to $\partial \mathcal{M}$ we get

$$\partial_{n^{co}[x]} y = 0.$$

Therefore, we prescribe Neumann boundary condition for y:

Variant I: Neumann boundary conditions for y

Given a surface $\mathcal{M}[x]$ parameterized by a mapping x we ask for a mapping $y[x]$, which solves the minimization problem

$$y[x] = \arg\min_y e^{\partial}[x, y], \quad \text{with} \tag{5.11}$$

$$e^{\partial}[x, y] = \int_{\mathcal{M}[x]} (y-x)^2 + \tilde{\tau} |\nabla_{\mathcal{M}[x]} y|^2 \, \mathrm{d}a - 2\tilde{\tau} \int_{\partial \mathcal{M}[x]} n^{co} \cdot y[x] \, \mathrm{d}\sigma$$

for given x and n^{co}. If y solves the minimization problem (5.11), we have for a test function $\psi \in H^1(\mathcal{M}[x])$

$$0 = \frac{1}{2\tilde{\tau}} \left\langle (e^{\partial})'[x], \psi \right\rangle = \int\limits_{\mathcal{M}[x]} \frac{y-x}{\tilde{\tau}} \cdot \psi + \nabla_{\mathcal{M}[x]} y \, \nabla_{\mathcal{M}[x]} \psi \, \mathrm{d}a - \int\limits_{\partial \mathcal{M}[x]} n^{co} \cdot \psi \, \mathrm{d}\sigma$$
$$= \int\limits_{\mathcal{M}[x]} \left(\frac{y-x}{\tilde{\tau}} - \Delta_{\mathcal{M}[x]} y \right) \cdot \psi \, \mathrm{d}a + \int\limits_{\partial \mathcal{M}[x]} \left(\partial_{n^{co}[x]} y - n^{co} \right) \cdot \psi \, \mathrm{d}\sigma \, .$$

Choosing $\psi \in H_0^1(\mathcal{M})$ we obtain by the Fundamental lemma that

$$\frac{y-x}{\tilde{\tau}} = \Delta_{\mathcal{M}[x]} y$$

almost everywhere in $\mathcal{M}$. Again by the Fundamental lemma with respect to $\partial \mathcal{M}$ we get

$$\partial_{n^{co}[x]} y = n^{co}.$$

Since $y = x + \tilde{\tau}\delta x$ with $\delta x := \Delta_{\mathcal{M}[x]} y$ we get

$$\begin{aligned} \partial_{n^{co}[x]} y &= \nabla_{\mathcal{M}[x]} y \cdot n^{co}[x] = \nabla_{\mathcal{M}[x]} (x + \tilde{\tau}\delta x) \cdot n^{co}[x] \\ &= \nabla_{\mathcal{M}[x]} x \cdot n^{co}[x] + O(\tilde{\tau}) \\ &= n^{co}[x] + O(\tilde{\tau}), \end{aligned}$$

so that $\partial_{n^{co}[x]} y$ converges to $n^{co}[x]$ as $\tilde{\tau}$ converges to 0 and therefore $n^{co}[x]$ converges to n^{co} as $\tilde{\tau}$ converges to 0. Let us remark that we still assume $\mathcal{M}[x]$ and $\mathcal{M}[y]$ to be C^2-surfaces. Finally, we end up with the following nested variational problem for the isotropic Willmore flow with boundary condition to be solved in each time step

$$x^{k+1} = \operatorname*{arg\,min}_{\{x \,|\, x = x^0 \text{ on } \partial \mathcal{M}[x^0]\}} w[x^k, x, y[x]] \quad \text{with} \tag{5.12}$$

$$y[x] = \operatorname*{arg\,min}_{y} e^{\partial}[x, y] \, . \tag{5.13}$$

Variant II: Implicit boundary conditions – integration domain $\widetilde{\mathcal{M}}[x]$

As in the semi-implicit case we can also incorporate the co-normal implicitly to avoid its calculation. The desired boundary condition can also be achieved by changing the integration domain of the mean curvature functional $e^{\partial}[\cdot]$ to $\widetilde{\mathcal{M}}[x]$. The corresponding nested variational problem is then given by

$$x^{k+1} = \operatorname*{arg\,min}_{\{x \,|\, x = x^0 \text{ on } \partial \mathcal{M}[x^0]\}} w[x^k, x, y[x]] \tag{5.14}$$

with

$$y[x] = \operatorname*{arg\,min}_{y} \tilde{e}^{\partial}[x, y] \, , \tag{5.15}$$

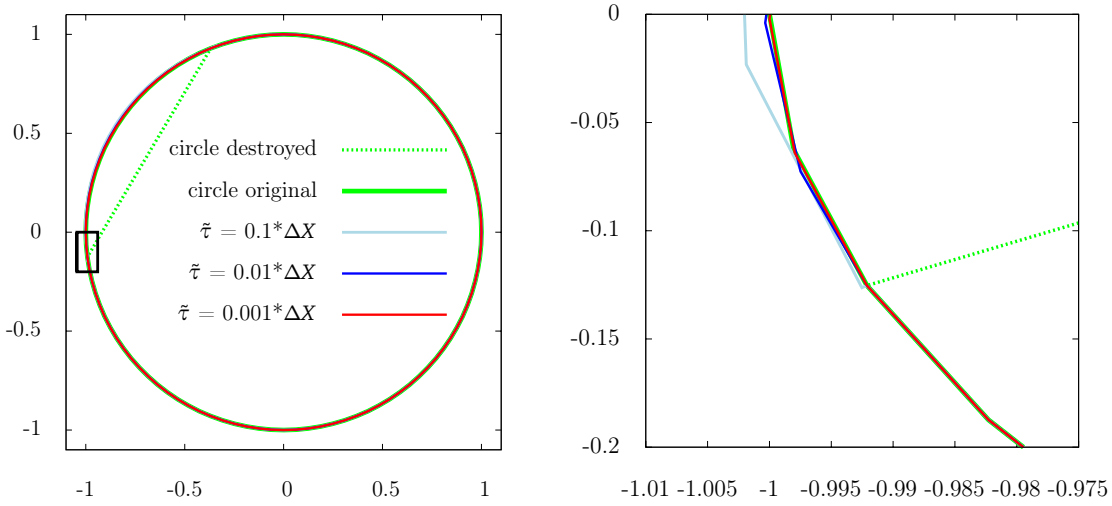

Figure 5.3: Solution of the boundary problem with Variant II for an initial destroyed circle (red line) of a circle with radius one (green line) for time step size $\tau = \Delta X = 0.0628$ and different values of the parameter $\tilde{\tau}$, $\tilde{\tau} = 0.1 * \Delta X$ (light blue line), $\tilde{\tau} = 0.01 * \Delta X$ (blue line), $\tilde{\tau} = 0.001 * \Delta X$ (dark blue line). The right picture is a clipping of the left picture. We see that $N^{co}[X]$ converges to N^{co} as $\tilde{\tau}$ converges to 0.

where

$$\tilde{e}^{\partial}[x,y] = \int_{\widetilde{\mathcal{M}}[x]} (y-x)^2 + \tilde{\tau}|\nabla_{\mathcal{M}[x]} y|^2 \,\mathrm{d}a\,.$$

For a test function $\psi \in H_0^1(\widetilde{\mathcal{M}})$ we have

$$\begin{aligned}
0 &= \frac{1}{2\tilde{\tau}} \left\langle (\tilde{e}^{\partial})'[x], \psi \right\rangle = \int_{\widetilde{\mathcal{M}}[x]} \frac{y-x}{\tilde{\tau}} \cdot \psi + \nabla_{\mathcal{M}[x]} y \, \nabla_{\mathcal{M}[x]} \psi \,\mathrm{d}a \\
&= \int_{\widetilde{\mathcal{M}}[x]} \frac{y-x}{\tilde{\tau}} \cdot \psi \,\mathrm{d}a + \int_{\mathcal{M}[x]} \nabla_{\mathcal{M}[x]} y \, \nabla_{\mathcal{M}[x]} \psi \,\mathrm{d}a + \int_{\mathcal{M}^{ext}[x]} \nabla_{\mathcal{M}[x]} y \, \nabla_{\mathcal{M}[x]} \psi \,\mathrm{d}a \\
&= \int_{\widetilde{\mathcal{M}}[x]} \frac{y-x}{\tilde{\tau}} \cdot \psi \,\mathrm{d}a - \int_{\mathcal{M}[x]} \Delta_{\mathcal{M}[x]} y \cdot \psi \,\mathrm{d}a + \int_{\partial\mathcal{M}[x]} \partial_{n^{co}[x]} y \cdot \psi \,\mathrm{d}\sigma \\
&\quad - \int_{\mathcal{M}^{ext}[x]} \Delta_{\mathcal{M}[x]} y \cdot \psi \,\mathrm{d}a + \int_{\partial\mathcal{M}^{ext}[x] \cap \partial\mathcal{M}[x]} \underbrace{\partial_{n^{co}_{ext}[x]}}_{=-n^{co}} y \cdot \psi \,\mathrm{d}\sigma \\
&= \int_{\widetilde{\mathcal{M}}[x]} \left(\frac{y-x}{\tilde{\tau}} - \Delta_{\mathcal{M}[x]} y \right) \cdot \psi \,\mathrm{d}a + \int_{\partial\mathcal{M}[x]} \left(\partial_{n^{co}[x]} y - \partial_{n^{co}} y \right) \cdot \psi \,\mathrm{d}\sigma\,,
\end{aligned}$$

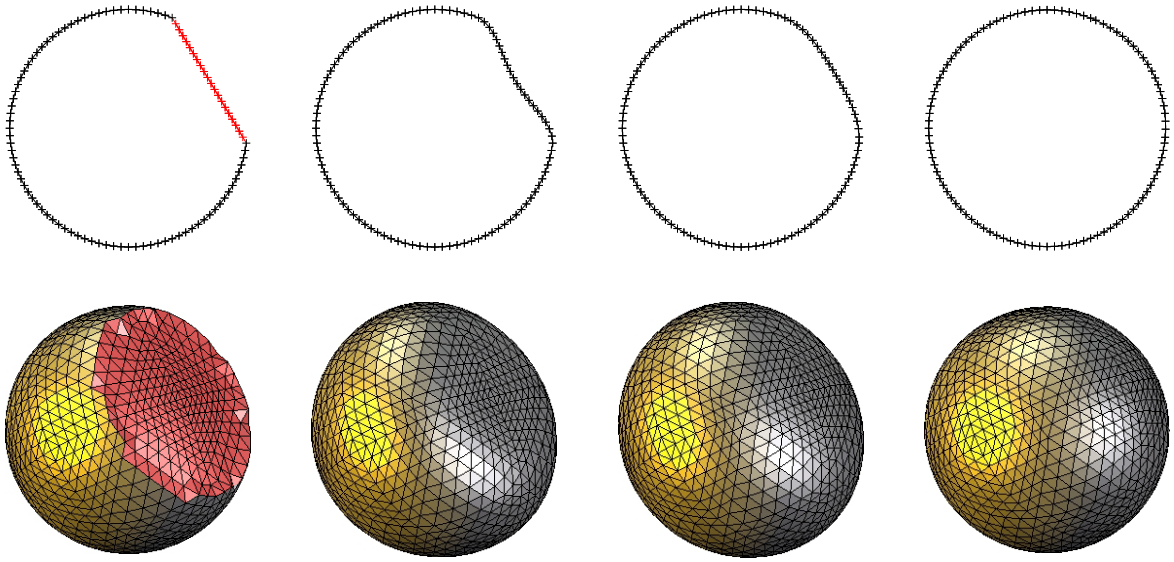

Figure 5.4: The grids of the evolution under the two step time discrete Willmore flow with Neumann boundary conditions for Y (Variant I) of the initial destroyed circle and destroyed sphere of Figure 5.1 are shown at the same times. Red crosses denote inner nodes, whereas black nodes are Dirichlet nodes for the curve X. The surface $\mathcal{M}[X^0]$ is marked in red on the left (bottom row).

where $n^{co}_{ext}[x]$ is the outer co-normal on the boundary of $\mathcal{M}^{ext}[x] = \widetilde{\mathcal{M}}[x] \setminus \mathcal{M}[x]$ and identical to the a priori given and prescribed vector field n^{co} on the boundary $\partial\mathcal{M}[x]$. With similar arguments as above we get that

$$\frac{y-x}{\tilde{\tau}} = \Delta_{\mathcal{M}[x]}\, y$$

almost everywhere in $\widetilde{\mathcal{M}} = \widetilde{\mathcal{M}}[x]$ and the boundary condition

$$\partial_{n^{co}} y = \partial_{n^{co}[x]} y$$

on $\partial\mathcal{M} = \partial\mathcal{M}[x]$. Since $y = x + \tilde{\tau}\delta x$ we get with the same arguments

$$\begin{aligned}
0 =& \partial_{n^{co}} y - \partial_{n^{co}[x]} y = \nabla_{\mathcal{M}[x]} y \cdot n^{co} - \nabla_{\mathcal{M}[x]} y \cdot n^{co}[x] \\
=& \nabla_{\mathcal{M}[x]}(x + \tilde{\tau}\delta x) \cdot n^{co} - \nabla_{\mathcal{M}[x]}(x + \tilde{\tau}\delta x) \cdot n^{co}[x] \\
=& \nabla_{\mathcal{M}[x]} x \cdot n^{co} - \nabla_{\mathcal{M}[x]} x \cdot n^{co}[x] + O(\tilde{\tau}) \\
=& (n^{co} - n^{co}[x]) + O(\tilde{\tau}),
\end{aligned}$$

so that $n^{co}[x]$ converges to n^{co} as $\tilde{\tau}$ converges to 0, where $\mathcal{M}[x]$ and $\mathcal{M}[y]$ are C^2-surfaces, cf. Figure 5.3.

5.2 Finite Element space discretization

In this Chapter we consider a Finite Element discretization. We use the notation of Chapter 3: Suppose a simplical mesh $\widetilde{\mathcal{M}}[X^0]$ with destroyed subset $\mathcal{M}[X^0] \subset \widetilde{\mathcal{M}}[X^0]$ is given. The remaining surface that is in good shape is again denoted by

$$\mathcal{M}^{ext}[X^0] := \widetilde{\mathcal{M}}[X^0] \setminus \mathcal{M}[X^0].$$

Either $\mathcal{M}[X^0]$ is a destroyed curve or surface patch or an initial blending surface closing the given surface $\mathcal{M}^{ext}[X^0]$. We seek a sequence $(\mathcal{M}[X^k])_{k=1,2\cdots}$ of discrete surfaces that solve the nested variational problem of the discrete Willmore flow corresponding to (5.12) (**Variant I**) or (5.14) (**Variant II**). $\mathcal{M}^{ext}[X]$ is as above supposed to be fixed in time. Let us review some notations and definitions. We define $\mathcal{M}^{int}[X] \subset \mathcal{M}[X] \subset \widetilde{\mathcal{M}}[X]$ with

$$\mathcal{M}[X] = \{T \in \widetilde{\mathcal{M}}[X] \;\big|\; T \cap \partial\widetilde{\mathcal{M}}[X] = \emptyset\}$$

and

$$\mathcal{M}^{int}[X] = \{T \in \mathcal{M}[X] \;\big|\; T \cap \partial\mathcal{M}[X] = \emptyset\}.$$

Elements T of the d-dimensional simplicial mesh $\mathcal{M}[X]$ are line segments of the polygonal curve for $d = 1$ and planar triangles of the triangular surface for $d = 2$. The index sets of the vertices of $\mathcal{M}^{int}[X]$, $\mathcal{M}[X]$, and $\widetilde{\mathcal{M}}[X]$ are I^{int}, I, and $\tilde{I}$, cf. Equation (2.45). Again, the set of nodes of $\mathcal{M}[X]$ is denoted by $\mathcal{N}$ and splits into interior nodes $\mathcal{N}^{int}$ and boundary nodes $\mathcal{N}^{\partial}$, i.e., $\mathcal{N} = \mathcal{N}^{int} \cup \mathcal{N}^{\partial}$ with index set $I^{\partial} = I \setminus I^{int}$.
The mapping $X = X(t) \in \mathcal{V}(\mathcal{M}[X])^3$ is considered as an element in the corresponding piecewise affine Finite Element space $\mathcal{V}(\mathcal{M}[X])^3$, cf. Equation (2.34), on the time-dependent surfaces. $\mathcal{V}^{int}(\mathcal{M}[X])$ are the linear Finite Element functions of $\mathcal{M}[X]$ with vanishing boundary values, cf. Equation (2.46).
To map between the function spaces $\mathcal{V}(\mathcal{M}[X])$ and $\mathcal{V}^{int}(\mathcal{M}[X]])$ we have defined restriction operators $R : \mathcal{V}(\mathcal{M}[X]) \to \mathcal{V}^{int}(\mathcal{M}[X])$ and extension operators $E : \mathcal{V}^{int}(\mathcal{M}[X]) \to \mathcal{V}(\mathcal{M}[X])$ that continues a function on $\partial\mathcal{M}[X]$ by 0. The corresponding block operators are denoted by $\mathbf{R} : \mathcal{V}(\mathcal{M}[X])^3 \to \mathcal{V}^{int}(\mathcal{M}[X])^3$ and $\mathbf{E} : \mathcal{V}^{int}(\mathcal{M}[X^]])^3 \to \mathcal{V}(\mathcal{M}[X])^3$.
Again, a bar on top of a discrete function indicates the corresponding nodal vector, *i.e.* $\bar{X}(t) = (\bar{X}_i(t))_{i\in I^{int}}$, where $\bar{X}_i(t) = (X_i^1(t), X_i^2(t), X_i^3(t))$ is the coordinate vector of the ith inner vertex of the mesh. As in Section 2.4 nodal vector in $\mathbb{R}^{3\sharp I}$ is then $E\bar{X} + \bar{X}^{ext}$, cf. Equation (2.49), where $\bar{X}^{ext}$ is the position vector for the boundary nodes with zero entries for all interior nodes.
Let $M[X]$ and $L[X]$ denote the mass and stiffness matrix on the discrete surface $\mathcal{M}[X]$ (cf. Equations (2.36), (2.44), (2.37)) with corresponding block matrices $\mathbf{M}[X]$ and $\mathbf{L}[X]$.

Variant I: Neumann boundary conditions for y

At first we explicitly encode the co-normal N^{co} that is a fixed function on $\mathcal{M}[X(t)]$ being piecewise constant on the edges for triangular surfaces and piecewise constant on the nodes for polygonal curves. If T is a triangle with at least one edge on $\partial\mathcal{M}[X(t)]$ than N^{co} lies in the plane of T and points outwards. If T is a line segment of a planar curve with vertices

X_1, X_2 and face $F_0 = (X_2 - X_1)$ than $N^{co} = (X_2 - X_1)$ if $X_1 \in \partial\mathcal{M}[X(t)]$ and $N^{co} = (X_1 - X_2)$ if $X_2 \in \partial\mathcal{M}[X(t)]$. We define the following vector

$$\bar{N}^{co}[X] := \left(\int_{\partial\mathcal{M}[X]} N^{co}\,\Phi_i \,\mathrm{d}\sigma \right)_{i\in I} \in \mathbb{R}^{3\sharp I}, .$$

Now, we have all the ingredients at hand to derive the fully discrete two step time discretization of Willmore flow with boundary conditions, cf. Figure 5.4. Given a discrete surface $\mathcal{M}[X^k]$ in time step k and fixed external surface $\mathcal{M}^{ext}[X]$ we define $X^{k+1} \in \mathcal{V}(\mathcal{M}[X^k])^m$ as the minimizer of the following spatially discrete, nested variational problem

$$X^{k+1} = \operatorname*{arg\,min}_{X\in\mathcal{V}(\mathcal{M}[X^k])^m} W^{\partial}[X^k, X, Y[X]]$$

with

$$Y[X] = \operatorname*{arg\,min}_{Y\in\mathcal{V}(\mathcal{M}[X])^m} E^{\partial}[X, Y],$$

where

$$\begin{aligned} E^{\partial}[X,Y] &:= \int_{\mathcal{M}[X]} (Y-X)^2 + \tilde{\tau}|\nabla_{\mathcal{M}[X]} Y|^2 \,\mathrm{d}a - 2\tilde{\tau}\int_{\partial\mathcal{M}[X]} N^{co}\cdot Y\,\mathrm{d}\sigma \qquad (5.16)\\ &= \mathbf{M}[X](\bar{Y} - \mathbf{E}\bar{X} - \bar{X}^{ext})\cdot(\bar{Y} - \mathbf{E}\bar{X} - \bar{X}^{ext})\\ &\quad + \tilde{\tau}\mathbf{L}[X]\bar{Y}\cdot\bar{Y} - 2\tilde{\tau}\bar{N}^{co}\cdot\bar{Y}, \end{aligned}$$

$$\begin{aligned} W^{\partial}[X^k, X, Y] &:= \int_{\mathcal{M}[X^k]} (X - X^k)^2\,\mathrm{d}a + \frac{\tau}{\tilde{\tau}^2}\int_{\mathcal{M}[X]} (Y-X)^2\,\mathrm{d}a \qquad (5.17)\\ &= \mathbf{RM}[X^k](\bar{X} - \bar{X}^k)\cdot(\bar{X} - \bar{X}^k)\\ &\quad + \frac{\tau}{\tilde{\tau}^2}\mathbf{M}[X](\bar{Y} - \mathbf{E}\bar{X} - \bar{X}^{ext})\cdot(\bar{Y} - \mathbf{E}\bar{X} - \bar{X}^{ext}) \end{aligned}$$

are the straightforward spatially discrete counterpart of the functionals $e^{\partial}[x,y]$ and $w[x^k,x,y]$, respectively. $Y[X]$ requires to solve

$$\begin{aligned} 0 &= \partial_Y E^{\partial}[X,Y](\Theta) = \partial_\epsilon\big|_{\epsilon=0} E^{\partial}[X, Y+\epsilon\,\Theta]\\ &= 2\int_{\mathcal{M}[X]} (Y-X)\cdot\Theta + \tilde{\tau}\nabla_{\mathcal{M}[X]} Y : \nabla_{\mathcal{M}[X]}\Theta\,\mathrm{d}a - 2\tilde{\tau}\int_{\partial\mathcal{M}[X]} N^{co}\cdot\Theta\,\mathrm{d}\sigma \end{aligned}$$

for all test functions $\Theta \in \mathcal{V}(\mathcal{M}[X])^m$. Therefore, the nodal vector $\bar{Y}[X]$ solves the linear system of equation

$$(\mathbf{M}[X] + \tilde{\tau}\mathbf{L}[X])\,\bar{Y}[X] = \mathbf{M}[X]\,(\mathbf{E}\bar{X} - \bar{X}^{ext}) + \tilde{\tau}\bar{N}^{co}.$$

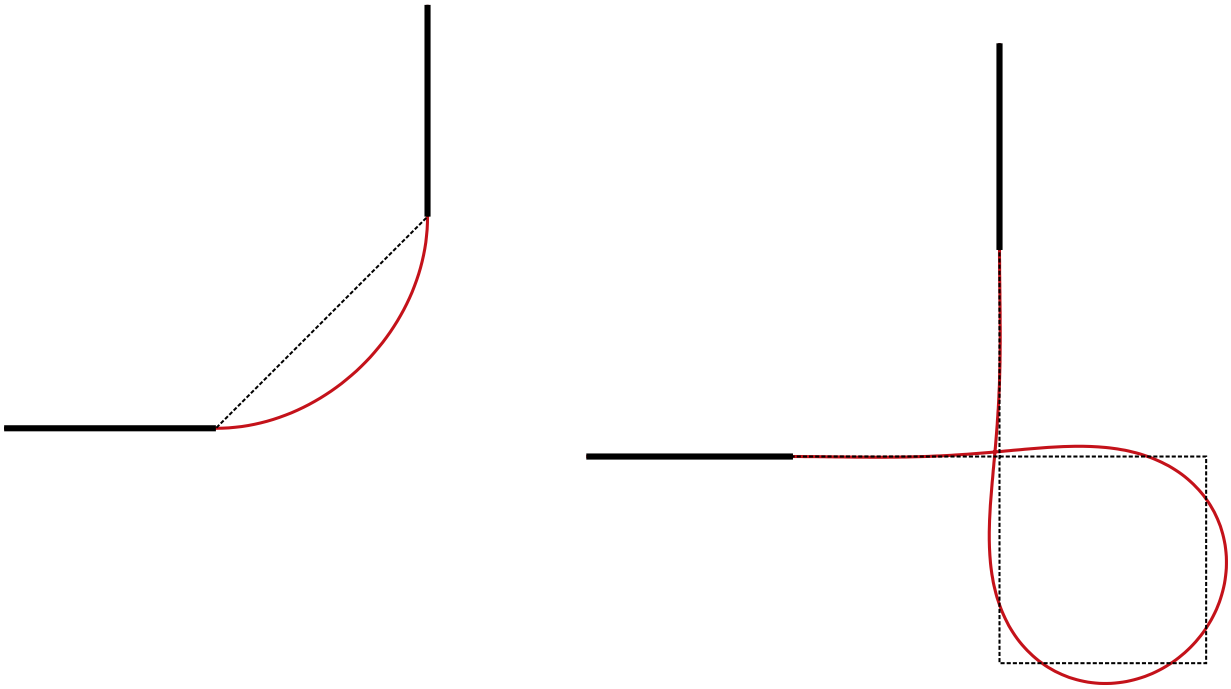

Figure 5.5: Several solutions of the blending problem for 50 and 215 inner nodes, respectively. The time step size was chosen of the order of the spatial grid size $\tau = \Delta X = 0.01386$. We show the curve at time $t = 0.02772$ (red line left picture), and $t = 0.04158$ (red line right picture). $\tilde{\tau} = 0.001 * \Delta X = 1.386 * 10^{-5}$. The solution on the right hand side is stable, whereas the red curve is still evolving and expanding, cf. also Figure 5.6. This can be avoided by adding the length of the curve multiplied by a constant to the Willmore energy, cf. Equation (5.20).

Variant II: Implicit boundary conditions – integration domain $\widetilde{\mathcal{M}}[x]$

Let $\widetilde{\mathbf{M}}$ and $\widetilde{\mathbf{L}}$ denote the mass and stiffness matrices corresponding to the integration domain $\widetilde{\mathcal{M}}[X]$ instead of $\mathcal{M}[X]$. Then we get the variational problem for the second variant: Given a discrete surface $\mathcal{M}[X^k]$ in time step k and fixed external surface $\mathcal{M}^{ext}[X]$ we define $X^{k+1} \in \mathcal{V}(\mathcal{M}[X^k])^m$ as the minimizer of the following spatially discrete, nested variational problem

$$X^{k+1} = \underset{X \in \mathcal{V}(\mathcal{M}[X^k])^m}{\arg\min} \; W^{\partial}[X^k, X, Y[X]]$$

with

$$Y[X] = \underset{Y \in \mathcal{V}(\mathcal{M}[X])^m}{\arg\min} \; \widetilde{E}^{\partial}[X, Y],$$

where

$$\begin{aligned}\widetilde{E}^{\partial}[X,Y] &:= \int_{\widetilde{\mathcal{M}}[X]} (Y-X)^2 + \tilde{\tau}|\nabla_{\mathcal{M}[X]} Y|^2 \,\mathrm{d}a \\ &= \widetilde{\mathbf{M}}[X](\bar{Y} - \mathbf{E}\bar{X} - \bar{X}^{ext})\cdot(\bar{Y} - \mathbf{E}\bar{X} - \bar{X}^{ext}) + \tilde{\tau}\widetilde{\mathbf{L}}[X]\bar{Y}\cdot\bar{Y}\end{aligned}$$

is the straightforward spatially discrete counterpart of the functional $\tilde{e}^{\partial}[x,y]$. $Y[X]$ requires to solve

$$\begin{aligned}0 = \partial_Y \widetilde{E}^{\partial}[X,Y](\Theta) &= \partial_\epsilon\big|_{\epsilon=0} \widetilde{E}^{\partial}[X, Y+\epsilon\,\Theta] \\ &= 2\int_{\widetilde{\mathcal{M}}[X]} (Y-X)\cdot\Theta + \tilde{\tau}\nabla_{\mathcal{M}[X]} Y : \nabla_{\mathcal{M}[X]}\Theta \,\mathrm{d}a\end{aligned}$$

for all test functions $\Theta \in \mathcal{V}(\mathcal{M}[X])^m$. Therefore, the nodal vector $\bar{Y}[X]$ solves the linear system of equation

$$\left(\widetilde{\mathbf{M}}[X] + \tilde{\tau}\widetilde{\mathbf{L}}[X]\right)\bar{Y}[X] = \widetilde{\mathbf{M}}[X]\,(\mathbf{E}\bar{X} - \bar{X}^{ext}).$$

5.3 Numerical solution of the optimization problem

We proceed as in the case without boundary condition and take into account the same duality technique to effectively compute the gradient and Hessian of the energy functional

$$\widehat{W}^{\partial}[X] := W^{\partial}[X^k, X, Y[X]]$$

and $\widetilde{W}^{\partial}[X^k, X, Y[X]]$ (Variant II), respectively. To avoid a direct computation of $\partial_X Y[X](\Theta)$ we rewrite the variation of $\widehat{W}^{\partial}$ with respect to X in a direction $\Theta \in \mathcal{V}(\mathcal{M}[X^k])^m$ as

$$\partial_X \widehat{W}[X](\Theta) = \partial_X W^{\partial}[X^k, X, Y[X]](\Theta) - \partial_X \partial_Y E^{\partial}[X,Y](P,\Theta), \tag{5.18}$$

where $P \in \mathcal{V}(\mathcal{M}[X^k])^m$ is the solution of the dual problem

$$\partial_Y^2 E^{\partial}[X, Y[X]](P,\Upsilon) = \partial_Y W^{\partial}[X^k, X, Y[X]](\Upsilon) \tag{5.19}$$

for all test functions $\Upsilon \in \mathcal{V}(\mathcal{M}[X^k])^m$. For Variant I P requires to solve the linear system of equations

$$(\mathbf{M}[X] + \tilde{\tau}\mathbf{L}[X])\,\bar{P} = \frac{\tau}{\tilde{\tau}^2}\mathbf{M}[X](\bar{Y} - \mathbf{E}\bar{X} - \bar{X}^{ext}),$$

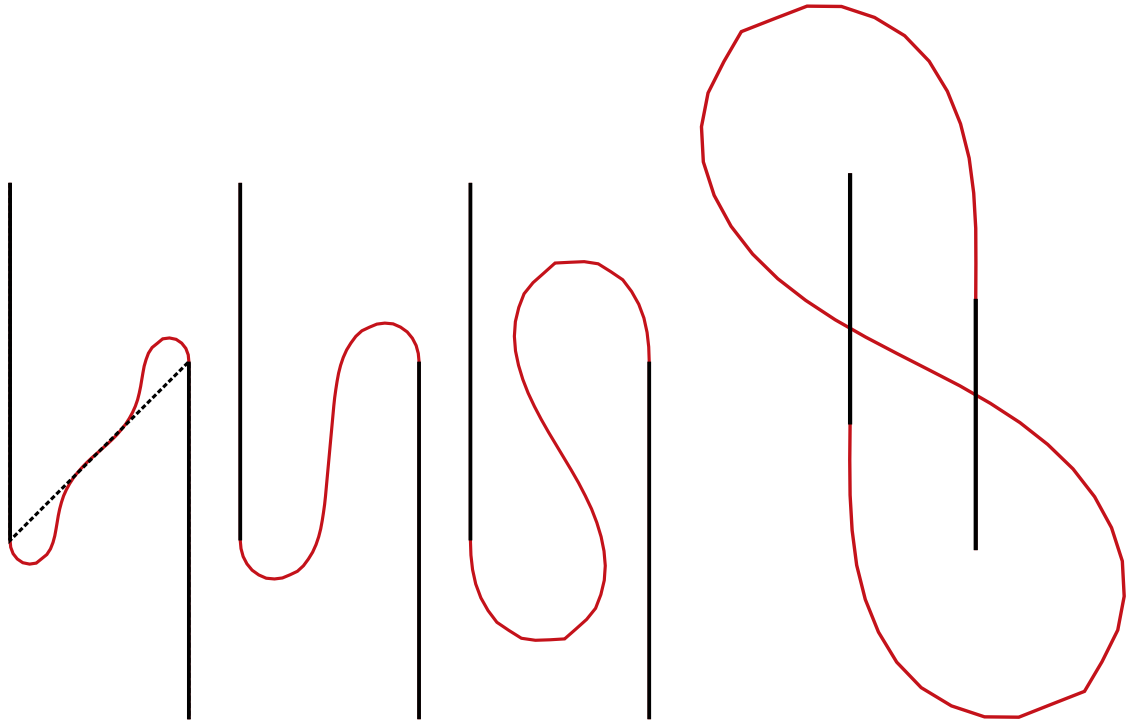

Figure 5.6: Different time steps of the Willmore flow for a blending problem with 50 inner nodes. The evolution expands for increasing time. The last curve was scaled by 0.3 so that it fits into the picture. Modifying the Willmore functional by adding the constant λ times length would prevent the expanding (cf. Figure 5.7). We show the curve at times $t = 0.078$, $t = 0.098$, $t = 0.118$, and $t = 0.392$. The time step size was chosen of the order of the spatial grid size $\tau = \Delta X = 0.0196$. $\tilde{\tau} = 0.001 * (\Delta X) = 1.96 * 10^{-5}$.

and the terms on the right hand side of (5.18) are to be evaluated as follows

$$\begin{aligned}\left(\partial_X W^{\partial}\right)[X^k, X, Y](\Theta) &= 2\,\mathbf{RM}[X^k](\bar{X} - \bar{X}^k)\cdot\bar{\Theta} + 2\frac{\tau}{\tilde{\tau}^2}\mathbf{M}[X](\mathbf{E}\bar{X} + \bar{X}^{ext} - \bar{Y})\cdot\mathbf{E}\bar{\Theta} \\ &\quad + \frac{\tau}{\tilde{\tau}^2}(\partial_X\mathbf{M}[X](\Theta))(\bar{Y} - \mathbf{E}\bar{X} - \bar{X}^{ext})\cdot(\bar{Y} - \mathbf{E}\bar{X} - \bar{X}^{ext}),\end{aligned}$$

$$\begin{aligned}\partial_X\partial_Y E^{\partial}[X, Y](P, \Theta) &= \partial_X\left(2\mathbf{M}[X](\bar{Y} - \mathbf{E}\bar{X} - \bar{X}^{ext})\cdot\bar{P}\right. \\ &\qquad \left. + 2\tilde{\tau}\mathbf{L}[X]\bar{Y}\cdot\bar{P} - 2\tilde{\tau}\bar{N}^{co}\right)(\Theta) \\ &= 2(\partial_X\mathbf{M}[X](\Theta))(\bar{Y} - \mathbf{E}\bar{X} - \bar{X}^{ext})\cdot\bar{P} - 2\mathbf{M}[X]\mathbf{E}\bar{\Theta}\cdot\bar{P} \\ &\quad + 2\tilde{\tau}(\partial_X\mathbf{L}[X](\Theta))\bar{Y}\cdot\bar{P}\,.\end{aligned}$$

For Variant II P solves

$$\left(\widetilde{\mathbf{M}}[X] + \tilde{\tau}\widetilde{\mathbf{L}}[X]\right)\bar{P} = \frac{\tau}{\tilde{\tau}^2}\mathbf{M}[X](\bar{Y} - \mathbf{E}\bar{X} - \bar{X}^{ext}).$$

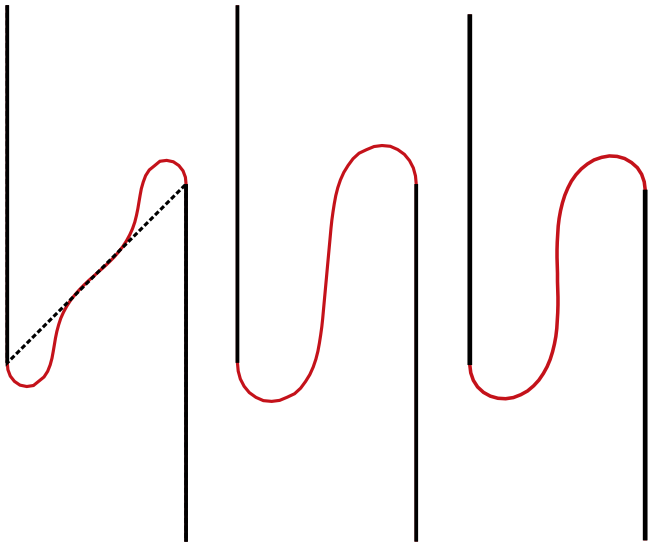

Figure 5.7: Different time steps of the Willmore flow for the blending problem of Figure 5.6. The evolution does not expand for increasing time, because we modified the Willmore functional by adding the constant λ times length of the curve, cf. Equation 5.20. λ was chosen 1.0. We show the curve at times $t = 0.078$, $t = 0.098$, and $t = 0.392$. The time step size was chosen of the order of the spatial grid size $\tau = \Delta X = 0.0196$. $\tilde{\tau} = 0.001 * \Delta X = 1.96 * 10^{-5}$.

We have

$$\begin{aligned}\partial_X \partial_Y \widetilde{E}^{\partial}[X,Y](P,\Theta) &= \partial_X \left(2\widetilde{\mathbf{M}}[X](\bar{Y} - \mathbf{E}\bar{X} - \bar{X}^{ext}) \cdot \bar{P} + 2\tilde{\tau}\widetilde{\mathbf{L}}[X]\bar{Y} \cdot \bar{P}\right)(\Theta) \\ &= 2(\partial_X \widetilde{\mathbf{M}}[X](\Theta))(\bar{Y} - \mathbf{E}\bar{X} - \bar{X}^{ext}) \cdot \bar{P} - 2\widetilde{\mathbf{M}}[X]\mathbf{E}\bar{\Theta} \cdot \bar{P} \\ &\quad + 2\tilde{\tau}(\partial_X \widetilde{\mathbf{L}}[X](\Theta))\bar{Y} \cdot \bar{P}\,.\end{aligned}$$

Finally, we obtain the descent direction in $\mathbb{R}^{m\sharp I}$ of the energy $\widehat{W}^{\partial}$ at a given simplicial mesh $\mathcal{M}[X]$ described by the nodal vector $\bar{X}$

$$\overline{\operatorname{grad}_X \widehat{W}^{\partial}[X]} = \left(\partial_X \widehat{W}^{\partial}[X](\Phi_r e_s)\right)_{r \in I^{int}, s=1,\cdots,m}\,,$$

where e_s denotes the sth coordinate direction in $\mathbb{R}^m$. We can solve the two step time discretization for the isotropic Willmore flow with boundary conditions with a gradient descent method (cf. Algorithm 4.1). The Hessian of $\widehat{W}^{\partial}[X]$ can be computed analogously. We have also implemented Algorithm 4.3 for the boundary case.

5.4 Numerical results

We have applied the developed numerical algorithm to the evolution of curves in $\mathbb{R}^2$ and of two dimensional surfaces in $\mathbb{R}^3$. Various numerical examples underline the stability of the new scheme, which enables time steps of the order of the spatial grid size.

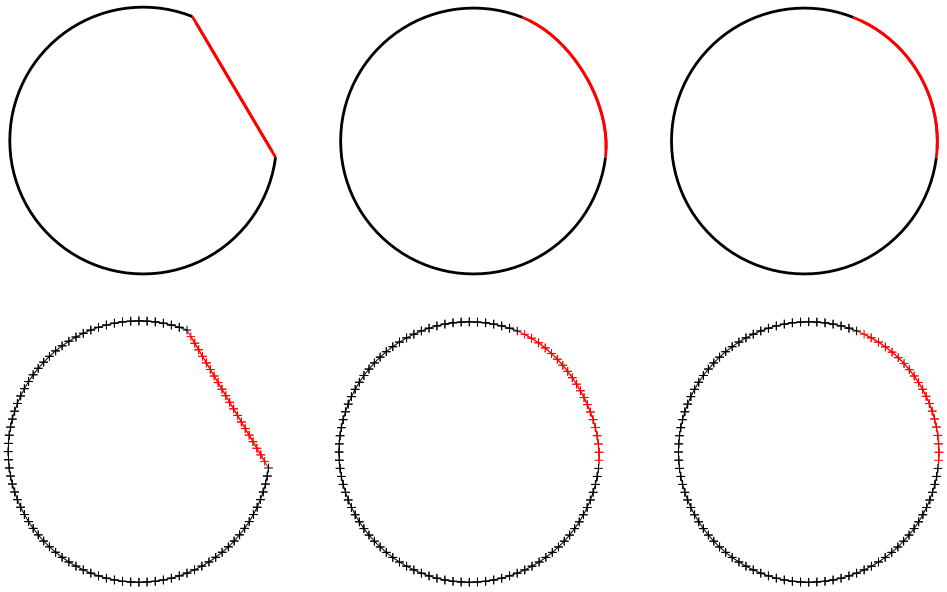

Figure 5.8: Different time steps of the Willmore flow of an original destroyed circle with 100 vertices is shown (top row). The corresponding grid is shown on the bottom row. Red crosses denote inner nodes, whereas black nodes are Dirichlet nodes for X. The time step size was chosen of the order of the spatial grid size $\tau = \Delta X = 0.0632847$. We show the curve at times $t = 0$, $t = \tau$, and $t = 2\tau$.

Elastic flow for curves with boundary conditions

As in Section 4.5.1 in Chapter 4 we penalize length in view of the scaling properties of the bending energy by adding $\lambda\, a[x]$ to the Willmore energy, where Lagrangian multiplier λ is a fixed constant and $a[x]$ denotes the length of the curve, cf. Figures 5.6 and 5.7. Therefore, in each time step, we have to solve the modified nested variational problem of the isotropic Willmore flow with boundary condition for polygonal curves

$$x^{k+1} = \operatorname*{arg\,min}_{\{x \,|\, x = x^0 \text{ on } \partial\mathcal{M}[x^0]\}} w[x^k, x, y[x]] + a[x] \quad \text{with} \tag{5.20}$$

$$y[x] = \operatorname*{arg\,min}_{y} e^{\partial}[x, y]\,,$$

cf. Equations (5.12) and (5.13). Let $\mathcal{M}[X]$ be a discrete curve in $\mathbb{R}^2$, i.e. each element T_i, $i \in I$, of a polygonal curve is a line segment with nodes X_{i-1} and X_i. $X_0 \neq X_{\sharp I}$ is possible. The index set of the inner nodes is I^{int} as above. The discrete length functional is given by

$$A[X] = \sum_{i \in I} Q_i,$$

where $Q_i = |X_i - X_{i-1}|$ is the length of the ith line segment. Then, in the modified discrete, nested variational problem, we have to solve

$$X^{k+1} = \operatorname*{arg\,min}_{X \in \mathcal{V}(\mathcal{M}[X^k])^2} W^{\partial}[X^k, X, Y[X]] + A[X] \quad \text{with} \tag{5.21}$$

$$Y[X] = \operatorname*{arg\,min}_{Y \in \mathcal{V}(\mathcal{M}[X])^2} E^{\partial}[X, Y]$$

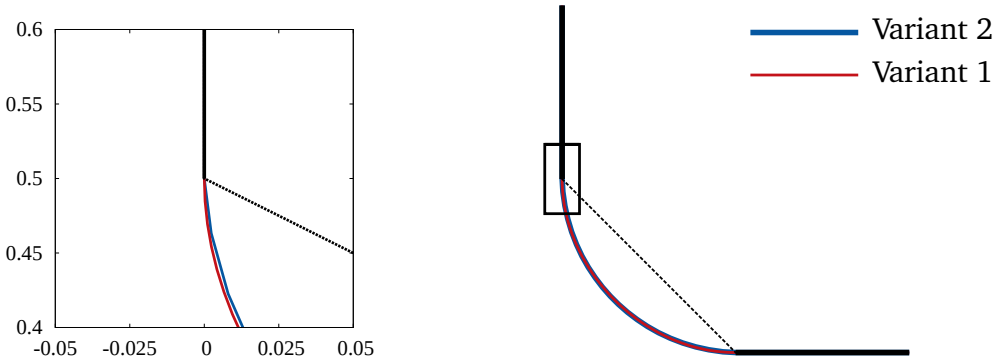

Figure 5.9: Comparison of the two variants. In Variant I, the co-normal N^{co} is explicitly encoded as an a priori given and prescribed vector field on the boundary $\partial\mathcal{M}[X^0]$ as Neumann data for Y. Replacing the integration domain by an external surface $\widetilde{\mathcal{M}}[X^0]$ without incorporating the co-normal N^{co} explicitly leads to Variant II. Both variants produce very similar results. The computational data were $\tau = \Delta X = 0.01386$ and $\tilde{\tau} = 0.001 * \Delta X = 1.386 * 10^{-5}$. We show the curve at time $t = 0.02772$, cf. Figure 5.5.

in each time step. W^{∂} and E^{∂} are given as in Equations (5.16) and (5.17). Since the gradient vector in $\mathbb{R}^{m\sharp I}$ of the discrete length functional is

$$\overline{\text{grad}_X A[X]} = L[X]\bar{X}$$

we have to add $L[X]\bar{X}$ to the descent direction in the corresponding algorithm.

As a first example for the resulting flow we consider the evolution of a destroyed circle towards a circle under the elastic flow (cf. the first rows in Figure 5.1 and 5.4). The computational parameters are $\Delta X = 0.0632847$, $\tau = h^4$ and $\lambda = 0.0$. If we choose $\tau = \Delta X$ we just need three time steps to restore the circle and the polygonal vertices stay well-distributed on the evolving segment of the curve. Therefore, solutions of the above variational problem do not exist for some geometric configurations if $\lambda = 0.0$. Another example is Figure 5.5 where two given curve segments have to be blended. The Willmore energy for a circular segment with an opening angle α and radius r is given by $\frac{\alpha}{r}$. Thus, for two given curve segments which have to be blended we can continue these segments by straight line segments and connect them by such a circular arc (cf. left configuration of Figure 5.5). As the length of the straight line segments tends to infinity the Willmore energy of the whole blending construction tends to zero (cf. right configuration of Figure 5.5). A similar construction is possible for half planes of codimension one, whose boundaries are parallel.
We also compared the two variants given in Section 5.1 (cf. Figure 5.9). The red curve shows the evolution results for boundary conditions explicitly encoded in the considered spaces with Neumann conditions (variant I). The blue curve shows the corresponding solution using variant II without incorporating the co-normal explicitly. From an application oriented point of view, the quality of the results is identical. They differ slightly in the corresponding parameterization. In general one will prefer variant II because it is easier to implement. Nevertheless, especially w.r.t. surface modeling it is important to have both methods at hand.

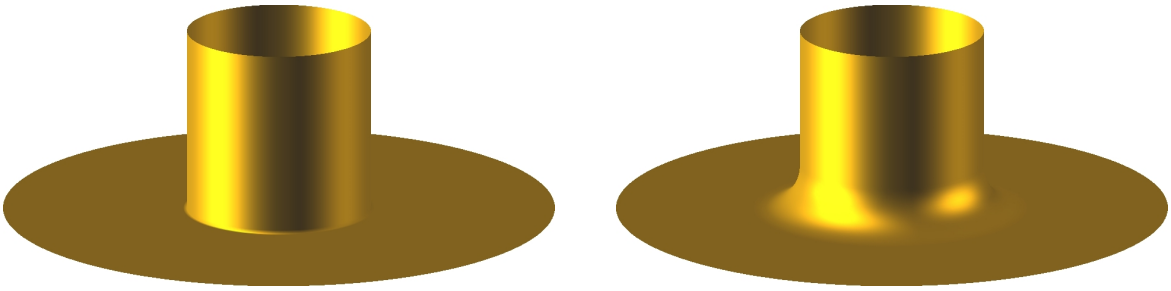

Figure 5.10: Solution of the blending problem of a cylinder and a disk with a circle shaped hole. The computational data are $\tau = \Delta X = 0.14$ and $\tilde{\tau} = (\Delta X)^4$. We show the surface at time steps $k = 0$ and 2.

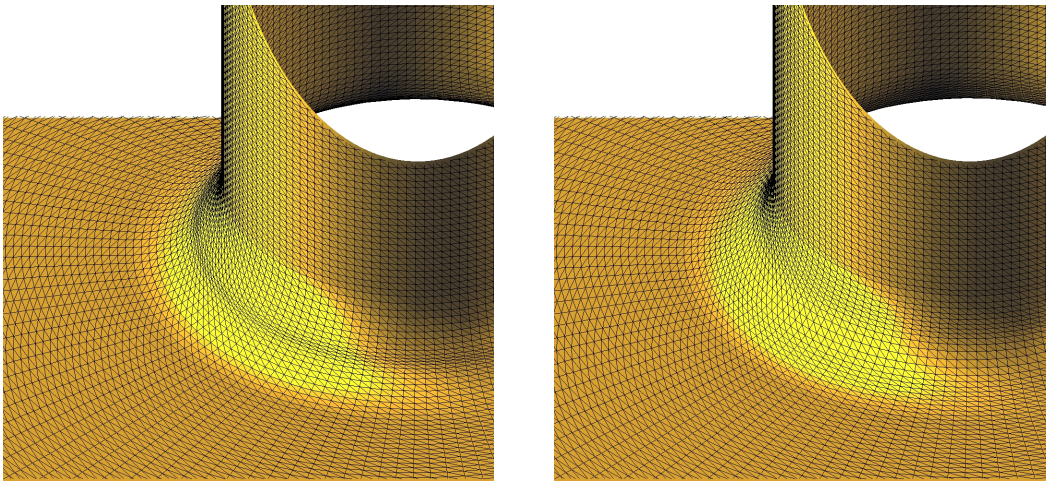

Figure 5.11: Solution of the blending problem of a cylinder and a disk with a circle shaped hole different values of the parameter $\tilde{\tau}$, $\tilde{\tau} = 0.1(\Delta X)^2$ (left), $\tilde{\tau} = (\Delta X)^4$ (right). The computational data are $h = \Delta X = 0.14$ and $\tau = \tilde{\tau} = (\Delta X)^4$. We show the surfaces at time step $k = 10$.

We also compared different values of the parameter $\tilde{\tau}$ for an initial destroyed circle of a circle with radius one (green dashed line of Figure 5.3) for time step $\tau = \Delta X = 0.0628$ and different values of the parameter $\tilde{\tau}$, $\tilde{\tau} = 0.1 * (\Delta X)$ (light blue line), $\tilde{\tau} = 0.01 * (\Delta X)$ (blue line), $\tilde{\tau} = 0.001 * (\Delta X)$ (red line). The smaller $\tilde{\tau}$ the better the approximation of the co-normal N^{co} by the co-normal of the solution of the two step time discretization of the Willmore flow problem with boundaries $N^{co}[X]$. Therefore, we start the iterations e.g. with $\tilde{\tau} = 0.1 * (\Delta X)$ and reduce $\tilde{\tau}$ at a later stage of the algorithm to achieve the desired smooth boundary conditions.

Surface blending

Figures 5.10 and 5.13 show the solution of a typical blending problem of a cylinder and a disk with a circle shaped hole. The two step time discretization leads to a smooth surface. We also compared different values for the time step size $\tilde{\tau}$ of the inner mean curvature problem, cf. Figure 5.11. If we choose $\tilde{\tau}$ smaller than $0.1\tilde{\tau}^4$ the grid degenerates, because the area

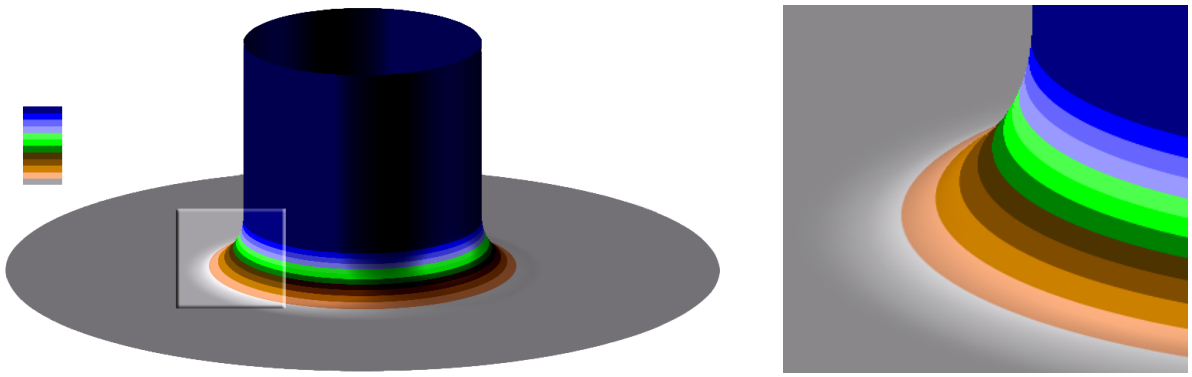

Figure 5.12: The surface corresponding to the solution of the blending problem of Figure 5.10 is color-coded with the z-coordinate value of the normal mapping $N[X]$. The grey value corresponds to a z-coordinate value one, whereas the dark blue value stands for a zero z-coordinate. The two step time discretization of the Willmore flow leads to a smooth blending.

of the triangles at the edge of the initial configuration converges to zero. In Figure 5.13 we compare the solution with the semi-implicit scheme of Chapter 3 with anisotropy $\gamma(z) = |z|$ (cf. Problem 3.3.2). The different algorithms lead to similar results. They differ in the parametrization in the neighborhood of the initial configuration. There, the area of the triangles for the semi-implicit scheme is greater than for the two step time discretization.

In the next example we pick up a blending problem of a higher genus topology already calculated by CLARENZ ET AL. [51]. The initial surface consists of edges and corners. Connecting 6 cylinders with the two step time discretization leads to a smooth blending, cf. Figure 5.14.

Surface restoration

In this section we consider surface restoration with the two step time discretization of the Willmore flow. In Figures 5.1 and 5.4 we show the evolution of a destroyed spherical surface. Since spheres are absolut minimizers of the Willmore energy, cf. Equation (1.3), one expect that the algorithm reconstruct the sphere. We apply variant I to the destroyed flat part with Dirichlet and Neumann boundary condition of the non-destroyed outer part of the sphere. Indeed, the surface evolve to the complete sphere.

The next examples show several surface restoration results for the Standford bunny [2]. In Figure 5.15 (first row) a small part of its flank is replaced by a disturbed surface patch that is color coded in red. The restoration with the corresponding Willmore surfaces with boundary conditions given by the outer surface is smooth at the patch boundary due to the boundary information and the normal taken from the outer surface. The isotropic Willmore flow is not able to restore patches with edges and corners, which is demonstrated in Figure 5.15. There, we destroyed the leg of the Standford bunny including the edge of the leg. Although the isotropic Willmore flow can not restore the edge, the resulting restoration leads to a good result. In Figure 5.16 a large part of the flank of the bunny is restored. The evolution leads to a smooth result.

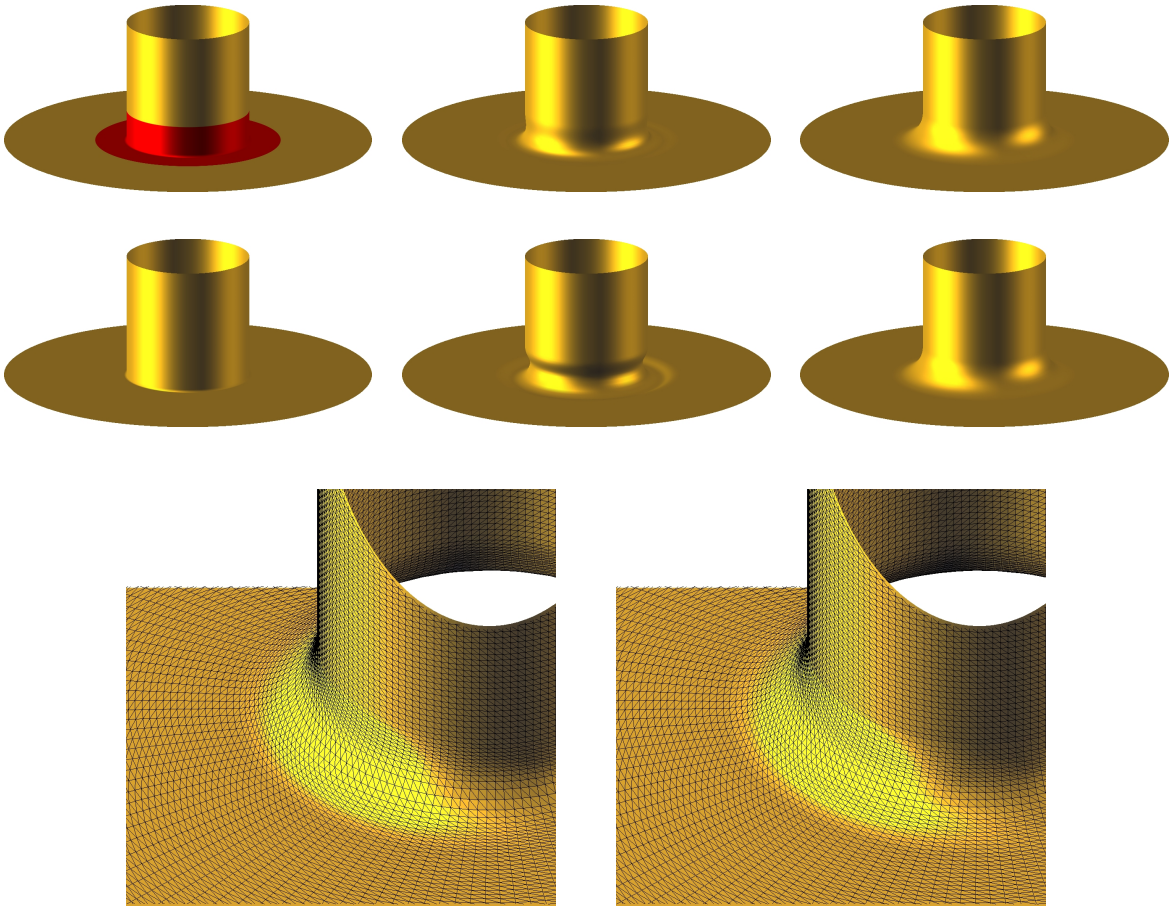

Figure 5.13: Comparison of the evolution of the blending problem of a cylinder and a disk with a circle shaped hole of the semi-implicit time discretization (first row) and the two step time discretization of Willmore flow (second row). The computational data are $\Delta X = 0.14$ and $\tau = \tilde{\tau} = (\Delta X)^4$. We show the surface at time steps $k = 0, 1, 10$. The surface patch $\mathcal{M}^0$ is marked in red. The grids of time step 10 are shown on the bottom. The grid on the left hand side corresponds to the semi-implicit time discretization, whereas the grid on the right hand side is a zoom for the two step time discretization of Willmore flow.

Figure 5.17 shows a real world restoration problem, where we reconstruct damaged regions of an Egea sculpture already discussed by CLARENZ ET AL. [51] and BOBENKO & SCHRÖDER [25]. The red colored domain of the model is replaced by the corresponding Willmore surface with boundary conditions given by the outer surface. Dirichlet boundary conditions for X and Neumann conditions for Y with a small time step size $\tilde{\tau}$ ensure smoothness of the restored surfaces.

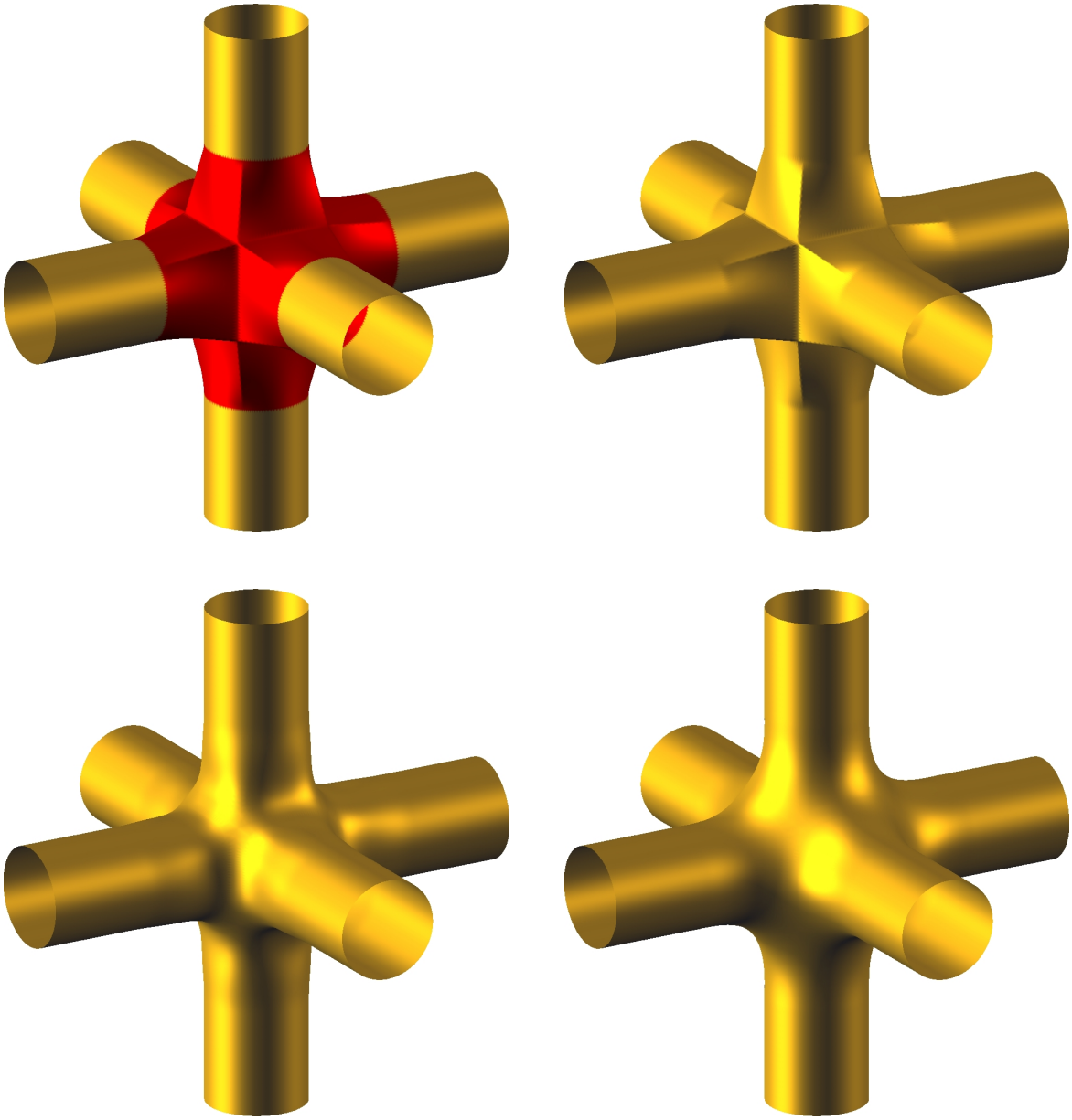

Figure 5.14: Solution of the blending problem of a higher genus topology. The boundary condition is determined by six cylinders. The grid size of the initial mesh varied between 0.0032 and 0.013. The computational data were $\tau = \tilde{\tau} = 10^{-6}$. We show the surface at time step $k = 0, 2$ and 4.

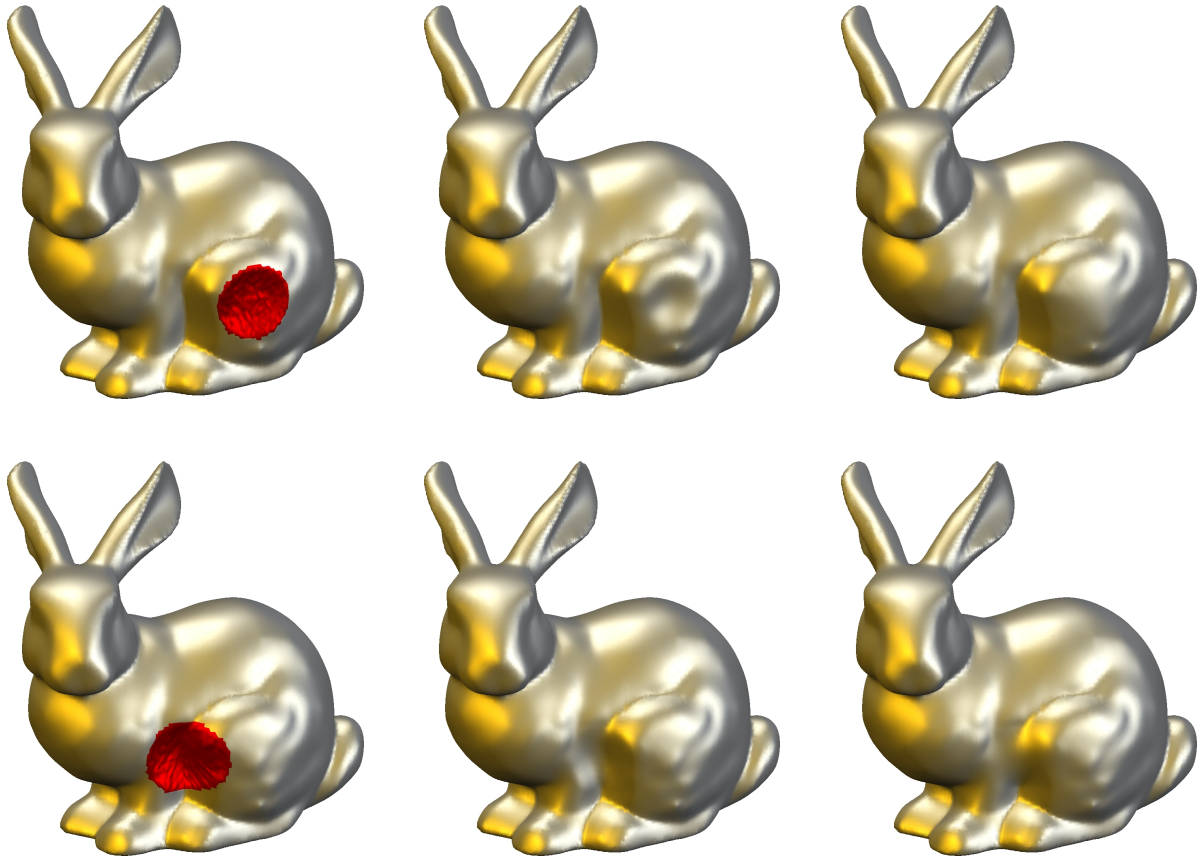

Figure 5.15: A small part of the flank of the Stanford bunny [2] is replaced by a disturbed surface patch that is color coded in red (first row). The restoration with the corresponding Willmore surface with boundary conditions given by the outer surface is smooth at the patch boundary due to the boundary information and the normal taken from the outer surface. The leg of the Stanford bunny including the edge of the leg is destroyed and replaced by a denoised surface patch in the second row. Although the isotropic Willmore flow can not restore the edge, the resulting restoration leads to a good result. The computational data were $\tau = (\Delta X) = 0.0265$ and $\tilde{\tau} = (\Delta X)^4$ for the first row, where we show the bunny at time steps 0, 2 and 4. In the second row we chose $\tau = \Delta X = 0.027$ and $\tilde{\tau} = (\Delta X)^4$. The bunny is shown at time steps 0, 3 and 4.

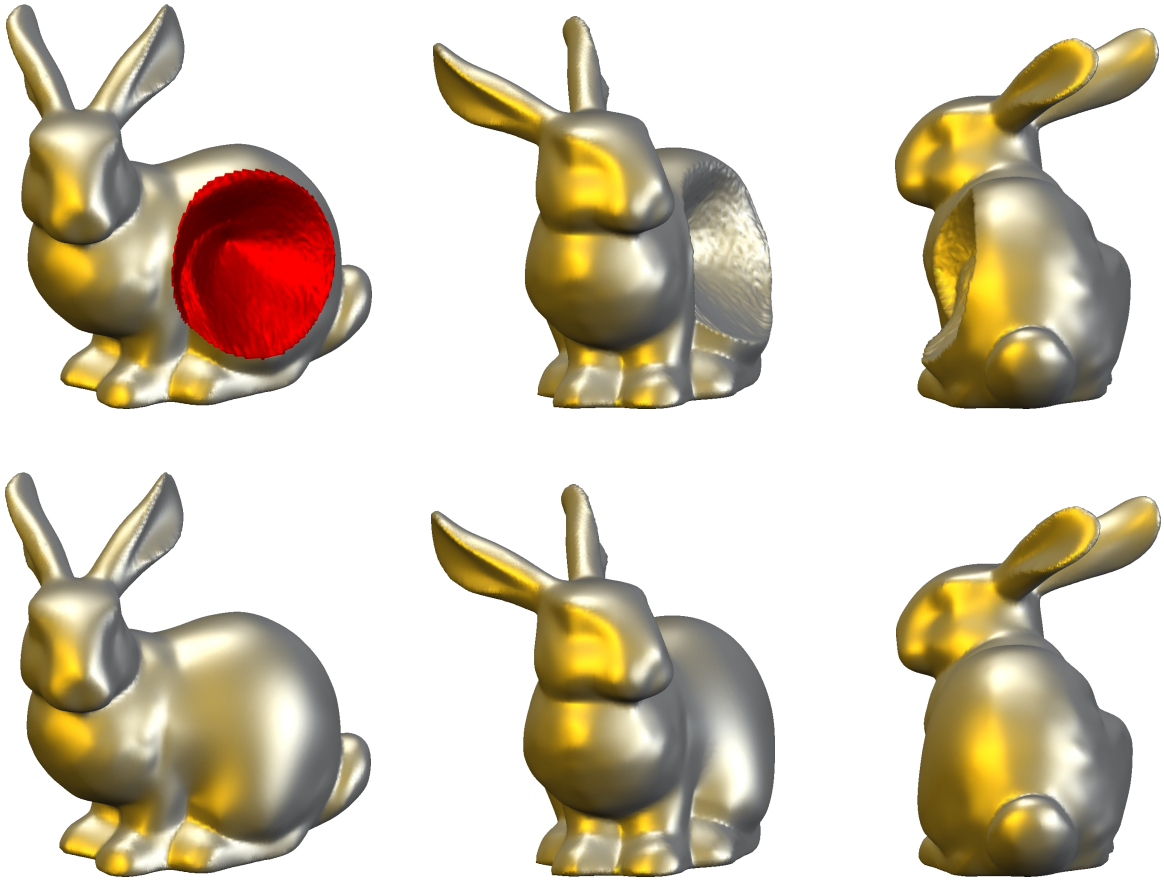

Figure 5.16: A large part of the flank of the Stanford bunny [2] is restored. The destroyed surface is shown on the top row. The part to be restored is color coded in red. The evolution leads to a smooth result that is shown on the bottom row. The grid size of the initial mesh varied between 0.000255 and 0.03366. The computational data were $\tau = 0.0001$ and $\tilde{\tau} = 0.00001$. We show the bunny at time step 10.

Figure 5.17: Evolution of an Egea head dataset. The model is courtesy of CYBERWARE [1]. The initial surface is shown in the top row. The areas of the surface to be restored are shown in red. The time step sizes were chosen as $\tau = 10^{-3}$ and $\tilde{\tau} = 10^{-7}$. We show the surface at time steps 0,2,4. The grid size of the initial mesh varied between 0.0013 and 0.012. The initial object was scaled to diameter 1.

Chapter 6

Two step time discretization of the anisotropic Willmore flow

THE gradient flow of the anisotropic Willmore energy of a surface, $\int \mathbf{h}_\gamma{}^2 \, \mathrm{d}a$, as a function of the generalized mean curvature, plays an important role in digital geometry processing like surface restoration especially if the edge or corner of a surface is destroyed as we saw in Chapter 3. In this chapter we will extend the two step time discretization for discrete isotropic Willmore flow from Chapter 4 to the anisotropic case. To evaluate the anisotropic Willmore energy on the unknown surface of the next time step, we first solve an inner, secondary variational problem describing a time step of anisotropic mean curvature motion, which only involves the anisotropy but not its derivatives. We define the mapping y as the minimizer of the L^2-distance between surfaces and the generalized surface area of $\mathcal{M}[y]$. In the isotropic case a single semi-implicit time step of mean curvature motion has to be solved in each time step. Now, we end up with a scheme for a single fully implicit time step of anisotropic mean curvature motion to be solved with a Newton approach. The difference quotient in time between the given surface and the next time step surface of the anisotropic mean curvature motion can again be regard as a time discrete, fully implicit approximation of the anisotropic mean curvature vector. Based on this anisotropic mean curvature vector, the generalized Willmore functional can be approximated. To solve the resulting nested variational problem in each time step a sequential quadratic programming approach and numerically relaxation theory from PDE constraint optimization are taken into account. The approach is applied to polygonal curves, where the anisotropy could be chosen almost crystalline. Various numerical examples underline again the stability of the new scheme, which enables time steps of the order of the spatial grid size.

6.1 Derivation of the two step time discretization

The abstract time-discrete variational problem of the anisotropic Willmore flow is given by

$$\operatorname{dist}(\mathcal{M}[x], \mathcal{M}[x^k])^2 + \tau \int\limits_{\mathcal{M}[x]} \mathbf{h}_\gamma{}^2 \, \mathrm{d}a \to \min,$$

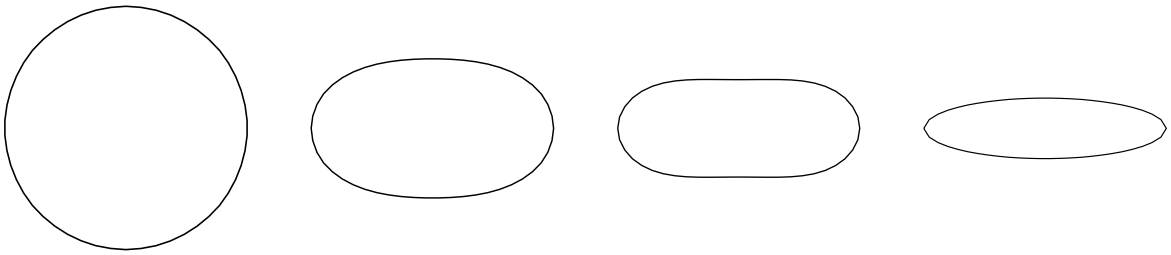

Figure 6.1: Different time steps of the anisotropic Willmore flow of an original circle with 50 vertices is shown. The time step size was chosen of the order of the spatial grid size $\Delta X = \tau = 0.1256$. The anisotropy $\gamma(z) = \sqrt{z_0^2 + 4z_1^2}$ is an ellipse (cf. Example 2.2.7).

where $h_\gamma = \mathrm{div}_{\mathcal{M}}(n_\gamma) = \mathrm{div}_{\mathcal{M}}(\gamma_z \circ n)$, cf. Definition 2.2.3, denotes the generalized mean curvature. Before we consider the actual time discretization of the anisotropic Willmore flow, we study the time discretization of the anisotropic mean curvature motion. Following the abstract approach as in the isotropic case the variational time discretization of the anisotropic mean curvature motion for a given surface $\mathcal{M} = \mathcal{M}[x]$ defines the mapping $y = y[x]$ of the next time step surface $\mathcal{M}[y]$ as the minimizer of the functional

$$\mathrm{dist}(\mathcal{M}[y], \mathcal{M}[x])^2 + 2\tilde{\tau} \int\limits_{\mathcal{M}[y]} \gamma(n)\,\mathrm{d}a\,,$$

where $\tilde{\tau}$ is the considered time step, $\mathrm{dist}(\cdot,\cdot)$ is the L^2- distance between surfaces and

$$a_\gamma[y] = \int\limits_{\mathcal{M}[y]} \gamma(n)\,\mathrm{d}a$$

the anisotropic surface area of $\mathcal{M}[y]$ as the underlying energy. We obtain the following variational problem:

Given a surface $\mathcal{M}[x]$ parameterized by a mapping x we ask for a mapping $y = y[x]$, which minimizes the functional

$$e_\gamma[x,y] = \int\limits_{\mathcal{M}[x]} (y-x)^2\,\mathrm{d}a + 2\tilde{\tau} \int\limits_{\mathcal{M}[y]} \gamma(n)\,\mathrm{d}a$$

for given x. As above the time step size $\tilde{\tau}$ is chosen in principle independent of the time step size for the actual time discrete anisotropic Willmore flow. The resulting weak form of the

corresponding Euler–Lagrange equations is

$$\begin{aligned}0 &= \int_{\mathcal{M}[x]} \frac{1}{\tilde{\tau}}(y-x)\cdot\theta \,\mathrm{d}a + \int_{\mathcal{M}[y]} \mathbf{h}_\gamma n\cdot\theta \,\mathrm{d}a \\ &= \int_{\mathcal{M}[x]} \frac{1}{\tilde{\tau}}(y-x)\cdot\theta \,\mathrm{d}a \\ &\quad + \int_{\mathcal{M}[y]} \gamma(n)\nabla_{\mathcal{M}[y]} y : \nabla_{\mathcal{M}[y]}\theta \,\mathrm{d}a - \int_{\mathcal{M}[y]} n^k \gamma_{z_l}(n)\nabla_{\mathcal{M}[y]} y_l \cdot \nabla_{\mathcal{M}[y]}\theta_k \,\mathrm{d}a\end{aligned}$$

for test functions θ, cf. Lemma 3.2.2. n^k denotes the kth coordinate of the normal n. Choosing $\gamma(n) = |n|$ isotropic we get

$$0 = \int_{\mathcal{M}[x]} (y-x)\cdot\theta \,\mathrm{d}a + \tilde{\tau}\int_{\mathcal{M}[y]} \nabla_{\mathcal{M}[y]} y : \nabla_{\mathcal{M}[y]}\theta \,\mathrm{d}a\,.$$

Comparing the corresponding Euler–Lagrange equations for the two step time discretization of the isotropic Willmore flow

$$0 = \int_{\mathcal{M}[x]} (y-x)\cdot\theta + \tilde{\tau}\nabla_{\mathcal{M}[x]} y : \nabla_{\mathcal{M}[x]}\theta \,\mathrm{d}a\,,$$

we end up with a fully implicit scheme. Now, we integrate over $\mathcal{M}[y]$ instead of the known surface $\mathcal{M}[x]$ in the second summand. A semi-implicit time discretization of the anisotropic mean curvature flow has been proposed by Clarenz, Dziuk & Rumpf [55] that is based on the schemes in Dziuk [81, 83] with convergence results for curves [83, 82]. They use the following time discretization, cf. Equation (16) in Clarenz, Dziuk & Rumpf [55],

$$\begin{aligned}0 &= \int_{\mathcal{M}[x]} \frac{1}{\tilde{\tau}}(y-x)\cdot\theta \,\mathrm{d}a \\ &\quad + \int_{\mathcal{M}[x]} \gamma(n)\nabla_{\mathcal{M}[x]} y : \nabla_{\mathcal{M}[x]}\theta \,\mathrm{d}a - \int_{\mathcal{M}[x]} n^k \gamma_{z_l}(n)\nabla_{\mathcal{M}[x]} x_l \cdot \nabla_{\mathcal{M}[x]}\theta_k \,\mathrm{d}a\,.\end{aligned}$$

In the corresponding Finite Element scheme they have to solve a linear system of equations. Since we integrate over the surface of the next time step, we have to solve a nonlinear system of equations with a Newton method in each time step.

Because of the time continuous evolution equation $\partial_t x = \mathbf{h}_\gamma n$ the difference quotient

$$\frac{y[x]-x}{\tilde{\tau}}$$

can be considered as a regularized approximation of the anisotropic mean curvature vector $\mathbf{h}_\gamma n$ on $\mathcal{M}[x]$. As in the isotropic case this enables us to define a time discretization of the

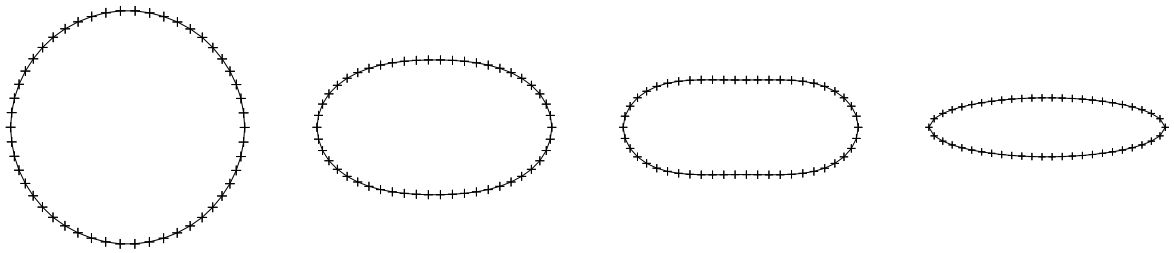

Figure 6.2: The grids of the evolution under Willmore flow of the initial circle of Figure 6.1 are shown at the same times.

anisotropic Willmore flow, which does no require the explicit evaluation of the anisotropic mean curvature on the unknown surface of the next time step. Indeed, in the abstract variational problem

$$\operatorname{dist}(\mathcal{M}[x],\mathcal{M}[x^k])^2+\tau\int\limits_{\mathcal{M}[x]}\mathbf{h}_\gamma{}^2\,\mathrm{d}a\to\min$$

we consider the same linearization of the L^2-distance as for anisotropic mean curvature motion and use the above approximation of the anisotropic Willmore energy. Finally, we obtain the following scheme:

Given an initial surface $\mathcal{M}[x^0]$ we define a sequence of surfaces $\mathcal{M}[x^k]$ with $k=1,\cdots$, where x^{k+1} minimizes the functional

$$w_\gamma[x^k,x,y[x]]=\int\limits_{\mathcal{M}[x^k]}(x-x^k)^2\,\mathrm{d}a+\frac{\tau}{\tilde\tau^2}\int\limits_{\mathcal{M}[x]}(y[x]-x)^2\,\mathrm{d}a$$

for given x_k. Hence, x^k is assumed to approximate $x(t_k)$ with $t_k=k\tau$ for the given time step τ. Thus, in each time step we have to solve the nested variational problem

$$\begin{aligned}x^{k+1}&=\arg\min_x w_\gamma[x^k,x,y[x]]\quad\text{with}\\ y[x]&=\arg\min_y e_\gamma[x,y]\,.\end{aligned}\tag{6.1}$$

6.2 Finite Element space discretization

Before using the space discretization of Section 2.4 to derive the fully discrete two step time discretization of the anisotropic Willmore flow, let us first review the basic notations. We consider simplicial meshes $\mathcal{M}[X]$ and as in Section 2.4 we use upper case letter for discrete quantities and lower case letter for the corresponding continuous quantities. Furthermore, a bar on top of a discrete function indicates the corresponding nodal vector. The corresponding Finite Element space is denoted by $\mathcal{V}(\mathcal{M}[X])^m$. Let $M[X]$ be the mass matrix and $L[X]$, $L^\gamma[X]$, $L^{N\otimes\gamma}[X]$ the stiffness matrices with corresponding block matrices $\mathbf{M}[X]$ and $\mathbf{L}[X]$,

$\mathbf{L}^{\gamma}[X]$, $\mathbf{L}^{N\otimes\gamma}[X]$. Given some initial surface $\mathcal{M}[X^0]$ we seek a sequence $(\mathcal{M}[X^k])_{k=1,2\dots}$ of discrete surfaces that solve the fully discrete two step time discretization of the anisotropic Willmore flow:

Given a discrete surface $\mathcal{M}[X^k]$ in time step k we define $X^{k+1} \in \mathcal{V}(\mathcal{M}[X^k])^m$ as the minimizer of the following spatially discrete, nested variational problem

$$\begin{aligned} X^{k+1} &= \operatorname*{arg\,min}_{X\in\mathcal{V}(\mathcal{M}[X^k])^m} W_\gamma[X^k, X, Y[X]] \quad \text{with} \\ Y[X] &= \operatorname*{arg\,min}_{Y\in\mathcal{V}(\mathcal{M}[X])^m} E_\gamma[X,Y], \end{aligned} \tag{6.2}$$

where

$$\begin{aligned} E_\gamma[X,Y] &:= \int_{\mathcal{M}[X]} (Y-X)^2 \,\mathrm{d}a + 2\,\tilde{\tau} \int_{\mathcal{M}[Y]} \gamma(N[Y])\,\mathrm{d}a \\ &= \mathbf{M}[X](\bar{Y}-\bar{X})\cdot(\bar{Y}-\bar{X}) + 2\,\tilde{\tau} \int_{\mathcal{M}[Y]} \gamma(N[Y])\,\mathrm{d}a, \end{aligned}$$

$$\begin{aligned} W_\gamma[X^k, X, Y] &:= \int_{\mathcal{M}[X^k]} (X-X^k)^2 \,\mathrm{d}a + \frac{\tau}{\tilde{\tau}^2} \int_{\mathcal{M}[X]} (Y-X)^2 \,\mathrm{d}a \\ &= \mathbf{M}[X^k](\bar{X}-\bar{X}^k)\cdot(\bar{X}-\bar{X}^k) + \frac{\tau}{\tilde{\tau}^2}\mathbf{M}[X](\bar{Y}-\bar{X})\cdot(\bar{Y}-\bar{X}) \end{aligned}$$

The first variation of the discrete anisotropic area functional

$$A_\gamma[Y] := \int_{\mathcal{M}[Y]} \gamma(N[Y])\,\mathrm{d}a$$

for some test function Θ is given by

$$\partial_Y A_\gamma[Y](\Theta) = \int_{\mathcal{M}[Y]} \gamma(N[Y])\,\nabla_{\mathcal{M}[Y]} Y : \nabla_{\mathcal{M}[Y]}\Theta \,\mathrm{d}a - \int_{\mathcal{M}[Y]} \gamma_{z_k}(N[Y]) N^l[Y]\cdot\nabla_{\mathcal{M}[Y]}\Theta_l \,\mathrm{d}a\,.$$

Therefore the first variation of E_γ with respect to Y is

$$\begin{aligned} \partial_Y E_\gamma[X,Y](\Theta) = 2 &\int_{\mathcal{M}[X]} (Y-X)\cdot\Theta \,\mathrm{d}a \\ &+ 2\tilde{\tau} \int_{\mathcal{M}[Y]} \gamma(N[Y])\,\nabla_{\mathcal{M}[Y]} Y : \nabla_{\mathcal{M}[Y]}\Theta \,\mathrm{d}a \\ &- 2\tilde{\tau} \int_{\mathcal{M}[Y]} \gamma_{z_k}(N[Y]) N^l[Y]\cdot\nabla_{\mathcal{M}[Y]}\Theta_l \,\mathrm{d}a\,. \end{aligned} \tag{6.3}$$

and the nodal vector $\bar{Y}[X]$ solves the nonlinear system of equations

$$\mathbf{M}[X](\bar{Y}[X]-\bar{X})+\tilde{\tau}\mathbf{L}^{\gamma}[Y]\bar{Y}[X]-\tilde{\tau}\mathbf{L}^{N\otimes\gamma}[Y]\bar{Y}[X]=0\,. \tag{6.4}$$

We solve this equation with a Newton method. In each Newton iteration and for each test function Θ we have to solve

$$\partial_Y F[Y](\Theta)\,\Delta Y=-F[Y]\,,$$

where

$$\begin{aligned} F[Y] &:= \mathbf{M}[X](\bar{Y}-\bar{X})+\tilde{\tau}\mathbf{L}^{\gamma}[Y]\bar{Y}-\tilde{\tau}\mathbf{L}^{N\otimes\gamma}[Y]\bar{Y}\,.\\ \partial_Y F[Y](\Theta) &= \mathbf{M}[X]+\tilde{\tau}\partial_Y\mathbf{L}^{\gamma}[Y](\Theta)\bar{Y}+\tilde{\tau}\mathbf{L}^{\gamma}[Y]\Theta\\ &\quad -\tilde{\tau}\partial_Y\mathbf{L}^{N\otimes\gamma}[Y](\Theta)\bar{Y}-\tilde{\tau}\mathbf{L}^{N\otimes\gamma}[Y]\Theta\,. \end{aligned}$$

If we define the vector

$$\mathbf{V}^{\gamma_z}[Y]:=\left(\mathbf{L}^{\gamma}[Y]-\mathbf{L}^{N\otimes\gamma}[Y]\right)\bar{Y}\,, \tag{6.5}$$

and the block matrix

$$\mathbf{L}^{\gamma_{zz}}[Y]:=\left(\mathbf{L}^{\gamma}[Y]-\mathbf{L}^{N\otimes\gamma}[Y]+\partial_Y\mathbf{L}^{\gamma}[Y](\Phi_r e_s)\bar{Y}-\partial_Y\mathbf{L}^{N\otimes\gamma}[Y](\Phi_r e_s)\bar{Y}\right)_{r\in I,s=0,\cdots,m}\,, \tag{6.6}$$

respectively, where Φ_r is the nodal test function corresponding to node r, we have to solve

$$\left(\mathbf{M}[X]+\tilde{\tau}\mathbf{L}^{\gamma_{zz}}[Y]\right)\Delta Y=-\left(\mathbf{M}[X](\bar{Y}-\bar{X})+\tilde{\tau}\mathbf{V}^{\gamma_z}[Y]\right)\,.$$

Obviously, it holds that

$$\partial_Y\mathbf{V}^{\gamma_z}[Y](\Theta)=\mathbf{L}^{\gamma_{zz}}[Y]\bar{\Theta}\,. \tag{6.7}$$

Finite Element space discretization for polygonal curves and triangular surfaces

Recalling Equations (2.17) and (2.18) we can simplify E_γ and $\partial_Y E_\gamma$, respectively, cf. Equation (6.3), for polygonal curves and triangulated surfaces. Let N_T denote the normal N_T of an element T for a simplicial mesh $\mathcal{M}[Y]$. In the case of polygonal curves the normal of an element T with face F_0 is given by

$$N_T[Y]=\frac{D^{\frac{\pi}{2}}F_0}{|F_0|}=\frac{D^{\frac{\pi}{2}}F_0}{|T|},$$

whereas for triangulated surfaces the surface normal for an element T consists of faces F_0,F_1,F_2 and is defined as

$$N_T[Y]=\frac{F_2\wedge F_1}{|F_2\wedge F_1|}=\frac{1}{2}\frac{F_2\wedge F_1}{|T|}\,,$$

cf. Equation (2.40) in Section 2.4. Let $D^{\frac{\pi}{2}}$ denote a clockwise rotation through the angle $\frac{\pi}{2}$ in the plane. Defining

$$N_T^F[Y]:=\frac{|T|}{\alpha}N_T[Y]$$

with $\alpha = 1$ for polygonal curves and $\alpha = 0.5$ for triangulated surfaces, i.e.

$$N_T^F[Y] = D^{\frac{\pi}{2}} F_0 ,$$

for polygonal curves and

$$N_T^F[Y] = F_2 \wedge F_1 ,$$

for triangulated surfaces, we get

$$E_\gamma[X,Y] = \mathbf{M}[X](\bar{Y} - \bar{X}) \cdot (\bar{Y} - \bar{X}) + 2\,\tilde{\tau}\,\alpha \sum_{T \in \mathcal{M}[Y]} \gamma(N_T^F[Y]) .$$

Therefore the first variation of E_γ is given by

$$\partial_Y E_\gamma[X,Y](\Theta) = 2\mathbf{M}[X](\bar{Y}[X] - \bar{X}) \cdot \bar{\Theta} + 2\,\tilde{\tau}\,\alpha \sum_{T \in \mathcal{M}[Y]} \gamma_z(N_T^F[Y]) \cdot \partial_Y N_T^F(\Theta) .$$

With the above definition (6.5) we get

$$\mathbf{V}^{\gamma_z}[Y] = \alpha \left(\sum_{T \in \mathcal{M}[Y]} \gamma_z(N_T^F[Y]) \cdot \partial_Y N_T^F(\Phi_r e_s) \right)_{rs}$$

and the nodal vector $\bar{Y}[X]$ solves

$$\mathbf{M}[X](\bar{Y}[X] - \bar{X}) + \tilde{\tau}\mathbf{V}^{\gamma_z}[Y] = 0 . \tag{6.8}$$

6.3 Numerical solution of the anisotropic optimization problem

As in the isotropic case, cf. Section 4.4, we would like to avoid a direct computation of $\partial_X Y[X](\Theta)$. Therefore we apply the same duality argument:

Defining $P \in \mathcal{V}(\mathcal{M}[X^k])^m$ as the solution of the dual problem

$$\partial_Y^2 E_\gamma[X, Y[X]](P, \Upsilon) = \partial_Y W_\gamma[X^k, X, Y[X]](\Upsilon) . \tag{6.9}$$

for all test functions $\Upsilon \in \mathcal{V}(\mathcal{M}[X^k])^m$ we obtain for the first variation of

$$\widehat{W_\gamma}[X] := W_\gamma[X^k, X, Y[X]]$$

with respect to X in a direction Θ

$$\partial_X \widehat{W_\gamma}[X](\Theta) = \partial_X W_\gamma[X^k, X, Y[X]](\Theta) - \partial_X \partial_Y E_\gamma[X,Y](P,\Theta). \tag{6.10}$$

The solution P of the dual problem (6.9) requires to solve

$$\begin{aligned} &\mathbf{M}[X]\bar{P} \cdot \bar{\Theta} + \tilde{\tau}\mathbf{L}^\gamma[Y]\bar{P} \cdot \bar{\Theta} - \tilde{\tau}\mathbf{L}^{N \otimes \gamma_z}[Y]\bar{P} \cdot \bar{\Theta} \\ &\qquad + \tilde{\tau}\partial_Y \mathbf{L}^\gamma[Y](\Theta)\bar{Y} \cdot \bar{P} - \tilde{\tau}\partial_Y \mathbf{L}^{N \otimes \gamma_z}[Y](\Theta)\bar{Y} \cdot \bar{P} = \frac{\tau}{\tilde{\tau}^2}\mathbf{M}[X](\bar{Y} - \bar{X}) \cdot \bar{\Theta} \end{aligned} \tag{6.11}$$

for all test functions Θ. With Definition (6.6) this reduces to solve the linear system of equations with block matrix $\mathbf{L}^{\gamma_{zz}}[Y]$ (cf. Equation (6.22) for simplical meshes)

$$(\mathbf{M}[X] + \tilde{\tau}\mathbf{L}^{\gamma_{zz}}[Y])\,\bar{P} = \frac{\tau}{\tilde{\tau}^2}\mathbf{M}[X](\bar{Y} - \bar{X})\,. \tag{6.12}$$

The terms on the right hand side of (6.10) are to be evaluated as follows

$$\begin{aligned}\left(\partial_X W_\gamma\right)[X^k, X, Y](\Theta) &= 2\,\mathbf{M}[X^k](\bar{X} - \bar{X}^k)\cdot\bar{\Theta} + 2\frac{\tau}{\tilde{\tau}^2}\mathbf{M}[X](\bar{X} - \bar{Y})\cdot\bar{\Theta} \\ &\quad + \frac{\tau}{\tilde{\tau}^2}\,(\partial_X\mathbf{M}[X](\Theta))(\bar{Y} - \bar{X})\cdot(\bar{Y} - \bar{X})\,,\end{aligned}$$

$$\partial_X\partial_Y E_\gamma[X, Y](P, \Theta) = 2(\partial_X\mathbf{M}[X](\Theta))(\bar{Y} - \bar{X})\cdot\bar{P} - 2\mathbf{M}[X]\bar{P}\cdot\bar{\Theta}\,.$$

In the concrete numerical algorithm we either perform a gradient descent method with the Armijo step size control starting from the initial position given by the previous time step (Algorithm 6.1) or a SQP approach (Algorithm 6.2). Let $\partial_X M[X](\Theta)$ and $\partial_Y L^{\gamma_{zz}}[Y](\Theta)$ denote the variation of the mass and stiffness matrix with respect to a variation Θ of the simplicial grid. As in Section 4.4, cf. Equations (4.18) and (4.19), we define the corresponding block operators as third order tensors $\partial_X\mathbf{M}$ and $\partial_Y\mathbf{L}^{\gamma_{zz}}$ that map a vector $\bar{V} = (V_j^k)_{j\in I, k=1,\cdots,m} \in \mathbb{R}^{m\sharp I}$ to a matrix via

$$(\partial_X\mathbf{M})\bar{V} = \left(\partial_X M_{(\tilde{r},\tilde{s})(j,k)}[X](\Phi_r e_s)V_j^k\right)_{r,\tilde{r}\in I, s,\tilde{s}=1,\cdots,m} \in \mathbb{R}^{m\sharp I, m\sharp I}$$

and

$$(\partial_Y\mathbf{L}^{\gamma_{zz}})\bar{V} = \left(\partial_Y L^{\gamma_{zz}}_{(\tilde{r},\tilde{s})(j,k)}[Y](\Phi_r e_s)V_j^k\right)_{r,\tilde{r}\in I, s,\tilde{s}=1,\cdots,m} \in \mathbb{R}^{m\sharp I, m\sharp I}\,.$$

We can compute the descent direction in $\mathbb{R}^{m\sharp I}$ of the energy $\widehat{W_\gamma}$ at a given simplicial mesh $\mathcal{M}[X]$ described by the nodal vector $\bar{X}$ and obtain

$$\begin{aligned}\overline{\operatorname{grad}_X\widehat{W_\gamma}[X]} &= \left(\partial_X\widehat{W_\gamma}[X](\Phi_r e_s)\right)_{r\in I, s=1,\cdots,m}\,, \\ &= 2\,\mathbf{M}[X^k](\bar{X} - \bar{X}^k) + 2\mathbf{M}[X]\left(\frac{\tau}{\tilde{\tau}^2}(\bar{X} - \bar{Y}) + \bar{P}\right) \\ &\quad + \left(\partial_X\mathbf{M}[X](\bar{Y} - \bar{X})\right)\left(\frac{\tau}{\tilde{\tau}^2}(\bar{Y} - \bar{X}) - 2\,\bar{P}\right)\,,\end{aligned} \tag{6.13}$$

where e_s denotes the sth coordinate direction in $\mathbb{R}^m$.

To derive the SQP approach we consider the following Lagrangian function for Problem (6.2)

$$L_\gamma[X, Y, P] = W_\gamma[X^k, X, Y] - \partial_Y E_\gamma[X, Y](P)$$

for the independent unknowns $X, Y \in \mathbb{R}^{m\sharp I}$ and Lagrange parameter $P \in \mathbb{R}^{m\sharp I}$ corresponding to the dual variable, cf. Equation (6.9). For any test functions $\Theta \in \mathcal{V}(\mathcal{M}[X^k])^m$ we have

$$\begin{aligned}\partial_X L_\gamma[X, Y, P](\Theta) &= \partial_X W_\gamma[X^k, X, Y](\Theta) - \partial_X\partial_Y E_\gamma[X, Y](P, \Theta), \\ \partial_Y L_\gamma[X, Y, P](\Theta) &= W_\gamma[X^k, X, Y](\Theta) - \partial_Y\partial_Y E_\gamma[X, Y](P, \Theta), \\ \partial_Z L_\gamma[X, Y, P](\Theta) &= -\partial_Y E_\gamma[X, Y](\Theta),\end{aligned}$$

Algorithm 6.1: Gradient decent method for two step time discretization of anisotropic Willmore flow

input data: surface $\mathcal{M}[X^0]$;
calculate spatial grid size ΔX^0;
set time step sizes $\tau = \Delta X^0$ and $\tilde{\tau} = \tau^2$;
set $\bar{X}^k = \bar{X}^0$;
set counter for the two step time discretization $k = 0$;
repeat
  set counter of the gradient decent method $l = 0$;
  set $\bar{X}^{k,l} = \bar{X}^k$;
  repeat
    solve $\left(\mathbf{M}[X^{k,l}](\bar{Y} - \bar{X}^{k,l}) + \tilde{\tau}\mathbf{V}^{\gamma_z}[Y] = 0\right)$ by a Newton method; // Eq. (6.4)
    solve $\left(\mathbf{M}[X^{k,l}] + \tilde{\tau}\mathbf{L}^{\gamma_{zz}}[Y]\right)\bar{P} = \frac{\tau}{\tilde{\tau}^2}\mathbf{M}[X^{k,l}](\bar{Y} - \bar{X}^{k,l})$; // Eq. (6.12)
    $D = \overline{\operatorname{grad}_X \widehat{W_\gamma}[X]}$; // Eq. (6.13)
    $\bar{X}^{k,l+1} = \bar{X}^{k,l} - \operatorname{ArmijoStepSize}\left[\widehat{W_\gamma}, X^{k,l}, D\right] D$;
    $l \leftarrow l + 1$;
  until $|\bar{X}^{k,l+1} - \bar{X}^{k,l}| < \epsilon$;
  $\bar{X}^{k+1} = \bar{X}^k$;
  $k \leftarrow k + 1$;
until $|\bar{X}^{k+1} - \bar{X}^k| < \epsilon$;

where the gradient of W_γ is given by

$$\operatorname{grad}_{[X,Y]} W_\gamma[X^k, X, Y] = \begin{pmatrix} 2\,\mathbf{M}[X^k](\bar{X} - \bar{X}^k) + 2\frac{\tau}{\tilde{\tau}^2}\mathbf{M}[X](\bar{X} - \bar{Y}) \\ 2\frac{\tau}{\tilde{\tau}^2}\mathbf{M}[X](\bar{Y} - \bar{X}) \end{pmatrix} \tag{6.14}$$

and the variation of E_γ with respect to Y by

$$-\partial_Y E_\gamma[X, Y] = 2\,\mathbf{M}[X](\bar{X} - \bar{Y}) - 2\,\tilde{\tau}\mathbf{V}^{\gamma_z}[V]. \tag{6.15}$$

We also define the matrix

$$\begin{aligned} A_\gamma[X, Y] :=& -\operatorname{grad}_{[X,Y]}\left(\partial_Y E_\gamma[X, Y]\right) \\ =& \begin{pmatrix} \left(\partial_X \mathbf{M}[X](\bar{Y} - \bar{X})\right)\left(\frac{\tau}{\tilde{\tau}^2}(\bar{Y} - \bar{X}) - 2\,\bar{P}\right) + 2\mathbf{M}[X]\bar{P} \\ -2\left(\mathbf{M}[X] + \tilde{\tau}\mathbf{L}^{\gamma_{zz}}[Y]\right)\bar{P} \end{pmatrix}. \end{aligned} \tag{6.16}$$

The last ingredient of the SQP approach is the Hessian $\operatorname{Hess}_{[X,Y]} L_\gamma[X^k, Y, P]$. Its components

Algorithm 6.2: SQP method for two step time discretization of anisotropic Willmore flow

input data: surface $\mathcal{M}[X^0]$;
calculate spatial grid size ΔX^0;
set time step sizes $\tau = \Delta X^0$ and $\tilde{\tau} = \tau^2$;
set $\bar{X}^k = \bar{X}^0$;
set counter for the two step time discretization $k = 0$;
repeat
  set counter of the SQP method $l = 0$;
  set $\bar{X}^{k,l} = \bar{X}^k$;
  set $\bar{Y}^l = \bar{X}^k$;
  set $\bar{P}^l = 0$;
  repeat
    calculate $W_\gamma[X^k, X^{k,l}, Y^l]$ and $\mathrm{grad}_{[X,Y]} W_\gamma[X^k, X^{k,l}, Y^l]$; // Eq. (6.14)
    calculate $\mathrm{Hess}_{[X,Y]} L_\gamma[X^{k,l}, Y^l, P^l]$; // Eq. (6.17)
    calculate $A_\gamma^T[X^{k,l}, Y^l]$ and $-\partial_Y E_\gamma[X^{k,l}, Y^l]$; // Eq. (6.16) and (6.15)
    solve (6.18), (6.19) to obtain $(\Delta\bar{X}^l, \Delta\bar{Y}^l)$ and $\bar{Z}^l$;
    set $\bar{X}^{k,l+1} = \bar{X}^{k,l} + \Delta\bar{X}^l$;
    set $\bar{Y}^{l+1} = \bar{Y}^l + \Delta\bar{Y}^l$;
    set $\bar{P}^{l+1} = \bar{Z}^l$;
    $l \leftarrow l + 1$;
  until $|(X^{k,l+1}, Y^{l+1}, P^{l+1}) - (X^{k,l}, Y^l, P^l)| < \epsilon$;
  $\bar{X}^{k+1} = \bar{X}^k$;
  $k \leftarrow k + 1$;
until $|\bar{X}^{k+1} - \bar{X}^k| < \epsilon$;

for the first row with respect to test functions Θ and Ψ are given by

$$\begin{aligned}
\partial_X \partial_X L_\gamma(\Theta, \Psi) = {} & 2\mathbf{M}[X^k]\bar{\Psi} \cdot \bar{\Theta} + 2\frac{\tau}{\tilde{\tau}^2}\mathbf{M}[X]\bar{\Psi} \cdot \bar{\Theta} \\
& + (\partial_X^2 \mathbf{M}[X](\Theta, \Psi))(\bar{Y} - \bar{X}) \cdot \left(\frac{\tau}{\tilde{\tau}^2}(\bar{Y} - \bar{X}) - 2\bar{P} \right) \\
& + 2(\partial_X \mathbf{M}[X](\Theta)) \left(\frac{\tau}{\tilde{\tau}^2}(\bar{X} - \bar{Y}) + \bar{P} \right) \cdot \bar{\Psi} \\
& + 2(\partial_X \mathbf{M}[X](\Psi)) \left(\frac{\tau}{\tilde{\tau}^2}(\bar{X} - \bar{Y}) + \bar{P} \right) \cdot \bar{\Theta}, \\
\partial_Y \partial_X L_\gamma(\Theta, \Psi) = {} & -2\frac{\tau}{\tilde{\tau}^2}\mathbf{M}[X]\bar{\Psi} \cdot \bar{\Theta} \\
& - 2(\partial_X \mathbf{M}[X](\Theta)) \left(\frac{\tau}{\tilde{\tau}^2}(\bar{X} - \bar{Y}) + \bar{P} \right) \cdot \bar{\Psi}
\end{aligned}$$

and for the second row we get

$$\partial_X \partial_Y L_\gamma(\Theta,\Psi) = \partial_Y \partial_X L(\Psi,\Theta),$$

$$\partial_Y \partial_Y L_\gamma(\Theta,\Psi) = 2\,\frac{\tau}{\tilde\tau^2}\mathbf{M}[X]\bar\Psi\cdot\bar\Theta - 2\,\tilde\tau\,\partial_Y \mathbf{L}^{\gamma_{zz}}[Y](\Psi)\bar P\cdot\bar\Theta,$$

so that the Hessian in the anisotropic case is

$$\mathrm{Hess}_{[X,Y]} L_\gamma[X^k,Y,P] = \begin{pmatrix} \partial_X\partial_X L_\gamma(\Phi_r e_s,\Phi_{\tilde r} e_{\tilde s}) & \partial_Y\partial_X L_\gamma(\Phi_r e_s,\Phi_{\tilde r} e_{\tilde s}) \\ \partial_X\partial_Y L_\gamma(\Phi_r e_s,\Phi_{\tilde r} e_{\tilde s}) & \partial_Y\partial_Y L_\gamma(\Phi_r e_s,\Phi_{\tilde r} e_{\tilde s}) \end{pmatrix}_{r,\tilde r\in I,s,\tilde s=1,\cdots,m} \tag{6.17}$$

The quadratic program to model Problem (6.2) is given by

$$\begin{aligned} \min_{(\Delta\bar X,\Delta\bar Y)} \quad & W_\gamma[X^k,X^{k,l},Y^l] + \mathrm{grad}_{[X,Y]} W_\gamma[X^k,X^{k,l},Y^l]\cdot(\Delta\bar X,\Delta\bar Y) \\ & + \frac{1}{2}(\Delta\bar X,\Delta\bar Y)^T \mathrm{Hess}_{[X,Y]} L_\gamma[X^{k,l},Y^l,P^l](\Delta\bar X,\Delta\bar Y) \end{aligned} \tag{6.18}$$

$$\text{subject to} \quad A_\gamma^T[X^{k,l},Y^l](\Delta\bar X,\Delta\bar Y) - \partial_Y E_\gamma[X^{k,l},Y^l] = 0 \tag{6.19}$$

and we can formulate the SQP Algorithm 6.2 to solve the two step time discretization for the anisotropic Willmore flow.

6.4 Anisotropic elastic flow of parametrized curves

6.4.1 Finite element space discretization

Let X be an one-dimensional polygonal closed curve with points $X_i \in \mathbb{R}^2$ and line segments T_i with endpoints X_i and X_{i+1}, $i = 0,\cdots,n-1$. The curve is parametrized contra-clockwise. For $X = (X^0,X^1) \in \mathbb{R}^2$ let $X^\perp := (-X^1,X^0)$ denote a clockwise rotation of X through the angle $\frac{\pi}{2}$ that is 90 degree. The normal $N_i[X]$ of the element T_i is given as

$$N_i = N_i[X] = \left(X_i - X_{i+1}\right)^\perp \frac{1}{\|X_i - X_{i+1}\|} = \begin{pmatrix} -\frac{(X_i^1 - X_{i+1}^1)}{\|X_i - X_{i+1}\|} \\ \frac{(X_i^0 - X_{i+1}^0)}{\|X_i - X_{i+1}\|} \end{pmatrix}.$$

Recalling Equations (2.17) and (2.18) it holds that

$$\gamma(N_i[X]) = \frac{1}{\|X_i - X_{i+1}\|}\gamma\left(\left(X_i - X_{i+1}\right)^\perp\right),$$

$$\gamma_z(N_i[X]) = \gamma_z\left(\left(X_i - X_{i+1}\right)^\perp\right).$$

Therefore, given fixed constant $\lambda > 0$ and a parameterization X^k at time step k, in each time step we have to solve the nested variational problem

$$X^{k+1} = \arg\min_X \left(W_\gamma[X^k, X, Y[X]] + \lambda A[X] \right) \quad \text{with} \tag{6.20}$$

$$Y[x] = \arg\min_Y E_\gamma[X, Y],$$

where

$$W_\gamma[X^k, X, Y] = \mathbf{M}[X^k](\bar{X} - \bar{X}^k) \cdot (\bar{X} - \bar{X}^k) + \frac{\tau}{\tilde{\tau}^2} \mathbf{M}[X](\bar{Y} - \bar{X}) \cdot (\bar{Y} - \bar{X}),$$

$$E_\gamma[X, Y] = \mathbf{M}[X](\bar{Y} - \bar{X}) \cdot (\bar{Y} - \bar{X}) + 2\,\tilde{\tau} \sum_{i=0,\cdots,n-1} \gamma\left((Y_i - Y_{i+1})^\perp \right), \tag{6.21}$$

and $A[X] = \sum_{i=0,\cdots,n-1} \|X_i - X_{i+1}\|$ denotes the length of the curve X as in the previous chapter.

Inner variational problem: Discrete anisotropic curve shortening flow

The inner variational problem solves one time step of the anisotropic mean curvature flow. In the case of curves we approximate the anisotropic mean curvature flow for one-dimensional interfaces, the anisotropic curve shortening flow. This two step time discretization is fast and efficient and allows us to choose the time step size of the order of the spatial grid size. The problem of anisotropic or isotropic mean curvature flow has been successfully studied in past years [96, 102, 20, 64, 63, 67, 83, 14, 13, 15].
Recalling again Equations (2.17) and (2.18), it holds that

$$\begin{aligned} E_\gamma[X, Y[X]] &= \mathbf{M}[X](\bar{Y} - \bar{X}) \cdot (\bar{Y} - \bar{X}) + 2\,\tilde{\tau} \sum_{i=0,\cdots,n-1} \gamma(N_i[Y])|T_i| \\ &= \mathbf{M}[X](\bar{Y} - \bar{X}) \cdot (\bar{Y} - \bar{X}) + 2\,\tilde{\tau} \sum_{i=0,\cdots,n-1} \gamma^\perp\left(Y_i - Y_{i+1}\right), \end{aligned}$$

where $\gamma^\perp := \gamma \circ D^{\frac{\pi}{2}}$. To solve the inner variational problem (6.8) we have to calculate the first variation of the anisotropic mean curvature energy E_γ. For a test function Θ we have

$$\begin{aligned} \partial_Y E_\gamma[X, Y[X]](\Theta) &= 2\mathbf{M}[X](\bar{Y} - \bar{X}) \cdot \bar{\Theta} + 2\,\tilde{\tau} \sum_{i \in I} \left(\gamma^\perp\right)_z (Y_i - Y_{i+1}) \cdot (\Theta_i - \Theta_{i+1}) \\ &= 2\mathbf{M}[X](\bar{Y} - \bar{X}) \cdot \bar{\Theta} + 2\,\tilde{\tau} \sum_{i \in I} \begin{pmatrix} \gamma_{z_1}\left((Y_i - Y_{i+1})^\perp\right) \\ -\gamma_{z_0}\left((Y_i - Y_{i+1})^\perp\right) \end{pmatrix} \cdot (\Theta_i - \Theta_{i+1}) \end{aligned}$$

Choosing $\Theta = \Phi_r\, e_s$ we get for the sum in the second summand

$$\begin{aligned} (\mathbf{V}^{\gamma_z}[Y])_{s,r} &= \sum_{i \in I} \left(\gamma^\perp\right)_z (Y_i - Y_{i+1}) \cdot ((\Phi_r\, e_s)_i - (\Phi_r\, e_s)_{i+1}) \\ &= \begin{pmatrix} \gamma^\perp_{z_1}\left((Y_{r-1} - Y_r)\right) \\ -\gamma_{z_0}\left((Y_{r-1} - Y_r)^\perp\right) \end{pmatrix} \cdot (-e_s) + \begin{pmatrix} \gamma_{z_1}\left((Y_r - Y_{r+1})^\perp\right) \\ -\gamma_{z_0}\left((Y_r - Y_{r+1})^\perp\right) \end{pmatrix} \cdot e_s \\ &= (2s-1)\,\gamma_{z_{1-s}}\left((Y_{r-1} - Y_r)^\perp\right) + (1-2s)\gamma_{z_{1-s}}\left((Y_r - Y_{r+1})^\perp\right). \end{aligned}$$

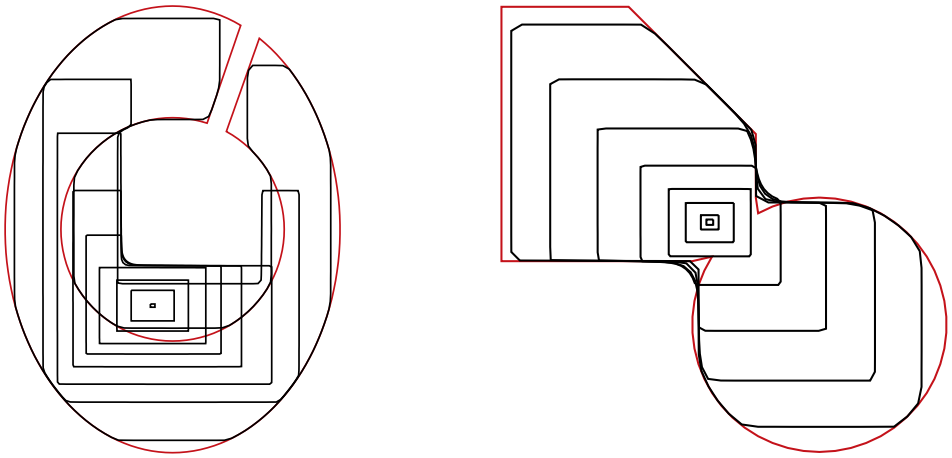

Figure 6.3: We pick up two examples of CHAMBOLLE [36] for the evolution under the anisotropic curve shortening flow with the variational time discretization of anisotropic mean curvature motion. The elliptical integrand is the regularized l^1-norm $\gamma(z) = \sum_{l=1}^{2} \sqrt{\epsilon|z|^2 + z_l^2}$ with $\epsilon = 0.000001$ (cf. Example 2.2.9). The time step $\tilde{\tau}$ is chosen of the order of the spatial grid size. The red curve is the initial curve that converges to a squared point. We show the evolution of the left examples for iterations 1, 20, 40, 60, 80, 100, 120, 140, 250 and for the second examples for iterations 1, 5, 10, 20, 30, 40, 60, 80.

To solve Equation (6.8) with a Newton method, we need the second variation of E_γ. For test functions Θ and Ψ we have

$$\begin{aligned}\partial_Y^2 E_\gamma[X, Y[X]](\Theta, \Psi) &= 2\mathbf{M}[X]\bar{\Theta}\cdot\bar{\Psi} + 2\,\tilde{\tau}\sum_{i\in I}\left(\gamma^\perp\right)_{zz}(Y_i - Y_{i+1})(\Theta_i - \Theta_{i+1})\cdot(\Psi_i - \Psi_{i+1}) \\ &= 2\mathbf{M}[X]\bar{\Theta}\cdot\bar{\Psi} \\ &\quad + 2\,\tilde{\tau}\sum_{i\in I}\begin{pmatrix} \gamma_{z_1z_1}\begin{pmatrix}(Y_i - Y_{i+1})^\perp\end{pmatrix} & -\gamma_{z_1z_0}\begin{pmatrix}(Y_i - Y_{i+1})^\perp\end{pmatrix} \\ -\gamma_{z_0z_1}\begin{pmatrix}(Y_i - Y_{i+1})^\perp\end{pmatrix} & \gamma_{z_0z_0}\begin{pmatrix}(Y_i - Y_{i+1})^\perp\end{pmatrix}\end{pmatrix} \\ &\qquad (\Theta_i - \Theta_{i+1})\cdot(\Psi_i - \Psi_{i+1})\end{aligned}$$

Choosing $\Theta = \Phi_r\, e_s$ and $\Psi = \Phi_{\tilde{r}}\, e_{\tilde{s}}$ we get for the sum in the second summand

$$\begin{aligned}L_{r\tilde{r}}^{\gamma_{z_sz_{\tilde{s}}}}[Y] &= \sum_{i\in I}\left(\gamma^\perp\right)_{zz}(Y_i - Y_{i+1})((\Phi_r\, e_s)_i - (\Phi_r\, e_s)_{i+1})\cdot((\Phi_{\tilde{r}}\, e_{\tilde{s}})_i - (\Phi_{\tilde{r}}\, e_{\tilde{s}})_{i+1}) \\ &= \left(\gamma^\perp\right)_{zz}(Y_{r-1} - Y_r)(-e_s)\cdot((\Phi_{\tilde{r}}\, e_{\tilde{s}})_{r-1} - (\Phi_{\tilde{r}}\, e_{\tilde{s}})_r) \\ &\quad + \left(\gamma^\perp\right)_{zz}(Y_r - Y_{r+1})e_s\cdot((\Phi_{\tilde{r}}\, e_{\tilde{s}})_r - (\Phi_{\tilde{r}}\, e_{\tilde{s}})_{r+1})\,.\end{aligned}$$

Therefore $L^{\gamma_{z_sz_{\tilde{s}}}}[Y] = \left(L_{r\tilde{r}}^{\gamma_{z_sz_{\tilde{s}}}}[Y]\right)_{r\tilde{r}}$ is a tridiagonal matrix

$$L^{\gamma_{z_sz_{\tilde{s}}}}[Y] = \operatorname{tridiag}(L_{r-1}^{\gamma_{z_sz_{\tilde{s}}}}, L_r^{\gamma_{z_sz_{\tilde{s}}}}, L_{r+1}^{\gamma_{z_sz_{\tilde{s}}}})$$

with its corresponding entries

$$\begin{aligned}
L_{r-1}^{\gamma_{z_s z_{\tilde{s}}}} &:= (2s-1)(1-2\tilde{s})\gamma_{z_{1-s}z_{1-\tilde{s}}}\left((Y_{r-1}-Y_r)^{\perp}\right),\\
L_{r}^{\gamma_{z_s z_{\tilde{s}}}} &:= (2s-1)(2\tilde{s}-1)\gamma_{z_{1-s}z_{1-\tilde{s}}}\left((Y_{r-1}-Y_r)^{\perp}\right)\\
&\quad +(1-2s)(1-2\tilde{s})\gamma_{z_{1-s}z_{1-\tilde{s}}}\left((Y_r-Y_{r+1})^{\perp}\right),\\
L_{r+1}^{\gamma_{z_s z_{\tilde{s}}}} &:= (1-2s)(2\tilde{s}-1)\gamma_{z_{1-s}z_{1-\tilde{s}}}\left((Y_r-Y_{r+1})^{\perp}\right)
\end{aligned}$$

in each row. With block matrix $\mathbf{L}^{\gamma_{zz}}[Y]$

$$\mathbf{L}^{\gamma_{zz}}[Y] = \begin{pmatrix} L^{\gamma_{z_0z_0}}[Y] & L^{\gamma_{z_0z_1}}[Y] \\ L^{\gamma_{z_1z_0}}[Y] & L^{\gamma_{z_1z_1}}[Y] \end{pmatrix}$$

we have to solve the following system of equations (cf. (6.12)) in each Newton iteration

$$(2\,\mathbf{M}[X] + 2\,\tilde{\tau}\mathbf{L}^{\gamma_{zz}}[Y])\,\Delta\bar{Y} = -\left(2\,\mathbf{M}[X](\bar{Y}-\bar{X}) + 2\,\tilde{\tau}\mathbf{V}^{\gamma_z}[Y]\right).$$

Numerical solution of the optimization problem

For the dual problem (6.9) we have to solve

$$\partial_Y^2 E_\gamma[X, Y[X]](P,\Theta) = \partial_Y W_\gamma[X^k, X, Y[X]](\Theta)$$

for all test functions Θ, $P = P_i\Phi_i$, $P_i \in \mathbb{R}^2$, $\{\Phi_i\}_{i\in I}$ the nodal basis on the curve. This is equivalent to solve the following linear system of equations (cf. 6.12)

$$(\mathbf{M}[X] + \tilde{\tau}\mathbf{L}^{\gamma_{zz}}[Y])\,\bar{P} = \frac{\tau}{\tilde{\tau}^2}\mathbf{M}[X](\bar{Y}-\bar{X}). \tag{6.22}$$

Implementing the SQP approach to solve the anisotropic Willmore flow, we need the first variation of $L^{\gamma_{z_s z_{\tilde{s}}}}[Y]$. We obtain for its derivatives with respect to a variation of node i in direction k

$$\partial_Y\left(L^{\gamma_{z_s z_{\tilde{s}}}}[Y]\right)(\Phi_i e_k) = \operatorname{tridiag}(\partial_Y L_{r-1}^{\gamma_{z_s z_{\tilde{s}}}}, \partial_Y L_r^{\gamma_{z_s z_{\tilde{s}}}}, \partial_Y L_{r+1}^{\gamma_{z_s z_{\tilde{s}}}})$$

where

$$\begin{aligned}
\partial_Y L_{r-1}^{\gamma_{z_s z_{\tilde{s}}}} &:= (2s-1)(1-2\tilde{s})(1-2\delta_{1k})\gamma_{z_{1-s}z_{1-\tilde{s}}z_{1-k}}\left((Y_{r-1}-Y_r)^{\perp}\right)(\delta_{i(r-1)}-\delta_{ir}),\\
\partial_Y L_{r}^{\gamma_{z_s z_{\tilde{s}}}} &:= (2s-1)(2\tilde{s}-1)(1-2\delta_{1k})\gamma_{z_{1-s}z_{1-\tilde{s}}z_{1-k}}\left((Y_{r-1}-Y_r)^{\perp}\right)(\delta_{i(r-1)}-\delta_{ir})\\
&\quad +(1-2s)(1-2\tilde{s})(1-2\delta_{1k})\gamma_{z_{1-s}z_{1-\tilde{s}}z_{1-k}}\left((Y_r-Y_{r+1})^{\perp}\right)(\delta_{ir}-\delta_{i(r+1)}),\\
\partial_Y L_{r+1}^{\gamma_{z_s z_{\tilde{s}}}} &:= (1-2s)(2\tilde{s}-1)(1-2\delta_{1k})\gamma_{z_{1-s}z_{1-\tilde{s}}z_{1-k}}\left((Y_r-Y_{r+1})^{\perp}\right)(\delta_{ir}-\delta_{i(r+1)}).
\end{aligned}$$

in each row. The corresponding block matrix $\partial_Y\left(\mathbf{L}^{\gamma_{zz}}[Y]\right)(\Phi_i e_k)$ is given by

$$\partial_Y\mathbf{L}^{\gamma_{zz}}[Y](\Phi_i e_k) = \begin{pmatrix} \partial_Y L^{\gamma_{z_0z_0}}[Y] & \partial_Y L^{\gamma_{z_0z_1}}[Y] \\ \partial_Y L^{\gamma_{z_1z_0}}[Y] & \partial_Y L^{\gamma_{z_1z_1}}[Y] \end{pmatrix}.$$

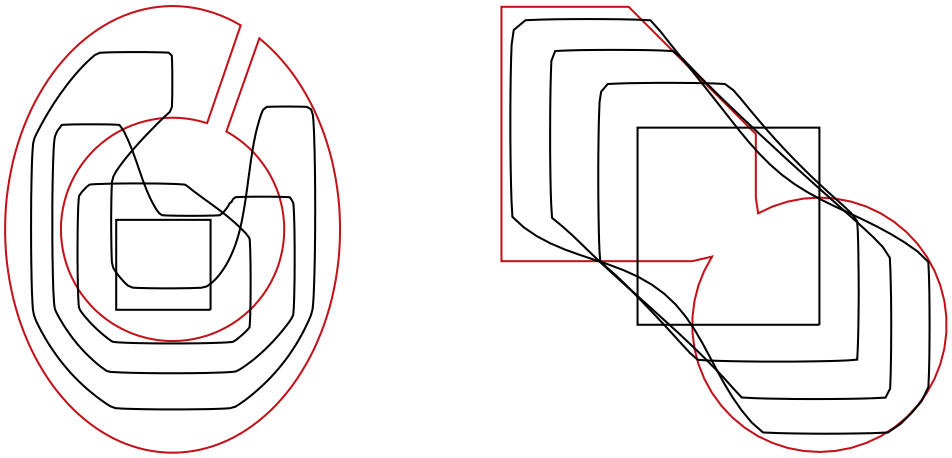

Figure 6.4: Evolution of the two examples from Figure 6.3 under the two step time discretization of the Willmore flow. The elliptical integrand is the regularized l^1-norm $\gamma(z) = \sum_{l=1}^{2} \sqrt{\epsilon|z|^2 + z_l^2}$ with $\epsilon = 0.0001$ (cf. Example 2.2.9). The time step τ is chosen of the order of the spatial grid size. $\tilde{\tau} = \tau^2$ and $\lambda = 0.03$. The initial red curves converge to a square. We show the evolution of the left examples for iterations 30, 60, 90, 120 and for the second examples for iterations 5, 10, 15, 20.

6.4.2 Numerical results

Comparison to exact solutions for radially symmetric evolution

At first we analyze the evolution of circles in the plane under the anisotropic Willmore flow with $\gamma(n) = |n|$ in comparison to the isotropic model of Chapter 4, cf. Table 6.1. As seen above, we first calculate a single fully implicit time step of anisotropic mean curvature motion with a Newton approach instead of a semi-implicit time step of mean curvature motion by solving a linear system of equations. To calculate the in space continuous and time discrete radially symmetric solutions for the inner variational problem we have to solve the mean curvature flow for y, that is

$$\dot{r}(t) = -r(t)^{-1}, \tag{6.23}$$

so that the evolution in time of the radius is given by

$$r(t) = \left(r_0^2 - 2t\right)^{\frac{1}{2}}.$$

Let $\tilde{r}$ be the radius of the curve y that solves the time discrete, but spatially continuous anisotropic mean curvature flow with $\gamma(n) = |n|$

$$\frac{y - x}{\tilde{\tau}} = \Delta_{\mathcal{M}[x]} y\,,$$

cf. Equation (4.26). Then, again by simple calculations, it holds that

$$\frac{\tilde{r} - r}{\tilde{\tau}} = -\frac{1}{\tilde{r}} \quad \Leftrightarrow \quad \tilde{r} = \frac{1}{2} r + \sqrt{\frac{r^2}{4} - \tilde{\tau}}\,,$$

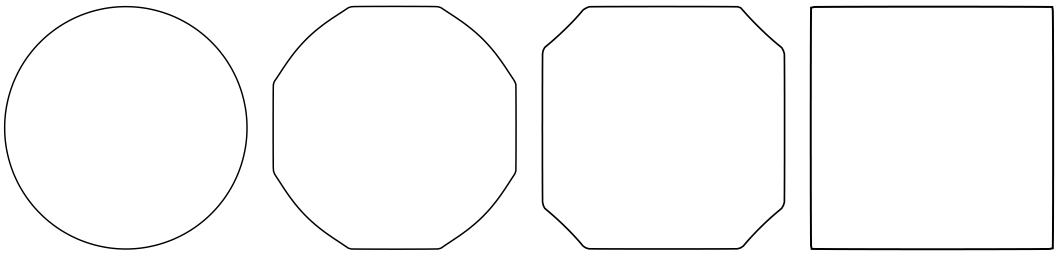

Figure 6.5: Evolution of a circle towards a square under the elastic flow with anisotropy $\gamma(z) = \sum_{l=1}^{2} \sqrt{\epsilon|z|^2 + z_l^2}$, where $\epsilon = 10^{-7}$ is shown. The example underlines that we can chose the anisotropy in our algorithm almost crystalline. The time step τ was chosen of the order of the spatial grid size, $\tilde{\tau} = (\Delta X)^2$ and $\lambda = 0.02$. The curves are scaled to diameter one.

which is an implicit first order scheme for the above ODE (6.23). In the isotropic case this led to the semi-implicit scheme, cf. Equation (4.27),

$$\frac{\tilde{r} - r}{\tilde{\tau}} = -\frac{\tilde{r}}{r^2} \quad \Leftrightarrow \quad \tilde{r} = \frac{r^3}{r^2 + \tilde{\tau}}.$$

Let $\tau, \tilde{\tau}$ be fixed and $x^k = \partial B_{r_k}$ be the circle with radius r_k, $x = \partial B_{r(\tau)}$ be the circle with radius $r := r(\tau)$ and $y = \partial B_{\left(\frac{1}{2}r \pm \sqrt{\frac{r^2}{4} - \tilde{\tau}}\right)}$ the time discrete solution of the evolution of the mean curvature flow. We consider the anisotropic Willmore energy for radial symmetric solutions without length term and $\gamma(n) = |n|$.

$$\begin{aligned} w_\gamma[r] &= \int_{\partial B_{r_k}} (x - x^k)^2 d\sigma + \frac{\tau}{\tilde{\tau}^2} \int_{\partial B_r} (y - x)^2 d\sigma \\ &= 2\pi r_k \left(r - r_k\right)^2 + \frac{\tau}{\tilde{\tau}^2} 2\pi r \left(-\frac{r}{2} \pm \sqrt{\frac{r^2}{4} - \tilde{\tau}} \right)^2 \end{aligned}$$

Therefore we get

$$\begin{aligned} 0 &= \partial_r w_\gamma[r] \\ &= 4\pi r_k (r - r_k) + 4\pi \frac{\tau}{\tilde{\tau}^2} r \left(-\frac{r}{2} \pm \sqrt{\frac{r^2}{4} - \tilde{\tau}} \right) \left(-\frac{1}{2} \pm \frac{r}{4\sqrt{\frac{r^2}{4} - \tilde{\tau}}} \right) \\ &\quad + 2\pi \frac{\tau}{\tilde{\tau}^2} \left(-\frac{r}{2} \pm \sqrt{\frac{r^2}{4} - \tilde{\tau}} \right)^2. \end{aligned}$$

That is equivalent to

$$\frac{r - r_k}{\tau} = -\frac{1}{4\tilde{\tau}^2 r_k} \left(3r^2 - 2\tilde{\tau} \pm \frac{-3r^3 + 8r\tilde{\tau}}{\sqrt{r^2 - 4\tilde{\tau}}} \right) ..$$

Step (k)	**isotropic** L^∞**-Error**	**anisotropic** L^∞**-Error**
0	$6.5339*10^{-6}$	$1.9203*10^{-6}$
1	$1.2954*10^{-5}$	$3.8035*10^{-6}$
2	$1.9278*10^{-5}$	$5.6505*10^{-6}$
3	$2.5494*10^{-5}$	$7.4619*10^{-6}$
4	$3.1608*10^{-5}$	$9.2389*10^{-6}$
5	$3.7623*10^{-5}$	$1.0982*10^{-5}$
10	$6.6292*10^{-5}$	$1.7635*10^{-5}$
10^2	$3.5202*10^{-4}$	$9.2909*10^{-5}$
10^3	$5.6003*10^{-4}$	$1.0451*10^{-4}$
10^4	$3.9209*10^{-3}$	$4.0398*10^{-4}$

Table 6.1: Comparison of the L^∞-Error between the exact solution $r_0((k+1)\tau)$ and the corresponding discrete solution computed by the SQP approach of the two step time discretization of the isotropic Willmore flow and the anisotropic Willmore flow with isotropic anisotropy $\gamma(z) = |z|$ for 2000 polygon vertices (cf. Table 4.1). The L^∞-Error is the maximum of the absolut value of the difference between $r_0((k+1)\tau)$ and $\|X^{k+1}\|$. The time step size equals the grid size. The L^∞-Error of the anisotropic version is smaller than the L^∞-Error of the isotropic algorithm.

Evolution in case of an ellipsoidal Wulff shape

As a first example for the resulting flow we consider the evolution of a curve towards an ellipse under the elastic flow with anisotropy $\gamma(z) = \sqrt{z_0^2 + 4z_1^2}$, cf. Figures 6.1 and 6.2. The initial parametrization is given as

$$x_0(t) = (\sin(t), \cos(t), 0) \text{ for } t \in [0, 2\pi].$$

The computational parameters are $\Delta X = 0.1256$, $\tau = \Delta X$ and $\lambda = 0.025$. In Figures 6.6 and 6.7 we show the evolution of a square towards an ellipse for different grid sizes.

Evolution in case of a cubical Wulff shape

The next example underlines that we can chose the anisotropy in our algorithm almost crystalline. The anisotropy is the regularized l^1-norm

$$\gamma(z) = \sum_{l=1}^{2} \sqrt{\epsilon|z|^2 + z_l^2},$$

with $\epsilon = 10^{-7}$, cf. Figure 6.5.

Evolution of a bunny model under the anisotropic Willmore flow

Figure 6.8 and 6.9 show the evolution of a bunny towards an ellipse for grid sizes $\Delta X = 0.03125$ and $\Delta X = 0.00865$ and in Figure 6.10 towards a square for grid size $\Delta X = 0.00865$.

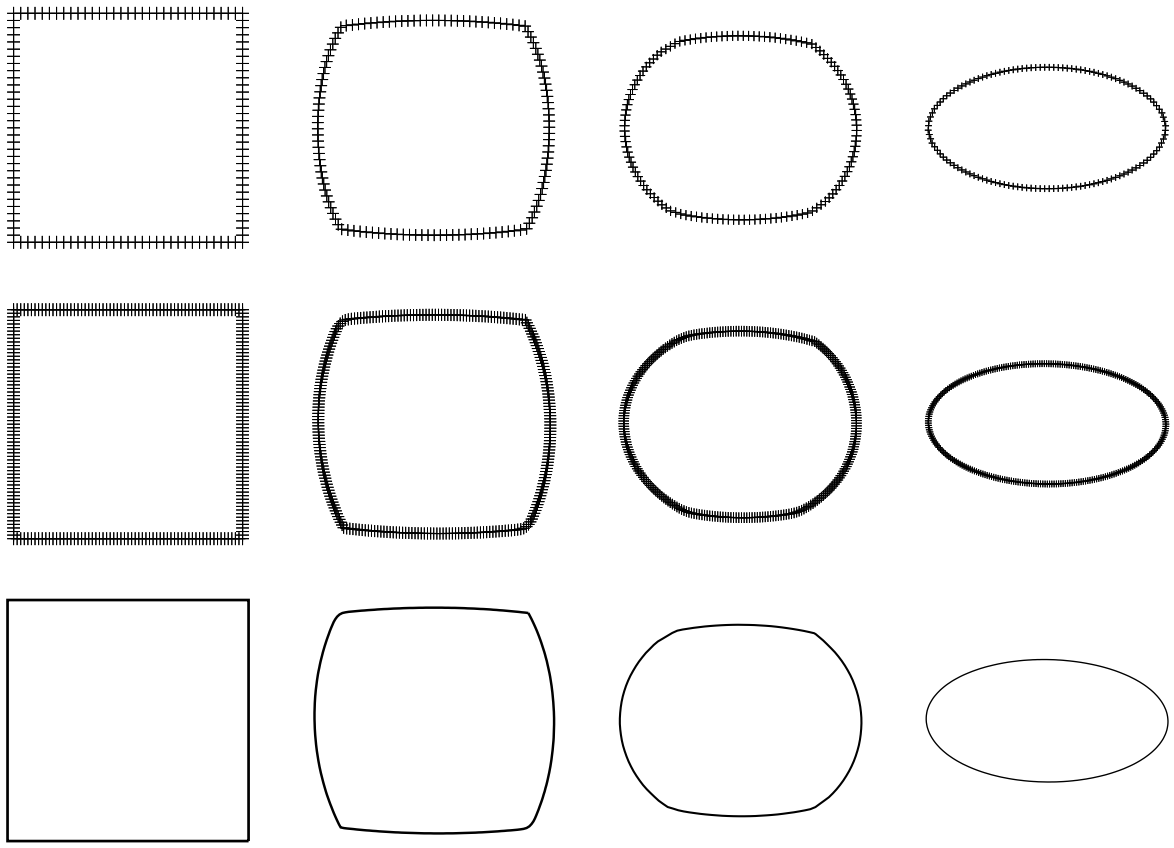

Figure 6.6: Anisotropic Willmore flow for an initial square with 128 (1st row) and 256 line segments (2nd and 3rd row) are shown at times $t = 0.0$, $t = 0.18732$, $t = 0.37464$ and $t = 0.56196$, where $\Delta X = 0.09366$ and $\Delta X = 0.046875$, respectively.

6.5 Remark on the anisotropic Willmore flow for surfaces

We have seen that the two step time discretization of the anisotropic Willmore flow of polygonal curves is stable and effectively allows for time steps of the order of the spatial grid size. In this thesis we also derived the scheme for the anisotropic Willmore flow for surfaces, but its implementation is ongoing research. Due to the fact that the formulation of the two step time discretization of the anisotropic Willmore flow incorporates only the anisotropy and not its derivatives, it seems to be promising that we can chose e.g. the regularized l^1-anisotropy $\gamma(z) = \sum_{l=1}^{3} \sqrt{\epsilon|z|^2 + z_l^2}$ with $\epsilon > 0.001$ in comparison to the semi-implicit scheme, where ϵ was chosen 0.01 or 0.001.

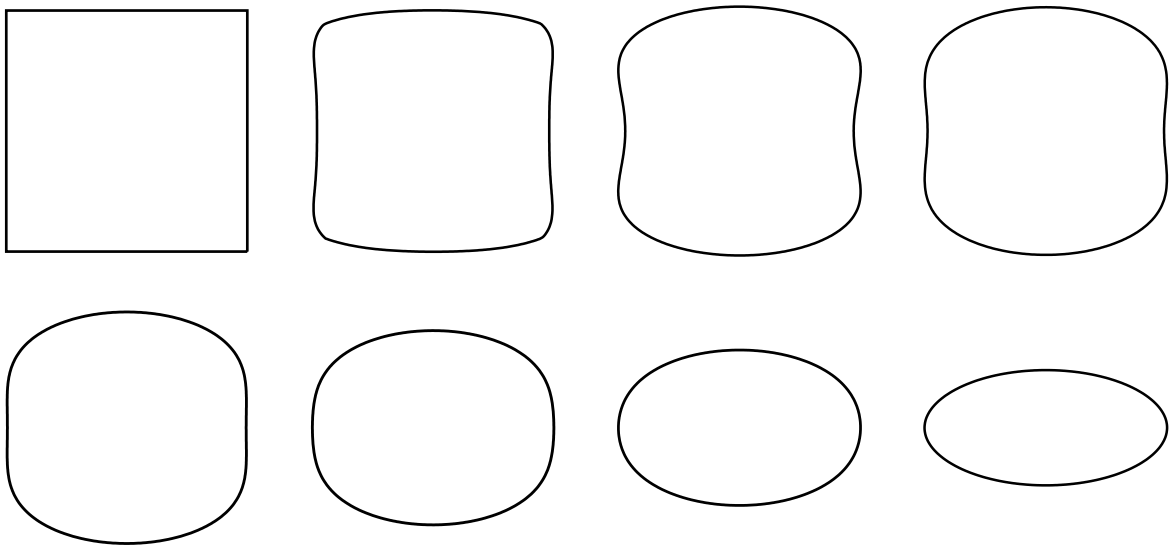

Figure 6.7: Anisotropic Willmore flow for an initial square with 1024 line segments is shown at times $t = 0.0$, $t = 0.048308$, $t = 0.096616$, $t = 0.132847$, $t = 0.18732$, $t = 0.37464$, $t = 0.46832$ and $t = 0.56196$, with $\tau = \Delta X = 0.02344$ and $\tilde{\tau} = (\Delta X)^2 = 5.5 * 10^{-4}$, cf. Figure 6.6.

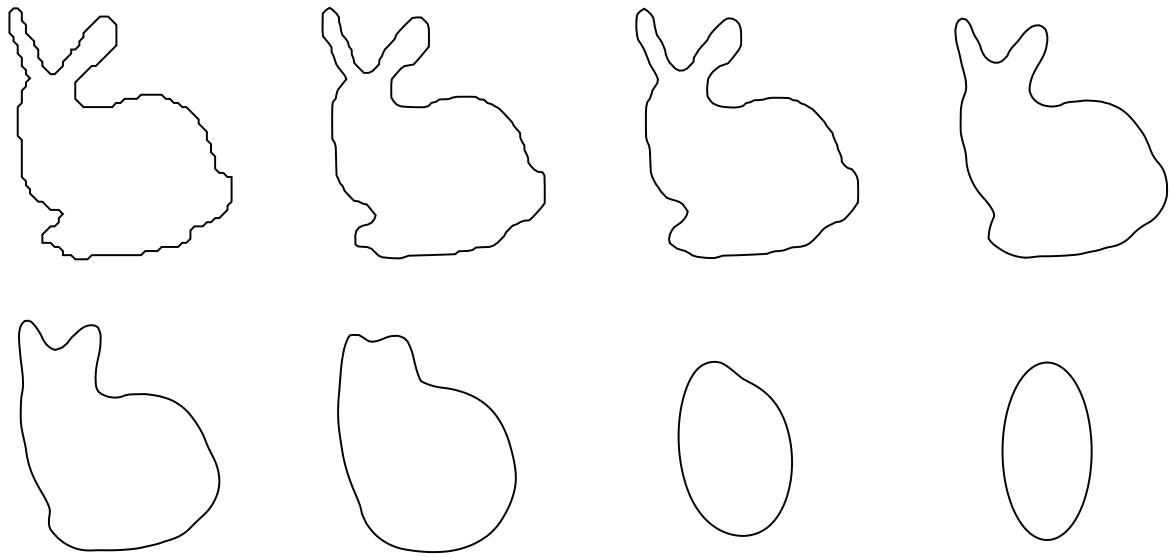

Figure 6.8: Evolution of a bunny with 218 nodes towards an ellipse. The time step size $\tau = \Delta X = 0.03125$ equals the spacial grid size. λ was chosen 0.025 and $\tau \tilde{=} (\Delta X)^2$. We show the bunny at time steps 0, 1, 2, 5, 7, 10, 14, 20.

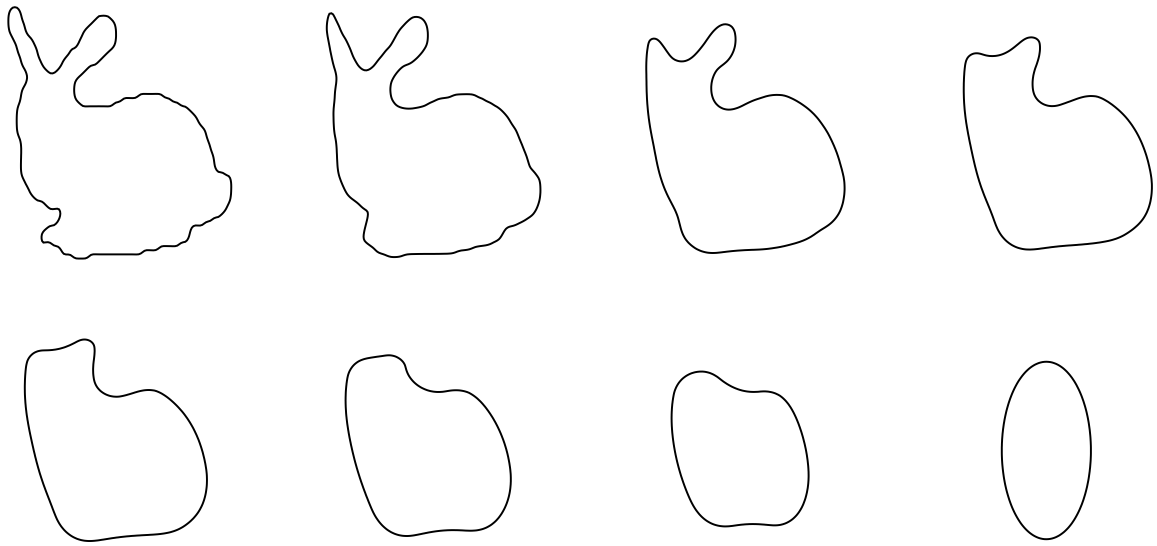

Figure 6.9: Evolution of a bunny with 436 nodes towards an ellipse. The time step size $\tau = \Delta X = 0.00865$ equals the spacial grid size. λ was chosen 0.025 and $\tau \doteq (\Delta X)^2$. We show the bunny at time steps 0, 5, 10, 30, 50, 100, 200, 300.

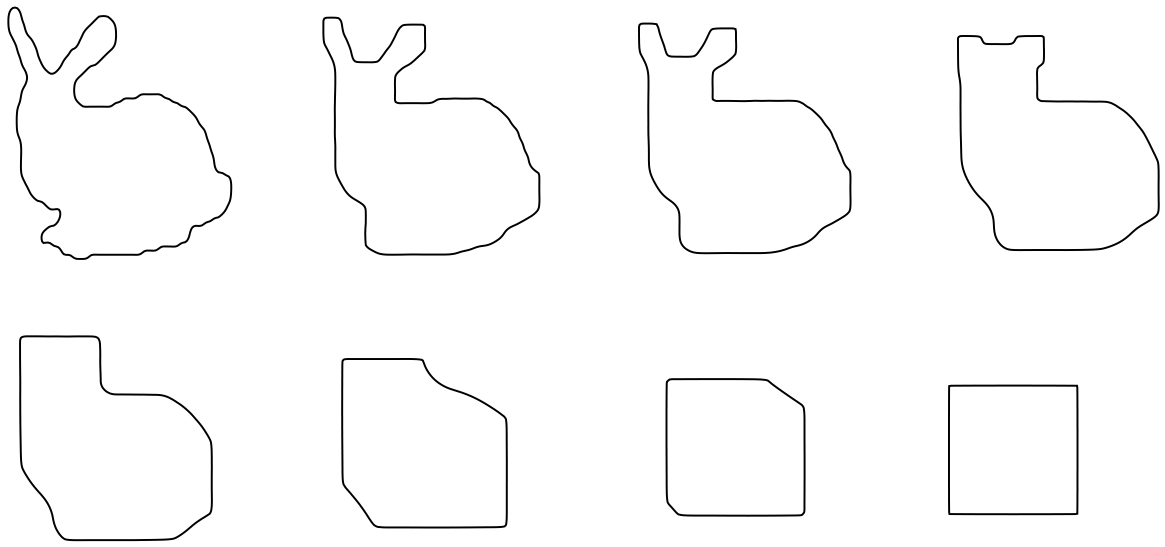

Figure 6.10: Evolution of a bunny with 436 nodes towards a square under the elastic flow with anisotropy $\gamma(z) = \sum_{l=1}^{2} \sqrt{\epsilon|z|^2 + z_l^2}$, where $\epsilon = 1.0e^{-7}$. The time step size $\tau = \Delta X = 0.00865$ equals the spacial grid size. $\tilde{\tau} = \tau$. λ was chosen 0.025. We show the bunny at time steps 0, 10, 20, 40, 60, 80, 150, 230, 250.

Chapter 7

Variational methods for surface matching

FINDING a correspondence between two surfaces is a fundamental step in many geometry processing operations. A correspondence between two surfaces is a mapping from one onto the other that respects certain properties of the surfaces. A variational method for matching three-dimensional surfaces based on finding a minimizing deformation between their two-dimensional parameter domains was developed by LITKE ET AL. [126]. In this chapter, we prove the existence of minimizers of the matching energy, which are the optimal matching deformations, applying the direct methods from the Calculus of Variations. We proof global injectivity and regularity of the optimal matching deformations, so that we can expect to obtain smooth deformations that are free of folds and singularities, cf. Figure 7.1. The matching energy does not lend itself to a robust numerical minimization, thus we establish a suitable approximation. In the minimization algorithm, already a gradient descent method require the calculation of the derivatives of the energy with respect to the deformations, which incorporate integrals over the boundary. We avoid this by extending the dependent-domain of integration to a superset and introducing a regularized characteristic function to ignore the energy contributions at some distance away from the formally dependent-domain. We prove the existence of minimizing deformations for the approximation and show by Γ-convergence that the sequence of minimizers of the approximating energy converges to the solution of the limit problem.
The approach is based on mapping geometric attributes like the metric and mean curvature into the two-dimensional parameter plane and employing well-established non-rigid matching techniques from **image processing** in the parameter domains of the surfaces, which avoids the problems that come with matching triangulations in three dimension [3, 177]. **Image matching**, also known as image registration, is one of the fundamental tasks in image processing. For a detailed exposition we refer to [53, 78, 52, 75, 146]. Given a reference image $u_A : \omega \to \mathbb{R}$ and a template image $u_B : \omega \to \mathbb{R}$ one asks for a general non rigid spatial deformation $\phi : \omega \to \omega$ such that $u_B \circ \phi$ is optimally correlated to u_A. The parameter domain $\omega \subset \mathbb{R}^2$ is supposed to be bounded with Lipschitz boundary. Searching for a direct correspondence between the image intensities the basic matching energy is given by

$$\mathcal{E}_m[\phi] := \int_\omega |u_A(\xi) \circ \phi - u_B(\xi)|^2 \, d\xi.$$

As boundary condition we constrain ϕ to be the identity on $\partial\omega$. In the surface matching

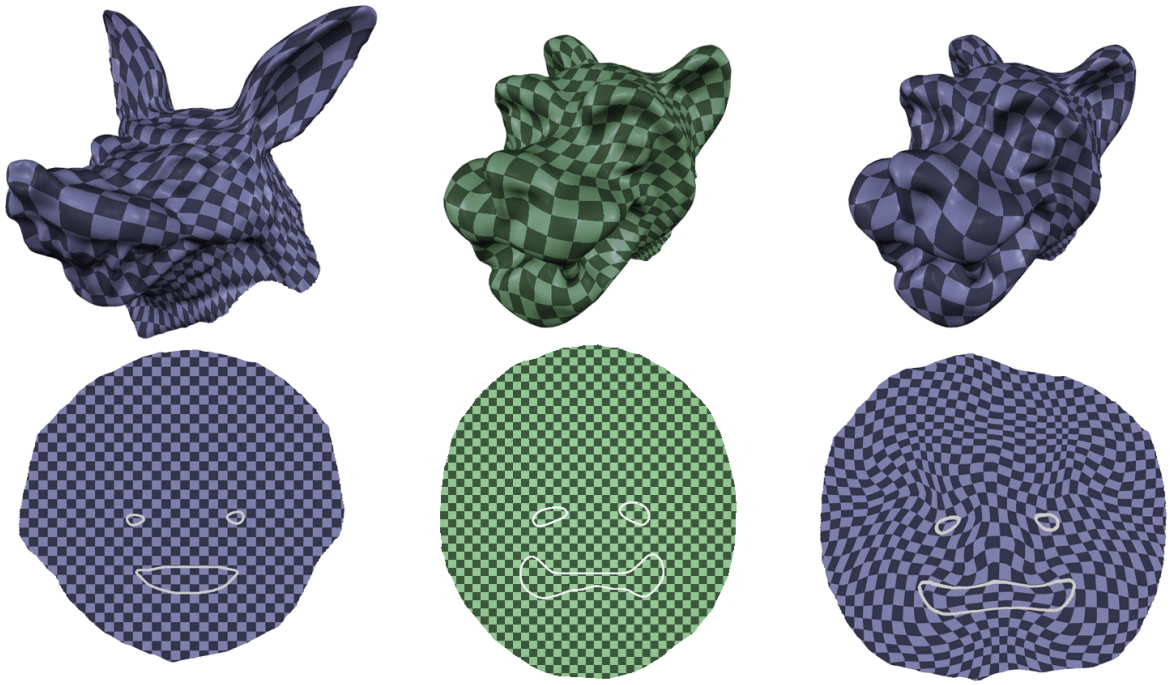

Figure 7.1: A checkerboard is texture mapped onto the surfaces (top). The optimal matching deformation between the first and second (green) surface is shown in the parameter domain on the right (bottom). It is smooth and regular, even where the distortion is high, e.g. around the outlines of the mouth and eyes. Image courtesy of LITKE ET AL. [126].

approach, this idea represented by a **bending energy** $\mathcal{E}_{bend}$ which measures the squared L^2-error with respect to mean curvatures of the two surfaces. The corresponding minimization problem is known to be ill-posed if one considers the infinite space of deformations [101, 165]. Therefore one ask for a suitable regularization energy. Different regularization approaches have been proposed [43, 42, 62]. We are searching for a regularization energy which in particular also allows to control area shrinkage and simultaneously ensures continuity and injectivity for the minimizing deformation. Therefore we confine to hyperelastic energy functionals $\mathcal{E}_{elast}[\phi]$ on deformations ϕ based on classical concepts from continuum mechanics and in particular from the theory of elasticity [44, 128]. Let ω be an isotropic elastic body where the identity represents the stress free deformation. Let us consider the change of length and area under a deformation ϕ. The length of a curve $\gamma : [0,1] \to \omega$ under the deformation ϕ is given by

$$a[\phi \circ \gamma] = \int_0^1 \left|\partial_t \left(\phi \circ \gamma\right)\right| \mathrm{d}t = \int_0^1 \sqrt{D\phi^T D\phi \dot{\gamma} \cdot \dot{\gamma}}\, \mathrm{d}t. \tag{7.1}$$

Hence, just as $\sqrt{\mathrm{tr}\left(A^T A\right)}$ measures the average change of length under a linear mapping A, the Frobenius norm $|D\phi|_2 = \sqrt{\mathrm{tr}\left(D\phi^T D\phi\right)}$, cf. Definition 2.1.8, controls the average

change of length under the linear mapping $D\phi$. The corresponding change of area in an isotropic elastic body is obviously measured by $\det(D\phi)$:

$$\text{area}(\phi(\tilde{\omega})) = \int_{\tilde{\omega}} |\det(D\phi(x))| \, \mathrm{d}x \tag{7.2}$$

for an area patch $\tilde{\omega} \subset \omega$. If $\det(D\phi(x)) < 0$, self penetration may be observed. The isotropic elastic energy which separately cares about length and area deformation and especially penalizes area shrinkage is then defined by

$$\mathcal{E}_{elast}[\phi] := \int_{\omega} W(|D\phi(x)|^2, \det(D\phi(x))) \, \mathrm{d}x,$$

where $W : \mathbb{R}^2 \to \mathbb{R}$ is supposed to be convex and fulfills a growth condition prescribed next. Clarenz, Litke & Rumpf [56] derived a class of simple energy functionals based on a set of natural axioms for measuring the distortion of a single parametrization. The concrete energy density is then

$$W(a,d) := \alpha_l a^{\frac{p}{2}} + \alpha_a \left(d^{\frac{r}{2}} + \beta d^{-\frac{s}{2}} \right), \tag{7.3}$$

with $r,s > 0$, $\alpha_l, \alpha_a, \beta > 0$, $a = a(A) = \operatorname{tr}\left(A^T A\right)$ and $d = d(A) = \det(A)$ for a matrix $A \in \mathbb{R}^{2,2}$. W depends on the principal invariants $\iota_A := (\operatorname{tr}(A), det(A))$ of the Jacobian matrix of the deformation ϕ. Here, $\alpha_l a^{\frac{p}{2}}$ controls the length change under the deformation. Since

$$\lim_{d\to\infty} \alpha_a \left(d^{\frac{r}{2}} + \beta d^{-\frac{s}{2}} \right) = \lim_{d\to 0} \alpha_a \left(d^{\frac{r}{2}} + \beta d^{-\frac{s}{2}} \right) = \infty$$

the second summand of the energy density penalizes area compression and expansion under the deformation. The energy $\widetilde{W} : \mathbb{R}^{2,2} \to \mathbb{R}$

$$\widetilde{W}(A) := W(|A|^2, \det(A))$$

is not convex, but *polyconvex* [58]. A function $\widetilde{F} : \mathbb{R}^{2,2} \to \mathbb{R}$, $A \mapsto \widetilde{F}(A)$ is referred to as polyconvex if there exists a convex function $F : \mathbb{R}^2 \to \mathbb{R}$ such that

$$\widetilde{F}(A) = F(A, \det A).$$

In our surface matching problem, we consider the surfaces as thin elastic shells. Then, surface deformations lead to tangential stretching and shearing, cf. Figure 1.2 (2) in the introduction. Therefore, we incorporate a **regularization energy** $\mathcal{E}_{reg}$ to control length and area changes in the induced non-rigid deformation between the two surfaces. Its energy density is given by (7.3) depending on a distortion tensor that measures distortion between tangential vectors on the two surfaces.

In an early work of Lee et al. [122], parameterizations of the meshes over a common parameter domain are used to establish a direct correspondence between them. Typically these methods are driven by user-supplied feature correspondences which are then used to drive a mutual parametrization. The main difficulty is the proper alignment of selected features

during the parameterizations process [115, 142, 153]. In our approach, we cover the two parameter domains of the surfaces to be matched with user-defined feature characteristics. A **feature energy** $\mathcal{E}_{\mathcal{F}}$ then measures the mismatch of features and we avoid point-wise constraints. GU & VEMURI [107] considered one-to-one correspondence of topological spheres through conformal maps with applications to brain matching. Therefore, they do not have to address the difficult problem of partial correspondences between surfaces with boundaries.

7.1 Variational model

Our goal is to correlate two surface patches, $\mathcal{M}_A$ and $\mathcal{M}_B$, through a non-rigid spatial deformation,

$$\phi_{\mathcal{M}} : \mathcal{M}_A \to \mathbb{R}^3$$

such that corresponding regions of $\mathcal{M}_A$ are mapped onto regions of $\mathcal{M}_B$. As already described in the introduction, we consider the first surface as a thin shell which we press into a mould representing the second surface, cf. Figure 1.2. One can distinguish between stresses induced by stretching and compression, and stresses induced by bending that occurs in the surface as it is being pressed. Thus, $\phi_{\mathcal{M}}$ can be regarded as the deformation of such a thin shell. We assume this deformation to be elastic. We give a short overview of the variational approach developed in LITKE ET AL. [126]. The matching energy consists of three energy contributions. A regularization energy measures the induced in-plane stresses, and the concrete energy density allows control over length and area distortion in this surface-to-surface deformation. Since we are aiming for a proper correspondence of shape, we incorporate the bending of normals in our energy. Furthermore, surfaces are characterized by geometric or texture features which should be matched properly as well. We reflect this in the variational approach with a third energy which penalizes a non-proper match of feature lines drawn on the surface.

7.1.1 Measuring distortion via a deformation

Let x_A and x_B be parametrizations of the surfaces $\mathcal{M}_A$ and $\mathcal{M}_B$ defined in an initial step, cf. Equation (2.12) in Section 2.1. Their metrics are defined on the parameter domains denoted by ω_A and ω_B, respectively,

$$g_C = Dx_C^T Dx_C \tag{7.4}$$

where $Dx_C \in \mathbb{R}^{3,2}$ is the Jacobian of the parameterization x_C, $C = A, B$. First, let us consider deformations $\phi : \omega_A \to \omega_B$ which are one-to-one. A deformation ϕ between the parameter domains induces a deformation between the surface patches $\phi_{\mathcal{M}} : \mathcal{M}_A \to \mathcal{M}_B$ defined by

$$\phi_{\mathcal{M}} := x_B \circ \phi \circ x_A^{-1}.$$

The complete mapping is illustrated in Figure 7.2. We have seen, cf. Equation (7.1) and (7.2), that, in elasticity, the distortion under an elastic deformation ϕ is measured by the Cauchy-Green strain tensor $D\phi^T D\phi$. We wish to adapt this definition to measure the distortion between tangent vectors on the two surfaces, as we did with the metric $g = Dx^T Dx$

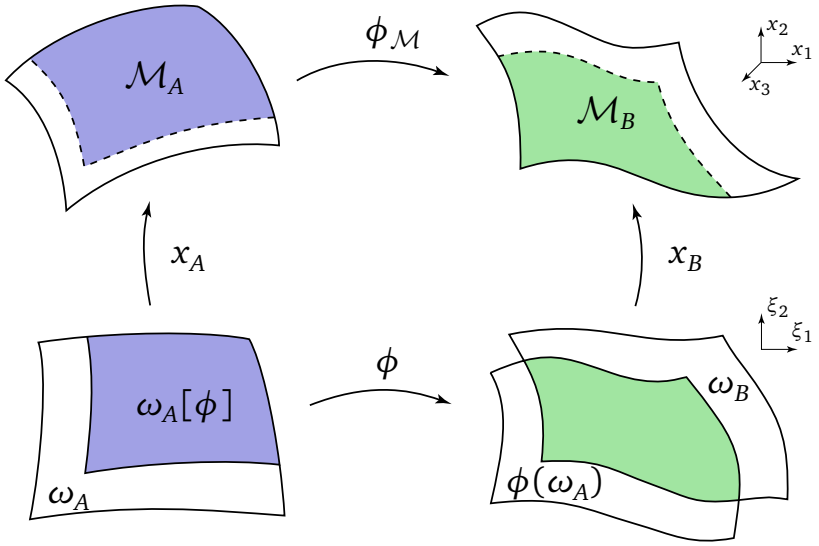

Figure 7.2: The matching function $\phi_{\mathcal{M}} := x_B \circ \phi \circ x_A^{-1}$ is a mapping between the corresponding shaded regions of the two surfaces. The partial correspondence is defined on $\omega_A[\phi] = \phi^{-1}(\phi(\omega_A) \cap \omega_B)$ in 2D. Image courtesy of LITKE ET AL. [126].

in Section 2.1,cf. Equation (2.13) and (2.14). Incorporating the metrics g_A and g_B at the deformed position, the distortion from the surface $\mathcal{M}_A$ onto the surface $\mathcal{M}_B$ is controlled by a distortion tensor $\mathcal{G}[\phi] \in \mathbb{R}^{2,2}$,

$$\mathcal{G}[\phi] = g_A^{-1} D\phi^T (g_B \circ \phi) D\phi \,, \tag{7.5}$$

acting on tangent vectors in the parameter domain ω_A. Mathematically, this tensor is defined implicitly via the identity $(g_A \mathcal{G}[\phi] v) \cdot w = (g_B \circ \phi) D\phi\, v \cdot D\phi\, w$ for tangent vectors v, w on the surface $\mathcal{M}_A$ and their images as tangent vectors $D\phi\, v, D\phi\, w$ on $\mathcal{M}_B$, where here we have identified tangent vectors on the surfaces with vectors in the parameter domains. As above $\sqrt{\operatorname{tr} \mathcal{G}[\phi]}$ measures the average *change of length* of tangent vectors from $\mathcal{M}_A$ when being mapped onto $\mathcal{M}_B$ and $\sqrt{\det \mathcal{G}[\phi]}$ measures the *change of area* under the deformation $\phi_{\mathcal{M}}$. The regularization energy is then defined by

$$\mathcal{E}_{reg}[\phi] = \int_{\omega_A} W(\operatorname{tr} \mathcal{G}[\phi], \det \mathcal{G}[\phi]) \sqrt{\det g_A}\, d\xi$$

with following energy density

$$W(a, d) = \alpha_l a^{\frac{p}{2}} + \alpha_a \left(d^{\frac{r}{2}} + \beta d^{-\frac{s}{2}} \right), \tag{7.6}$$

cf. Equation (7.3), with $2 < p < \infty$, $r > 1$, $s > \frac{p}{p-2}$ and $\alpha_l, \alpha_a, \beta > 0$. $a = a(A) = \operatorname{tr} \mathcal{G}[\phi]$ controls length distortion, whereas $d = d(A) = \det \mathcal{G}[\phi]$ penalizes area expansion and d^{-1} area compression. The weights α_l, α_a are chosen by the user preference to the relative importance of length and area distortion.

7.1.2 Measuring bending via a deformation

When we press a given surface $\mathcal{M}_A$ into the mould of a surface $\mathcal{M}_B$, a major source of stress results from the bending of normals. We assume these stresses to be elastic as well and to depend on changes in normal variations under the deformation. Variations of normals are represented in the metric by the shape operator. We define the shape operator $S \in \mathbb{R}^{2,2}$ of the surface $\mathcal{M}$ with respect to the parameterization x as the representation of the normal variation in the metric, i.e.

$$(g\,S\,v)\cdot w = Dn\,v\cdot Dx\,w\,,$$

where n is the normal field on $\mathcal{M}$. Thus $S_A = g_A^{-1}(Dx_A)^T Dn_A$. For $S_B[\phi]$ at the deformed position $\phi_{\mathcal{M}}(x)$ with respect to the metric g_A, we obtain

$$\begin{aligned}(g_A S_B[\phi]\,v)\cdot w &= D(n_B\circ\phi)\,v\cdot D(x_B\circ\phi)\,w\\ &= (Dn_B\circ\phi)\,D\phi\,v\cdot(Dx_B\circ\phi)\,D\phi\,w\end{aligned}$$

and deduce

$$\begin{aligned}S_B[\phi] &= g_A^{-1}\,D\phi^T\,(Dx_B\circ\phi)^T\,(Dn_B\circ\phi)\,D\phi\\ &= g_A^{-1}\,D\phi^T\,(g_B\circ\phi)(S_B\circ\phi)\,D\phi,\end{aligned}$$

where S_B is the shape operator of the surface $\mathcal{M}_B$ taking into account the original metric g_B. Up to a factor $\frac{1}{2}$, the average change of the normal variation on the tangent space $\mathcal{T}_x\mathcal{M}_A$ is given by

$$\begin{aligned}\operatorname{tr}\left(S_B[\phi]-S_A\right) &= \operatorname{tr}\left(g_A^{-1}\,D\phi^T\,(g_B\circ\phi)(S_B\circ\phi)\,D\phi - S_A\right)\\ &= \operatorname{tr}\left((S_B\circ\phi)\,D\phi\;g_A^{-1}\,D\phi^T\,(g_B\circ\phi) - S_A\right)\\ &= \operatorname{tr}\left((S_B\circ\phi)\,D\phi\;\mathcal{G}[\phi]\,D\phi^{-1} - S_A)\right),\end{aligned}$$

where we use that $\operatorname{tr}(A+B)=\operatorname{tr}(A)+\operatorname{tr}(B)$ and $\operatorname{tr}(AB)=\operatorname{tr}(BA)$. Neglecting the impact of the metric distortion $\mathcal{G}[\phi]$, we decouple bending completely from tangential distortion. If $\mathcal{G}[\phi]$ is the identity mapping $\mathbb{I}$, we have

$$\operatorname{tr}(S_B\circ\phi)-\operatorname{tr}(S_A)$$

as a local *measure for the bending of normals*. Since the trace of the shape operator is the mean curvature, we can instead aim to compare the mean curvature $\mathbf{h}_B = \operatorname{tr}(S_B)$ of the surface $\mathcal{M}_B$ at the deformed position $\phi_{\mathcal{M}}(x)$ and the mean curvature $\mathbf{h}_A = \operatorname{tr}(S_A)$ of the surface $\mathcal{M}_A$. A similar observation was used by GRINSPUN ET AL. [105] to define a bending energy for discrete thin shells. Finally, we define the following bending energy

$$\mathcal{E}_{bend}[\phi] = \int_{\omega_A} (\mathbf{h}_B\circ\phi - \mathbf{h}_A)^2\sqrt{\det g_A}\,d\xi\,. \tag{7.7}$$

By minimizing this energy, we ensure that the deformation properly matches mean curvature on the surfaces, although an energy depending solely on $\mathbf{h}_B\circ\phi-\mathbf{h}_A$ does not recognize, if the deformation aligns a curve with positive curvature on the first surface to a curve with negative curvature on the second surface and vice versa.

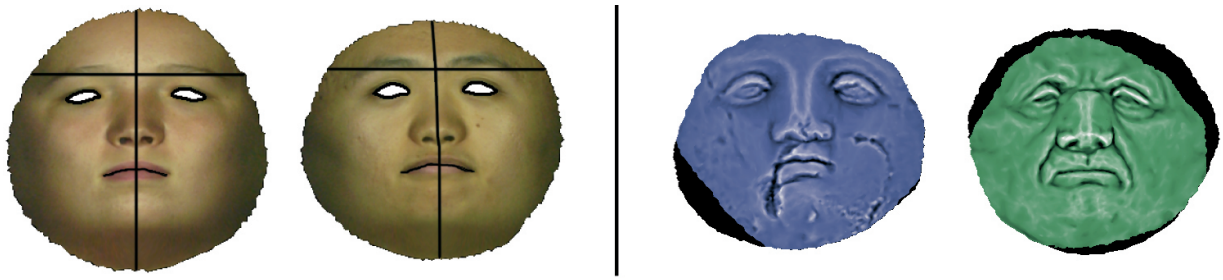

Figure 7.3: The two-dimensional parameter domains of the three-dimensional surfaces of Figures 7.5 and 7.6 are shown. Quantities such as texture maps can be mapped onto the domains. The desired feature sets are marked in the image domains (left). For surfaces with boundaries, a partial correspondence is often desired. The correspondence is defined where their parameter domains intersect under the matching deformation (right). The unmatched regions are in black. Image courtesy of LITKE ET AL. [126].

7.1.3 Matching features

To match geometric or texture features properly, we incorporate a correspondence of feature sets in the variational approach to match characteristic lines drawn on the surface. We denote the feature sets by $\mathcal{F}_{\mathcal{M}_A} \subset \mathcal{M}_A$ and $\mathcal{F}_{\mathcal{M}_B} \subset \mathcal{M}_B$ on the respective surfaces. Furthermore, let $\mathcal{F}_A \subset \omega_A$ and $\mathcal{F}_B \subset \omega_B$ be the corresponding sets on the parameter domains. The feature sets on the surface have co-dimension two. We are aiming for a proper match of these sets via the deformation, i.e.

$$\phi_{\mathcal{M}}(\mathcal{F}_{\mathcal{M}_A}) = \mathcal{F}_{\mathcal{M}_B}$$

or in terms of differences,

$$\mathcal{F}_{\mathcal{M}_A} \setminus \phi_{\mathcal{M}}^{-1}(\mathcal{F}_{\mathcal{M}_B}) = \emptyset \qquad \text{and} \qquad \mathcal{F}_{\mathcal{M}_B} \setminus \phi_{\mathcal{M}}(\mathcal{F}_{\mathcal{M}_A}) = \emptyset,$$

so that the energy

$$\mathcal{E}_{\mathcal{H}} := \mathcal{H}^1\left(\mathcal{F}_{\mathcal{M}_A} \setminus \phi_{\mathcal{M}}^{-1}(\mathcal{F}_{\mathcal{M}_B})\right) + \mathcal{H}^1\left(\mathcal{F}_{\mathcal{M}_B} \setminus \phi_{\mathcal{M}}(\mathcal{F}_{\mathcal{M}_A})\right) \tag{7.8}$$

with one-dimensional Hausdorff measure $\mathcal{H}^1$ penalizes a non proper match of one-dimensional feature lines drawn on the surface. But, numerically, we mark the desired feature sets in the image domains that are discretized by regular grids. Therefore, the actual feature lines are pixel lines or regions drawn by the user on the texture image with a pen of at least one pixel width, cf. Figure 7.3. Thus, the feature lines are now two-dimensional sets and we propose the feature energy

$$\mathcal{E}_{\mathcal{F}}[\phi] = \gamma_{\mathcal{F}}\left(\mathcal{L}_A\left(\mathcal{F}_A \setminus \phi^{-1}(\mathcal{F}_B)\right) + \mathcal{L}_B\left(\mathcal{F}_B \setminus \phi(\mathcal{F}_A)\right)\right), \tag{7.9}$$

where

$$\mathcal{L}_A(\Omega) := \int_{\omega_A} \chi_\Omega \sqrt{\det g_A}\, d\xi \tag{7.10}$$

is the Lebesgue measure of a set Ω with respect to the metric g_A on ω_A. $\mathcal{L}_B(\Omega)$ is defined analogously:

$$\mathcal{L}_B(\Omega) := \int_{\omega_B} \chi_\Omega \sqrt{\det g_B}\, d\xi. \tag{7.11}$$

Let $\mathcal{L}(\cdot)$ denote the Lebesgue measure. $\gamma_{\mathcal{F}}$ is a fixed constant of order one in case of feature sets that have a variable width (e.g. eyes on a face) and $\frac{1}{w}$ for feature lines with constant width w. This energy is an approximation of the length of one-dimensional feature lines and the one-dimensional Hausdorff measure, respectively, as the width of the feature sets tends to zero.

7.2 Existence of an optimal surface matching

Our final matching energy consists of three different cost functionals. The class of energy functionals that measure the regularity of a surface deformation,

$$\mathcal{E}_{reg}[\phi] = \int_{\omega_A} W(\operatorname{tr} \mathcal{G}[\phi], \det \mathcal{G}[\phi]) \sqrt{\det g_A}\, d\xi \tag{7.12}$$

with the energy density given as in Equation (7.6). Since we also want to match surfaces where certain subregions of $\mathcal{M}_A$ have no corresponding counter part on $\mathcal{M}_A$ and vise versa, we cannot expect that $\phi(\omega_A) = \omega_B$, cf. Figure 7.3. But assuming high enough regularity of the parameterizations, the metric function g_B is continuous and we denote its continuous extension of g_B onto $\phi(\omega_A) \cup \omega_B$ again by g_B. Hence the energy $\mathcal{E}_{reg}$ is well defined. As above motivated, the following bending energy, cf. Equation (7.7),

$$\mathcal{E}_{bend}[\phi] = \int_{\omega_A} (\mathbf{h}_B \circ \phi - \mathbf{h}_A)^2 \sqrt{\det g_A}\, d\xi\,,$$

measures the bending of normals to ensure a proper correspondence of the shape. $\mathbf{h}_A$ and $\mathbf{h}_B$, respectively, denote the mean curvature of the corresponding surfaces. If $\phi(\omega_A) \neq \omega_B$ we incorporate the characteristic function χ_{ω_B} into the energy density and define $\phi_{\mathcal{M}}$ only on $x_A(\omega_A[\phi])$ where

$$\omega_A[\phi] := \phi^{-1}(\phi(\omega_A) \cap \omega_B)$$

is the corresponding subset of the parameter domain ω_A. We define the new bending energy as

$$\mathcal{E}_{bend}[\phi] = \int_{\omega_A} \chi_{\omega_B} \circ \phi \left(\mathbf{h}_B \circ \phi - \mathbf{h}_A\right)^2 \sqrt{\det g_A}\, d\xi\,. \tag{7.13}$$

Supposing that g_B, initially only defined on ω_B, is extended to $\mathbb{R}^2$ it is still useful for $\mathcal{E}_{reg}$ to control the regularity of the deformation outside the actual matching domain $\omega_A[\phi]$. The

third energy contribution $\mathcal{E}_{\mathcal{F}}$, cf. (7.9), penalizes a non-proper match of two-dimensional feature lines marked in the images domains. We define the global matching energy

$$\mathcal{E}[\phi] := \beta_{bend}\,\mathcal{E}_{bend}[\phi] + \beta_{reg}\,\mathcal{E}_{reg}[\phi] + \beta_{\mathcal{F}}\,\mathcal{E}_{\mathcal{F}}[\phi]\,, \tag{7.14}$$

which measures the quality of a matching deformation ϕ on the domain ω_A. The weights $\beta_{bend}, \beta_{reg}, \beta_{\mathcal{F}}$ are chosen by the user's preference. Applying the direct method in the Calculus of Variations, cf. DACOROGNA [58], it is possible to prove the existence of minimizing deformations for the matching energy:

Theorem 7.2.1. (Existence of minimizing deformations.)
Suppose $\mathcal{M}_A$ and $\mathcal{M}_B$ are $\mathcal{C}^2-$surfaces. Let x_A and x_B be their bi-Lipschitz continuous parameterizations over the bounded parameter domains ω_A and ω_B with Lipschitz boundary. Consider the total energy (7.14) *with β_{bend}, β_{reg}, $\beta_{\mathcal{F}} > 0$ and the three energy contributions $\mathcal{E}_{bend}[\phi]$ (cf. 7.13), $\mathcal{E}_{reg}[\phi]$ (cf. 7.12), and $\mathcal{E}_{\mathcal{F}}[\phi]$, cf. Equation* (7.9)*, acting on deformations from the set of admissible deformations*

$$\mathcal{A} := \Bigg\{ \phi \in H^{1,p}(\omega_A, \mathbb{R}^2);\ \det D\phi \in L^r(\omega_A),\ \det D\phi > 0 \text{ a.e. in } \omega_A\,, \\ \int_{\omega_A} \det D\phi\, d\xi \leq \mathcal{L}\left(\phi(\omega_A)\right) \Bigg\} \tag{7.15}$$

with $2 < p < \infty$ and $r > 1$. Furthermore, we assume

$$\widetilde{W}(D\phi, \det D\phi) := W\left(\operatorname{tr} \mathcal{G}[\phi], \det \mathcal{G}[\phi]\right)$$

to be convex and that the following growth condition holds:

$$W(a,d) \geq \alpha_l\, a^{\frac{p}{2}} + \alpha_a \left(d^{\frac{r}{2}} + \beta d^{-\frac{s}{2}}\right), \tag{7.16}$$

where α_l, α_a, $\beta > 0$ and $s > \frac{p}{p-2}$. We denote the feature sets on the parameter domains by $\mathcal{F}_A \subset \omega_A$ and $\mathcal{F}_B \subset \omega_B$. $\mathcal{F}_A$ and $\mathcal{F}_B$ are supposed to have Lipschitz boundaries with non-vanishing Lebesgue measure $\mathcal{L}_A(\mathcal{F}_A) > 0$ and $\mathcal{L}_B(\mathcal{F}_B) > 0$. Let $\phi_{\mathcal{F}} \in \mathcal{A}$ be given in such way that the regularization and bending energy of $\phi_{\mathcal{F}}$ are finite and that there exists $\theta < 1$ such that

$$\mathcal{L}_A\left(\mathcal{F}_A \setminus \phi_{\mathcal{F}}^{-1}(\mathcal{F}_B)\right) + \mathcal{L}_B\left(\mathcal{F}_B \setminus \phi_{\mathcal{F}}(\mathcal{F}_A)\right) \leq \theta\, \left(\mathcal{L}_A(\mathcal{F}_A) + \mathcal{L}_B(\mathcal{F}_B)\right). \tag{7.17}$$

If $\beta_{\mathcal{F}}$ fulfills

$$\beta_{bend}\,\mathcal{E}_{bend}[\phi_{\mathcal{F}}] + \beta_{reg}\,\mathcal{E}_{reg}[\phi_{\mathcal{F}}] \leq (1-\theta)\,\beta_{\mathcal{F}}\,\gamma_{\mathcal{F}}\, \left(\mathcal{L}_A(\mathcal{F}_A) + \mathcal{L}_B(\mathcal{F}_B)\right), \tag{7.18}$$

then $\mathcal{E}$ attains its minimum over all deformations $\phi \in \mathcal{A}$ and the minimizer ϕ is continuous and injective in the sense that

$$\operatorname{card} \phi^{-1}(\xi) = 1 \text{ for almost all } \xi \in \phi(\omega_A).$$

There exists a continuous deformation $\psi \in H^{1,\sigma}(\phi(\omega_A))$ with $\sigma = \frac{p(1+s)}{s+p}$, which is almost everywhere on $\phi(\omega_A)$ the inverse of ϕ.

Proof. First, let us remark on the constraint of the set of admissible deformation. Local injectivity of the deformation is ensured by $\det D\phi > 0$ a.e. in ω_A and prevents local overfolding in the interior of the parameter domain. Still, global injectivity can be violated. The additional constraint $\int_{\omega_A} \det D\phi \, d\xi \leq \mathcal{L}(\phi(\omega_A))$ enforces that the mapping is injective in the sense that $\operatorname{card} \phi^{-1}(\xi) = 1$ for almost all $\xi \in \phi(\omega_A)$, because for general deformations we get from the area formula, cf. AMBROSIO ET AL. [6, Theorem 2.71], that

$$\int_{\omega_A} \det D\phi \, d\xi = \int_{\phi(\omega_A)} \operatorname{card}\left(\phi^{-1}(\xi)\right) d\xi.$$

Nevertheless self-contact on the boundary of the deformed parameter domain $\phi(\omega_A)$ is still possible.

We give a brief sketch for the existence proof that relies on the following ingredients:

(i) Estimate from below. There exists $c \in \mathbb{R}$ such that for all $\phi \in \mathcal{A}$ we have $\mathcal{E}[\phi] > c$.

(ii) Compactness. Every sequence $(\phi^k) \subset \mathcal{A}$ that fulfills $\mathcal{E}[\phi^k] < C$ has a subsequence which converges w.r.t. the weak topology in $H^{1,p}$ to $\phi \in \mathcal{A}$.

(iii) Lower-semicontinuity. For every converging sequence $\phi^k \rightharpoonup \phi$ w.r.t. the weak topology in $H^{1,p}$ the energy fulfills

$$\mathcal{E}[\phi] \leq \liminf_{k\to\infty} \mathcal{E}[\phi^k].$$

Then, the proof of existence proceeds as follows. Due to the first condition **(i)** we choose a minimizing sequence (ϕ^k) such that $\inf_{\psi\in\mathcal{A}} \mathcal{E}[\psi] = \liminf_{k\to\infty} \mathcal{E}[\phi^k]$, which by **(ii)** has a subsequence converging to some $\phi \in \mathcal{A}$. Denoting the subsequence again by (ϕ^k) we deduce together with **(iii)**

$$\mathcal{E}[\phi] \leq \liminf_{k\to\infty} \mathcal{E}[\phi^k] = \inf_{\psi\in\mathcal{A}} \mathcal{E}[\psi].$$

The proof of the theorem proceeds in 6 steps. Following BALL [8, 9] we show that the minimizing sequence (ϕ^k) is uniformly convergent to $\phi \in \mathcal{C}^0(\bar{\omega}_A)$ (Step 1 and 2) and that $\det D\phi > 0$ a.e. on ω_A (Step 3). The volume of the neighborhood of the set $\partial\omega_B \cup \partial\mathcal{F}_B$ can be controlled following the singularity control of DROSKE & RUMPF [76] in Step 4 and 5. Based on CIARLET & NEČAS [47], ϕ fulfills the additional constraint $\int_{\omega_A} \det D\phi \, d\xi \leq \mathcal{L}(\phi(\omega_A))$ and we infer that $\phi \in \mathcal{A}$ (Step 6).

Step 1. $\phi_{\mathcal{F}} \in \mathcal{A}$ and $\mathcal{E}[\phi_{\mathcal{F}}] < \infty$, thus

$$\underline{E} := \inf_{\psi\in\mathcal{A}} \mathcal{E}[\psi] < \infty\,.$$

Due to the growth condition (7.16) on W we get $\underline{E} \geq 0$. Let us consider a minimizing sequence

$$\left(\phi^k\right)_{k=0,1,\ldots} \subset \mathcal{A} \quad \text{with} \quad \mathcal{E}[\phi^k] \to \inf_{\psi\in\mathcal{A}} \mathcal{E}[\psi].$$

We denote by $\overline{E}$ an upper bound of the energy $\mathcal{E}$ on this sequence. From the bi-Lipschitz assumption on the parameterizations x_A and x_B we deduce that $g_A^{-1} \in L^\infty(\omega_A)$ and $g_B \in L^\infty(\omega_B)$ and that they are uniformly positive definite. It holds

$$\operatorname{tr}\left(g_A^{-1} A^T (g_B \circ \phi) A\right) = \operatorname{tr}\left(\left((g_B \circ \phi)^{\frac{1}{2}} A g_A^{-\frac{1}{2}}\right)^T \left((g_B \circ \phi)^{\frac{1}{2}} A g_A^{-\frac{1}{2}}\right)\right)$$

and hence,

$$|A|_g := \sqrt{\operatorname{tr}\left(g_A^{-1} A^T (g_B \circ \phi) A\right)}$$

is a norm on linear mappings $A \in \mathbb{R}^{2,2}$ and we can estimate due to the norm equivalence in finite dimension and the bi-Lipschitz assumptions on the parametrization x_A:

$$\begin{aligned}\int_{\omega_A} \left(\operatorname{tr} \mathcal{G}[\phi]\right)^{\frac{p}{2}} \sqrt{\det g_A}\, d\xi &= \int_{\omega_A} \left|(g_B \circ \phi)^{\frac{1}{2}} D\phi\, g_A^{-\frac{1}{2}}\right|_2^p \sqrt{\det g_A}\, d\xi = \int_{\omega_A} \left|D\phi\right|_g^p \sqrt{\det g_A}\, d\xi \\ &\geq C_g \int_{\omega_A} \left|D\phi\right|_2^p d\xi = \left\|D\phi\right\|_{L^p(\omega_A)}^p \end{aligned} \tag{7.19}$$

with constant $C_g > 0$. Together with (7.16) and (7.19) we infer that there exists a constant $C > 0$ such that

$$\mathcal{E}[\phi^k] \geq C \left(\left\|D\phi^k\right\|_{L^p(\omega_A)}^p + \left\|\det D\phi^k\right\|_{L^r(\omega_A)}^r\right).$$

Thus, the sequence $\left\{\left(D\phi^k, \det D\phi^k\right)\right\}_{k=0,1,\dots}$ is uniformly bounded in $L^p \times L^r$. Because of the reflexivity of $H^{1,p} \times L^r$ for $\infty > p, r > 1$, cf. ALT [5, Examples 6.10 (2) and (3)], we can extract a weakly convergent subsequence, again denoted by an index k, such that

$$\left(D\phi^k, \det D\phi^k\right) \rightharpoonup \left(D\phi, d\right)$$

in $H^{1,p} \times L^r$ with $d \in L^r(\omega_A)$. By BALL [8, Lemma 6.1 (i) and Theorem 6.2] or CIARLET [44, Section 7.6, Theorem 7.6-1.] we get that $d = \det D\phi$.

Step 2 assures the control of the $H^{1,p}$-norm. The constraint (7.17) implies the boundedness of the L^p-norm of the deformations. Using (7.17) and (7.18) we obtain that $\left\{\phi^k\right\}_{k=0,1,\dots}$ is uniformly bounded in $H^{1,p}(\omega_A)$:

Applying the general Poincaré-Lemma, cf. ALT [5, 6.15], to estimate the L^p-norm of ϕ^k we have to show that its assumption are fulfilled, i.e. that there exists a constant C_0, such that

$$\phi_{\mathcal{F}} + \xi \in \left\{\phi^k\right\}_{k=0,1,\dots} \Rightarrow \|\xi\| \leq C_0$$

for all $\xi \in \mathbb{R}^2$. If this is not the case, we modify the set $\left\{\phi^k\right\}_{k=0,1,\dots}$ as follows:

Assume that there exists $\phi^{\tilde{k}} \in \left\{\phi^k\right\}_{k=0,1,\dots}$ such that

$$\phi^{\tilde{k}} = \phi_{\mathcal{F}} + \xi$$

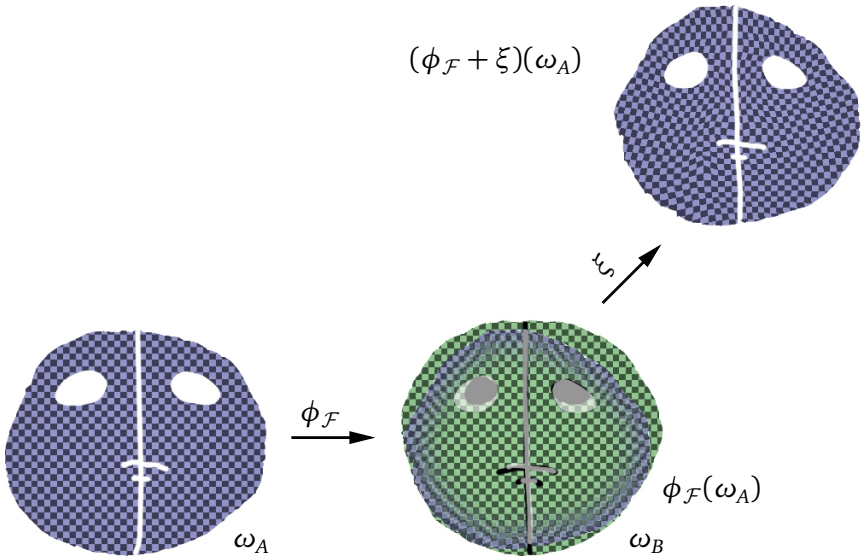

Figure 7.4: There exists $\theta < 1$ such that $\mathcal{L}_A(\mathcal{F}_A \setminus \phi_{\mathcal{F}}^{-1}(\mathcal{F}_B)) + \mathcal{L}_B(\mathcal{F}_B \setminus \phi_{\mathcal{F}}(\mathcal{F}_A)) \leq \theta\,(\mathcal{L}_A(\mathcal{F}_A) + \mathcal{L}_B(\mathcal{F}_B))$ for $\phi_{\mathcal{F}} \in \mathcal{A}$. $(\phi_{\mathcal{F}} + \xi)$ shifts $\mathcal{F}_A$ out of ω_B if $\|\xi\| \geq \operatorname{diam}(\omega_B) + \operatorname{diam}(\phi_{\mathcal{F}}(\omega_A))$.

and $\|\xi\|$ large enough such that $\phi^{\tilde{k}}(\omega_A) \cap \omega_B = \emptyset$ and therefore

$$\mathcal{E}_{\mathcal{F}}[\phi^{\tilde{k}}] = \gamma_{\mathcal{F}}\,\left(\mathcal{L}_A(\mathcal{F}_A) + \mathcal{L}_B(\mathcal{F}_B)\right)\,, \tag{7.20}$$

cf. Figure 7.4. Since $\beta_{\mathcal{F}}$ fulfills Equation (7.18), we obtain

$$\mathcal{E}[\phi_{\mathcal{F}}] = \underbrace{\beta_{bend}\,\mathcal{E}_{bend}[\phi_{\mathcal{F}}] + \beta_{reg}\,\mathcal{E}_{reg}[\phi_{\mathcal{F}}]}_{\overset{(7.18)}{\leq}(1-\theta)\beta_{\mathcal{F}}\gamma_{\mathcal{F}}\left(\mathcal{L}_A(\mathcal{F}_A)+\mathcal{L}_B(\mathcal{F}_B)\right)} + \beta_{\mathcal{F}} \underbrace{\mathcal{E}_{\mathcal{F}}[\phi_{\mathcal{F}}]}_{\overset{(7.17)}{\leq}\theta\,\gamma_{\mathcal{F}}\left(\mathcal{L}_A(\mathcal{F}_A)+\mathcal{L}_B(\mathcal{F}_B)\right)}$$

$$\leq \beta_{\mathcal{F}}\gamma_{\mathcal{F}}\,\left(\mathcal{L}_A(\mathcal{F}_A) + \mathcal{L}_B(\mathcal{F}_B)\right) \overset{(7.20)}{=} \beta_{\mathcal{F}}\,\mathcal{E}_{\mathcal{F}}[\phi^{\tilde{k}}] \leq \mathcal{E}[\phi^{\tilde{k}}]\,.$$

We replace $\phi^{\tilde{k}}$ by $\phi_{\mathcal{F}}$ without loosing the minimal sequence property. Hence the image of the feature set $\mathcal{F}_A$ under ϕ^k remains in ω_B, i.e. $\phi^k(\mathcal{F}_A) \cap \omega_B \neq \emptyset$, for all k. ϕ^k does not shift $\mathcal{F}_A$ out of ω_B and we deduce for $C_0 := \operatorname{diam}(\omega_B) + \operatorname{diam}(\phi_{\mathcal{F}}(\omega_A)) < \infty$

$$\phi_{\mathcal{F}} + \xi \in \left\{\phi^k\right\}_{k=0,1,\ldots} \Rightarrow \|\xi\| \leq C_0\,. \tag{7.21}$$

Since ω_A has Lipschitz-boundary, $2 < p < \infty$, and Equation (7.21) we can apply the general Poincaré-Lemma, cf. Alt [5, 6.15], and obtain that there exists a constant $C < \infty$ with

$$\left\|\phi^k\right\|_{L^p(\omega_A)} \leq C\,\left(\left\|D\phi^k\right\|_{L^p(\omega_A)} + 1\right)\,.$$

Therefore,

$$\left\|\phi^k\right\|_{H^{1,p}(\omega_A)} \leq C\,\left(\left\|D\phi^k\right\|_{L^p(\omega_A)} + 1\right)\,.$$

Let us assume without loss of generality that the sequence of energy values $\mathcal{E}[\phi^k]$ is monotone decreasing and for given $\epsilon > 0$ we get

$$\mathcal{E}[\phi^k] \leq \underline{E} + \epsilon\,.$$

Using again the equivalence of norms in finite dimension, cf. Equation (7.19), we deduce

$$\begin{aligned}\left\|\phi^k\right\|^p_{H^{1,p}(\omega_A)} &\leq C\,\left(\left\|D\phi^k\right\|^p_{L^p(\omega_A)} + 1\right) = C\,\left(\int_{\omega_A} \left|D\phi^k\right|^p_2\,d\xi + 1\right)\\ &\leq C\,\left(\mathcal{E}[\phi^k] + 1\right) \leq C\,\left(\underline{E} + \epsilon + 1\right).\end{aligned}$$

Finally, we obtain that $\left\{\phi^k\right\}_{k=0,1,\ldots}$ is uniformly bounded in $H^{1,p}(\omega_A)$. Due to the reflexivity of $H^{1,p}$ we can extract a weakly convergent subsequence. Since ω_A has Lipschitz boundary and $p > 2$ the Sobolev space $H^{1,p}(\omega_A, \mathbb{R}^2)$ is compactly embedded in $\mathcal{C}^0(\bar{\omega}_A)$ by Sobolev's embedding theorem. Hence, we can again extract a uniformly convergent subsequence and obtain $\phi \in \mathcal{C}^0(\bar{\omega}_A)$.

Step 3. Controlling the set

$$\mathcal{S}_\epsilon := \left\{ x \in \omega_A \middle|\ \det D\phi \leq \epsilon \right\}$$

where the volume shrinks by a factor of more than ϵ for the limit deformation we show that $\det D\phi > 0$ a.e. on ω_A. For given $\epsilon > 0$ we denote by $k(\epsilon)$ the smallest index such that

$$\mathcal{E}[\phi^k] \leq \mathcal{E}[\phi^{k(\epsilon)}] \leq \underline{E} + \epsilon \qquad \forall k \geq k(\epsilon)\,.$$

From Step 1 we know that the sequence $\Psi^k := \left(D\phi^k, \det D\phi^k\right)$ converges weakly to $\Psi := \left(D\phi, \det D\phi\right)$ in $L^p \times L^r$. By Mazur's Lemma, cf. EKELAND & TÉMAM [88, p.6], there exists a family of weights

$$\left(\left(\lambda_i^k\right)_{k(\epsilon)\leq i\leq k}\right)_{k\geq k(\epsilon)}$$

with $\lambda_i^k \geq 0$ and $\sum_{i=k(\epsilon)}^k \lambda_i^k = 1$, such that

$$\sum_{i=k(\epsilon)}^k \lambda_i^k \Psi^i \underset{\substack{k\to\infty\\ L^p\times L^r}}{\longrightarrow} \Psi \qquad \text{and} \qquad \sum_{i=k(\epsilon)}^k \lambda_i^k \phi^i \underset{\substack{k\to\infty\\ L^p}}{\longrightarrow} \phi\,.$$

For simplicity we omit $\sum_{i=k(\epsilon)}^k$ and assume sum convention. Due to the bi-Lipschitz assumptions on the parameterizations x_A and x_B we get

$$\left(\det g_A^{-1}\right)^{-\frac{s}{2}} \left(\det g_B \circ \phi\right)^{-\frac{s}{2}} \sqrt{\det g_A} \geq \widetilde{C} \qquad \text{on } \mathcal{S}_\epsilon. \tag{7.22}$$

Furthermore, we have

$$\det \mathcal{G}[\phi] = \det(g_A^{-1} g_B)\,(\det D\phi)^2 \tag{7.23}$$

and

$$\operatorname{tr} \mathcal{G}[\phi] = \left|(g_B \circ \phi)^{\frac{1}{2}} D\phi\, g_A^{-\frac{1}{2}}\right|^2_2. \tag{7.24}$$

Now, due to the growth condition, the convexity of $\widetilde{W}$, Fatou's Lemma, Equations (7.22) and (7.23) we estimate

$$\begin{aligned}
&\beta_{reg}\,\alpha_a\,\beta\,\widetilde{C}\,\epsilon^{-s}\,\mathcal{L}(\mathcal{S}_\epsilon)\\
&\leq \beta_{reg}\int_{\mathcal{S}_\epsilon}\alpha_a\,\beta\,\widetilde{C}\,\left((\det D\phi)^2\right)^{-\frac{s}{2}}\,d\xi \leq \beta_{reg}\int_{\mathcal{S}_\epsilon}\alpha_a\,\beta\,\left(\det \mathcal{G}[\phi]\right)^{-\frac{s}{2}}\,\sqrt{\det g_A}\,d\xi\\
&\leq \beta_{reg}\int_{\mathcal{S}_\epsilon} W\left(\operatorname{tr}\mathcal{G}[\phi],\det\mathcal{G}[\phi]\right)\,\sqrt{\det g_A}\,d\xi = \beta_{reg}\int_{\mathcal{S}_\epsilon}\widetilde{W}(\Psi)\,\sqrt{\det g_A}\,d\xi\\
&\leq \beta_{reg}\int_{\mathcal{S}_\epsilon}\liminf_{k\to\infty}\widetilde{W}(\lambda_i^k\Psi^i)\,\sqrt{\det g_A}\,d\xi \leq \beta_{reg}\int_{\mathcal{S}_\epsilon}\liminf_{k\to\infty}\lambda_i^k\widetilde{W}(\Psi^i)\,\sqrt{\det g_A}\,d\xi\\
&\leq \liminf_{k\to\infty}\lambda_i^k\,\beta_{reg}\int_{\mathcal{S}_\epsilon}\widetilde{W}(\Psi^i)\,\sqrt{\det g_A}\,d\xi\\
&\leq \liminf_{k\to\infty}\lambda_i^k\,\beta_{reg}\int_{\omega_A}\widetilde{W}(\Psi^i)\,\sqrt{\det g_A}\,d\xi + \beta_{bend}\mathcal{E}_{bend}[\phi^i] + \beta_F\mathcal{E}_F[\phi^i]\\
&\leq \overline{E}
\end{aligned}$$

and infer

$$\mathcal{L}(\mathcal{S}_\epsilon) \leq \frac{\overline{E}\epsilon^s}{\beta_{reg}\,\alpha_a\,\beta\,\widetilde{C}} =: C_S\epsilon^s\,.$$

Since

$$\mathcal{L}(S_0) \leq \mathcal{L}(S_\epsilon), \qquad \forall\epsilon > 0,$$

we infer that $\mathcal{L}(S_0) = 0$ and thus $\det D\phi > 0$ a.e. on ω_A.

Step 4 deals with the singularity set $\mathcal{S}_B := \partial\omega_B \cup \partial\mathcal{F}_B$. Since $\partial\omega_B$ and $\partial\mathcal{F}_B$ have Lipschitz-boundary we know that for given $\delta > 0$ there exists $\epsilon_B(\delta) = \epsilon_B > 0$ such that

$$\mathcal{L}\left(B_{\epsilon_B}(\mathcal{S}_B)\right) \leq \delta\,.$$

From this and the injectivity, cf. BALL [9, Theorem 1 (ii)], we especially deduce the estimate

$$\mathcal{L}\left(\phi^{-1}\left(B_{\epsilon_B}(\mathcal{S}_B)\right)\setminus\mathcal{S}_\epsilon\right) \leq \frac{1}{\epsilon}\int\limits_{\phi^{-1}\left(B_{\epsilon_B}(\mathcal{S}_B)\right)}\det D\phi\,d\xi = \frac{1}{\epsilon}\,\mathcal{L}\left(B_{\epsilon_B}(\mathcal{S}_B)\right) \leq \frac{\delta}{\epsilon},$$

for all $\epsilon > 0$. Hence, we can control the preimage of the neighborhood of the singularity set $\mathcal{S}_B$ with respect to ϕ but restricted to $\omega_A\setminus\mathcal{S}_\epsilon$.

In **Step 5** we show the lower-semicontinuity of the functional $\mathcal{E}$. The measure of the set

$$\mathcal{R}_{\epsilon,\delta} := \left(\phi^{-1}(B_{\epsilon_B}(\mathcal{S}_B)) \setminus \mathcal{S}_\epsilon\right) \cup \mathcal{S}_\epsilon\,,$$

can be estimated in terms of ϵ and δ (cf. Step 3 and 4), i.e.

$$\mathcal{L}\left(\mathcal{R}_{\epsilon,\delta}\right) \leq \frac{\delta}{\epsilon} + C_S \epsilon^s\,.$$

On account of the uniform convergence of the ϕ^i the sequence of $(\chi_{\omega_B} \circ \phi^i \left(\mathbf{h}_B \circ \phi^i - \mathbf{h}_A\right)^2)$ converges uniformly to $\chi_{\omega_B} \circ \phi \left(\mathbf{h}_B \circ \phi - \mathbf{h}_A\right)^2$ on $\omega_A \setminus \mathcal{R}_{\epsilon,\delta}$, due to the uniform continuity of $\mathbf{h}_A$ and $\mathbf{h}_B$ since $\mathcal{M}_A$ and $\mathcal{M}_B$ are $\mathcal{C}^2$-surfaces (cf. Step 2) and the discontinuities of χ_{ω_B} are in $\mathcal{R}_{\epsilon,\delta}$. There exists an index, again denoted by $k(\epsilon)$, so that for all $i \geq k(\epsilon)$

$$\chi_{\omega_B} \circ \phi \left(\mathbf{h}_B \circ \phi - \mathbf{h}_A\right)^2 - \chi_{\omega_B} \circ \phi^i \left(\mathbf{h}_B \circ \phi^i - \mathbf{h}_A\right)^2 \leq \epsilon \quad \text{in } \omega_A \setminus \mathcal{R}_{\epsilon,\delta}\,. \tag{7.25}$$

Analogously, $\chi_{\mathcal{F}_A}\left(1 - \chi_{\mathcal{F}_B} \circ \phi^i\right)$ converges uniformly to $\chi_{\mathcal{F}_A}\left(1 - \chi_{\mathcal{F}_B} \circ \phi\right)$ and $\chi_{\mathcal{F}_B} \circ \phi^i \left(1 - \chi_{\mathcal{F}_A}\right)$ to $\chi_{\mathcal{F}_B} \circ \phi \left(1 - \chi_{\mathcal{F}_A}\right)$ and there exists an index, denoted by $k(\epsilon)$, so that for all $i \geq k(\epsilon)$

$$\chi_{\mathcal{F}_A}\left(1 - \chi_{\mathcal{F}_B} \circ \phi\right) - \chi_{\mathcal{F}_A}\left(1 - \chi_{\mathcal{F}_B} \circ \phi^i\right) \leq \epsilon \quad \text{in } \omega_A \setminus \mathcal{R}_{\epsilon,\delta}\,.$$

Now we are able to estimate $\mathcal{E}[\phi]$:
Using again the convexity of $\widetilde{W}$, Fatou's Lemma and Mazur's Lemma we obtain for $\mathcal{E}_{reg}[\phi]$

$$\begin{aligned}
\mathcal{E}_{reg}[\phi] &= \int_{\omega_A} \widetilde{W}(\Psi)\sqrt{\det g_A}\,d\xi \leq \int_{\omega_A} \liminf_{k\to\infty} \lambda_i^k \widetilde{W}(\Psi^i)\sqrt{\det g_A}\,d\xi \\
&\leq \liminf_{k\to\infty} \lambda_i^k \int_{\omega_A} \widetilde{W}(\Psi^i)\sqrt{\det g_A}\,d\xi = \liminf_{k\to\infty} \lambda_i^k \mathcal{E}_{reg}[\phi^i]
\end{aligned}$$

From Equation (7.25) we infer an estimation for $\mathcal{E}_{bend}[\phi]$

$$\begin{aligned}
\mathcal{E}_{bend}[\phi] = &\int_{\omega_A \setminus \mathcal{R}_{\epsilon,\delta}} \chi_{\omega_B} \circ \phi \left(\mathbf{h}_B \circ \phi - \mathbf{h}_A\right)^2 \sqrt{\det g_A}\,d\xi \\
&+ \int_{\mathcal{R}_{\epsilon,\delta}} \underbrace{\chi_{\omega_B} \circ \phi \left(\mathbf{h}_B \circ \phi - \mathbf{h}_A\right)^2 \sqrt{\det g_A}}_{\leq \left(\|\mathbf{h}_B\|_\infty^2 + \|\mathbf{h}_A\|_\infty^2\right)\|\det g_A\|_\infty^{\frac{1}{2}} =: C_\infty < \infty} d\xi \\
\leq &\liminf_{k\to\infty} \lambda_i^k \int_{\omega_A \setminus \mathcal{R}_{\epsilon,\delta}} \Big(\chi_{\omega_B} \circ \phi \left(\mathbf{h}_B \circ \phi - \mathbf{h}_A\right)^2 - \chi_{\omega_B} \circ \phi^i \left(\mathbf{h}_B \circ \phi^i - \mathbf{h}_A\right)^2 \\
&\qquad + \chi_{\omega_B} \circ \phi^i \left(\mathbf{h}_B \circ \phi^i - \mathbf{h}_A\right)^2\Big) \sqrt{\det g_A}\,d\xi \\
&+ C_\infty\, \mathcal{L}(\mathcal{R}_{\epsilon,\delta}) \\
\leq &\epsilon\, \mathcal{L}(\omega_A) + \liminf_{k\to\infty} \lambda_i^k \int_{\omega_A} \chi_{\omega_B} \circ \phi^i \left(\mathbf{h}_B \circ \phi^i - \mathbf{h}_A\right)^2 \sqrt{\det g_A}\,d\xi + C_\infty\, \mathcal{L}(\mathcal{R}_{\epsilon,\delta})\,.
\end{aligned}$$

Thus

$$\mathcal{E}_{bend}[\phi] \leq \liminf_{k\to\infty} \lambda_i^k \, \mathcal{E}_{bend}[\phi^i] + \epsilon \, \mathcal{L}(\omega_A) + C_\infty \, \mathcal{L}(\mathcal{R}_{\epsilon,\delta}) \, .$$

To get an estimation for the feature energy we reformulate this energy:

$$\begin{aligned} \frac{1}{\gamma_{\mathcal{F}}} \mathcal{E}_{\mathcal{F}}[\phi] &= \int_{\omega_A} \chi_{\mathcal{F}_A} \left(1 - \chi_{\mathcal{F}_B} \circ \phi\right) \sqrt{\det g_A} \, d\xi \\ &\quad + \int_{\omega_A} \chi_{\mathcal{F}_B} \circ \phi \left(1 - \chi_{\mathcal{F}_A}\right) \sqrt{\det g_B(\phi(\xi))} \det D\phi \, d\xi \\ &=: \mathcal{E}_{\mathcal{F}_1}[\phi] + \mathcal{E}_{\mathcal{F}_2}[\phi] \end{aligned} \tag{7.26}$$

Controlling the volume of the preimage of the neighborhood of the set $\partial \mathcal{F}_B$ we infer an estimation for the first summand $\mathcal{E}_{\mathcal{F}_1}[\phi]$:

$$\begin{aligned} \mathcal{E}_{\mathcal{F}_1}[\phi] &= \int_{\omega_A} \chi_{\mathcal{F}_A} \left(1 - \chi_{\mathcal{F}_B} \circ \phi\right) \sqrt{\det g_A} \, d\xi \\ &= \int_{\omega_A \setminus \mathcal{R}_{\epsilon,\delta}} \chi_{\mathcal{F}_A} \left(1 - \chi_{\mathcal{F}_B} \circ \phi\right) \sqrt{\det g_A} \, d\xi + \int_{\mathcal{R}_{\epsilon,\delta}} \underbrace{\chi_{\mathcal{F}_A} \left(1 - \chi_{\mathcal{F}_B} \circ \phi\right)}_{\leq 1} \underbrace{\sqrt{\det g_A}}_{\leq \left\| \det g_A \right\|_\infty^{\frac{1}{2}} := C_A} \, d\xi \\ &\leq \liminf_{k\to\infty} \lambda_i^k \int_{\omega_A \setminus \mathcal{R}_{\epsilon,\delta}} \left(\chi_{\mathcal{F}_A} \left(1 - \chi_{\mathcal{F}_B} \circ \phi\right) - \chi_{\mathcal{F}_A} \left(1 - \chi_{\mathcal{F}_B} \circ \phi^i\right)\right) \sqrt{\det g_A} \, d\xi \\ &\quad + \liminf_{k\to\infty} \lambda_i^k \int_{\omega_A \setminus \mathcal{R}_{\epsilon,\delta}} \chi_{\mathcal{F}_A} \left(1 - \chi_{\mathcal{F}_B} \circ \phi^i\right) \sqrt{\det g_A} \, d\xi + C_A \mathcal{L}(\mathcal{R}_{\epsilon,\delta}) \\ &\leq C_A \epsilon \, \mathcal{L}(\omega_A) + \liminf_{k\to\infty} \lambda_i^k \int_{\omega_A} \chi_{\mathcal{F}_A} \left(1 - \chi_{\mathcal{F}_B} \circ \phi^i\right) \sqrt{\det g_A} \, d\xi \end{aligned}$$

We get

$$\mathcal{E}_{\mathcal{F}_1}[\phi] \quad \leq \quad C_A \epsilon \, \mathcal{L}(\omega_A) \; + \; \liminf_{k\to\infty} \lambda_i^k \int_{\omega_A} \chi_{\mathcal{F}_A} \left(1 - \chi_{\mathcal{F}_B} \circ \phi^i\right) \sqrt{\det g_A} \, d\xi \; + \; C_A \mathcal{L}(\mathcal{R}_{\epsilon,\delta}).$$

Since $\lambda_i^k \det D\phi^i \to \det D\phi$ converges in $L^r(\omega_A \setminus \mathcal{R}_{\epsilon,\delta})$ and

$$\chi_{\mathcal{F}_B} \circ \phi^i \left(1 - \chi_{\mathcal{F}_A}\right) \sqrt{\det g_B(\phi^i(\xi))} \to \chi_{\mathcal{F}_B} \circ \phi \left(1 - \chi_{\mathcal{F}_A}\right) \sqrt{\det g_B(\phi(\xi))}$$

converges uniformly on $\omega_A \setminus \mathcal{R}_{\epsilon,\delta}$, its product converges weakly in $L^1(\omega_A \setminus \mathcal{R}_{\epsilon,\delta})$, cf. ALT [5, Ü 6.2/6.3]. In particular we can choose an index, again denoted by $k(\epsilon)$, to ensure that

$$\left| \int\limits_{\omega_A \setminus \mathcal{R}_{\epsilon,\delta}} \chi_{\mathcal{F}_B} \circ \phi \left(1 - \chi_{\mathcal{F}_A}\right) \sqrt{\det g_B(\phi(\xi))} \det D\phi \, d\xi \right.$$
$$\left. - \int\limits_{\omega_A \setminus \mathcal{R}_{\epsilon,\delta}} \chi_{\mathcal{F}_B} \circ \phi^i \left(1 - \chi_{\mathcal{F}_A}\right) \sqrt{\det g_B(\phi^i(\xi))} \lambda_i^k \det D\phi^i \, d\xi \right| \le \epsilon \,.$$

Splitting the second summand $\mathcal{E}_{\mathcal{F}_2}[\phi]$ in (7.26) into the integral over $\omega_A \setminus \mathcal{R}_{\epsilon,\delta}$ and $\mathcal{R}_{\epsilon,\delta}$

$$\begin{aligned}
\mathcal{E}_{\mathcal{F}_2}[\phi] &= \int\limits_{\omega_A \setminus \mathcal{R}_{\epsilon,\delta}} \chi_{\mathcal{F}_B} \circ \phi \left(1 - \chi_{\mathcal{F}_A}\right) \sqrt{\det g_B(\phi(\xi))} \det D\phi \, d\xi \\
&\quad + \int\limits_{\mathcal{R}_{\epsilon,\delta}} \chi_{\mathcal{F}_B} \circ \phi \left(1 - \chi_{\mathcal{F}_A}\right) \sqrt{\det g_B(\phi(\xi))} \det D\phi \, d\xi \\
&=: \mathcal{E}_{\mathcal{F}_2}^{\omega_A \setminus \mathcal{R}_{\epsilon,\delta}}[\phi] + \mathcal{E}_{\mathcal{F}_2}^{\mathcal{R}_{\epsilon,\delta}}[\phi]
\end{aligned}$$

we get for the first term

$$\begin{aligned}
\mathcal{E}_{\mathcal{F}_2}^{\omega_A \setminus \mathcal{R}_{\epsilon,\delta}}[\phi] &= \int\limits_{\omega_A \setminus \mathcal{R}_{\epsilon,\delta}} \chi_{\mathcal{F}_B} \circ \phi \left(1 - \chi_{\mathcal{F}_A}\right) \sqrt{\det g_B(\phi(\xi))} \det D\phi \, d\xi \\
&= \liminf_{k \to \infty} \Big(\int\limits_{\omega_A \setminus \mathcal{R}_{\epsilon,\delta}} \chi_{\mathcal{F}_B} \circ \phi \left(1 - \chi_{\mathcal{F}_A}\right) \sqrt{\det g_B(\phi(\xi))} \det D\phi \, d\xi \\
&\qquad - \int\limits_{\omega_A \setminus \mathcal{R}_{\epsilon,\delta}} \chi_{\mathcal{F}_B} \circ \phi^i \left(1 - \chi_{\mathcal{F}_A}\right) \lambda_i^k \sqrt{\det g_B(\phi^i(\xi))} \det D\phi^i \, d\xi \\
&\qquad + \int\limits_{\omega_A \setminus \mathcal{R}_{\epsilon,\delta}} \chi_{\mathcal{F}_B} \circ \phi^i \left(1 - \chi_{\mathcal{F}_A}\right) \lambda_i^k \sqrt{\det g_B(\phi^i(\xi))} \det D\phi^i \, d\xi \Big) \\
&\le \epsilon + \liminf_{k \to \infty} \lambda_i^k \int\limits_{\omega_A} \chi_{\mathcal{F}_B} \circ \phi^i \left(1 - \chi_{\mathcal{F}_A}\right) \sqrt{\det g_B(\phi^i(\xi))} \det D\phi^i \, d\xi.
\end{aligned}$$

The second integral $\mathcal{E}_{\mathcal{F}_2}^{\mathcal{R}_{\epsilon,\delta}}[\phi]$ can be estimated as follows

$$\begin{aligned}\mathcal{E}_{\mathcal{F}_2}^{\mathcal{R}_{\epsilon,\delta}}[\phi] &= \int_{\mathcal{R}_{\epsilon,\delta}} \underbrace{\chi_{\mathcal{F}_B}\circ\phi\left(1-\chi_{\mathcal{F}_A}\right)}_{\leq 1} \underbrace{\sqrt{\det g_B(\phi(\xi))}}_{\leq \left\|\det g_B\circ\phi\right\|_\infty^{\frac{1}{2}}:=C_B} \det D\phi\, d\xi \\ &\leq C_B \int_{\mathcal{S}_\epsilon} \det D\phi\, d\xi + C_B \int_{\phi^{-1}(B_{\epsilon_B}(\mathcal{S}_B))} \det D\phi\, d\xi \\ &\leq C_B\,\epsilon\mathcal{L}(\mathcal{S}_\epsilon) + C_B\,\mathcal{L}(B_{\epsilon_B(\mathcal{S}_B)}) \leq C_B\,C_S\,\epsilon^{s+1} + C_B\,\delta.\end{aligned} \tag{7.27}$$

Therefore

$$\mathcal{E}_{\mathcal{F}}[\phi] \leq \liminf_{k\to\infty} \lambda_i^k \mathcal{E}_{\mathcal{F}}[\phi^i] + \epsilon\,\gamma_{\mathcal{F}}(C_A\,\mathcal{L}(\omega_A)+1) + \gamma_{\mathcal{F}}\,C_B\,C_S\,\epsilon^{s+1} + \gamma_{\mathcal{F}}\,C_B\,\delta + C_A\,\mathcal{L}(\mathcal{R}_{\epsilon,\delta}),$$

and we receive for the total energy $\mathcal{E}[\phi]$

$$\begin{aligned}\mathcal{E}[\phi] \leq &\liminf_{k\to\infty} \lambda_i^k \mathcal{E}[\phi^i] + \epsilon\left(\beta_{bend}\,\mathcal{L}(\omega_A) + \beta_{\mathcal{F}}\gamma_{\mathcal{F}}\left(C_A\,\mathcal{L}(\omega_A)+1\right)\right) \\ &+ \beta_{bend}\,C_\infty\,\mathcal{L}(\mathcal{R}_{\epsilon,\delta}) + \beta_{\mathcal{F}}\gamma_{\mathcal{F}}\,C_B\,C_S\,\epsilon^{s+1} + \beta_{\mathcal{F}}\gamma_{\mathcal{F}}\,C_B\,\delta + \beta_{\mathcal{F}}\,C_A\,\mathcal{L}(\mathcal{R}_{\epsilon,\delta}).\end{aligned}$$

For given $\bar{\epsilon}$ we choose ϵ and then δ and the dependent ϵ_B small enough and $k(\bar{\epsilon})$ large enough to ensure that

$$\begin{aligned}&\epsilon\left(\beta_{bend}\,\mathcal{L}(\omega_A) + \beta_{\mathcal{F}}\gamma_{\mathcal{F}}\left(C_A\,\mathcal{L}(\omega_A)+1\right)\right) \\ &\qquad + \beta_{bend}\,C_\infty\,\mathcal{L}(\mathcal{R}_{\epsilon,\delta}) + \beta_{\mathcal{F}}\gamma_{\mathcal{F}}\,C_B\,C_S\,\epsilon^{s+1} + \beta_{\mathcal{F}}\gamma_{\mathcal{F}}\,C_B\,\delta + \beta_{\mathcal{F}}\,C_A\,\mathcal{L}(\mathcal{R}_{\epsilon,\delta}) \leq \bar{\epsilon}\,.\end{aligned}$$

Hence, we get $\mathcal{E}[\phi] \leq \underline{E} + \bar{\epsilon}$ for all $\bar{\epsilon} > 0$ and conclude

$$\mathcal{E}[\phi] \leq \underline{E} = \inf_{\psi\in\mathcal{A}} \mathcal{E}[\psi]\,.$$

Step 6. Following the proof of Theorem 5 in CIARLET & NEČAS [47] and using the weak continuity of $\det D\phi$ we get that the set of admissible deformations is weakly closed and conclude that

$$\int_{\omega_A} \det D\phi\, d\xi \leq \mathcal{L}(\phi(\omega_A))$$

to deduce that $\phi \in \mathcal{A}$. Due to CIARLET & NEČAS [47, Theorem 1] the minimizer is injective almost everywhere in the sense that

$$\operatorname{card}\phi^{-1}(\xi) = 1 \text{ for almost all } \xi \in \phi(\omega_A)\,.$$

In particular the deformation ϕ is almost everywhere invertible.

Now, if ϕ is a diffeomorphism with inverse $\psi = \phi^{-1}$, we deduce that the candidate for the gradient of the inverse $\left(D\phi\right)^{-1}$ is in L^σ with $\sigma = \frac{p(1+s)}{s+p}$:

According to Step 1 there exists a constant $c > 0$ such that

$$\mathcal{E}[\phi] \geq c \left(\left\| D\phi \right\|^p_{L^p(\omega_A)} + \left\| \det D\phi \right\|^r_{L^r(\omega_A)} + \left\| \det D\phi^{-1} \right\|^s_{L^s(\omega_A)} \right). \tag{7.28}$$

Then, together with Hölder's inequality, we get that

$$D\psi(\xi) = (D\phi)^{-1}(\xi) = \det D\phi^{-1} \underbrace{\begin{pmatrix} \phi_{2,2} & -\phi_{1,2} \\ -\phi_{2,1} & \phi_{1,1} \end{pmatrix}}_{=:C[\phi] \in L^p, (7.28)}$$

$$\begin{aligned} \Rightarrow \int_{\phi(\omega_A)} \left\| D\psi \right\|^\sigma d\tilde{\xi} &= \int_{\omega_A} \left(|\det D\phi^{-1}| \, \|\!| C[\phi] |\!\| \right)^\sigma |\det D\phi| \, d\xi \\ &\leq \left(\int_{\omega_A} |\det D\phi|^{\frac{p(1-\sigma)}{p-\sigma}} \right)^{\frac{p-\sigma}{p}} \left(\int_{\omega_A} \|\!| C[\phi] |\!\| \right)^{\frac{\sigma}{p}}. \end{aligned}$$

Due to Equation (7.28), $\det D\phi \in L^{-s}$. Since

$$\frac{p(1-\sigma)}{p-\sigma} = -s \Leftrightarrow \sigma = \frac{(s+1)p}{s+p}$$

we conclude that $\psi \in H^{1,\sigma}(\phi(\omega_A))$. We have that $\sigma > 2$. Then, following the technical proof of BALL [9] that is based on a smoothing argument, one can show that ϕ is a diffeomorphism with inverse ψ a.e. and its gradient at the deformed position is actually $D\phi^{-1}$. By Sobolev's embedding theorem ψ is continuous. □

Remark 7.2.1. As seen above, polyconvexity implies under suitable growth conditions weak lower semicontinuity which allow to prove existence of minimizers applying the framework of the direct methods in the calculus of variations for regularization energies with polyconvex integrands. Practically, we consider the energy density that fulfills equality in Equation (7.16), i.e.

$$\begin{aligned} \widetilde{W}(A,d) &:= \alpha_l \left(\operatorname{tr}\left(g_A^{-1} A^T \, g_B(\phi) A \right) \right)^{\frac{p}{2}} \\ &\quad + \alpha_a \Big(\underbrace{\det(g_A^{-1} g_B(\phi))^{\frac{r}{2}}}_{=:C_1>0} d^r + \beta \underbrace{\det(g_A^{-1} g_B(\phi))^{-\frac{s}{2}}}_{=:C_2>0} d^{-s} \Big) \\ &= \alpha_l \left(\operatorname{tr}\left(g_A^{-1} A^T \, g_B(\phi) A \right) \right)^{\frac{p}{2}} + \alpha_a \left(C_1 \, d^r + \beta \, C_2 \, d^{-s} \right) \end{aligned}$$

with $A = D\phi$ and $d = \det D\phi$. If the conditions of Theorem 7.2.1 hold, this energy is convex, because its second variations are positive, cf. CIARLET [44, Theorem 4.7-7], and we get that $\widetilde{W}$ is *polyconvex*. The first variations of $\widetilde{W}(A,d)$ with respect to A in a direction $G \in \mathbb{R}^{2,2}$ and

d in a direction $g \in \mathbb{R}^2$ are given by

$$\begin{aligned}\partial_A \widetilde{W}(A,d)(G) &= \frac{\partial}{\partial \epsilon}\Big|_{\epsilon=0} \widetilde{W}(A+\epsilon G, d) \\ &= \alpha_l \frac{p}{2} \operatorname{tr}\left(g_A^{-1} A^T g_B(\phi) A\right)^{\frac{p}{2}-1} 2 \operatorname{tr}\left(g_A^{-1} A^T g_B(\phi) G\right),\end{aligned}$$

$$\begin{aligned}\partial_d \widetilde{W}(A,d)(g) &= \frac{\partial}{\partial \epsilon}\Big|_{\epsilon=0} \widetilde{W}(A, d+\epsilon g) \\ &= \alpha_a \left(C_1 r\, d^{r-1} g - \beta\, C_2 s\, d^{-s-1} g\right).\end{aligned}$$

We get for the second variations of $\widetilde{W}(A,d)$ with respect to A in a direction $(G,H) \in \mathbb{R}^{2,2} \times \mathbb{R}^{2,2}$ and with respect to d in a direction $(g,h) \in \mathbb{R}^2$

$$\begin{aligned}\partial_A^2 \widetilde{W}(A,d)(G,H) &= \frac{\partial}{\partial \epsilon}\Big|_{\epsilon=0} \partial_A \widetilde{W}(A+\epsilon H, d)(G) \\ &= \alpha_l \frac{p}{2} \left(\frac{p}{2}-1\right) \operatorname{tr}\left(g_A^{-1} A^T g_B(\phi) A\right)^{\frac{p}{2}-2} \\ &\quad \operatorname{tr}\left(g_A^{-1} A^T g_B(\phi) H\right) \operatorname{tr}\left(g_A^{-1} A^T g_B(\phi) G\right) \\ &\quad + \alpha_l \frac{p}{2} \operatorname{tr}\left(g_A^{-1} A^T g_B(\phi) A\right)^{\frac{p}{2}-1} \operatorname{tr}\left(g_A^{-1} H^T g_B(\phi) G\right),\end{aligned}$$

$$\begin{aligned}\partial_d^2 \widetilde{W}(A,d)(g,h) &= \frac{\partial}{\partial \epsilon}\Big|_{\epsilon=0} \partial_d \widetilde{W}(A, d+\epsilon h)(g) \\ &= \alpha_a \left(C_1 r\,(r-1)\, d^{r-2} h\, g + \beta\, C_2 s\,(s+1)\, d^{-s-2} h\, g\right).\end{aligned}$$

For $d > 0$ and all $g \in \mathbb{R}$, $G \in \mathbb{R}^{2,2}$ we get the desired positiv second variations

$$\begin{aligned}\partial_A^2 \widetilde{W}(A,d)(G,G) &= \alpha_l \frac{p}{2} \left(\frac{p}{2}-1\right) \operatorname{tr}\left(g_A^{-1} A^T g_B(\phi) A\right)^{\frac{p}{2}-2} \operatorname{tr}\left(g_A^{-1} A^T g_B(\phi) G\right)^2 \\ &\quad + \alpha_l \frac{p}{2} \operatorname{tr}\left(g_A^{-1} A^T g_B(\phi) A\right)^{\frac{p}{2}-1} \operatorname{tr}\left(g_A^{-1} G^T g_B(\phi) G\right) > 0,\end{aligned}$$

$$\partial_d^2 \widetilde{W}(A,d)(g,g) = \alpha_a C_1 r\,(r-1)\, d^{r-2} g^2 + \alpha_a \beta\, C_2 s\,(s+1)\, d^{-s-2} g^2 > 0.$$

7.3 Fully practical approximation

In the minimization algorithm, descent directions are needed which involve derivatives of the energy with respect to the deformation ϕ. In taking these derivatives, integrals over the variable boundary $\partial\omega_A[\phi]$ appear. Since these are tedious to treat numerically, for the sake of simplicity we rely on another approximation. Our strategy here is to change the domain of integration $\omega_A[\phi]$ to a superset ω which extends beyond the boundary $\partial\omega_A[\phi]$. Doing so means that special treatment of boundary integrals is no longer necessary, although we are now required to evaluate the integrands of the energies outside of ω_A, and similarly for deformed positions outside of ω_B. To achieve this, we extend our surface quantities onto $\omega \setminus \omega_A$ and $\omega \setminus \omega_B$, respectively, by applying a harmonic extension with natural boundary conditions on $\partial\omega$ to g_A, g_B and $\mathbf{h}_A$, $\mathbf{h}_B$, e.g. we define $\mathbf{h}_A$ as the solution of Laplace's equation on $\omega \setminus \omega_A$ with vanishing flux on $\partial\omega$. Additionally, we introduce a regularized characteristic function

$$\chi^\epsilon_{\mathcal{A}}(\xi) = \max(1 - \epsilon^{-1}\mathrm{dist}(\xi, \mathcal{A}), 0) \tag{7.29}$$

to ignore the energy contributions at some distance ϵ away from $\omega_A[\phi]$. Thus, instead of dealing with a deformation dependent-domain $\omega[\phi]$ in the definition of our different energy contributions, we always integrate over the *whole* image domain ω and replace χ_{ω_B} by the product of the two regularized characteristic functions

$$\chi^\epsilon(\xi) = \chi^\epsilon_{\omega_A}(\xi)\,\chi^\epsilon_{\omega_B}(\phi(\xi))$$

in the bending energy integrand and insert the regularized characteristic function of ω_A as an additional factor in the regularization and feature energy integrand. We denote the resulting energies by

$$\mathcal{E}^\epsilon_{reg},\ \mathcal{E}^\epsilon_{bend},\ \text{and}\ \mathcal{E}^\epsilon_{\mathcal{F}},$$

respectively. We define the energy

$$\mathcal{E}^\epsilon[\phi] := \beta_{bend}\,\mathcal{E}^\epsilon_{bend}[\phi] + \beta_{reg}\,\mathcal{E}^\epsilon_{reg}[\phi] + \beta_{\mathcal{F}}\,\mathcal{E}^\epsilon_{\mathcal{F}}[\phi], \tag{7.30}$$

which measures the quality of a matching deformation ϕ on the domain ω. Following the techniques of the proof already used in the existence proof of Theorem 7.2.1 it is possible to prove the existence of minimizing deformations for the approximation of the matching energy:

Theorem 7.3.1. (Existence of minimizing deformations for $\mathcal{E}^\epsilon$.)
Suppose $\mathcal{M}_A$ and $\mathcal{M}_B$ are $\mathcal{C}^2-$surfaces with bi-Lipschitz continuous parameterizations x_A and x_B over the bounded parameter domains ω_A and ω_B with Lipschitz boundary. The feature sets on the parameter domains are denoted by $\mathcal{F}_A \subset \omega_A$ and $\mathcal{F}_B \subset \omega_B$ and are supposed to have Lipschitz boundaries with non-vanishing Lebesgue measure $\mathcal{L}_A(\mathcal{F}_A) > 0$ and $\mathcal{L}_B(\mathcal{F}_B) > 0$. Let $\phi_{\mathcal{F}} \in \mathcal{A}$ be given analogously to Theorem 7.2.1. Let ω be a compact superset of $\omega_A[\phi_{\mathcal{F}}] = \phi^{-1}_{\mathcal{F}}(\phi_F(\omega_A) \cap \omega_B)$, i.e. $\mathrm{diam}(\omega) > \mathrm{diam}(\omega_B) + \mathrm{diam}(\phi_F(\omega_A))$. Suppose that the surface quantities g_A, g_B and $\mathbf{h}_A$, $\mathbf{h}_B$ are extended onto $\omega \setminus \omega_A$ and $\omega \setminus \omega_B$, respectively, such that $g_A^{-1} \in L^\infty(\omega)$ and $g_B \in L^\infty(\omega)$ and that they are uniformly positive definite and that $\mathbf{h}_A$,

$\mathbf{h}_B$ *are uniformly continuous. We achieve this by applying a harmonic extension with natural boundary conditions on* $\partial\omega$ *to* g_A, g_B *and* $\mathbf{h}_A$, $\mathbf{h}_B$, *e.g. we define* $\mathbf{h}_A$ *as the solution of Laplace's equation on* $\omega \setminus \omega_A$ *with vanishing flux on* $\partial\omega$, *i.e.*

$$\begin{aligned} \Delta f &= 0 \qquad && \text{on } \omega \setminus \omega_C \\ f &= f_C && \text{on } \partial\omega_C \\ \partial_n f &= 0 && \text{on } \partial\omega, \end{aligned}$$

where n *denotes the normal on* $\partial\omega$ *and* $f_C = g_C$ *or* $f_C = \mathbf{h}_C$ *with* $C = A, B$. *Consider the total energy* (7.30) *with* β_{bend}, β_{reg}, $\beta_{\mathcal{F}} > 0$ *and* $\beta_{\mathcal{F}}$ *as in Theorem 7.2.1 and the three energy contributions*

$$\begin{aligned} \mathcal{E}^{\epsilon}_{reg}[\phi] &= \int_{\omega} \chi^{\epsilon}_{\omega_A} W(\operatorname{tr} \mathcal{G}[\phi], \det \mathcal{G}[\phi]) \sqrt{\det g_A}\, d\xi \\ \mathcal{E}^{\epsilon}_{bend}[\phi] &= \int_{\omega} \chi^{\epsilon}_{\omega_A} \chi^{\epsilon}_{\omega_B} \circ \phi \left(\mathbf{h}_B \circ \phi - \mathbf{h}_A \right)^2 \sqrt{\det g_A}\, d\xi \\ \mathcal{E}^{\epsilon}_{\mathcal{F}}[\phi] &= \int_{\omega} \chi^{\epsilon}_{\omega_A} \chi^{\epsilon}_{\mathcal{F}_A} \left(1 - \chi^{\epsilon}_{\mathcal{F}_B} \circ \phi \right) \sqrt{\det g_A}\, d\xi \\ &\quad + \int_{\omega} \chi^{\epsilon}_{\omega_A} \chi^{\epsilon}_{\mathcal{F}_B} \circ \phi \left(1 - \chi^{\epsilon}_{\mathcal{F}_A} \right) \sqrt{\det g_B(\phi(\xi))}\, \det D\phi\, d\xi \end{aligned}$$

acting on deformations from the set of admissible deformations

$$\begin{aligned} \mathcal{A}^{\sharp} := \Big\{ \phi : \omega \to \omega,\ \phi \in H^{1,p}(\omega),\ \det D\phi \in L^r(\omega),\ \det D\phi > 0 \text{ a.e. in } \omega, \\ \int_{\omega} \det D\phi\, d\xi \le \mathcal{L}\left(\phi(\omega)\right) \Big\}, \end{aligned} \tag{7.31}$$

with $2 < p < \infty$ *and* $r > 1$. *Furthermore, we assume*

$$\widetilde{W}(D\phi, \det D\phi) := W\left(\operatorname{tr} \mathcal{G}[\phi], \det \mathcal{G}[\phi]\right)$$

to be convex and that the growth condition (7.16) *of Theorem 7.2.1 holds, where* $s > \frac{p}{p-2}$. *Then* $\mathcal{E}^{\epsilon}$ *attains its minimum over all deformations* $\phi \in \mathcal{A}^{\sharp}$ *and the minimizer* ϕ *is continuous and injective in the sense that*

$$\operatorname{card} \phi^{-1}(\xi) = 1 \text{ for almost all } \xi \in \phi(\omega_A).$$

There exists a continuous deformation $\psi \in H^{1,\sigma}(\phi(\omega_A))$ *with* $\sigma = \frac{p(1+s)}{s+p}$, *which is almost everywhere the inverse of* ϕ.

Proof. Following the proof of Theorem 7.2.1 , we get the desired existence of minimizing deformations for $\mathcal{E}^{\epsilon}$. Let us remark that $\chi^{\epsilon}_{\omega_A}$ and $\chi^{\epsilon}_{\mathcal{F}_B}$ are uniformly continuous, even Lipschitz-continuous and bounded and that we do not have to control the set $\mathcal{S}_B = \partial\omega_B \cup \partial\mathcal{F}_B$. □

The aim of the next section is to study the behavior of the minimizers when the regularization parameter ϵ goes to zero and verify a *variational convergence* of this approximation.

7.3.1 Γ-convergence of the approximated surface matching energy

The convergence of variational functionals is a central interest in many research areas where approximation of variational functionals appear. Γ-convergence is probably the most general notion of variational convergence and provides a well-developed framework for a large class of problems. First, we will collect definitions and Theorems, that will be need in the forthcoming section. We refer to DAL MASO [59] and BRAIDES [29] for comprehensive overviews on this topic.

Definition 7.3.1. (Γ-convergence.)
Let $(\mathcal{A}, d)$ be a metric space. We say that a sequence $\mathcal{E}^\epsilon : \mathcal{A} \to \overline{\mathbb{R}} := \mathbb{R} \cup \{-\infty, \infty\}$ of functionals Γ-convergences to $\mathcal{E} : \mathcal{A} \to \overline{\mathbb{R}}$, iff for all $\phi \in \mathcal{A}$ we have

1. **(**lim inf**-inequality.)** For every sequence (ϕ_ϵ) converging to ϕ in $\mathcal{A}$

$$\mathcal{E}[\phi] \leq \liminf_{\epsilon \to 0} \mathcal{E}^\epsilon[\phi_\epsilon]\,. \tag{7.32}$$

2. **(**lim sup**-inequality.)** There exists a sequence (ϕ_ϵ) converging to ϕ in $\mathcal{A}$ such that

$$\mathcal{E}[\phi] \geq \limsup_{\epsilon \to 0} \mathcal{E}^\epsilon[\phi_\epsilon]\,. \tag{7.33}$$

The function $\mathcal{E}$ is referred to as the Γ-limit of $(\mathcal{E}^\epsilon)$ and denoted by $\mathcal{E} = \Gamma - \lim_{\epsilon \to 0} \mathcal{E}^\epsilon$.

Definition 7.3.2. (Coerciveness conditions.)
Let $(\mathcal{A}, d)$ be a metric space. A function $\mathcal{E} : \mathcal{A} \to \mathbb{R}$ is *coercive* if for every $t \in \overline{\mathbb{R}}$ the closure of the set $\{\mathcal{E} \leq t\}$ is compact, cf. DAL MASO [59, Definition 1.12].
A sequence $(\mathcal{E}^\epsilon)$ is *equi-coercive* on the space $\mathcal{A}$ if for every $t \in \mathbb{R}$ there exists a closed compact subset K_t of $\mathcal{A}$, such that $\{\mathcal{E}^\epsilon \leq t\} \subset K_t$ for every ϵ, cf. DAL MASO [59, Definition 1.12].

Proposition 7.3.2. *Let $(\mathcal{A}, d)$ be a metric space. The sequence $(\mathcal{E}^\epsilon)$ is equi-coercive iff there exists a lower semicontinuous coercive function $G : \mathcal{A} \to \overline{\mathbb{R}}$ such that $\mathcal{E}_\epsilon \geq G$ on $\mathcal{A}$ for every $\epsilon > 0$.*

Proof. A proof can be found in DAL MASO [59, Proposition 7.7]. □

Theorem 7.3.3. *Let $(\mathcal{A}, d)$ be a metric space, $(\mathcal{E}^\epsilon)$ be a sequence of equi-coercive functionals on $\mathcal{A}$, and let $\mathcal{E} := \Gamma - \lim_{\epsilon \to 0} \mathcal{E}^\epsilon$. Then, there exists a minimum point $\phi \in \mathcal{A}$ of $\mathcal{E}$, i.e. $\phi \in \arg\min_{\mathcal{A}} \mathcal{E}$, with*

$$\min_{\mathcal{A}} \mathcal{E} = \mathcal{E}(\phi) = \lim_{\epsilon \to 0} \inf_{\mathcal{A}} \mathcal{E}^\epsilon\,.$$

Moreover, if (ϕ_ϵ) is a precompact sequence such that

$$\lim_{\epsilon \to 0} \mathcal{E}^\epsilon[\phi_\epsilon] = \lim_{\epsilon \to 0} \inf_{\mathcal{A}} \mathcal{E}^\epsilon\,,$$

then for every subsequence of (ϕ_ϵ) converging to ϕ, ϕ is a minimum point of $\mathcal{E}$.

Proof. A proof can be found in BRAIDES [29, Theorem 1.21] or DAL MASO [59, Theorem 7.23]. □

Now, we study the surface matching functionals $\mathcal{E}^\epsilon$ defined in Equation (7.30) with respect to Γ-convergence. To prove Γ-convergence and equi-coercivity the function space as to be a metric space. Since $H^{1,p}(\omega)$ is not metrizable with respect to its weak topology, we extend the overall energies $\mathcal{E}$, cf. Equation (7.14), and $\mathcal{E}^\epsilon$, cf. Equation (7.30), that are defined for deformations ϕ in the set of admissible deformations $\mathcal{A}^\sharp$, cf. (7.15), to the $L^p(\omega, \mathbb{R}^2)$-space by ∞. We define the set of admissible deformations by

$$\widetilde{\mathcal{A}} := \mathcal{A}^\sharp \cup L^p(\omega, \mathbb{R}^2). \tag{7.34}$$

Then, the extensions of the energies are

$$\widetilde{\mathcal{E}}[\phi] := \begin{cases} \mathcal{E}[\phi] & \phi \in \mathcal{A}^\sharp \\ \infty & \text{else} \end{cases} \tag{7.35}$$

and

$$\widetilde{\mathcal{E}}^\epsilon[\phi] := \begin{cases} \mathcal{E}^\epsilon[\phi] & \phi \in \mathcal{A}^\sharp \\ \infty & \text{else.} \end{cases} \tag{7.36}$$

We get the following Γ-convergence result:

Theorem 7.3.4. *Let the assumptions of Theorem 7.2.1 and Theorem 7.3.1 be fulfilled. The overall energies $\widetilde{\mathcal{E}}$, cf. Equation* (7.35)*, and $\widetilde{\mathcal{E}}^\epsilon$, cf. Equation* (7.36)*, are defined for deformations ϕ in the set of admissible deformations $\widetilde{\mathcal{A}}$, cf. Definition* (7.34)*. Then*

$$\Gamma - \lim_{\epsilon \to 0} \widetilde{\mathcal{E}}^\epsilon = \widetilde{\mathcal{E}}$$

with respect to the topology of $L^p(\omega, \mathbb{R}^2)$.

Proof. The proof relies on the techniques already used in the proof of Theorem 7.2.1, especially the restriction to the complement of a set whose measure is arbitrary small. At first we show the lim inf-inequality 7.32 that is

$$\widetilde{\mathcal{E}}[\phi] \leq \liminf_{\epsilon \to 0} \widetilde{\mathcal{E}}^\epsilon[\phi_\epsilon] \quad \forall \phi_\epsilon \to \phi \text{ in } L^p(\omega, \mathbb{R}^2).$$

Case 1. If $\phi \in L^p(\omega, \mathbb{R}^2) \setminus \mathcal{A}^\sharp$, its energy is given by $\widetilde{\mathcal{E}}[\phi] = \infty$.

(a) If $\phi_\epsilon \in L^p(\omega, \mathbb{R}^2) \setminus \mathcal{A}^\sharp$ for all $\epsilon > 0$, $\widetilde{\mathcal{E}}^\epsilon[\phi] = \infty$ and the lim inf-inequality is fulfilled.

(b) Assume that there exists a subsequence, again denoted by ϵ, with $\phi_\epsilon \in \mathcal{A}^\sharp$ converging to $\phi \notin H^{1,p}(\omega, \mathbb{R}^2)$. Then, for all $\delta > 0$ exists an $\epsilon_0 > 0$, such that

$$\widetilde{\mathcal{E}}^\epsilon[\phi_\epsilon] = \mathcal{E}^\epsilon[\phi_\epsilon] \geq c \left\| D\phi_\epsilon \right\|_{L^p}^p > \delta \tag{7.37}$$

for all $\epsilon < \epsilon_0$ with constant $c > 0$, cf. Equation (7.19) in Step 1 of Theorem 7.2.1. Therefore, $\liminf_{\epsilon \to 0} \widetilde{\mathcal{E}}^\epsilon[\phi^\epsilon] = \infty$ and the lim inf-inequality is fulfilled.

Case 2. Let $\phi \in \mathcal{A}^\sharp$. Since $\widetilde{\mathcal{E}}^\epsilon[\phi^\epsilon] = \infty$ for $\phi_\epsilon \in L^p(\omega, \mathbb{R}^2) \setminus \mathcal{A}^\sharp$, let w.l.o.g. $\phi_\epsilon \in \mathcal{A}^\sharp$.

Then, $\widetilde{\mathcal{E}}^\epsilon[\phi^\epsilon] = \mathcal{E}^\epsilon[\phi^\epsilon]$ and $\widetilde{\mathcal{E}}[\phi] = \mathcal{E}[\phi]$. Let $\phi_\epsilon \to \phi$ in $L^p(\omega, \mathbb{R}^2)$. If the sequence $\{D\phi^\epsilon\}$ is not bounded in $L^p(\omega, \mathbb{R}^2)$ we have that $\widetilde{\mathcal{E}}^\epsilon[\phi^\epsilon] = \infty$ and the lim inf-inequality is fulfilled, cf. Inequality (7.37). Because of the reflexivity of $H^{1,p}$ for $\infty > p, r > 1$, cf. ALT [5, Example 6.10 (3)], we can extract a weakly convergent subsequence, again denoted by an index k, such that $\phi_\epsilon \rightharpoonup \phi$ in $H^{1,p}(\omega, \mathbb{R}^2)$. By Sobolev's embedding theorem, we know that the Sobolev space $H^{1,p}(\omega, \mathbb{R}^2)$ is compactly embedded in $\mathcal{C}^0(\omega, \mathbb{R}^2)$. Therefore, $\mathcal{A}^\sharp \subset\subset \mathcal{C}^0(\overline{\omega}, \overline{\omega})$ and hence ϕ_ϵ converges uniformly to $\phi \in \mathcal{C}^0 \cap H^{1,p}$. Now, for $\delta > 0$, we choose $\sigma_B(\delta) = \sigma_B > 0$, such that $\mathcal{L}(B_{\mathcal{S}_B}(\partial\omega_B)) \leq \delta$ (Step 4 of Theorem 7.2.1). We set

$$S_\sigma := \left\{ x \in \omega \,\middle|\, \det D\phi(x) \leq \sigma \right\},$$

and estimate its Lebesgue measure by $\mathcal{L}(S_\sigma) \leq M\sigma^s$. The measure of the preimage of the neighborhood of the singularity set of $\mathcal{S}_B := \partial\omega_B \cup \partial\mathcal{F}_B$ can be controlled by

$$\mathcal{L}\left(\phi^{-1}\left(B_{\sigma_B}(\mathcal{S}_B)\right) \setminus S_\sigma\right) \leq \frac{\delta}{\sigma}.$$

As in Step 5 of Theorem 7.2.1, we define the set

$$\mathcal{R}_{\sigma,\delta} := \left(\phi^{-1}\left(B_{\sigma_B}(\mathcal{S}_B)\right) \setminus S_\sigma\right) \cup S_\sigma$$

whose measure can be estimated by

$$\mathcal{L}\left(\mathcal{R}_{\sigma,\delta}\right) \leq \frac{\delta}{\sigma} + M\sigma^s.$$

We observe that $\chi_{\omega_B} \circ \phi_\epsilon \left(\mathbf{h}_B \circ \phi_\epsilon - \mathbf{h}_A\right)^2$ converges uniformly to $\chi_{\omega_B} \circ \phi \left(\mathbf{h}_B \circ \phi - \mathbf{h}_A\right)^2$ on $\omega \setminus \mathcal{R}_{\sigma,\delta}$. Analogously, $\chi_{\mathcal{F}_A}\left(1 - \chi_{\mathcal{F}_B} \circ \phi_\epsilon\right)$ converges uniformly to $\chi_{\mathcal{F}_A}\left(1 - \chi_{\mathcal{F}_B} \circ \phi\right)$ and $\chi_{\mathcal{F}_B} \circ \phi_\epsilon \left(1 - \chi_{\mathcal{F}_A}\right)$ to $\chi_{\mathcal{F}_B} \circ \phi \left(1 - \chi_{\mathcal{F}_A}\right)$ on $\omega \setminus \mathcal{R}_{\sigma,\delta}$.

We estimate for $\mathcal{E}_{bend}$:

$$\begin{aligned}
\mathcal{E}_{bend}[\phi] = &\int_{\omega_A \setminus \mathcal{R}_{\sigma,\delta}} \chi_{\omega_B} \circ \phi \, \left(\mathbf{h}_B \circ \phi - \mathbf{h}_A\right)^2 \sqrt{\det g_A}\, d\xi \\
&+ \int_{\mathcal{R}_{\sigma,\delta}} \chi_{\omega_B} \circ \phi \, \left(\mathbf{h}_B \circ \phi - \mathbf{h}_A\right)^2 \sqrt{\det g_A}\, d\xi \\
\leq &C_\infty \mathcal{L}(\mathcal{R}_{\sigma,\delta}) + \int_{\omega_A \setminus \mathcal{R}_{\sigma,\delta}} \left(\chi_{\omega_B} \circ \phi \, \left(\mathbf{h}_B \circ \phi - \mathbf{h}_A\right)^2 \right. \\
&\qquad \left. - \chi_{\omega_B} \circ \phi_\epsilon \left(\mathbf{h}_B \circ \phi_\epsilon - \mathbf{h}_A\right)^2\right) \sqrt{\det g_A}\, d\xi \\
&+ \int_{\omega_A \setminus \mathcal{R}_{\sigma,\delta}} \chi_{\omega_B} \circ \phi_\epsilon \, \left(\mathbf{h}_B \circ \phi_\epsilon - \mathbf{h}_A\right)^2 \sqrt{\det g_A}\, d\xi.
\end{aligned}$$

We further estimate

$$\begin{aligned}\mathcal{E}_{bend}[\phi] \leq & C_\infty \mathcal{L}(\mathcal{R}_{\sigma,\delta}) + \sigma C_A \mathcal{L}(\omega_A) \\ & + \int_{\omega_A} \underbrace{\chi_{\omega_B} \circ \phi_\epsilon}_{\leq \chi^\epsilon_{\omega_B} \circ \phi_\epsilon} \left(\mathbf{h}_B \circ \phi_\epsilon - \mathbf{h}_A\right)^2 \sqrt{\det g_A}\, d\xi \\ \leq & C_\infty \mathcal{L}(\mathcal{R}_{\sigma,\delta}) + \sigma C_A \mathcal{L}(\omega_A) + \mathcal{E}^\epsilon_{bend}[\phi_\epsilon].\end{aligned}$$

For given arbitrary $\overline{\sigma}$, on can choose σ and then δ, such that

$$\mathcal{E}_{bend}[\phi] \leq \overline{\sigma} + \mathcal{E}^\epsilon_{bend}[\phi_\epsilon] \qquad \forall \epsilon > 0,$$

and therefore

$$\mathcal{E}_{bend}[\phi] \leq \liminf_{\epsilon \to 0} \mathcal{E}^\epsilon_{bend}[\phi_\epsilon].$$

Using the convexity of $\widetilde{W}$, the semicontinuity of the determinant, Fatou's Lemma and the inequality $\chi_{\omega_A} \leq \chi^\epsilon_{\omega_A}$ we obtain for the regularization energy:

$$\begin{aligned}\mathcal{E}_{reg}[\phi] = & \int_{\omega_A} \widetilde{W}(D\phi, \det D\phi) \sqrt{\det g_A}\, d\xi \\ \leq & \int_{\omega} \liminf_{\epsilon \to 0} \chi^\epsilon_{\omega_A} \widetilde{W}(D\phi_\epsilon, \det D\phi_\epsilon) \sqrt{\det g_A}\, d\xi \\ \leq & \liminf_{\epsilon \to 0} \int_{\omega} \chi^\epsilon_{\omega_A} \widetilde{W}(D\phi_\epsilon, \det D\phi_\epsilon) \sqrt{\det g_A}\, d\xi\end{aligned}$$

and therefore

$$\mathcal{E}_{reg}[\phi] \leq \liminf_{\epsilon \to 0} \mathcal{E}^\epsilon_{reg}[\phi_\epsilon].$$

We define, cf. Step 5 of Theorem 7.2.1,

$$\begin{aligned}\frac{1}{\gamma_{\mathcal{F}}} \mathcal{E}_{\mathcal{F}}[\phi] = & \int_{\omega_A} \chi_{\mathcal{F}_A} \left(1 - \chi_{\mathcal{F}_B} \circ \phi\right) \sqrt{\det g_A}\, d\xi \\ & + \int_{\omega_A} \chi_{\mathcal{F}_B} \circ \phi \left(1 - \chi_{\mathcal{F}_A}\right) \sqrt{\det g_B(\phi(\xi))} \det D\phi \, d\xi \\ = & : \mathcal{E}_{\mathcal{F}_1}[\phi] + \mathcal{E}_{\mathcal{F}_2}[\phi]. \end{aligned} \tag{7.38}$$

$\mathcal{E}^\epsilon_{\mathcal{F}_1}$ and $\mathcal{E}^\epsilon_{\mathcal{F}_2}$ are defined analogously.

We choose ϵ small enough, such that $\sigma_B > \epsilon$, and infer the following estimation for $\mathcal{E}_{\mathcal{F}_1}$:

$$
\begin{aligned}
&\int_{\omega_A} \chi_{\mathcal{F}_A}\left(1-\chi_{\mathcal{F}_B}\circ\phi\right)\sqrt{\det g_A}\,d\xi \\
=&\int_{\omega_A\setminus\mathcal{R}_{\sigma,\delta}} \chi_{\mathcal{F}_A}\left(1-\chi_{\mathcal{F}_B}\circ\phi\right)\sqrt{\det g_A}\,d\xi + \int_{\mathcal{R}_{\sigma,\delta}} \chi_{\mathcal{F}_A}\left(1-\chi_{\mathcal{F}_B}\circ\phi\right)\sqrt{\det g_A}\,d\xi \\
\leq&\int_{\omega_A\setminus\mathcal{R}_{\sigma,\delta}} \left(\chi_{\mathcal{F}_A}\left(1-\chi_{\mathcal{F}_B}\circ\phi\right)-\chi_{\mathcal{F}_A}\left(1-\chi_{\mathcal{F}_B}\circ\phi_\epsilon\right)\right)\sqrt{\det g_A}\,d\xi \\
&+\int_{\omega_A\setminus\mathcal{R}_{\sigma,\delta}} \chi_{\mathcal{F}_A}\left(1-\chi_{\mathcal{F}_B}\circ\phi_\epsilon\right)\sqrt{\det g_A}\,d\xi + C_A\mathcal{L}(\mathcal{R}_{\sigma,\delta}). \\
\leq& C_A\sigma\,\mathcal{L}(\omega_A) + C_A\mathcal{L}(\mathcal{R}_{\sigma,\delta}) + \int_{\omega_A\setminus\mathcal{R}_{\sigma,\delta}} \underbrace{\chi_{\mathcal{F}_A}\left(1-\chi_{\mathcal{F}_B}\circ\phi_\epsilon\right)}_{=\chi^\epsilon_{\mathcal{F}_A}\left(1-\chi^\epsilon_{\mathcal{F}_B}\circ\phi_\epsilon\right)}\sqrt{\det g_A}\,d\xi \\
\leq& C_A\sigma\,\mathcal{L}(\omega_A) + C_A\mathcal{L}(\mathcal{R}_{\sigma,\delta}) + \mathcal{E}^\epsilon_{\mathcal{F}_1}[\phi_\epsilon]
\end{aligned}
$$

Using (7.27) of Step 5 in Theorem 7.2.1 $\mathcal{E}_{\mathcal{F}_2}$, cf. Equation (7.38), can be estimated via

$$
\begin{aligned}
&\int_{\omega_A} \chi_{\mathcal{F}_B}\circ\phi\left(1-\chi_{\mathcal{F}_A}\right)\sqrt{\det g_B(\phi(\xi))}\det D\phi\,d\xi \\
\leq&\int_{\omega_A\setminus\mathcal{R}_{\sigma,\delta}} \chi_{\mathcal{F}_B}\circ\phi\left(1-\chi_{\mathcal{F}_A}\right)\sqrt{\det g_B(\phi(\xi))}\det D\phi \\
&\qquad -\chi_{\mathcal{F}_B}\circ\phi_\epsilon\left(1-\chi_{\mathcal{F}_A}\right)\sqrt{\det g_B(\phi_\epsilon(\xi))}\det D\phi_\epsilon\,d\xi \\
&+\int_{\mathcal{R}_{\sigma,\delta}} \chi_{\mathcal{F}_B}\circ\phi\left(1-\chi_{\mathcal{F}_A}\right)\sqrt{\det g_B(\phi(\xi))}\det D\phi\,d\xi \\
&+\int_{\omega_A\setminus\mathcal{R}_{\sigma,\delta}} \chi_{\mathcal{F}_B}\circ\phi_\epsilon\left(1-\chi_{\mathcal{F}_A}\right)\sqrt{\det g_B(\phi_\epsilon(\xi))}\det D\phi_\epsilon\,d\xi \\
\leq&\sigma\,C_B\,\mathcal{L}(\omega_A) + C_B\,M\,\sigma^{s+1} + C_B\,\delta + \int_{\omega_A\setminus\mathcal{R}_{\sigma,\delta}} \underbrace{\chi_{\mathcal{F}_B}\circ\phi_\epsilon\left(1-\chi_{\mathcal{F}_A}\right)}_{=\chi^\epsilon_{\mathcal{F}_B}\circ\phi_\epsilon\left(1-\chi^\epsilon_{\mathcal{F}_A}\right)}\sqrt{\det g_B(\phi_\epsilon(\xi))}\det D\phi_\epsilon\,d\xi.
\end{aligned}
$$

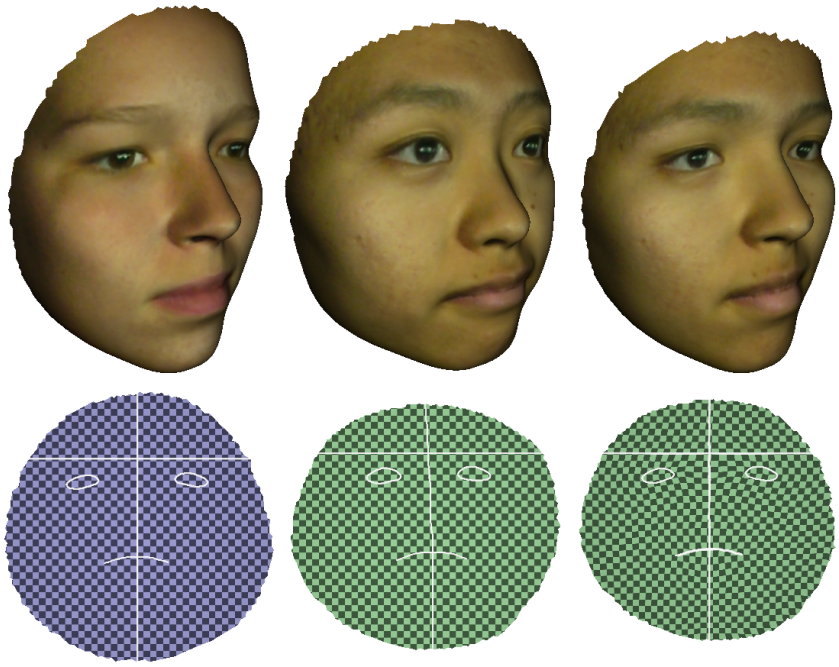

Figure 7.5: The optimal matching deformation between the first and second surface is shown in the parameter domain on the right (bottom). Quantities such as texture maps can be mapped between the surfaces (third surface, top). Image courtesy of LITKE ET AL. [126].

Therefore

$$\mathcal{E}_{\mathcal{F}}[\phi] \leq \sigma\, \gamma_{\mathcal{F}}((C_A + C_B)\mathcal{L}(\omega_A)) + \gamma_{\mathcal{F}}\, C_A \mathcal{L}(\mathcal{R}_{\sigma,\delta}) + \gamma_{\mathcal{F}}\, C_B\, M\, \sigma^{s+1} + \gamma_{\mathcal{F}}\, C_B\, \delta + \mathcal{E}^{\epsilon}_{\mathcal{F}}[\phi_\epsilon].$$

For given arbitrary $\overline{\sigma}$, on can choose σ and than δ, such that

$$\mathcal{E}_{\mathcal{F}}[\phi] \leq \overline{\sigma} + \mathcal{E}^{\epsilon}_{\mathcal{F}}[\phi_\epsilon] \qquad \forall \epsilon < \sigma_B,$$

and therefore

$$\mathcal{E}_{\mathcal{F}}[\phi] \leq \liminf_{\epsilon \to 0} \mathcal{E}^{\epsilon}_{\mathcal{F}}[\phi_\epsilon].$$

Collecting the tree terms of the total energy we get

$$\mathcal{E}[\phi] \leq \liminf_{\epsilon \to 0} \beta_{bend} \mathcal{E}^{\epsilon}_{bend}[\phi_\epsilon] + \liminf_{\epsilon \to 0} \beta_{reg} \mathcal{E}^{\epsilon}_{reg}[\phi_\epsilon] + \beta_{\mathcal{F}} \liminf_{\epsilon \to 0} \mathcal{E}^{\epsilon}_{\mathcal{F}}[\phi_\epsilon] \leq \liminf_{\epsilon \to 0} \mathcal{E}^{\epsilon}[\phi_\epsilon],$$

that is the lim inf-inequality (7.32).

To obtain the desired lim sup-inequality we have to show that for each $\phi \in L^p(\omega, \mathbb{R}^2) \cup \mathcal{A}^\sharp$, there exists a sequence (ϕ_ϵ), $\phi_\epsilon \in L^p(\omega, \mathbb{R}^2) \cup \mathcal{A}^\sharp$ with $\phi_\epsilon \to \phi$ in $L^p(\omega, \mathbb{R}^2)$, such that

$$\widetilde{\mathcal{E}}[\phi] \geq \limsup_{\epsilon \to 0} \widetilde{\mathcal{E}}^\epsilon[\phi_\epsilon].$$

We set $\phi_\epsilon := \phi$.

Case 1. $\phi \in Ł^p(\omega, \mathbb{R}^2) \setminus \mathcal{A}^\sharp$. It holds that

$$\widetilde{\mathcal{E}}[\phi] = \infty = \limsup_{\epsilon \to 0} \widetilde{\mathcal{E}}^\epsilon[\phi_\epsilon]$$

and the lim sup-inequality is fulfilled.

Case 2. $\phi \in \mathcal{A}^\sharp$. Then, $\widetilde{\mathcal{E}}^\epsilon[\phi^\epsilon] = \mathcal{E}^\epsilon[\phi^\epsilon]$ and $\widetilde{\mathcal{E}}[\phi] = \mathcal{E}[\phi]$. Since $\partial\omega_A$ has Lipschitz-boundary and is bounded we know that for given $\bar{\epsilon} > 0$ there exists $\epsilon_A > 0$ such that

$$\mathcal{L}\left(B_{\epsilon_A}(\partial\omega_A)\right) \leq \bar{\epsilon}\,.$$

We obtain for all $\epsilon \leq \epsilon_A$

$$\begin{aligned}
\mathcal{E}^\epsilon_{bend}[\phi] &= \int_\omega \chi^\epsilon_{\omega_A}\chi^\epsilon_{\omega_B} \circ \phi(\mathbf{h}_B \circ \phi - \mathbf{h}_A)^2 \sqrt{\det g_A}\, d\xi \\
&= \int_{\omega \setminus \left(B_{\epsilon_A}(\partial\omega_A) \cup \mathcal{R}_{\sigma,\delta}\right)} \chi_{\omega_A}\chi_{\omega_B} \circ \phi(\mathbf{h}_B \circ \phi - \mathbf{h}_A)^2 \sqrt{\det g_A}\, d\xi \\
&\quad + \int_{B_{\epsilon_A}(\partial\omega_A) \cup \mathcal{R}_{\sigma,\delta}} \chi^\epsilon_{\omega_A}\chi^\epsilon_{\omega_B} \circ \phi(\mathbf{h}_B \circ \phi - \mathbf{h}_A)^2 \sqrt{\det g_A}\, d\xi \\
&\leq \mathcal{E}_{bend}[\phi] + \mathcal{L}(B_{\epsilon_A}(\partial\omega_A)) \left(\frac{\delta}{\sigma} + M\sigma^s\right) C_\infty C_A.
\end{aligned}$$

Analogously, we estimate $\mathcal{E}^\epsilon_{reg}[\phi]$ and $\mathcal{E}^\epsilon_{\mathcal{F}}[\phi]$. Hence, we get the desired lim sup-inequality (7.33)

$$\limsup_{\epsilon \to 0} \mathcal{E}^\epsilon[\phi_\epsilon] = \limsup_{\epsilon \to 0} \mathcal{E}^\epsilon[\phi] \leq \mathcal{E}[\phi]$$

and conclude the Γ-convergence of $\mathcal{E}^\epsilon$ to $\mathcal{E}$. □

In order to apply Theorem 7.3.3, we have to prove the equi-coercivity of $(\mathcal{E}^\epsilon)$. From the proof of Theorem 7.2.1, we also know that $\mathcal{E}_{reg}$ is lower semicontinuous, i.e.

$$\mathcal{E}_{reg}[\phi] \leq \liminf_{\epsilon \to 0} \mathcal{E}_{reg}[\phi_\epsilon] \quad \forall \phi_\epsilon \rightharpoonup \phi \text{ in } H^{1,p}\,.$$

Due to the growth condition of W, $\beta_{reg}\mathcal{E}_{reg}$ is coercive. Since $\mathcal{E}^\epsilon \geq \beta_{reg}\mathcal{E}_{reg}$ the equi-coercivity follows by Proposition 7.3.2.

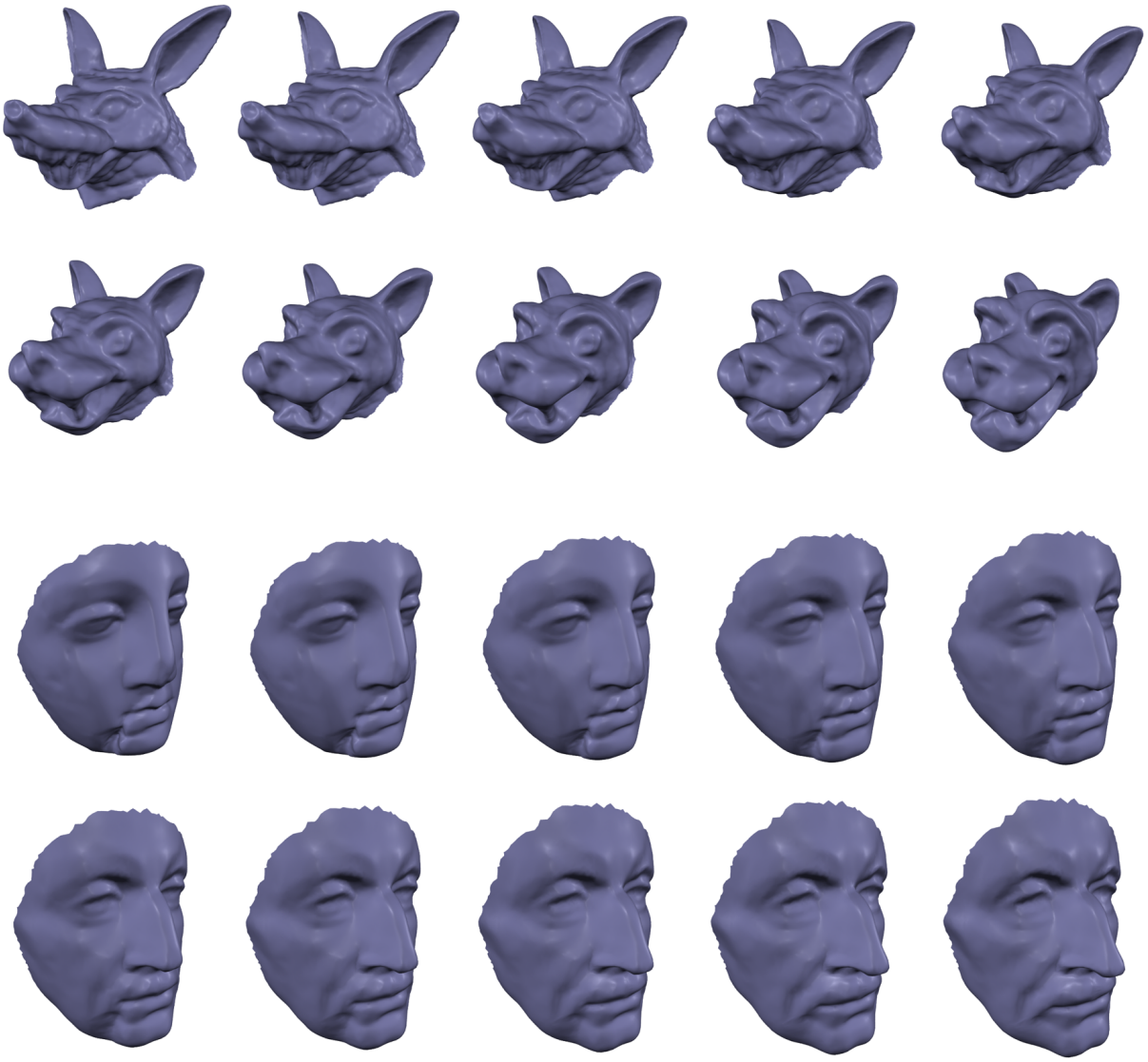

Figure 7.6: 3D morphs between two different faces. Images courtesy of LITKE ET AL. [126].

7.4 Some applications revisited

Figures 7.1 and 7.5 show two examples of surface matching. One application of surface matching is texture mapping. In Figure 7.5 the texture of the second surface is mapped onto the first with $\phi_{\mathcal{M}}^{-1}$. The result underlines also the accuracy of the match, especially around the eyes and mouth. 3D morphs between two different faces based on a linear blend $x \leftarrow \lambda x + (1-\lambda)\phi_{\mathcal{M}}(x)$, $x \in \mathcal{M}_A$ and $\lambda \in [0,1]$, is shown in Figure 7.6, which also demonstrates that the algorithm is good at matching surfaces where certain features does not have an exact correspondences, e. g. as the crack in the surface of Figure 7.6. For details on the matching algorithm we refer to LITKE ET AL. [126].

Bibliography

[1] Cyberware. http://www.cyberware.com/.

[2] Stanford scanning repository. http://graphics.stanford.edu/data/3Dscanrep/.

[3] B. Allen, B. Curless, and Z. Popović. The space of human body shapes: reconstruction and parameterization from range scans. *ACM Transactions on Graphics*, 22(3):587–594, 2003.

[4] F. Almgren, J. E. Taylor, and L. Wang. Curvature-driven flows: a variational approach. *SIAM Journal on Control and Optimization (SICON)*, 31(2):387–438, 1993.

[5] H. Alt. *Lineare Funktionalanalysis, 4. Auflage*. Springer, 2006.

[6] L. Ambrosio, N. Fusco, and D. Pallara. *Functions of bounded variation and free discontinuity problems*. Oxford Mathematical Monographs. Oxford University Press, New York, 2000.

[7] L. Armijo. Minimization of functions having Lipschitz continuous first partial derivatives. *Pacific Journal of Mathematics*, 16(1):1–3, 1966.

[8] J. Ball. Convexity conditions and existence theorems in nonlinear elasiticity. *Archive for Rational Mechanics and Analysis*, 63:337–403, 1977.

[9] J. Ball. Global invertibility of Sobolev functions and the interpenetration of matter. *Proceedings of the Royal Society of Edinburgh*, 88A:315–328, 1988.

[10] E. Bänsch, F. Hausser, O. Lakkis, A. Voigt, and B. Li. Finite Element method for epitaxial growth with attachment-detachment kinetics. *Journal of Computational Physics*, 194:409–434, 2004.

[11] E. Bänsch, P. Morin, and R. Nochetto. Finite Element methods for surface diffusion: the parametric case. *Journal of Computational Physics*, 203, no. 1:321–343, 2005.

[12] E. Bänsch, P. Morin, and R. H. Nochetto. Surface diffusion of graphs: Variational formulation, error analysis and simulation. *SIAM Journal on Mathematical Analysis*, 42(2):773–799, 2004.

[13] J. W. Barrett, H. Garcke, and R. Nürnberg. On the variational approximation of combined second and fourth order geometric evolution equations. *SIAM Journal on Scientific Computing*, 29(3):1006–1041, 2007.

[14] J. W. Barrett, H. Garcke, and R. Nürnberg. A parametric Finite Element method for fourth order geometric evolution equations. *Journal of Computational Physics*, 222(1):441–467, 2007.

[15] J. W. Barrett, H. Garcke, and R. Nürnberg. Numerical approximation of anisotropic geometric evolution equations. *IMA Journal of Numerical Analysis*, 28(2):292–330, 2008.

[16] M. Bauer and E. Kuwert. Existence of minimizing Willmore surfaces of prescribed genus. *International Mathematics Research Notices*, 10:553–576, 2003.

[17] H. Behnke and F. Sommer. *Theorie der analytischen Funktionen einer komplexen Veränderlichen*. Springer, Berlin, 1965.

[18] G. Bellettini, V. Caselles, A. Chambolle, and M. Novaga. Crystalline mean curvature flow of convex sets. Technical Report 7641, UMR CNRS, October 2004.

[19] G. Bellettini and L. Mugnai. Anisotropic geometric functionals and gradient flows. *Banach Center Publications*, 86:21–43, 2009.

[20] G. Bellettini and M. Paolini. Anisotropic motion by mean curvature in the context of Finsler geomety. *QUADERNO*, 49:1–23, 1994.

[21] M. Bergner, A. Dall'Acqua, and S. Fröhlich. Symmetric Willmore surfaces of revolution satisfying natural boundary conditions. Technical report, Universität Magdeburg, 2008. preprint.

[22] M. Bertalmio, A. Bertozzi, and G. Sapiro. Navier-stokes, fluid dynamics, and image and video inpainting. In *IEEE Proceedings of the International Conference on Computer Vision and Pattern Recognition*, volume 1, pages 355–362, 2001.

[23] M. Bertalmio, G. Sapiro, V. Caselles, and C. Ballester. Image inpainting. In *Proceedings of SIGGRAPH 2000*, pages 417–424, New Orleans, USA, July 2000.

[24] W. Blaschke. *Vorlesungen über Differentialgeometrie Bd.3: Differentialgeometrie der Kreise und Kugeln*. Springer, 1923.

[25] A. Bobenko and P. Schroeder. Discrete Willmore flow. In *SIGGRAPH (Courses)*. ACM Press, 2005.

[26] J. S. Bode. *Mean Curvature Flow of Cylindrical Graphs*. PhD thesis, Max-Planck-Instituts für Gravitationsphysik und Freie Universität Berlin, 2007.

[27] T. Bonnesen and W. Fenchel. *Theorie der Konvexen Körper*. Chelsea Publishing Company, 1948.

[28] D. Braess. *Finite Elemente*. Springer, Berlin / Heidelberg / New York, 1997.

[29] A. Braides. Γ-*Convergence for Beginners*. Oxford Lectures Series in Mathematics and Its Applications. Oxford University Press, 2002.

[30] S. C. Brenner and L. R. Scott. *The mathematical theory of Finite Element methods*. Springer-Verlag, 2002.

[31] M. Burger. Numerical simulation of anisotropic surface diffusion with curvature-dependent energy. *Journal of Computational Physics*, 203 (2):602–625, 2005.

[32] M. Burger. Surface diffusion including adatoms. *Communications in Mathematical Sciences*, 4(1):1–51, 2006.

[33] J. W. Cahn and D. W. Hoffmann. A vector thermodynamics for anisotropic surfaces. I. Fundamentals and applications to plane surface junctions. *Surface Science*, 31:368–388, 1972.

[34] J. W. Cahn and D. W. Hoffmann. A vector thermodynamics for anisotropic surfaces. II. Curved and facetted surfaces. *Acta Metallurgica*, 22:1205–1214, 1974.

[35] P. B. Canham. The Minimum Energy of Bending as a Possible Explanation of the Biconcave Shape of the Human Red Blood Cell. *Journal of Theoretical Biology*, 26:61–81, 1970.

[36] A. Chambolle. An algorithm for mean curvature motion. *Interfaces and Free Boundaries*, 6:195–218, 2004.

[37] A. Chambolle and M. Novaga. Convergence of an algorithm for anisotropic mean curvature motion. *SIAM Journal on Mathematical Analysis*, 37:1978–1987, 2006.

[38] I. Chavel. *Eigenvalues in Riemannian Geometry*. Academic Press, 1984.

[39] I. Chavel. *Riemannian Geometry. A Modern Introduction*. Cambridge University Press, 2006.

[40] B.-Y. Chen. An Invariant of Conformal Mappings. In *Proceedings of the American Mathematical Society*, volume 40, pages 563–564, 1973.

[41] B.-Y. Chen. Some conformal invariants of submanifolds and their applications. *Bollettino della Unione Matematica Italiana*, 4(10):380–385, 1974.

[42] G. E. Christensen, S. C. Joshi, and M. I. Miller. Volumetric transformations of brain anatomy. *IEEE Transactions on Medical Imaging*, 16, no. 6:864–877, 1997.

[43] G. E. Christensen, R. D. Rabbitt, and M. I. Miller. Deformable templates using large deformation kinematics. *IEEE Transactions on Medical Imaging*, 5, no. 10:1435–1447, 1996.

[44] P. G. Ciarlet. *Three-Dimensional Elasticity*. Elsevier, New York, 1988.

[45] P. G. Ciarlet. *Theory of plates*, volume II of *Mathematical elasticity*. Elsevier, Amsterdam, 1997.

[46] P. G. Ciarlet. *Mathematical Elasticity, Vol. III: Theory of Shells*. Studies in Mathematics and its Applications. Elsevier, Amsterdam, 2000.

[47] P. G. Ciarlet and J. Nečas. Injectivity and self-contact in nonlinear elasticity. *Archive for Rational Mechanics and Analysis*, 97:171–188, 1987.

[48] U. Clarenz. *Sätze über Extremalen zu parametrischen Funktionalen*. Dissertation, Rheinische Friedrich–Wilhelms–Universität Bonn, 1999.

[49] U. Clarenz. Enclosure theorems for extremals of elliptic parametric functionals. *Calculus of Variations and Partial Differential Equations*, 15:313–324, 2002.

[50] U. Clarenz. The Wulff-shape minimizes an anisotropic Willmore functional. *Interfaces and Free Boundaries*, 6(3):351–359, 2004.

[51] U. Clarenz, U. Diewald, G. Dziuk, M. Rumpf, and R. Rusu. A Finite Element method for surface restoration with smooth boundary conditions. *Computer Aided Geometric Design*, 21(5):427–445, 2004.

[52] U. Clarenz, M. Droske, S. Henn, M. Rumpf, and K. Witsch. Computational methods for nonlinear image registration. DFG Schwerpunktprogramm 1114, Preprint 79, Januar 2005.

[53] U. Clarenz, M. Droske, and M. Rumpf. Towards fast non–rigid registration. In *Inverse Problems, Image Analysis and Medical Imaging, AMS Special Session Interaction of Inverse Problems and Image Analysis*, volume 313, pages 67–84. AMS, 2002.

[54] U. Clarenz and G. Dziuk. Grid optimization via conformal reparametrization. to be published, 2005.

[55] U. Clarenz, G. Dziuk, and M. Rumpf. On generalized mean curvature flow in surface processing. In H. Karcher and S. Hildebrandt, editors, *Geometric analysis and nonlinear partial differential equations*, pages 217–248. Springer, 2003.

[56] U. Clarenz, N. Litke, and M. Rumpf. Axioms and variational problems in surface parameterization. *Computer Aided Geometric Design*, 21(8):727–749, 2004.

[57] U. Clarenz and H. von der Mosel. On surfaces of prescribed f-mean curvature. *Pacific Journal of Mathematics*, 213(1):15–36, 2004.

[58] B. Dacorogna. *Direct Methods in the Calculus of Variations*. Applied Mathematical Sciences 78. Springer–Verlag, Berlin, 1989.

[59] G. Dal Maso. *An Introduction to* Γ*-Convergence*. Birkhäuser, 1993.

[60] A. Dall'Acqua, K. Deckelnick, and H.-C. Grunau. Classical solutions to the Dirichlet problem for Willmore surfaces of revolution. *Advances in Calculus of Variations*, 1(4):379–397, 2008.

[61] A. Dall'Acqua, H.-C. Grunau, S. Fröhlich, and F. Schieweck. Symmetric Willmore surfaces of revolution satisfying arbitrary Dirichlet boundary data. Technical report, Universität Magdeburg, 2008. preprint.

[62] C. A. Davatzikos, R. N. Bryan, and J. L. Prince. Image registration based on boundary mapping. *IEEE Transaction Medical Imaging*, 15(1):112–115, 1996.

[63] K. Deckelnick and G. Dziuk. A fully discrete numerical scheme for weighted mean curvature flow. *Numerische Mathematik*, 91(3):423–452, 2002.

[64] K. Deckelnick and G. Dziuk. Mean curvature flow and related topics. In *Frontiers in numerical analysis. 10th LMS-EPSRC numerical analysis summer school, Durham, UK, July 7-19, 2002*. Springer. Universitext 63-108, 2003.

[65] K. Deckelnick and G. Dziuk. Error analysis of a Finite Element method for the Willmore flow of graphs. *Interfaces and Free Boundaries*, 8:21–46, 2006.

[66] K. Deckelnick and G. Dziuk. Error analysis for the elastic flow of parametrized curves. *Preprint Fakultät für Mathematik und Physik*, 14(07):1–25, 2007.

[67] K. Deckelnick, G. Dziuk, and C. M. Elliott. Computation of geometric partial differential equations and mean curvature flow. *Acta Numerica*, 14:139–232, 2005.

[68] K. Deckelnick, G. Dziuk, and C. M. Elliott. Fully discrete Finite Element approximation for anisotropic surface diffusion of graphs. *SIAM Journal on Mathematical Analysis*, 43(33):1112–1138, 2005.

[69] K. Deckelnick, G. Dziuk, and C. M. Elliott. Fully discrete simi-implicit second order splitting for anisotropic surface diffusion of graphs. *SIAM Journal on Numerical Analysis*, 43:1112–1138, 2005.

[70] M. Desbrun, M. Meyer, P. Schröder, and A. H. Barr. Implicit fairing of irregular meshes using diffusion and curvature Flow. In *Proceedings of SIGGRAPH 99*, Computer Graphics Proceedings, Annual Conference Series, pages 317–324, Aug. 1999.

[71] U. Diewald. *Anisotrope Krümmungsflüsse parametrischer Flächen sowie deren Anwendung in der Flächenverarbeitung*. Dissertation, Universität Duisburg-Essen, Campus Duisburg, 2005.

[72] U. Diewald, S. Morigi, and M. Rumpf. A cascadic geometric filtering approach to subdivision. *Computer Aided Geometric Design*, 19:675–694, 2002.

[73] M. P. do Carmo. *Riemannian geometry*. Birkhäuser, Boston, 1992.

[74] M. P. do Carmo. *Differential forms and applications*. Springer, 1994.

[75] M. Droske. *On Variational Problems and Gradient Flows in Image Processing*. Dissertation, Universität Duisburg-Essen, Campus Duisburg, 2005.

[76] M. Droske and M. M. Rumpf. A variational approach to non-rigid morphological image matching. *SIAM Journal on Applied Mathematics*, 64(2):668–687, 2004.

[77] M. Droske and M. Rumpf. A level set formulation for Willmore flow. *Interfaces and Free Boundaries*, 6(3):361–378, 2004.

[78] M. Droske and M. Rumpf. A variational approach to non-rigid morphological registration. *SIAM Journal on Applied Mathematics*, 64(2):668–687, 2004.

[79] Q. Du, C. Liu, and X. Wang. Simulating the deformation of vesicle membranes under elastic bending energy in three dimensions. *Journal of Computational Physics*, 212:757–777, 2006.

[80] G. Dziuk. Finite Elements for the Beltrami operator on arbitrary surfaces. In S. Hildebrandt and R. Leis, editors, *Partial Differential Equations and Calculus of Variations*, pages 142–155. Springer, 1988.

[81] G. Dziuk. An algorithm for evolutionary surfaces. *Numerische Mathematik*, 58:603–611, 1991.

[82] G. Dziuk. Convergence of a semi-discrete scheme for the curve shortening flow. *Mathematical Models and Methods in Applied Sciences*, 4:589–606, 1994.

[83] G. Dziuk. Discrete anisotropic curve shortening flow. *SIAM Journal on Numerical Analysis*, 36(6):1808–1830, 1999.

[84] G. Dziuk. Computational parametric Willmore flow. *Preprint Fakultät für Mathematik und Physik, Universität Freiburg*, 13-07, 2007.

[85] G. Dziuk, E. Kuwert, and R. Schätzle. Evolution of elastic curves in $\mathbb{R}^n$: Existence and computation. *SIAM Journal on Mathematical Analysis*, 33, no. 5(5):1228–1245, 2002.

[86] I. Eckstein, A. A. Joshi, C.-C. Kuo, J. R. Leahy, and M. Desbrun. Generalized Surface Flows for Deformable Registration and Cortical Matching. In *Medical Image Computing and Computer-Assisted Intervention – MICCAI 2007*, pages 692–700, 2007.

[87] I. Eckstein, J.-P. Pons, Y. Tong, C.-C. J. Kuo, and M. Desbrun. Generalized surface flows for mesh processing. In *SGP '07: Proceedings of the fifth Eurographics symposium on Geometry processing*, pages 183–192, Aire-la-Ville, Switzerland, Switzerland, 2007. Eurographics Association.

[88] I. Ekeland and R. Témam. *Convex Analysis and Variational Problems*, volume 28 of *Classics in applied mathematics*. SIAM, Society for Industrical and Applied Mathematics, 1999.

[89] E. Evans. Bending Resistance and Chemically Induced Moments in Membrane Bilayers. *Biophysical Journal*, 14(12):923–931, 1974.

[90] E. Fein. *d3f – ein Programmpaket zur Modellierung von Dichteströmungen*. GRS, Braunschweig, 1998.

[91] E. Fein. *r3t – a program suite to model transport and retention in porous media*. GRS, Braunschweig, 2003.

[92] I. Fonseca and S. Müller. A uniqueness proof for the Wulff theorem. *Proceedings of the Royal Society of Edinburgh*, 119:125–136, 1991.

[93] G. Friesecke, R. James, and S. Müller. A theorem on geometric rigidity and the derivation of nonlinear plate theory from three dimensional elasticity. *Communications on Pure and Applied Mathematics*, 55(11):1461–1506, 2002.

[94] G. Friesecke, R. D. James, and S. Müller. Rigorous derivation of nonlinear plate theory and geometric rigidity. Technical report, Max-Planck-Institut, Leipzig, 2001.

[95] P. Frolkovic, M. Lampe, and G. Wittum. r3t - software package for numerical simulations of radioactive contaminant transport in groundwater. Technical report, WiR, 2005.

[96] M. Gage and R. Hamilton. The heat equation shrinking convex plane curves. *Journal of Differential Geometry*, 23(1):69–96, 1986.

[97] M. Gage and R. Hamilton. Numerical approximation of anisotropic geometric evolution equations. *Journal of Differential Geometry*, 23:69–96, 1986.

[98] T. Geßner, B. Haasdonk, R. Kende, M. Lenz, R. Neubauer, M. Metscher, M. Ohlberger, W. Rosenbaum, M. Rumpf, R. Schwörer, M. Spielberg, and U. Weikard. A procedural interface to hierarchical grids. Technical report, SFB 256, Rheinische Friedrich–Wilhelms–Universität Bonn, 1999.

[99] Y. Giga. Surface evolution equations: a level set method. Technical report, Hokkaido University Technical Report Series in Mathematics No. 71, 2002.

[100] D. Gilbarg and N. Trudinger. *Elliptic partial differential equations of second order*. Grundlehren der Mathematischen Wissenschaften. 224. Berlin-Heidelberg-New York: Springer–Verlag, 1992.

[101] L. Gottesfeld Brown. A survey of image registration techniques. *ACM Computing Surveys*, 24(4):325–376, 1992.

[102] M. A. Grayson. The heat equation shrinks embedded plane curves to round points. *Journal of Differential Geometry*, 26(2):285–314, 1987.

[103] G. Greiner. Variational Design and Fairing of Spline Surfaces. In *Computer Graphics Forum (Proc. Eurographics '94)*, volume 13, pages 143–154, 1994.

[104] G. Greiner, J. Loos, and W. Wesselink. Data dependent thin plate energy and its use in interactive surface modeling. *Computer Graphics Forum (Proc. Eurographics '96)*, 15(3):175–186, 1996.

[105] E. Grinspun, A. N. Hirani, M. Desbrun, and P. Schröder. Discrete shells. In *2003 ACM SIGGRAPH / Eurographics Symposium on Computer Animation*, pages 62–67, 2003.

[106] E. Grinspun, P. Krysl, and P. Schröder. CHARMS: A Simple Franmework for Adaptive Simulation. In *Computer Graphics (SIGGRAPH '02 Proceedings)*, 2002.

[107] X. Gu and B. C. Vemuri. Matching 3D shapes using 2D conformal representations. In *Medical Image Computing and Computer-Assisted Intervention – MICCAI 2004*, pages 771–780, 2004.

[108] J. Haslinger and R. A. E. Mäkinen. *Introduction to shape optimization: theory, approximation, and computation*. Society for Industrial and Applied Mathematics (SIAM), Philadelphia, PA, USA, 2003.

[109] W. Helfrich. Elastic properties of lipid bilayers: Theory and possible experiments. *Zeitschrift für Naturforschung*, 28c:693–703, 1973.

[110] M. Hinze, R. Pinnau, M. Ulbrich, and S. Ulbrich. *Optimization with PDE Constraints*, volume 23 of *Mathematical Modelling: Theory and Applications*. Springer, 2009.

[111] J. Jost. *Riemannian geometry and geometric analysis*. Springer, 1998.

[112] W. Karush. *Minima of Functions of Several Variables with Inequalities as Side Constraints*. M.sc. dissertation, Dept. of Mathematics, University of Chicago, Chicago, Illinois, 1939.

[113] W. Klingenberg. *A course in differential geometry*. Springer-Verlag, New York, 1978.

[114] L. Kobbelt, S. Campagna, J. Vorsatz, and H.-P. Seidel. Interactive multi-resolution modeling on arbitrary meshes. *ACM SIGGRAPH '98 proceedings*, pages 105–114, 1998.

[115] V. Kraevoy and A. Sheffer. Cross-parameterization and compatible remeshing of 3D models. *ACM Transactions on Graphics*, 23(3):861–869, Aug. 2004.

[116] H. W. Kuhn and A. W. Tucker. Nonlinear programming. In *Proceedings of 2nd Berkeley Symposium*, pages 481–492. University of California Press, 1951.

[117] E. Kuwert and R. Schätzle. The Willmore flow with small initial energy. *Journal of Differential Geometry*, 57(3):409–441, 2001.

[118] E. Kuwert and R. Schätzle. Gradient flow for the Willmore functional. *Communications in Analysis and Geometry*, 10(5):1228–1245 (electronic), 2002.

[119] E. Kuwert and R. Schätzle. Removability of Point Singularities of Willmore Surfaces. Preprint SFB 611, Bonn, 2002.

[120] E. Kuwert and R. Schätzle. Removability of point singularities of Willmore surfaces. *Annals of Mathematics (2)*, 160(1):315–357, 2004.

[121] E. Kuwert and R. Schätzle. Closed surfaces with bounds on their Willmore energy. Technical report, Universität Freiburg, 2008.

[122] A. Lee, D. Dobkin, W. Sweldens, and P. Schroeder. Multiresolution mesh morphing. *Proceedings of SIGGRAPH 99*, pages 343–350, 1999.

[123] J. M. Lee. *Riemannian manifolds: an introduction to curvature*. Springer, 1997.

[124] K. Leichtweiß. *Konvexe Mengen*. Springer-Verlag, Berlin–Heidelberg–New York, 1980.

[125] K. Leschke, F. Pedit, and U. Pinkall. Willmore tori in the 4–sphere with nontrivial normal bundle. *Annals of Mathematics*, 332:381–394, 2005.

[126] N. Litke, M. Droske, M. Rumpf, and P. Schröder. An image processing approach to surface matching. In M. Desbrun and H. Pottmann, editors, *Third Eurographics Symposium on Geometry Processing*, pages 207–216, 2005.

[127] S. Luckhaus and T. Sturzenhecker. Implicit time discretization for the mean curvature flow equation. *Calculus of Variations and Partial Differential Equations*, 3:253–271, 1995.

[128] J. E. Marsden and T. J. R. Hughes. *Mathematical foundations of Elasticity*. Prentice–Hall, Englewood Cliffs, 1983.

[129] U. Mayer and G. Simonett. A numerical scheme for axisymmetric solutions of curvature driven free boundary problems with applications to the Willmore flow. *Interphases and Free Boundaries*, 4(1):89–109, 2002.

[130] O. Nemitz. *Anisotrope Verfahren in der Bildverarbeitung: Gradientenflüsse, Level-Sets und Narrow Bands*. Dissertation, Rheinische Friedrich–Wilhelms–Universität Bonn, 2008.

[131] J. Nitsche. Boundary value problems for variational integrals involving surfaces curvatures. *Quarterly of Applied Mathematics*, LI, no. 2:363–387, 1993.

[132] J. Nitsche. Periodic surfaces that are extremal for energy functionals containing curvature functions. In H. Davis and J. Nitsche, editors, *Proceedings of Workshop Statistical Thermodynamics and Differential Geometry of Microstructured Materials*. IMA vol. in Math. and its Appl., Springer, 1993.

[133] J. Nocedal and S. J. Wright. *Numerical Optimization*. Springer, New York / Berlin, 1999.

[134] N. Olischläger. Optimale konforme Parametrisierungen von topologischen Sphären. Diploma thesis, Universität Duisburg-Essen, Campus Duisburg, 2005.

[135] N. Olischläger and M. Rumpf. Two Step Time Discretization of Willmore Flow. In *Proceedings of the 13th IMA International Conference on Mathematics of Surfaces XIII*, pages 278–292, Berlin, Heidelberg, 2009. Springer-Verlag.

[136] F. Otto. The geometry of dissipative evolution equations: the porous medium equation. *Communications in Partial Differential Equations*, 26(1-2):101–174, 2001.

[137] B. Palmer. Variational Problems which are Quadratic in the Surface Curvatures. In *AIP Conference Proceedings: Curvature and Variational Modeling in Physics and Biophysics*, volume 1002, pages 33–70, 2007.

[138] B. Palmer. Equilibria for anisotropic bending energies. *Journal of Mathematical Physics*, 50(2), 2009.

[139] U. Pinkall and I. Sterling. Willmore surfaces. *The Mathematical Intelligencer*, 9(2):38–43, 1987.

[140] A. Polden. Closed Curves of Least Total Curvature. *SFB 382 Tübingen, Preprint*, 13:, 1995.

[141] A. Polden. *Curves and Surfaces of Least Total Curvature and Fouth–Order Flows*. Ph.d. dissertation, Universität Tübingen, Tübingen, Germany, 1996.

[142] E. Praun, W. Sweldens, and P. Schröder. Consistent mesh parameterizations. In *Proceedings of ACM SIGGRAPH 2001*, Computer Graphics Proceedings, Annual Conference Series, pages 179–184, 2001.

[143] S. D. Rane, J. Remus, and G. Sapiro. Wavelet-domain reconstruction of lost blocks in wireless image transmission and packet-switched networks. In *Image Processing. 2002. Proceedings. 2002 International Conference on 22-25 Sept. 2002, Vol.1*, 2002.

[144] T. Rivière. Analysis aspects of Willmore surfaces. *Inventiones mathematicae*, (174):1–45, 2008.

[145] R. T. Rockafellar. *Convex Analysis*. Princeton University Press, New Jersey, 1970.

[146] M. Rumpf. Variational methods in image matching and motion extraction in level set and pde based reconstruction methods: Applications to inverse problems and image processing. 2009.

[147] M. Rumpf and A. Wierse. GRAPE, Eine Interaktive Umgebung für Visualisierung und numerik. *Informatik, Forschung und Entwicklung*, 7:145–151, 1992.

[148] R. Rusu. An algorithm for the elastic flow of surfaces. *Interfaces and Free Boundaries*, 7:229–239, 2005.

[149] T. V. Savina, A. A. Golovin, and S. H. Davis. Faceting of a growing crystal surface by surface diffusion. *Physical Review*, 67 (021606):021606–1 — 021606–16, 2003.

[150] Schätzle. The Willmore boundary problem. *Calculus of Variations and Partial Differential Equations*, 2009. to appear.

[151] R. Schneider and L. Kobbelt. Discrete Fairing of Curves and Surfaces based on Linear Curvature Distribution. In *Curve and Surface Design: Saint-Malo*, pages 371–380, 1999.

[152] R. Schneider and L. Kobbelt. Generating fair meshes with G^1 boundary conditions. In *Geometric Modeling and Processing Conference Proceedings*, pages 251–261, 2000.

[153] J. Schreiner, A. Asirvatham, E. Praun, and H. Hoppe. Inter-surface mapping. *ACM Transactions on Graphics*, 23(3):870–877, 2004.

[154] U. Seifert. Configurations of fluid membranes and vesicles. *Advances in Physics*, 46:13–137, 1997.

[155] L. Simon. Lectures on geometric measure theory. In *Proceedings of the Centre for Mathematical Analysis*, volume 3. Australian National University, Canberra, 1984.

[156] L. Simon. Existence of surfaces minimizing the Willmore functional. *Communications in Mathematical Analysis*, 1:281–326, 1993.

[157] G. Simonett. The Willmore flow near spheres. *Differential and Integral Equations*, 14(8):1005–1014, 2001.

[158] M. Spivak. *A Comprehensive Introduction to Differential Geometry, five volumes*. Publish or Perish Press, 1979.

[159] J. E. Taylor. Unique structure of solutions to a class of nonelliptic variational problems. In *Proceedings of Symposia in Pure Mathematics*, volume 27, pages 419–427, 1975.

[160] J. E. Taylor. Crystalline variational problems. *Bulletin of the American Mathematical Society*, 84:568–588, 1978.

[161] J. E. Taylor. Some crystalline variational techniques and results. *Astérisque*, 154–155:307–320, 1987.

[162] G. team. *GRAPE Manual*. Rheinische Friedrich–Wilhelms–Universität Bonn, 1997.

[163] V. Thomée. *Galerkin finite element methods for parabolic problems*, volume 25 of *Springer Series in Computational Mathematics*. Springer-Verlag, Berlin, 2nd edition, 2006.

[164] T. Topping. Towards the Willmore conjecture. *Calculus of Variations and Partial Differential Equations*, 11(4):361–393, 2000.

[165] P. A. van den Elsen, E.-J. J. Pol, and M. A. Viergever. Medical image matching: A review with classification. *IEEE Engineering in Medicine and Biology*, 12:26–39, 1993.

[166] J. Van Tiel. *Convex Analysis: An Introductory Text*. John Wiley & Sons Ltd, 1984.

[167] J. L. Weiner. On a problem of Chen, Willmore, et al. *Indiana University Math. J.*, 27:19–35, 1978.

[168] W. Welch and A. Witkin. Variational surface modeling. In *SIGGFRAPH Computer Graphics*, volume 26, pages 157–166, 1992.

[169] J. H. White. A global invariant of conformal mappings in space. In *Proceedings of the American Mathematical Society*, volume 38, pages 162–164, 1973.

[170] T. Willmore. *Riemannian Geometry*. Claredon Press, Oxford, 1993.

[171] T. J. Willmore. *An introduction to differential geometry*. Oxford University Press, 1959.

[172] T. J. Willmore. *Total curvature in Riemannian Geometry*. Ellis Horwood Series in Mathematics and its Applications. Wiley, New York, 1982.

[173] T. J. Willmore. Surfaces in Conformal Geometry. *Annals of Global Analysis and Geometry*, 18(3–4):255–264, 2000.

[174] G. Wulff. Zur Frage der Geschwindigkeit des Wachstums und der Auflösung der Kristallflächen. *Zeitschrift der Kristallographie*, 34:449–530, 1901.

[175] G. Xu and Q. Pan. G^1 surface modelling using fourth order geometric flows. *Computer–Aided Design*, 38(4):392–403, 2006.

[176] S. Yoshizawa and A. G. Belyaev. Fair triangle mesh generation with discrete elastica. In *GMP '02: Proceedings of the Geometric Modeling and Processing – Theory and Applications (GMP'02)*, pages 119–123, Washington, DC, USA, 2002. IEEE Computer Society.

[177] L. Zhang, N. Snavely, B. Curless, and S. M. Seitz. Spacetime faces: high resolution capture for modeling and animation. *ACM Transactions on Graphics*, 23(3):548–558, Aug. 2004.